CONTROL AND MANIPULATION OF SMALL MOLECULES IN THE SCANNING TUNNELING MICROSCOPE

by
Scott Andrew Holmes

A thesis submitted to
The University of Birmingham
for the degree of
DOCTOR OF PHILOSPHY

Nanoscale Physics, Chemistry and Engineering Research Laboratory
School of Physics and Astronomy
College of Engineering and Physical Sciences
University of Birmingham
31 January 2017

Abstract

In this thesis methodologies for manipulation and control of two different surface-molecule systems are explored. Thermal effects play a key role in all of the mechanisms studied. The first methodology studied is self-assembly of dimethyl-disulfide on Au(111). Conformational change and diffusion of Au-adatom-dithiolate complexes are investigated over the temperature range 77 K to 200 K. The second manipulation methodology is non-local manipulation of Si(111) − 7×7: PhCl. Non-local desorption of the chemisorbed molecules by hole injection is studied in the temperature range 77 K to 293 K, and compared to previous results on the electron-induced process in the same temperature range. It is found that desorption proceeds through the physisorbed state for both carriers, but that there is an additional mechanism which differs depending on the charge carrier. Non-local manipulation of physisorbed chlorobenzene is studied at low temperature, where a new species is found to be created in non-local manipulation experiments at 4.6 K. It is speculated that this is a result of efficient dissociation of the physisorbed molecules.

Acknowledgements

This thesis would not have been completed without the help of a great many people. Firstly, I would like to thank my supervisor Richard Palmer, for giving me the opportunity to study at NPRL, and his advice and encouragement throughout the PhD. I would also like to thank my co-supervisor Quanmin Guo, for always being willing to help, both in the lab and out. In addition, I gratefully acknowledge the support of EPSRC for providing the funding for my PhD.

The help of everyone who has read or commented on sections of my thesis is greatly appreciated, and I apologise for my lack of brevity. Thank you Patrick, Shane, and Quanmin (again). I would especially like to thank Wolfgang for his tireless help with last minute corrections; he helped make a stressful time far less stressful.

My mentor Tian taught me how to use the intransigent machine that is a scanning tunneling microscope, and his 'just keep pulsing' attitude has got me through a number of difficult experimental times. Thanks Tian.

In addition, I would like to thank everyone in the lab who has made my time at Birmingham a pleasure. Particularly, my sibling PhD students: Caroline, for keeping in touch to share the pain of writing up; Dogan, for being an example of a perfectly organised being, and his unceasing optimism; Nan, for being both a nice person to be around and a frighteningly efficient PhD student; And, last (but most certainly not least) Will for somehow managing to survive living with me both in and outside the lab for a whole year, and still being an incredibly supportive friend at the end of it.

I would also like to thank my family for their constant encouragement throughout my life, and say congratulations to my sister for beginning her journey towards writing one of these pages herself.

Lastly, I would like to thank my partner Rachel for still being with me at the end of this process. I can't thank her enough.

Contents

CHAPTER 1

Introduction

1.1 Overview

There is great interest in molecular structures on surfaces and their manipulation, both to study the limits of our ability to control physical structures, and to exploit these techniques to create new surface functionalities. This thesis examines two methods of controlling and structuring molecules at the nanoscale.

The first of these is non-local manipulation of chlorobenzene on the silicon surface, investigating the effects of temperature on the hole-induced desorption of chlorobenzene in the scanning tunneling microscope, and the electron-induced dissociation of the molecules at low temperature. In these experiments it was found that temperature has a strong effect on the result of non-local manipulation experiments, and that it can be used to tailor the outcome of the non-local experiments. Building upon previous work in our group, these experiments constitute one of the most complete studies of the interactions between charge carriers from a scanning tunneling microscope tip and adsorbates on a semiconductor surface. These results are particularly relevant to other experiments which probe the interaction of low energy electrons with adsorbates, such as photodesorption and electron scattering from molecules at surfaces, as they constitute atomically resolved studies of these processes.

The second set of experiments investigates the various dynamical processes that can take place in the low-coverage phase of a self-assembled monolayer of alkanethiolates on gold, such as diffusion and conformational change, and the effect of temperature on these processes. Thiolate based self-assembled monolayers are one of the most studied self-assembled systems. They act as model systems to help understand the behaviour of more complicated systems. The experiments in this thesis study the behaviour of the low coverage phase in great detail, helping to understand the forces that play a role in the formation of these monolayers and their relative strengths. In addition, several new stable structures were studied which seem to play an important role at sites with

lower coordination surface atoms. Together, these results may be particularly important when considering monolayer protected metal clusters, where the high surface curvature means that the molecular packing plays a smaller role in determining the structure of the protective monolayer, and there is an abundance of lower-coordinated sites. Both experiments aim to exert control over surfaces at the smallest scales via mechanisms that affect many molecules at once, either by manipulation using charge carriers from the scanning tunneling microscope, or by careful choice of surface molecule system.

The remainder of this chapter introduces scanning tunneling microscopy, the main analytical technique of the thesis, before looking in detail at its application to atomic manipulation and self-assembly. Chapter 2 looks at the technical details of the experimental methods used. Chapter 3 then details the experiments on the dynamical processes occurring in the low coverage methanethiolate phase. Chapter 4 explores the effect of temperature on non-local atomic manipulation via hole injection. Finally, Chapter 5 studies the physisorbed state of chlorobenzene to try and open up new non-local manipulation channels.

1.2 Scanning tunneling microscopy

Scanning probe microscopy (SPM) is one of a number of present day techniques which can be used to investigate surfaces at the atomic scale, but the only one that can be used to manipulate them atom-by-atom. It excels at providing information on the local electronic and geometric structure of surfaces, making the SPM a useful tool for imaging individual surface features that can be difficult to investigate via diffraction based techniques, which rely on periodic repetition of features to generate a signal. However, this strength can also be a weakness of the instrument, as it is important to repeat time consuming experiments to ensure their statistical significance.

SPM techniques all generate an image by rastering a probe across a surface with atomic precision, recording some signal of interest as a function of position. In the case of

the scanning tunneling microscope (STM) this signal is the current of electrons tunneling across the vacuum gap between a metal tip and a conductive sample. It is the ability of this probe to address individual atomic locations that makes SPM uniquely capable of manipulating structures on the atomic scale in a sophisticated manner. This is not possible with other techniques such as scanning transmission electron microscopy (STEM), which only allow for imaging and spectroscopic analysis[1]. Manipulation can take many forms and will be investigated in more detail in Section 1.3.

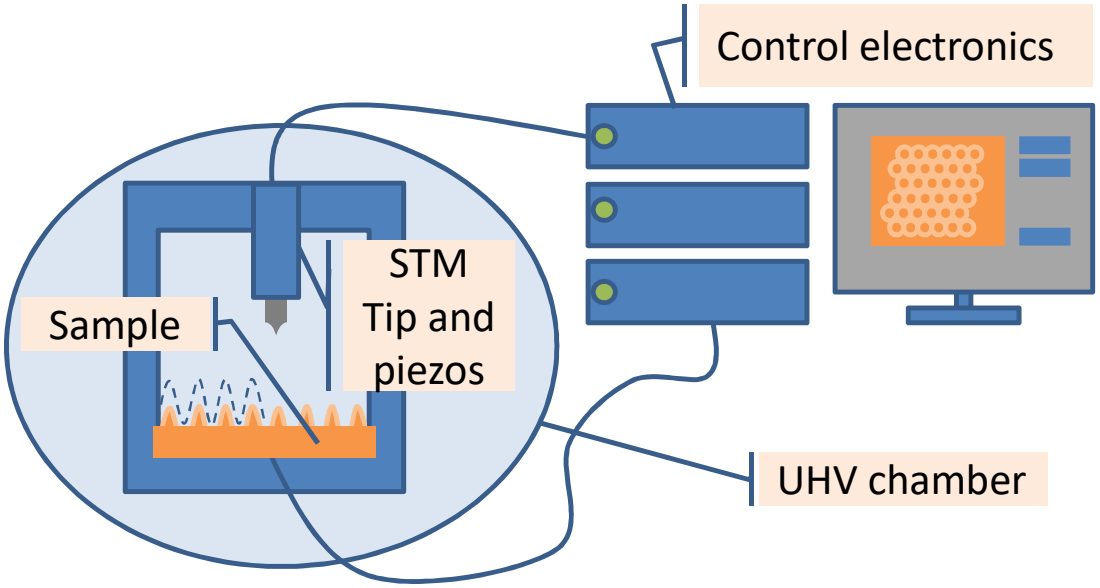

Figure 1.1: A simple schematic of a UHV scanning tunneling microscope, showing control electronics and a tip and sample attached to the STM head inside a UHV chamber. The UHV chamber is not required for STM operation but is shown here for completeness.

1.2.1 STM theory

An understanding of the origin of the tunneling current between tip and sample is crucial to interpreting the images and other data acquired using the STM, as it is this variation of the current in response to changes in tip-sample separation that is the key to the resolution obtainable with the STM. In addition, the sensitivity of the tunneling current

[1]There are some instances of manipulation of nanoscale objects such as clusters using the electron beam in STEM, but these methods do not provide anywhere near the level of control available in STM.

to the surface electronic structure allows for spectroscopy on individual atomic sites, known as scanning tunneling spectroscopy (STS). However, the difficulty in disentangling the geometric and electronic contributions to the tunneling current is one of the main difficulties in interpreting STM images.

The tunneling current is a quantum phenomenon arising from electrons tunneling through the energy barrier between tip and sample. The simplest theoretical treatment of the system is to model the system as a particle tunneling through an energy barrier in one dimension, as found in many undergraduate textbooks [1]. Solving the Schrödinger equation such that the wavefunction and its derivative are continuous across the boundary gives the following transmission probability:

$$T = \frac{16k_0^2\kappa^2}{\left(k_0^2 + k_1^2\right)^2} e^{-2\kappa d}, \tag{1.1}$$

where d is the width of the gap, and k_0 and k_1 are the particle wavevectors outside and inside the gap respectively, $\kappa = ik_1$ is a real quantity. The main insight to be gained from this simple treatment is that the tunneling probability decays exponentially across the vacuum gap. This exponential decay of the transmission probability, and hence tunneling current, is what gives the STM its incredible resolution normal to the sample surface: a minute change in the vacuum gap gives an exponentially larger change in the tunneling current.

The simple barrier penetration approach does not consider any details of the potential experienced by the particle outside of the vacuum barrier, completely ignoring the band structure of the tip and sample materials. A more complete approach to tunneling between two materials separated by a vacuum gap, developed by Bardeen, has been adapted to the STM system [2–4]. It uses methods from perturbation theory to include tip and sample electronic structure, whilst still remaining relatively uncomplicated. The Schrödinger

equation for the complete tip-sample system is,

$$i\hbar\frac{\partial\Psi(z,t)}{\partial t} = \left[-\frac{\hbar^2}{2m}\frac{\partial^2}{\partial^2 z} + U_{\text{tip}} + U_{\text{samp}}\right]\Psi(z,t), \tag{1.2}$$

where z is the distance between tip and sample, m is the mass of the tunneling electron, $\Psi(z,t)$ is its wavefunction, and $U_{\text{tip/samp}}$ is the potential experienced inside the tip or sample, respectively. This equation is treated perturbatively, working from the solutions for each electrode in the absence of the other. The presence of the second potential implies that electrons in a stationary state of one electrode at $t = 0$ can evolve into stationary states of the other electrode over time. Writing ψ^{tip} as χ and ψ^{samp} as ϕ and substituting

$$\Psi(z,t) = \chi_n(z)e^{-iE_nt/\hbar} + \sum_{m=0}^{\infty} c_m(t)\phi_m(z)e^{-iE_mt/\hbar} \tag{1.3}$$

into Equation (1.2) allows the probability amplitudes for tunneling between a specific tip and sample state to be determined (for full derivation steps see [4, page 49 and 50]), giving

$$p_{nm}(t) = \frac{2\pi t}{\hbar}|M_{nm}|^2\rho_{\text{s}}(E_m)\delta(E_m - E_n), \tag{1.4}$$

where p_{nm} is the probability of tunneling from state n to state m, and ρ_{s} is the density of states in the sample. The quantity M_{nm} is an associated matrix element

$$M_{nm} = \int_{z>s} \chi_n U_{\text{s}}\phi_m^* \text{dV}, \tag{1.5}$$

where s is a value of z chosen to lie between tip and sample[2], it contains the details of the coupling between each tip and surface state. Finally, the delta function expresses the *elastic tunneling condition*, which arises in the derivation of Equation (1.4), and implies that tunneling only occurs between states of the same energy.

To derive an expression for the tunneling current, the probability of tunneling from

[2]Note that it is not necessary to integrate over all space as U_{samp} will be zero, hence the given integration region.

each specific tip state is integrated over all contributing tip states. It is therefore necessary to approximate the energy dependence of the tunneling matrix element. As would be expected given the barrier penetration approach presented in Equation (1.1), the matrix element can be shown to be proportional to $\exp(-\kappa_n s)$, where $\kappa_n = (\sqrt{2mE_n}/\hbar)$. Substitution of this energy dependence into Equation (1.4) implies the tunneling current is of the form

$$I = \frac{4\pi e}{\hbar} \int_{E_f}^{E_f+eV} \rho_{\mathrm{s}}(E)\rho_{\mathrm{t}}(E-eV)|M(0)|^2 \exp\left(\frac{2\sqrt{2mE}s}{\hbar}\right) \mathrm{d}E. \tag{1.6}$$

Importantly the exponential dependence of M causes the majority of the contribution to the tunneling current to come from around the Fermi level of the tip[3]. Tunneling from states lower in energy is exponentially suppressed. When imaging at negative bias most of the tunneling current comes from around the Fermi level of the sample. This has important consequences for probing surface electronic structure as it implies that at negative bias the sample images the tip electronic structure rather than the other way around [5]. An important point is that now all of the z dependence of the tunneling current is contained in the energy independent part of the matrix element, which measures the overlap of tip and sample states in the vacuum gap.

The addition of the surface and tip electronic structure into this theory of the tunneling junction enables it to explain the spectroscopic capabilities of the STM. Simply differentiating Equation (1.6) gives

$$\left(\frac{\mathrm{d}I}{\mathrm{d}E}\right)_{E=eV} \approx A(z)\rho_s(E_f+eV)\rho_t(E_f) \propto \frac{\mathrm{d}I}{\mathrm{d}V}, \tag{1.7}$$

where $A(z)$ is energy independent, and contains all other details apart from the density-of-states (DOS). This equation indicates that the change of tunneling current with applied bias is proportional to the DOS of the sample, a property which can be exploited to

[3]The extra factor of two in the exponential in Equation (1.6) arises when squaring M.

map electronic states of the surface with atomic precision. As in most spectroscopy the energetic position of the spectroscopic features is the quantity of interest: the overall intensity of the signal is less important. Typically spectra are normalized as

$$G(V) = \frac{\mathrm{d}I/\mathrm{d}V}{\overline{I/V}}, \tag{1.8}$$

where I/V is usually averaged to avoid divergences when the denominator gets smaller than the numerator.

So far the discussion has not covered evaluating the above overlap orbitals. Using the approximation that the tip apex is spherical and substituting a generic spherically symmetric wavefunction into Equation (1.6), together with bloch-wavefunctions for the surface states, will yield the well known Tersoff-Hamann approximation [6]. This approximation describes the result of imaging with an s-wave tip state, and is applicable for feature sizes $>0.3\,\mathrm{nm}$ [4], however it can not explain atomic resolution in the STM without the inclusion of higher angular momentum tip states. The Tersoff-Hamann approximation does allow for estimates of STM images to be derived from modelling by density functional theory (DFT), as it predicts that the STM images the local density of states (LDOS) of the sample at the centre of curvature of the tip apex, a quantity which is easily extracted from theoretical models. Tip states that arise from atomic states with greater angular dependence, such as a p_z state or a d_{z^2} state, provide greater spatial resolution [4]. One modern exploitation of this is to attach a molecule with highly orientated states to the tip and use this as the tip apex, usually CO, producing very high resolution images, particularly of adsorbates [7]. The symmetry in the overlap integral between tip and sample states implies that imaging a surface of s-states with a p-state tip gives the same image as imaging a surface of p-states with an s-state tip, this is called the reciprocity principle [4, 8]. The tip can in essence be thought to provide an image response function for the STM, where it is always convoluted with surface structure.

The theory described above is vital for the interpretation of STM images and scanning

tunneling spectra (STS). Three key phenomena should be noted: firstly, the distance dependence of the tunneling current, obvious from the most basic treatment; secondly, the presence of an energy dependence of the tunneling probability; and finally, a tunneling matrix element. The distance dependence gives STM images their geometric contribution, and the latter two points represent the contribution of the surface and tip electronic structure to the imaging process. Importantly it is possible for one component of the imaging process to obscure the other. For instance, crossing from an area with higher conductivity (larger matrix element or DOS) to one of lower conductivity (smaller matrix element or DOS) in constant current mode will cause the tip to move towards the surface in order to maintain the current set-point, utilising the tip-sample separation dependence of the current to compensate for the decreased coupling between states, this gives the appearance of a depression: even though in reality the low conductivity area could even protrude physically from the surface. This is very important when examining STM images, but is also important when comparing spectra between two areas. The aim is to extract the variation in electronic structure, but in the spectra this can be convoluted with geometric variation of the sample. This is highlighted in the work of Krenner et al. [9], which examines how the method of taking spectra affects maps of confined electronic states on surfaces.

The STM is capable of operating in many environments, liquid phase [10], ambient conditions [11], and vacuum (see Section 1.3) are the most common. Though a vacuum environment is not necessary for STM operation it is desirable as it allows for samples to be maintained in a clean state for long periods. It is also a necessity for low temperature STM as at cryogenic temperatures the sticking coefficient of the surface will be ~ 1, meaning that any adventitious material will stick immediately, rapidly covering the surface with physisorbed material. Vacuum also allows for the use of tungsten tips, which would become covered with an oxide layer in ambient conditions [12], leading to unpredictable behaviour.

1.3 Atomic manipulation

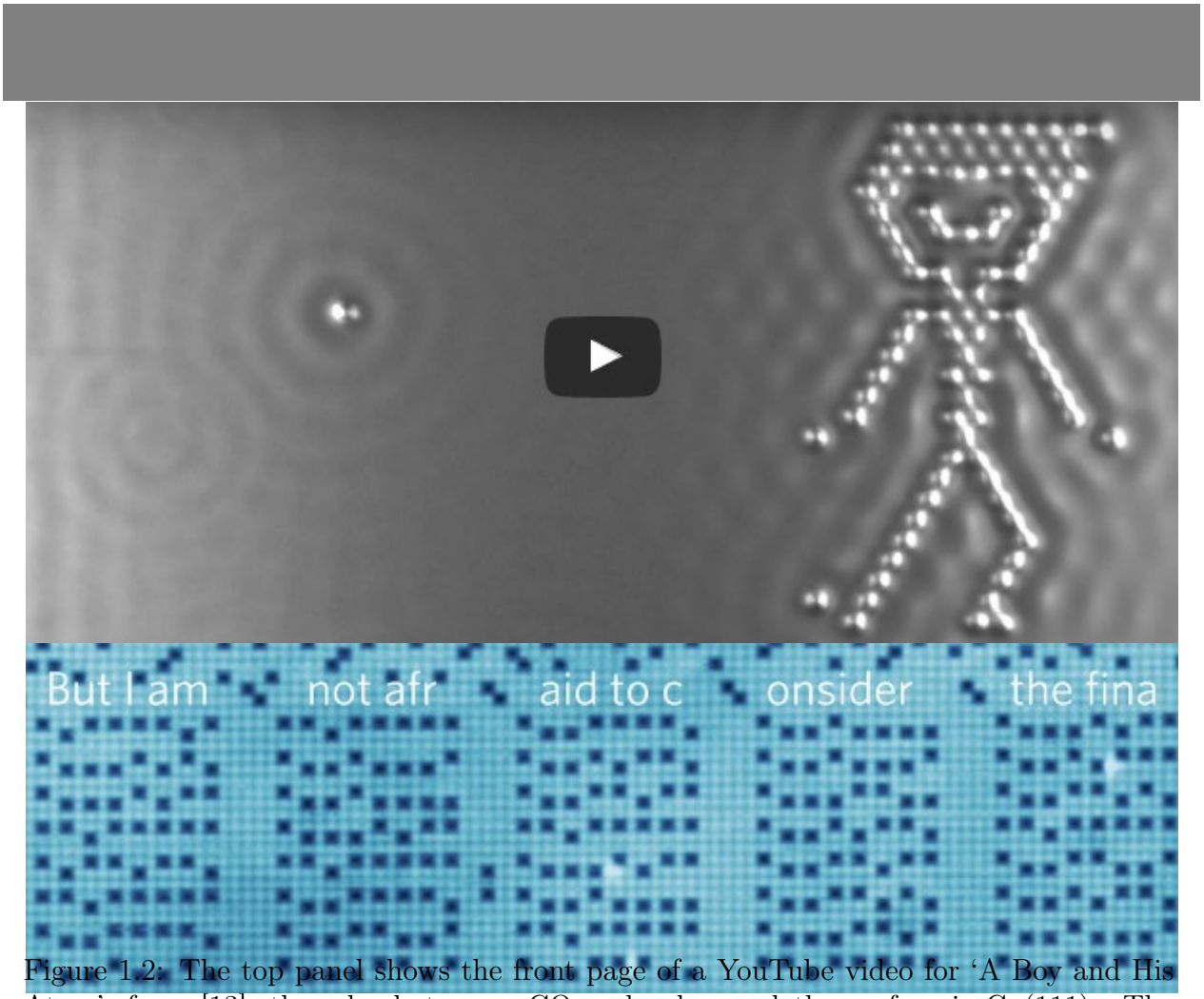

Figure 1.2: The top panel shows the front page of a YouTube video for 'A Boy and His Atom', from [13], the adsorbates are CO molecules, and the surface is Cu(111). The bottom panel shows the beginning of Feynmans speech, 'There's plenty of room at the bottom', written in chlorine atoms on Cu(100), and is reproduced in part from [14].

The basic premise of atomic manipulation is to use the STM tip to move or otherwise alter a surface adsorbate. The first instance of atomic manipulation in STM was by Eigler and Schweizer [15] in 1990, individually moving atoms to write IBM in Xe atoms on the Nickel(110) surface. The techniques used in this experiment have evolved to the point that it is now possible to produce an entire stop motion animation out of atoms [13], and make proof-of-principle data storage three orders of magnitude more dense than the best hard-drives available today [14], shown in Figure 1.2. However, despite the ultimate precision

arrived at using these techniques, their serial nature makes them slow, and therefore more interesting as an investigation of fundamental physics than nanoscale construction.

Mechanisms of manipulation can either utilise the physical presence of the STM tip or can be more indirect: relying on the tunnelling electrons or the electric field to affect the adsorbate. Of greatest relevance to this thesis is the discovery that electrons from the STM tip could be used to manipulate atoms and molecules: in essence using the STM tip as a source of few-eV hot electrons that can initiate reactions in a manner analogous to electron scattering in the gas-phase, or more importantly on surfaces. These electrons can initiate a wide variety of different processes opening up a rich field of research. One of the main benefits of electron driven techniques is the additional control that is offered, allowing for the tip to also manipulate the adsorbate's internal structure. Several distinct manipulation methodologies exist, being defined by the method which is used to deliver electrons from the STM tip to the molecules of interest: broadly, these are scanning-style, local manipulation, and non-local manipulation by point-injection.

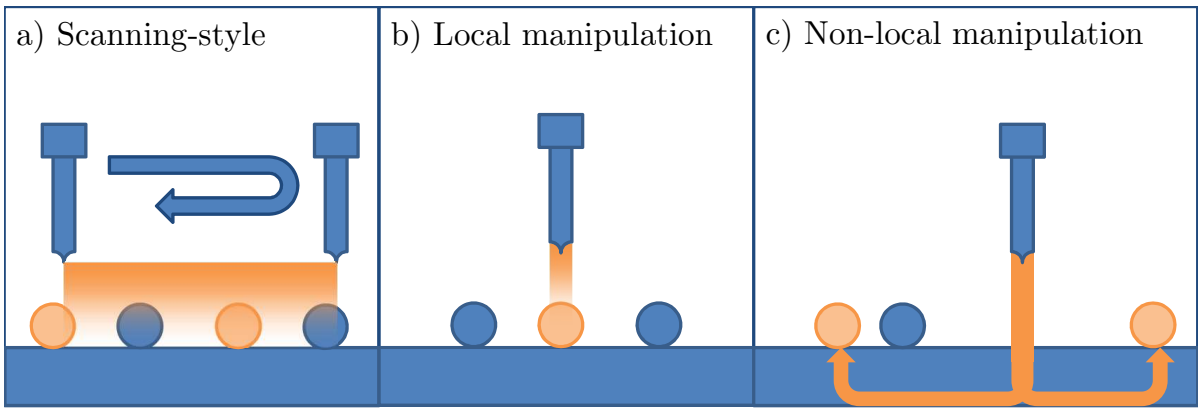

Figure 1.3: A schematic indicating the types of injection possible in the STM. Each figure shows a surface (blue rectangle) decorated with adsorbates (circles). In each case orange is used to indicate injected electrons and the adsorbates they manipulate. Panel a) shows the scanning-style, the tip is shown moving over the surface, delivering a constant flux of electrons over an area. Panel b) shows local injection, where the tip injects directly into one adsorbate. Panel c) shows non-local manipulation where the tip injects electrons into the surface, through which they travel to distant adsorbates.

The methodology used by many early experiments on molecular manipulation with electrons from the STM tip can be referred to as the *scanning-style*: the experiment

involves performing scans at some passive parameters before and after a scan at a set of manipulation parameters and comparing these passive scans to identify any manipulated adsorbates [16, 17, are two examples]. The passive scanning regime is chosen such that the molecules are not affected by the tip, the manipulation regime is chosen such that the tip induces some change in the adsorbate. The manipulation scans can be performed at a variety of parameters to probe how the adsorbates react to different energies and rates of electron injection. The drawback of this technique is that it actually probes a combination of two processes: those initiated by injection directly into the adsorbate when the tip passes over it, called *local* manipulation; and those triggered by electrons which have travelled to the adsorbate from a distant point-injection site through a surface resonance, called *non-local* manipulation.

The local manipulation process allows investigation of a wide range of electron-induced processes such as making and breaking chemical bonds [18, 19], and inducing molecular switching [20], rotation [21], translation [22] and conformational change [23]. However, despite the interesting physics that can be studied using this process, only one molecule can be manipulated at a time. Manipulation of many molecules in parallel would be a useful technique to apply in nanoscale device fabrication, and can be achieved in a number of ways using methods involving polymerisation [24, 25], chain reactions [26, 27], or the non-local process described above. Polymerisation and chain reactions tend to be applicable to only restricted sets of molecules and overlayers which arrange the molecules in the correct manner to allow for a reaction to occur; on the other hand, the non-local process seems to be applicable to a broad class of molecules and surfaces, and closely mimics electron irradiation from a macroscopic source, this suggests it could be a useful scalable technique for parallel molecular manipulation. In addition, the integral role played by surface states in the non-local process makes it a useful tool to investigate surface charge transport.

Before discussing non-local manipulation in detail, a quick introduction to desorption induced by electronic transitions is given. A molecule on a surface has a complicated elec-

tronic and vibrational structure, for simplicity this is usually reduced to a one-dimensional system in the direction normal to the surface. Using a semi-classical approach based on the Born-Oppenheimer approximation, the electron dynamics can be thought of as taking place on a potential energy surface (PES) which is a function of nuclear position along some coordinate normal to the surface. Electron capture on the ground state leads to a temporary negative ion, which evolves for a short lifetime on an excited state PES before returning to the ground state. Desorption results if sufficient kinetic energy is gained on the excited PES to allow the molecule to leave the surface on return to the groundstate PES. If multiple electronic excitations are required, the process may involve a sequence of vibrational excitations of the ground state leading to desorption. There are several mechanisms for the above, described in detail in [28–30].

1.3.1 Non-local manipulation

A non-local manipulation experiment is one where charge is injected into a surface decorated with adsorbates, before then travelling from the injection location to an adsorbate and triggering a manipulation event. To identify and study this process an area of substrate covered in adsorbates is imaged at a passive voltage before and after a charge injection into an area of substrate locally free of adsorbates, any changes between the images can then be related to the injection performed. A number of surface-adsorbate pairings have been studied, including a variety of atoms [31–33] and molecules [34–38] on both metal [35, 37, 38] and semiconductor [31, 33, 36, 39] surfaces, and diverse manipulation channels are possible, such as desorption [36], diffusion [31, 33], dissociation [35, 37, 38] and polymerisation [34]. Experiments have grown steadily more sophisticated, to the point where it is possible to identify the surfaces states responsible for the charge transport[40], and control the manipulation channels which the distant adsorbate takes[38].

The first reported examples of non-local manipulation were on the $\mathrm{Si}(111) - 7 \times 7$

surface, the very first case being manipulation of the adatoms of the surface [32]. Imaging an area of Si(111)−7×7 before and after a point injection of charge into the surface revealed a number of displaced adatoms. At room temperatures these adatoms will rapidly return to their initial positions, but at lower temperatures ($T < 175\,\mathrm{K}$) they can remain in a transient bonding configuration for long enough to be imaged. This process was found to occur when the injected electrons possessed more than ∼2 eV of energy, and was sensitive to the injected current. Measuring the reaction rate as a function of current allows for the number of electrons required for a reaction to be deduced. A linear dependence implies a single electron per reaction, a quadratic one implies two electrons and so on. The authors proposed that electrons in a surface state at this energy could excite vibrational excitations in the surface adatoms causing them to move out of the surface.

Several further experiments on Si(111) − 7×7 found that the non-local process was not limited to just adatom excitation. Experiments by Nakamura et al. [31] on Si(111)−7×7: Cl found that it was possible to initiate several processes in a non-local manner using either electrons or holes from the STM tip. Chlorine can be induced to diffuse or desorb, depending on the charge carrier injected and the injection parameters used. This is the first example of non-local manipulation of an adsorbate by electrons transported over the surface in a surface resonance[4]. The electron-induced process requires a bias above 3 V, the hole process requires a bias $\sim -2\,\mathrm{V}$ and in addition shows some structure similar to the surface states appearing in STS, hinting at their important role.

Experiments by Nouchi et al. [34] on multilayers of C_{60} on Si(111) − 7×7 found that the fullerenes could be induced to polymerise by electrons from the STM tip. This polymerisation occurred in a ring around the injection site. The reasons for this were uncertain, with the authors speculating that it was a result of competition between polymerisation and depolymerisation, and intimately tied to the carrier propagation in the C_{60} layers. Areas of lower reaction rate around the injection site are common to a number of non-

[4]I have not included hydrogen desorption as the first example, as early experiments primarily used higher energy field emitted electrons.

local experiments and recent results on the Si(111) − 7×7: PhCl system have helped to understand this phenomenon, they will be discussed in Section 1.4.

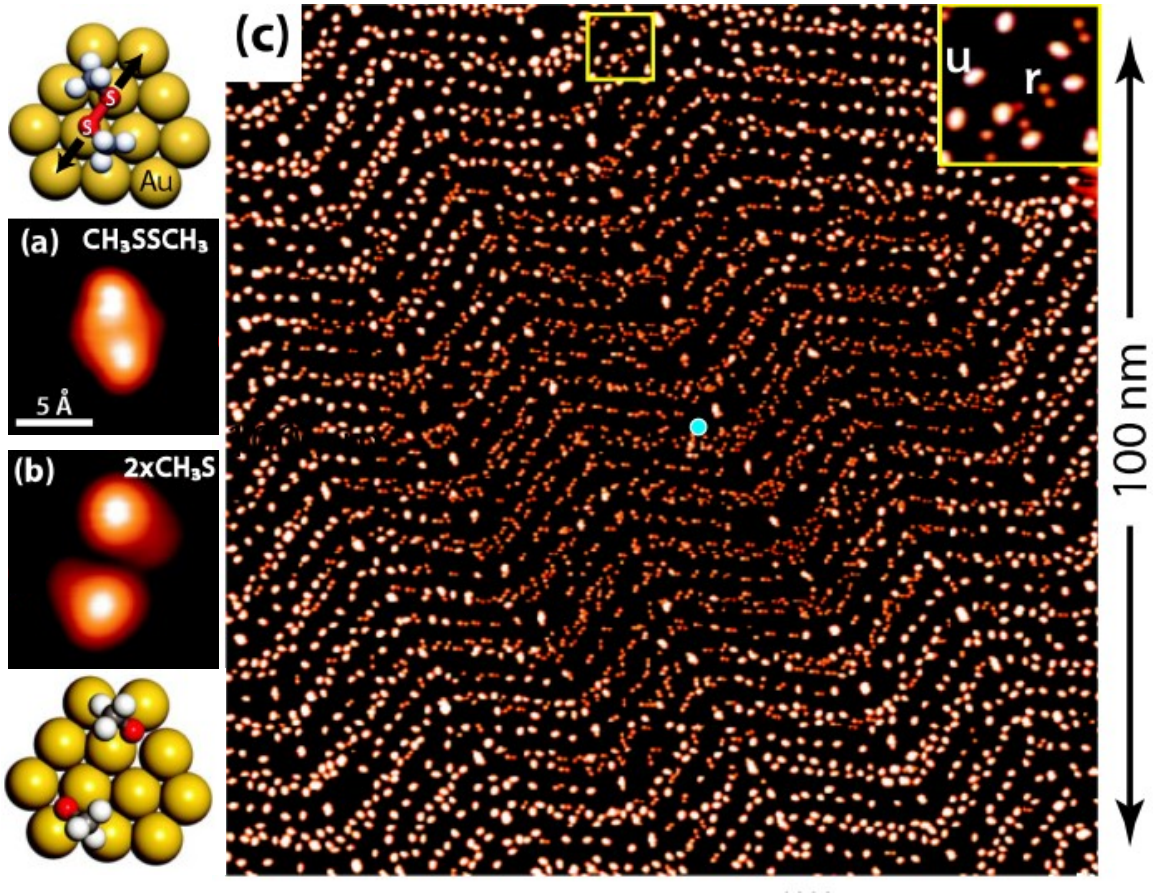

Figure 1.4: Figure reproduced from [35]. Panel c) shows the result of an electron injection into the Au(111) surface decorated with physisorbed dimethyl-disulfide. Molecules in a large area around the injection location (indicated with a blue dot) have dissociated. Panels a) and b) show the reactant and products respectively. These are indicated by u and r in the inset of panel c).

Later experiments found that non-local manipulation processes were also possible on a number of metal surfaces: these include the manipulation of CH_3SSCH_3 on Au(111), Cu(111), Cu(110) and Au(100) [35] and the manipulation of $F_{16}CuPc$ on the (111) surfaces of Ag and Au [37]. In the first case, the S-S bond in the physisorbed CH_3SSCH_3 species is broken and the molecular fragments adsorb onto the surface. An example of such an experiment is shown in Figure 1.4. The reaction exhibits a voltage threshold at around

1.4 V, and by measuring the reaction rate as a function of current it was determined that only one electron is required per reaction event. The radial decay of the dissociation probability was well described by an exponential decay with a decay length of ∼5 nm (though this neglected a geometric factor of $1/r^2$). In the second case, C-F bonds within the molecule can be broken leading to a change in the molecule's appearance in the STM. These experiments were conducted on a full molecular overlayer. The non-local process occurs only for electron injection, with different thresholds and length scales on the two different surfaces, and is sensitive to the injected current, leading to the proposal that the electron transport occurs in a metal-molecule interface state. Interestingly, the number of electrons required to trigger a local manipulation process depends on the substrate, with 2 electrons participating on Ag, 4 on Au. The authors state that the non-local reaction likely occurs sequentially, as it would be improbable that molecules distant from the tip capture multiple electrons within the lifetime of the initial excitation, though it is also possible that the dominant local process differs from the non-local one. They did not measure the current dependence of the non-local process.

More recent experiments have found that it is also possible to trigger different reactions at a distance depending on the injection parameters used. Hahn et al. [38] studied the dissociation of oxygen on Ag(110) and found that it was possible to dissociate oxygen both locally and non-locally. They found that two possible dissociation pathways existed, one that could be triggered by both hot-electrons and hot-holes ($O_{ffh} - O_{ffh}$), the other that could only be triggered by hot-holes ($O_{ffh} - O_{sb}$). These processes are summarised in Figure 1.5, together with STM images. In addition, the hot-hole process was more selective when performed non-locally than when the dissociation was triggered by a local injection: 95% of non-local reactions led to ($O_{ffh} - O_{sb}$) but only 78% to 85% of local reactions (depending on injection current). Interestingly, the non-local process required only a single electron, whereas the local process was dominated by a two electron (three hole) process. However, lower injection biases were used for the local injections, so it is possible that a different reaction pathway was followed. This difference between the

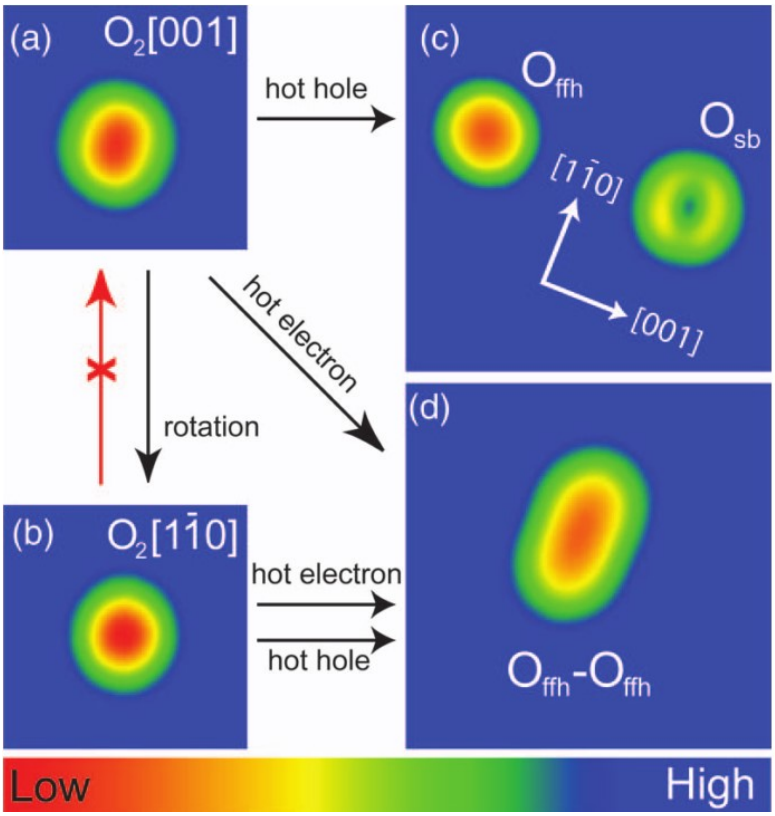

Figure 1.5: Figure reproduced from [38] showing the possible reactions that can be triggered on Ag(110) via non-local injection. Panels a) and b) show the initial molecular states. Panels c) and d) the reaction products. These reactions are triggered non-locally and affect a substantial number of molecules around the injection site.

number of charge carriers required for the local and non-local processes may also be important for the F_{16}CuPc systems mentioned previously.

1.4 Nonlocal manipulation of chlorobenzene on silicon

The Si(111) $-$ 7$\times$7: PhCl system studied in this thesis is a good model system for investigating non-local manipulation because the possible manipulation channels and their behaviours are well understood, meaning that attention can be focussed on the mechanisms, and effect of experimental parameters on non-local manipulation into already well-established molecular reaction channels. This was neither the first system to exhibit the non-local process, nor the first time it was observed on the silicon surface, but is

probably amongst the most comprehensively studied example of this phenomenon, still yielding fascinating new results after over 10 years of study (first results in 1999 [41], first non-local study 2010 [36]). Understanding of the various facets of the non-local process on this surface is a result of a combination of many non-local, local and scanning-style experiments. The system exhibits three reaction pathways – desorption, dissociation, and diffusion – all of which are dependent on injection voltage and current, and also system temperature. Non-local experiments at varied temperature (77 K to above room temperature) supported by local manipulation and scanning tunneling spectroscopy studies have revealed details of the desorption mechanism and surface transport [36, 40, 42, 43]. These studies indicate the specific surface states responsible for the transport, and how these determine the manipulation thresholds and radial desorption probability distributions. Scanning type experiments have been used to investigate dissociation [44–46] and desorption [44, 46–49] by charge injection from the STM tip at room temperature and above. These studies help to clarify the details of the desorption mechanism.

1.4.1 STM of chlorobenzene on silicon

Before going into detail on the manipulation processes possible in this system it is necessary to understand the appearance of the system in STM. A schematic of the full 7×7 reconstruction is given in Figure 1.6, and Figure 1.7 shows the appearance of the surface in STM. The Si(111) $-$ 7$\times$7 reconstruction is very complex, and took many years to understand completely [50, 51]. Takayanagi et al. [51] proposed the dimer-adatom-stacking fault (DAS) model in 1985, based on transmission electron diffraction data and taking into account data from practically every available surface technique of the time. Confirming the DAS model of the Si(111) surface was one of the early triumphs of the STM technique [52, 53].

The DAS reconstruction involves the top three layers of the silicon surface, with the fourth layer having the same structure as the unreconstructed surface. Key features in

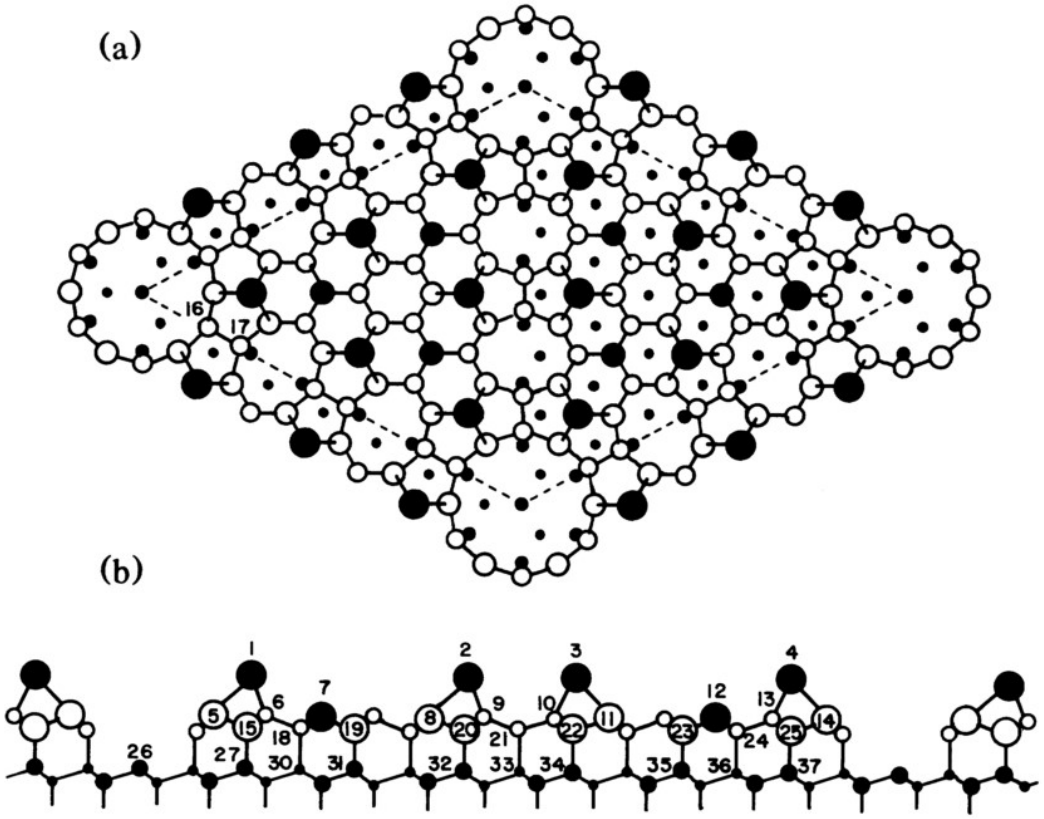

Figure 1.6: Figure reproduced from [54]. Schematic of the first three layers of the DAS model, a) is a top down representation, b) shows a side view. The large black circles in a) are the adatoms which are visible in STM, the mid sized black circles are the rest atoms, which are not visible but may participate in bonding. The empty circles and black dots lie in the next two layers respectively.

STM are the adatoms and rest atoms in the top two layers. The adatoms are the only surface atoms visible in conventional STM, but the rest atoms of the second layer play a role in surface bonding, and have been imaged using non-contact AFM [55–57].

Chlorobenzene has been established to bond in a 2,5 di-sigma butterfly geometry between an adatom and a rest atom of the surface [58]. Temperature programmed desorption (TPD) and electron energy loss spectroscopy (EELS) were used to determine the bonding. STM imaging corroborated this bonding location, showing a dark, apparently missing, adatom which could be attributed to the involvement of the adatom dangling bond in bonding to the molecule, altering the density of states at typical tunneling parameters (1V, 50pA) and causing the tip to have to approach the surface to yield the same

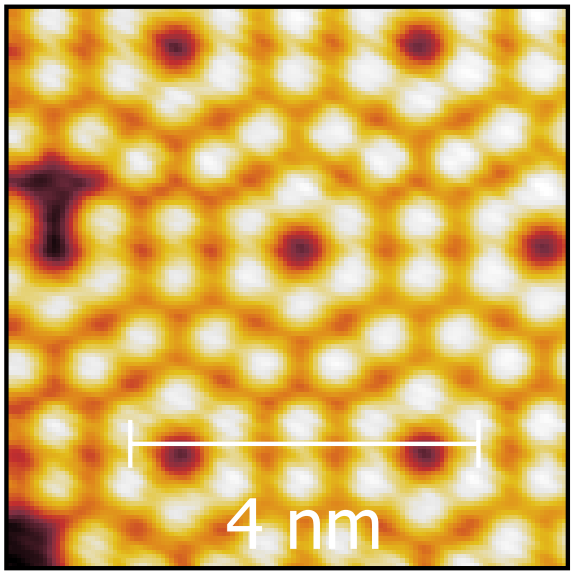

Figure 1.7: STM image taken at 1V, 50pA showing the adatom features of several unit cells. A defect can be seen as a missing adatom on the left of the image.

tunneling current [59]. Further to this, STS found that the spectral features associated with the rest atom vanished upon chlorobenzene adsorption [60]. In this bonding configuration one carbon atom bonds to an adatom, and another carbon bonds to an adjacent rest atom, it is not normally possible to distinguish which rest atom the chlorobenzene is bonded to when imaging at 1V.

There are 18 possible PhCl bonding locations in a 7×7 unit cell, of which six can be occupied at any one time (there are only six available rest atoms). As a result of the symmetry of the unit cell these 18 bonding locations all fall into 4 categories, which are labelled according to the adatom involved in the bonding, and whether it is in the faulted or unfaulted half of the unit cell [51]. All of the adatoms in each half of the unit cell can be labelled as corner or middle adatoms, this leads to faulted and unfaulted middle (FM,UM) and faulted and unfaulted corner (FC,UC) adatoms. Each middle adatom adjoins two rest atoms, each corner adatom adjoins one, similarly each exposed rest atom adjoins two middle adatoms and one corner adatom. With some STM tips it is possible to distinguish the bonding orientation using scans at 2V bias, as this reveals a symmetry axis of the molecule which can be used to determine the bonding location unambiguously [45, 48].

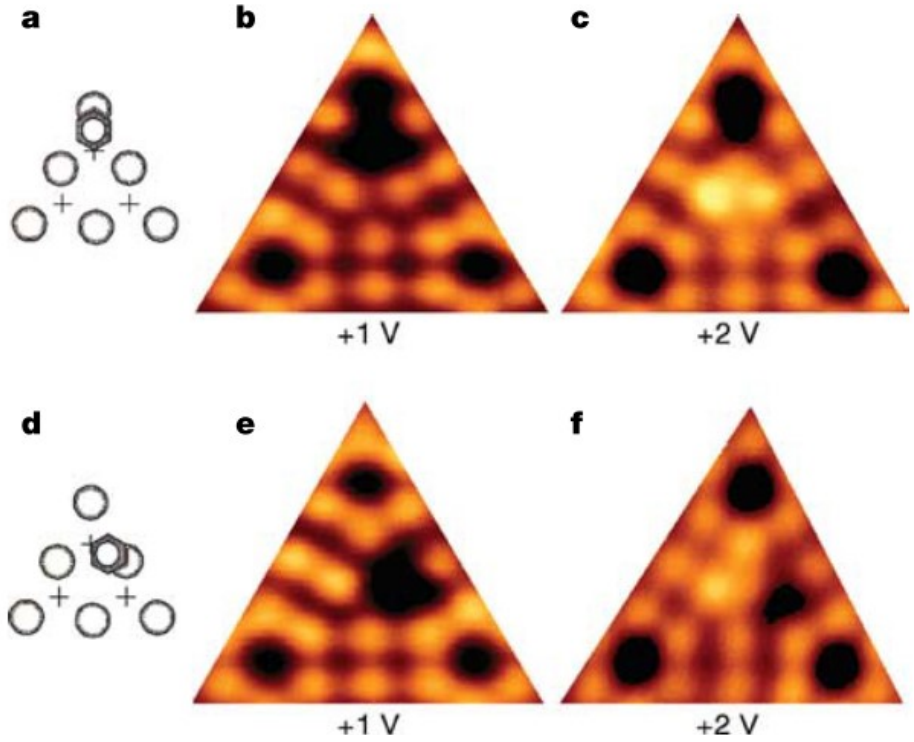

Figure 1.8: Figure from [45] , showing the how the bonding location on the surface is identified. The leftmost panels a) and d) show schematics of the bonding, where open circles indicate adatom positions, and crosses indicate rest atom positions. Panels b) and e) show how the molecules appear at passive scanning parameters, finally panels c) and f) show how imaging at 2V reveals the molecular orientation by illuminating a bright feature near the bonding rest atom.

1.4.2 Quantifying manipulation

In the case of Si(111) $-$ 7$\times$7: PhCl the manipulation event triggered in non-local experiments is desorption (and to a lesser extent diffusion), the signature for this in an image is a change of a dark adatom associated with an adsorbed molecule into its usual bright state [36]. Figure 1.9 shows the result of a non-local desorption experiment. Notice the reduction in the number of dark features near the injection location (marked with an X). The number of dark-to-bright events and the initial molecular population form the non-local dataset. The radial dependence of the desorption probability can be extracted by fitting changes in the molecular populations of annular bins around the injection location

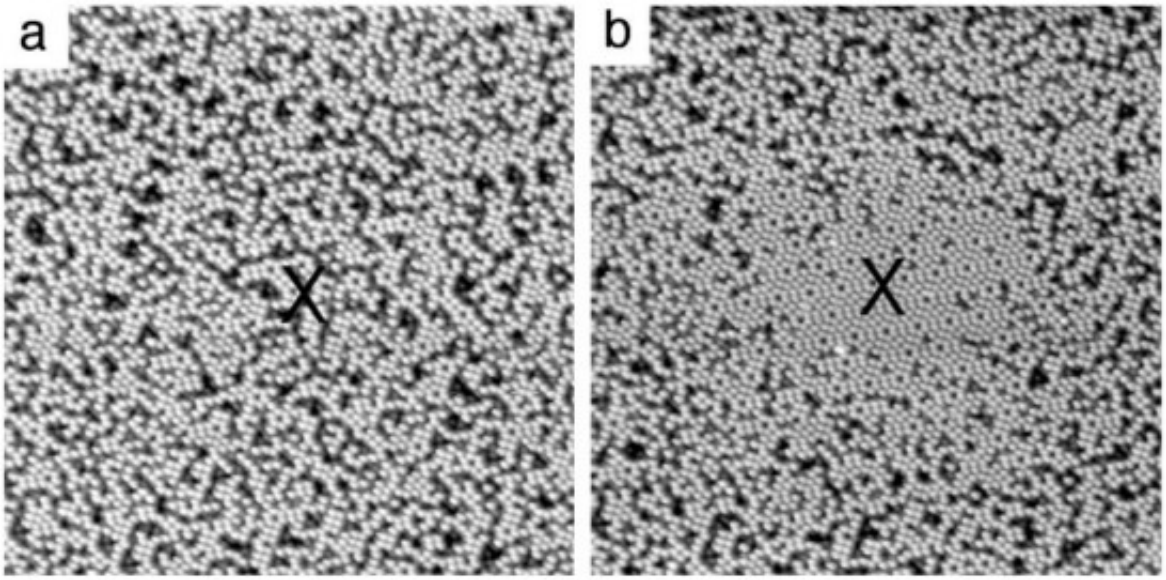

Figure 1.9: Figure from [36] showing the non-local desorption of chlorobenzene molecules from the Si(111) $-$ 7 $\times$ 7 surface. The brighter features are Si adatoms, and the dark features chlorobenzene molecules. The injection location is denoted by a cross. Notice the large area devoid of molecules around the injection location, where the clean 7 $\times$ 7 reconstruction is visible.

using a simple rate equation model (adapted from [36, 61]).

$$\frac{\mathrm{d}N(r,t)}{\mathrm{d}t} = -\sigma_{\mathrm{mol}}(V,T)n_e(r,V,I,T)N(r,t), \tag{1.9}$$

where the molecular cross-section $\sigma_{\mathrm{mol}}(V,T)$ is the probability of a single electron instigating a reaction after reaching a specific molecule, $n_e(r,V,I,T)$ is the temperature dependent rate of arrival of electrons at a molecule at radius r with sufficient energy to trigger a reaction, and $N(r,t)$ is the number of molecules in an annulus of width 10 Å at radius r. The variables V, I, and T are the injection bias, injection current and sample temperature, respectively. This implies that

$$\sigma_{\mathrm{tot}}(r,V,I,T) = \sigma_{\mathrm{mol}}(T)n_e(r,V,I,T) = -\ln\left(\frac{\Delta N(r)}{N(r,t=0)}\right), \tag{1.10}$$

where $\Delta N(r) = N(r, t = t_{\text{inj}}) - N(r, t = 0)$, and t_{inj} is the length of the injection in seconds. The desorption probability $\sigma_{\text{tot}}(r, T)$ contains details of both the surface transport and the electron capture process at the molecule.

Scanning style experiments will usually yield a ΔN for the whole image which is dominated by a non-local process averaged over many tip-adsorbate distances [5]. The local process should be less prominent as a result of the small amount of time the tip spends injecting directly into the molecule compared to the amount of time spent injecting into the surface. Information on the radial dependence of $\sigma_{\text{tot}}(r, T)$ is lost in a scanning-style experiment, but it is still possible to extract estimates of the effect of the variation of an injection parameter on the magnitude of the desorption probability.

In the Si(111) $-$ 7$\times$7: PhCl system the current dependence for desorption is relatively uncomplicated, and was first determined in [47] using scanning-style experiments. These indicated that desorption was a one-electron process. The rate of desorption was plotted vs current and fitted to an expression of the form $R \propto I^n$. This procedure yields a straight line on a logarithmic plot, the gradient of which gives the number of electrons involved in the reaction [32, 62]. In later non-local experiments the process was confirmed to be one-electron by checking that the non-local process is identical for all currents and times, when normalised by the injected charge: if this were not the case it would imply a more complicated current dependence.

In addition to desorption, the Si(111) $-$ 7$\times$7: PhCl system exhibits molecular dissociation. By injecting at high voltages ($> 3V$) it is possible to break the carbon-chlorine bond [41, 45]. In order to identify dissociation events further scans must be recorded in addition to the usual passive scans. Chlorine atoms appear dark at 1 V, so are indistinguishable from chlorobenzene molecules bonded to the surface; however, at 3 V chlorine atoms appear brighter than adatoms. By recording additional scans at 3 V after the manipulation process it is possible to identify dissociation events by the appearance of new bright features at 3 V .

[5] Note, this is lateral distance over the surface, not separation normal to the surface.

There are several stages to the non-local mechanism that have been studied in great detail in the Si(111)$-$7×7: PhCl system. These are the behaviour of the charge carriers on injection, their subsequent transport to the molecule, and the desorption and dissociation mechanisms at the molecule. These will be discussed in the following subsections.

1.4.3 Surface transport

Carriers from the STM tip are injected into a surface state at an energy determined by the bias used for the experiment. Each charge carrier then travels outwards over the surface ballistically for a short time before rapidly scattering inelastically to the minima of the surface state band it is in. At the band minima it undergoes diffusive motion over the surface until it is scattered out of the surface state entirely, this scattering process determines the surface state lifetime τ_{out}. This model is supported by several experimental features: the different thresholds for desorption found in the non-local and local injection processes, dependence on molecule bonding site and injection site, the bias and temperature dependence of the non-local length scale, and a suppressed region near the injection site.

Local desorption experiments (where electrons are injected directly into the molecule) find that desorption can be triggered at 1.4 V [43]. For non-local manipulation, the corresponding threshold is found to be ∼2.1 V [36, 43]. In both cases electrons with energy greater than 1.4 eV are required, but below ∼2.1 V there is no surface state to transport the electrons to the molecule, preventing the non-local process.

The above reasoning is supported by STS maps from [36], shown in panel a) of Figure 1.10, which find a state with onset ∼2.1 V. It was also found that the total desorption yield for injection at various sites within the unit cell closely matched the DOS integrated between the onset of the surface state and the injection energy (correctly weighted to account for the tunneling probability). This behaviour is shown in panel b) of Figure 1.10. There is also a dependence on the molecular adsorption site, though this could

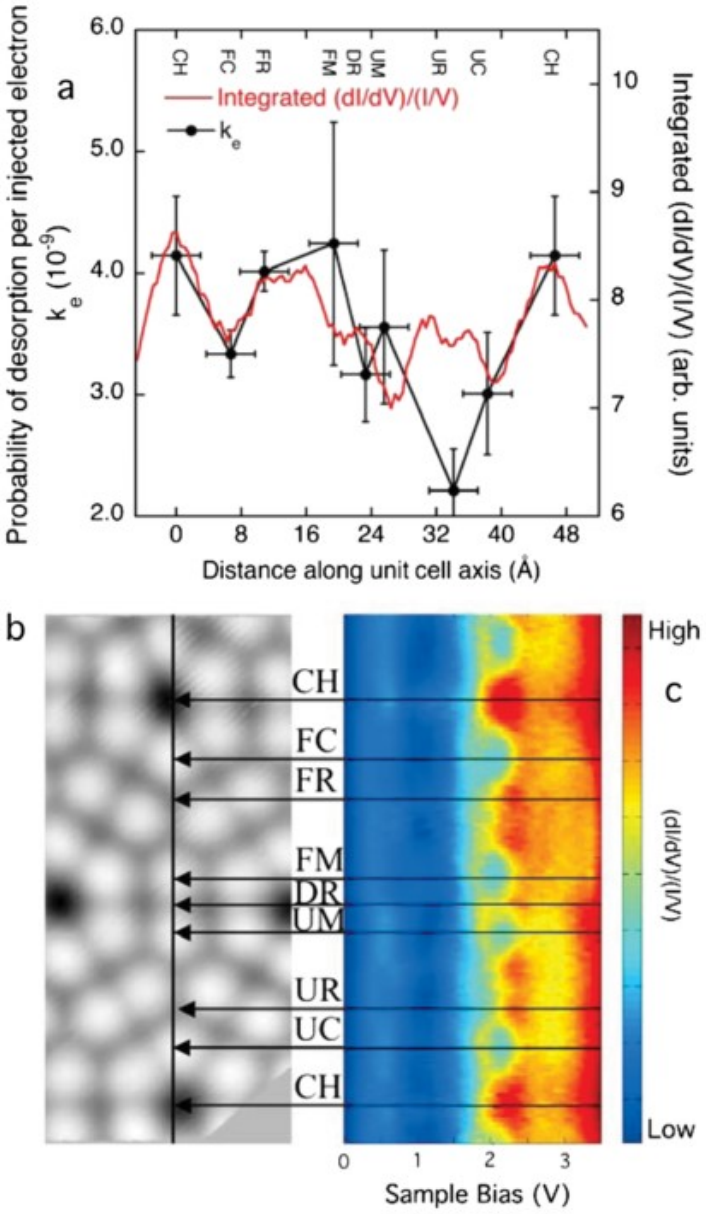

Figure 1.10: Figure from [36] shows a comparison between the probability of desorption per electron compared to the integrated DOS at a number of injection locations. Panel a) shows the good agreement between the probability of tunneling into the relevant surface state and the probability of a manipulation event, b) shows the raw STS map and the corresponding injection locations.

be related to either the surface state-molecule coupling or the strength of the adsorbate-substrate bond.

Diffusive motion was postulated in [43] to account for the observed increase in the length scale of the non-local process, which could not be rationalised in terms of the

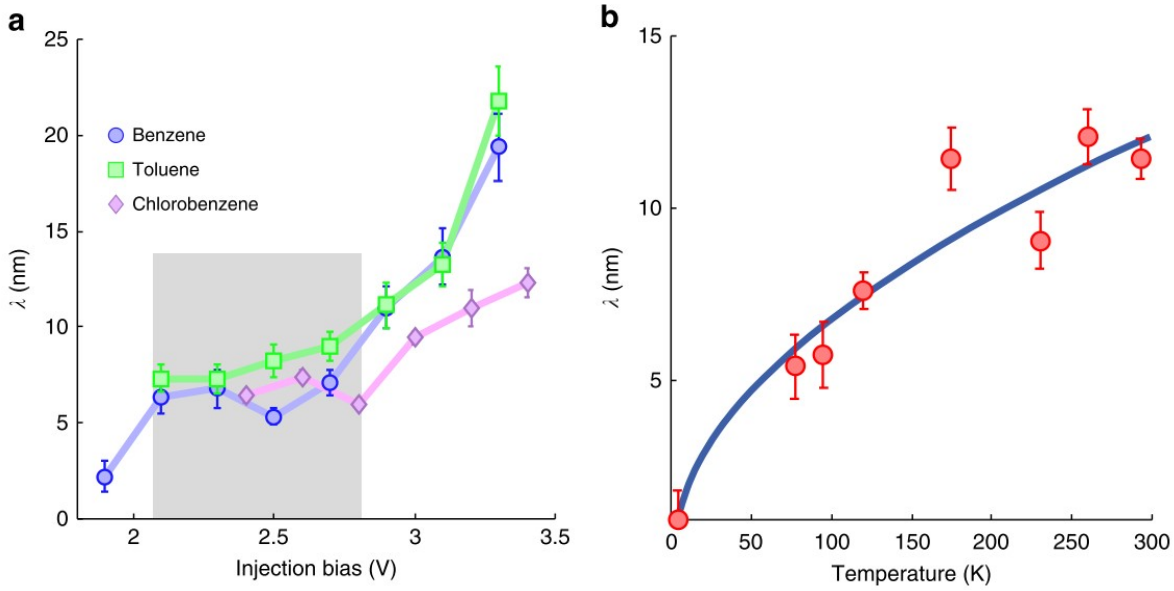

Figure 1.11: Figure from [43]. Panel a) depicts the relationship between non-local decay length and injection bias as extracted using bessel function fits to the radial distribution of non-local events. Panel b) shows the dependence of this decay length on temperature.

older purely ballistic transport model used in [36]. Solving for 2D diffusion with decay from a point source gives a bessel function for the radial distribution of electrons in the surface. This was found to give an excellent fit to the radial distribution of the desorption probability, and allows a decay length to be extracted. The decay length is found to increase with increasing temperature, which was explained to as a result of increased phonon scattering. The dependence of the decay length on bias and temperature is shown in Figure 1.11.

The dependence of the non-local decay length on bias was also studied in [43], where it was found that above the ∼2.1 V threshold the decay length showed a plateau (shown by a shaded region in Figure 1.11), before rising again at higher voltages. The ∼2.1 V surface state was identified with a state found at (1.94 ± 0.15) eV above the fermi-level in photoemission [63]. This state was found to be the U2 back-bond state of the 7×7 reconstruction, and is proposed to be responsible for the non-local charge transport (for a detailed overview of silicon surface states see [64, 65]). The explanation for this behaviour in the non-local model is that most of the surface transport which leads to desorption

occurs diffusively at the bottom of the surface state, injected carriers above this energy rapidly lose their excess energy so it does not affect the desorption process. This behaviour is analogous to that found in these photoemission experiments [66], and diffusion constants extracted from the radial distributions using the lifetime from [66] were $(3 \pm 2)\,\mathrm{cm^2 s^{-1}}$, similar to but slightly less than other literature values.

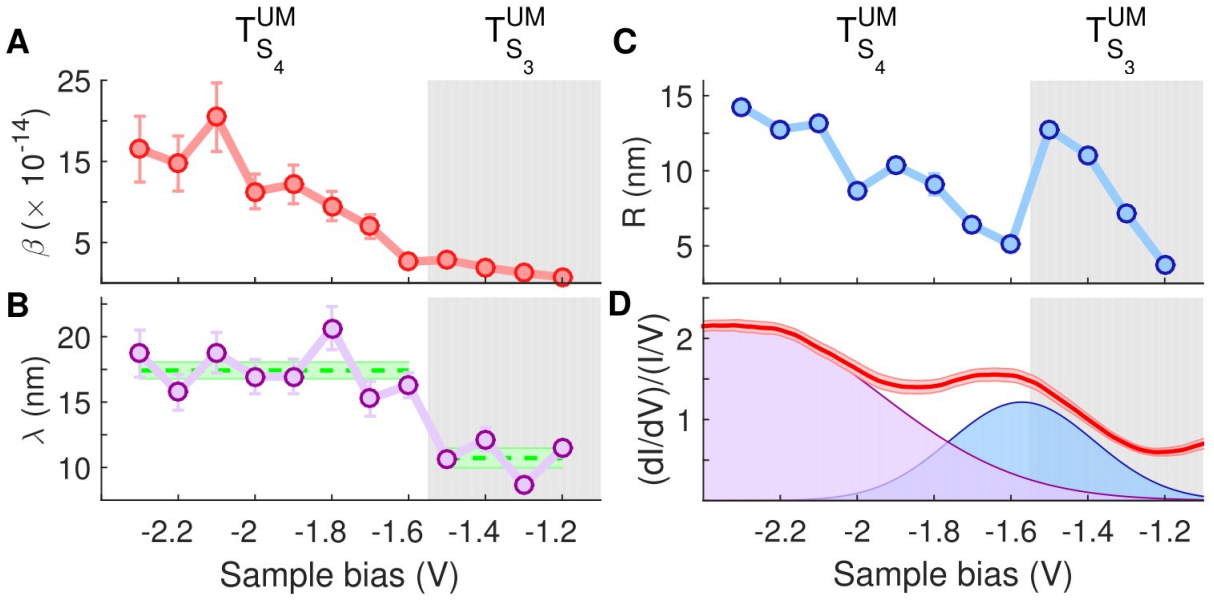

Figure 1.12: Figure from [40] showing the variation of various parameters with sample bias. Panel A shows the overall magnitude of the non-local effect, panel B the decay length, panel C the radius of the suppression region described in the text. Panel D shows STS spectra, fitted to gaussians. The shaded area on each panel shows where the non-local process occurs primarily in the lower energy state, the unshaded area the upper state.

This bias dependent behaviour was also found for injected holes in [40], where it is especially prominent as there are more occupied surface states available in the relevant energy range (S1-3 in inverse photo emission studies, see [67] for a summary). As a result up to three plateaus could be found as a function of injection bias. An example of the bias dependence of the non-local process for holes is shown in Figure 1.12. Here, each surface state is found to have a different characteristic length scale.

Near the injection site, the desorption is lower than expected given the fit to the data at points further from the injection location. It is suggested that this suppression results

from the rapid ballistic transport of holes at an energy higher up in the surface state they tunnel into, before they relax and travel diffusively over the surface in the bottom of the surface state band. The authors assume that in the region where the carriers travel in a ballistic manner no desorption occurs: the injected carriers travel out from the tip until they scatter, as the dominant scattering mechanism is unlikely to be scattering off of the molecules, it is only carriers which are scattered back into this region in their diffusive transport that can instigate a desorption event. This phenomena is seen in many non-local manipulation studies [34–36].

Ballistic transport followed by diffusive transport at the bottom of the surface state is simulated in the paper by an *inflation* region, where the carriers are modelled by a spreading wave-packet for a certain inflation time, followed by diffusive transport initiated from this electron distribution. By fitting the data, an inflation time of (11 ± 1) fs is found, which is in good agreement with relaxation times measured in the U1 surface state (40 fs [65]) and bulk (10 fs [68]) of silicon. The measured size of the suppression region is found to increase with increasing distance above the surface band edge as expected from the model and also change non-monotonically at the onset of a new surface band.

Together the results described here strongly support a model of hot-carrier induced reactions following transport in a surface state selected by injection bias voltage. They suggest that carriers travel outwards ballistically for a very short time before relaxing to the bottom of the surface state band they are injected into, after which they undergo a much longer diffusive motion at the bottom of the band, before undergoing a scattering process to other states where they can no longer cause a non-local manipulation event. This leads to a radial electron distribution characterised by a suppressed region near the injection site followed by a radial decay. The size of the suppressed region is determined by the excess energy above a surface band edge, which determines how far that carrier travels before it first scatters. The decay length is constant within a surface band, and indicates how long carriers can stay at the bottom of the surface band before being scattered to other states.

1.4.4 Molecular processes

Once a molecule captures an electron or hole it can then either desorb, diffuse or dissociate. The physisorbed state is now understood to play a major role in all of the above processes, so will first be explained. The role of the physisorbed state in desorption and dissociation will then be discussed.

The physisorbed state of chlorobenzene has not been studied in detail in STM, but a study of benzene [69] on the Si(111)−7×7 surface had found that the benzene molecule first binds to the surface in a strongly Van-der-Waals bound, mobile, physisorbed state, which then later chemisorbs strongly after overcoming a thermal barrier of (0.30 ± 0.03) eV. The physisorbed molecule can also desorb with a barrier of $\sim$0.4 eV. Chlorobenzene adsorption at 110 K follows similar trends to benzene as observed by TPD, and is predicted by DFT to have a similar, though slightly deeper physisorbed well. Physisorbed chlorobenzene has been observed to be stable in STM imaging at similar temperatures to benzene (50 K to 100 K).

Thermal desorption and diffusion of chemisorbed chlorobenzene occur at room temperature. Using passive scanning parameters to observe the changes in molecular populations over time it was found that the energy barriers to desorption and diffusion were (0.98 ± 0.08) eV and (0.84 ± 0.04) eV respectively. The diffusion activation energy was ascribed to the barrier between chemisorbed and physisorbed states of the chlorobenzene molecule: on thermal excitation into the physisorbed state the molecule is capable of motion over the surface, before again entering the more strongly bound and immobile chemisorbed state. The exact bonding location of the molecule on the surface can alter the depth of the chemisorption well and the diffusion barrier slightly, as studied in [61], but the site-averaged values above will be used here for easier comparison with other data in this section.

Using the information on the physisorbed state of the molecules, together with the barriers for desorption and diffusion of the chemisorbed molecule studied above, a complete

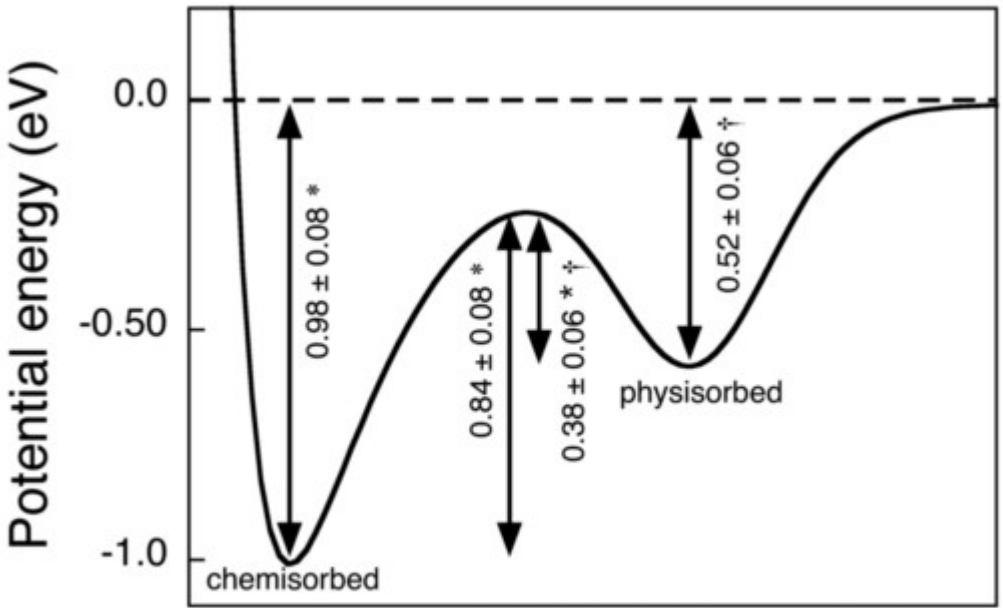

Figure 1.13: Figure from [46], showing the potential energy surface for the Si(111) − 7× 7: PhCl system. The values marked with a * are deduced in the paper, those marked with a † are from [69].

picture of the 1D potential energy surface (PES) normal to the surface can be deduced, shown in Figure 1.13. The agreement in the position of the top of the barrier between physisorbed and chemisorbed as deduced from experiments on both species supports this picture.

Dissociation in the Si(111) − 7 × 7: PhCl system was first studied by Lu et al. [41] in 1999. This study shows the dissociation process and how it may be identified, it also highlights the local nature of the reaction, which the authors termed localised atomic reaction (LAR), where the reaction product is found very close to the position of the initial reactant. A subsequent study by Sloan and Palmer [45] varied the current systematically and examined the spatial distribution of chlorine products to elucidate the dissociation mechanism [45]. Each dissociation experiment consists of a consecutive series of images taken every volt from 1 V to 4 V and back down again, with each image allowing a different feature of the surface to be determined. The 4 V scan is considered the manipulation scan, though the 3V scan is also above threshold, a higher voltage scan is used to produce

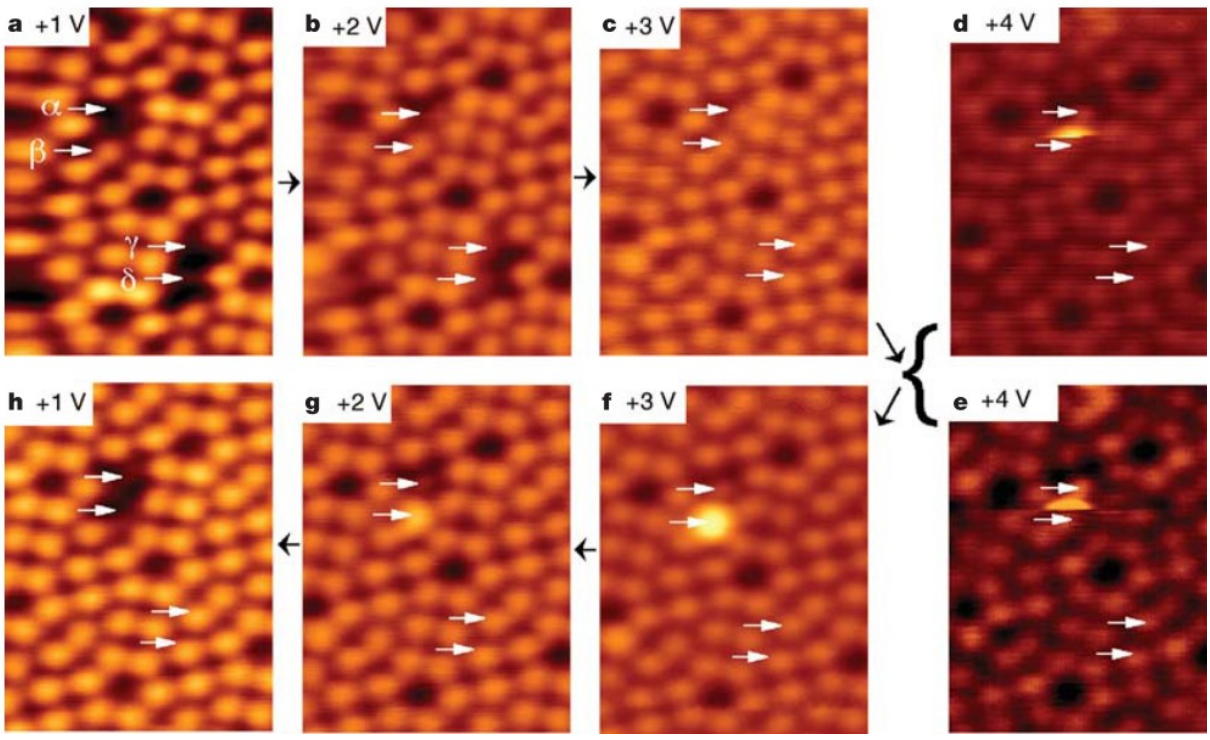

Figure 1.14: Figure from [45], showing the results of a scanning-style experiment at room temperature. The labels α and β show the signature of a dissociation event, γ and δ show desorption of two molecules. The image panels are recorded in alphabetical order, with the 4 V scan being the manipulation scan.

sufficient events to analyse the spatial distribution of the chlorine products. By comparing the location of the chlorine features (bright at 3 V) to the location of the molecule parent (dark at 1 V, intermediate brightness at 2 V) it can be determined at which angle to the symmetry axis of the molecule the chlorine is emitted, and what distance over the surface it has travelled. By performing the same experiments at a variety of tunneling currents (this time performing the manipulation at 3 V) the variation of the dissociation rate with current can be measured and compared with that for desorption. Further details of bias thresholds and current dependence of the dissociation process are given in [44].

In perhaps the most interesting result of the paper it was found that two 3 eV electrons were necessary to break the carbon-chlorine bond, together providing far more energy than would seem to be required from ab-initio calculations on the system (1.9 eV). A second

comprehensive study of the Si(111) − 7×7: PhCl system was conducted by Sakulsermsuk et al. [46] looking at the variation of the dissociation yield with temperature. Analogous scanning-style experiments to those described above were conducted at a range of temperatures between 295 K and 330 K. Crucially, it is pointed out that the analysis of Sloan and Palmer [45] did not correctly account for electron-induced desorption of molecules, which competes with dissociation at this temperature and reduces the number of molecules available to dissociate. When desorption was taken into account, the process was in fact found to be instigated by 1.4 electrons. This non-integer number is the result of measuring two processes simultaneously, a one-electron and two-electron dissociation process. The rate of dissociation was also found to increase with temperature. In [46] the authors propose a model where dissociation can occur via either a temperature independent two-electron process, or a temperature dependent one-electron process, both in parallel with electron-induced desorption. It is then possible to extract the temperature dependence of the one-electron process by fitting the initial, desorbed and dissociated populations to a rate equation model. Using this model it was found that the one-electron dissociation process showed Arrhenius type behaviour with an activation energy of (0.8 ± 0.2) eV.

The similarity between the barrier for thermal excitation to the physisorbed state and that for one-electron dissociation led the authors to propose a model for one-electron dissociation where the molecule dissociates exclusively in the the physisorbed state. In order to dissociate the molecule it must first be promoted to this physisorbed state by either thermal or electronic means. The result of this is that at room temperature dissociation requires two electrons – one to promote the molecule from chemisorbed to physisorbed, and one to dissociate – and at higher temperatures only one electron is required – one electron dissociation of molecules transiently populating the physisorbed state as a result of thermal excitation. This model of combined thermal and electronic processes is one of the key topics of investigation of this thesis. Particularly because a two-electron process should be suppressed in a non-local experiment as a result of the much lower probability of having two consecutive electronic excitations within the lifetime of an excited state.

So, in a one-electron regime it may be possible to initiate non-local dissociation.

The physisorbed state was also found to play a role in the non-local desorption process, where a study of non-local desorption at a variety of temperatures between 77K and 295K found that the non-local process also shows thermal activation [42]. It was found that non-local desorption induced by electron injection showed Arrhenius behaviour with two activation energies. At low temperature a process with a small activation energy of (21 ± 4) meV dominates, whereas at higher temperature a mechanism with an activation energy of (450 ± 170) meV is dominant. The low temperature regime was speculated to be related to surface phonon modes, and is studied in more detail in Chapter 4. The high temperature activation energy is very similar to the depth of the physisorbed well given above. This similarity suggests that at high temperature, desorption may also occur from the physisorbed well. This leads to a model whereby electronic excitation promotes the molecule to the physisorbed state, where it can either diffuse, desorb or dissociate, depending on the experimental parameters. If it desorbs it does so thermally, leading to the barrier measured in [42], otherwise it can reattach to the surface leading to diffusion, or capture a second electron and perform a two-electron dissociation (vanishingly unlikely in a non-local situation).

The work described in this subsection shows the importance of the physisorbed state in many of the manipulation processes possible on Si(111) $-$ 7$\times$7: PhCl. The importance of this state, particularly for dissociation, suggests that it might be interesting to study in isolation, by preparing the Si(111) $-$ 7 $\times$ 7: PhCl system at low temperature, where chemisorption is prevented by the barrier between physisorbed and chemisorbed states. This study is described in Chapter 5.

1.5 Self-assembly

An alternative method of controlling adsorbates on surfaces is to exploit the properties of the adsorbate to create surface structures with no outside influence: self-assembly.

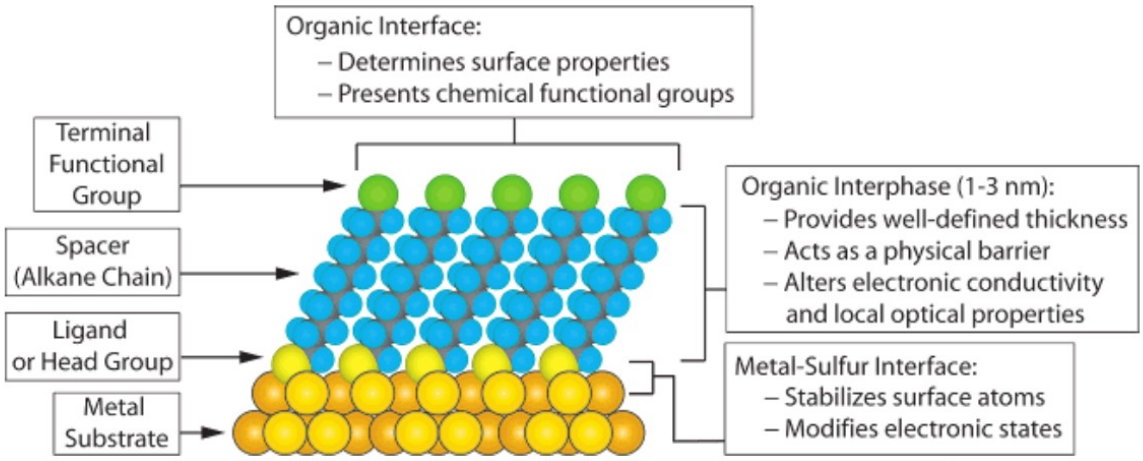

Figure 1.15: Schematic of a standing-up thiolate SAM from [70] showing the main parts of the SAM and their purpose.

The modern concept of a self-assembled monolayer (SAM) is based around the idea of a tailored molecule, which bonds covalently to the substrate and presents a functional outer layer: typically, the molecule consists of a headgroup (responsible for the bonding) and a functional unit attached to this headgroup, which is chosen based on the desired properties of the overlayer [70].

SAMs have been formed on many surfaces with many bonding headgroups, a detailed compilation being presented in table 1 of this review [70]. Metals are the most commonly studied surface for SAMs, followed by semiconductors, with several oxide surfaces being studied around the time of the review. Among metals, gold is studied most often [71, gives a recent review] given its relatively inert nature and easy fabrication [72]. This allows it to be studied with relatively low expense in ambient and 'dirty' environments [70]. Single crystal gold is also used; although it is more expensive it is easier to process in the long run, as repeated sputter-anneal cycles can be less intense as the material becomes progressively more pure. The large volume of literature on gold also means that the surface is well characterised for SAM growth [70, 71, 73, contain a selection of several hundred papers]. In addition, gold is biocompatible [74, 75], an important feature when

attempting to use SAMs in biological applications, where the cell in contact with the SAM must not be damaged.

The range of applicability of SAMs is vast, and their ease of preparation and functionalization has allowed them to go from acting as model systems to being useful day-to-day tools in physics, chemistry and biology labs around the world. SAMs can be used to adjust many surface properties such as corrosion resistance [76, 77], friction coefficient [78, 79], and wettability [80]. Their ability to change surface properties can also be exploited in lithographic processes [81, 82]. In addition, they can be used to facilitate the attachment of biological specimens to surfaces [83–85], and even facilitate the detection of biological activity through electrical [86] or fluorescent [87] signals. They can also be used to control the structures of nanoparticles and alter their surface characteristics [88–90], as well as controlling surface crystallisation [91]. Finally, SAMs have diverse uses in molecular machinery and circuitry: playing an important role in nanomechanical devices [92], and acting as test beds for molecular wires [93, 94], electronics [95] and spintronics [96].

1.6 Self-assembly of thiolates on gold

The most studied example of the above systems is that of thiolates on gold [70, 71, 73]. These molecules use sulfur atoms as their headgroup to bind organic molecules to the surface. Typically the organic molecule will be an alkane chain, in many cases with a further functional group opposite the sulfur. Thiolate SAMs exhibit a broad range of surface phases depending on coverage and may have any of a number of functional units appended to the end of the alkane chain to present on the outer side of the overlayer.

Despite their ubiquity, there are still many unresolved questions regarding thiolate SAMs, possibly the most surprising being ‘what is the exact nature of the bonding between SAM and surface?’ This has only recently begun to be understood, but is a key property of the SAM. This section introduces the gold surface, before briefly introducing the bonding between gold and SAM, and finally looking at the modern interpretation of

the bonding between alkanelthiolates and the gold surface. This last area is explored for low coverage phases in Chapter 3, where the various dynamical processes possible within the low coverage phase, such as diffusion and conformational switching, are studied in detail over a range of temperatures. This study aims to increase our understanding of the low coverage phase where steric effects play a less dominant role compared to the full coverage phases, and as a result the surface-adsorbate bond plays an important role.

1.6.1 The gold surface

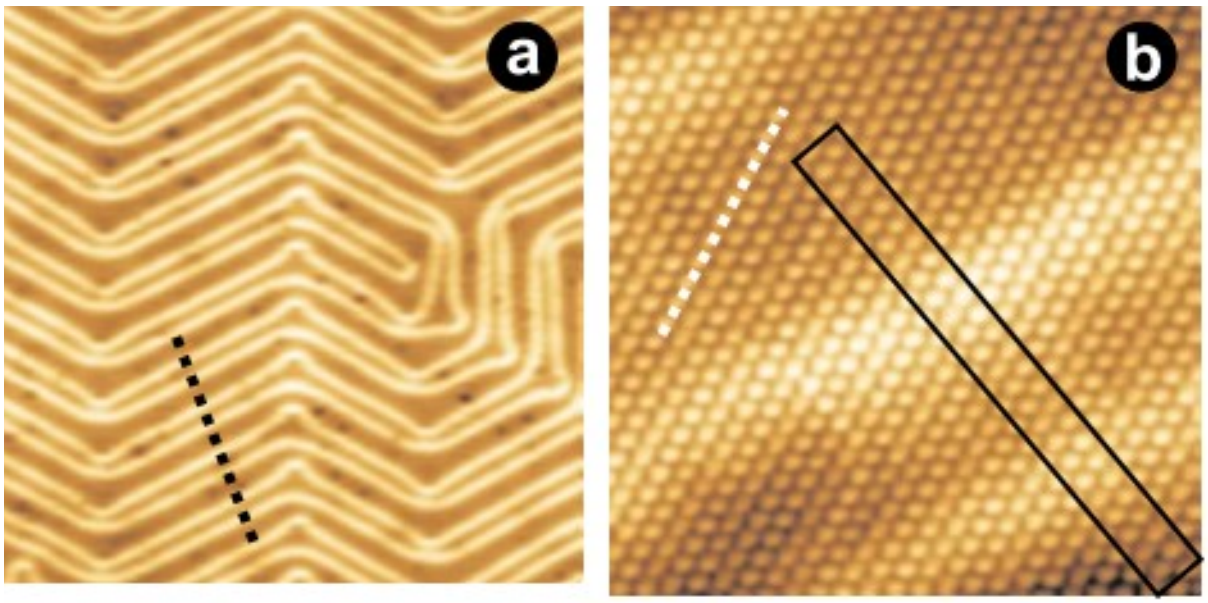

Figure 1.16: Figure reproduced in part from [97], showing STM images of the gold surface. On the left, a) shows the large scale herringbone reconstruction, on the right b) shows atomic resolution. A unit cell is indicated in black.

Gold is a noble metal with an fcc structure in the bulk. The Au(111) surface is particularly special as it is the only metal whose (111) surface reconstructs [98]. The surface reconstruction of gold was hinted at before the advent of STM [99–104] but again confirmation of the surface atomic structure came from a number of STM studies [105–107]. In addition STM revealed large scale ordering of the Au surface that was not resolved by any of the other techniques [98].

The gold surface reconstruction is complicated, with features on many different length

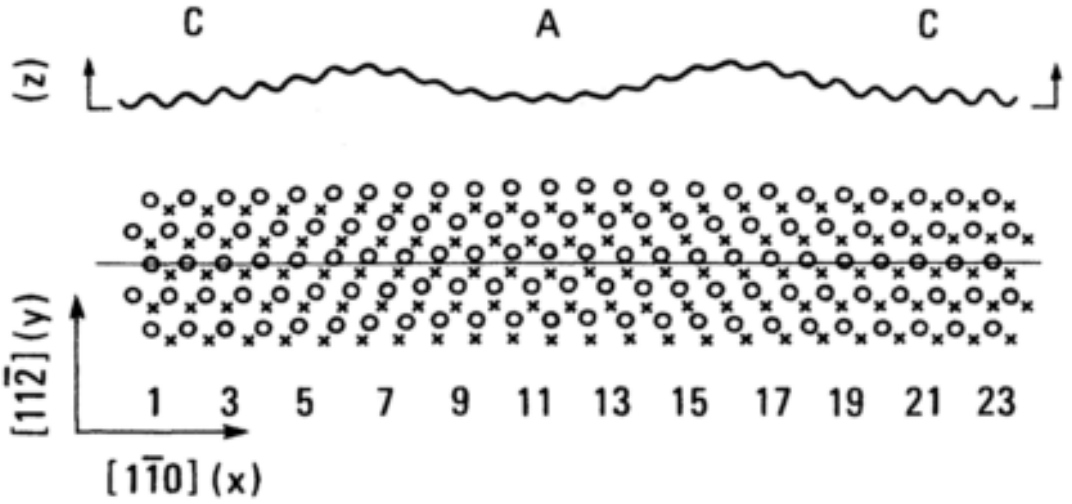

Figure 1.17: Figure reproduced from [107], showing a schematic of the gold unit cell. The top panel shows topography normal to the surface. The bottom panel shows the lateral positions of the top layer atoms as open circles, and the second layer atoms as crosses. The labels A and C mark areas of HCP and FCC stacking, respectively.

scales. These comprise a $22 \times \sqrt{3}$ unit cell exhibiting uniaxial contraction along the $[\bar{1}10]$ direction, with two paired dislocation lines separating areas of FCC and HCP stacking, a superstructure of domains with various orientations, elbow sites occurring at domain boundaries, and monatomic steps between terraces of width 1 nm to 100 nm. A schematic of the atom positions in the unit cell is shown in Figure 1.17, and atomically resolved images of the surface are presented in Figure 1.16.

The unit cell exhibits a contraction of the surface hexagonal lattice by about 5% along the [110] direction, compared to the bulk lattice [101], which leads to 23 surface atoms occupying the same space as 22 atoms would in the bulk. This compressive stress and overoccupation results in the formation of dislocation lines, as they allow for two areas of more favourable alignment with the underlying lattice [108]. Recent DFT studies suggest that the stacking varies more or less continuously over the unit cell, with the actual HCP and FCC regions being only a few atoms wide [108]. In order to relax strain isotropically over the surface, three orientations of the $22 \times \sqrt{3}$ unit cell are necessary. These order in a herringbone superstructure, which provides a long range relaxation of stress at the expense of an increase in local stress associated with the formation of a domain wall [98].

At boundaries between domains of different unit cell orientation, the dislocation lines must bend, which leads to another of the main features of the Au(111) surface: elbow sites. The elbow sites formed are of two types, *bulged* and *pinched*. Both elbow sites can be preferential sites for adsorption, due to the altered bonding environments they present, and are often found occupied by adsorbates present on the surface [109–111].

1.6.2 Structures of thiolate self-assembled monolayers on gold

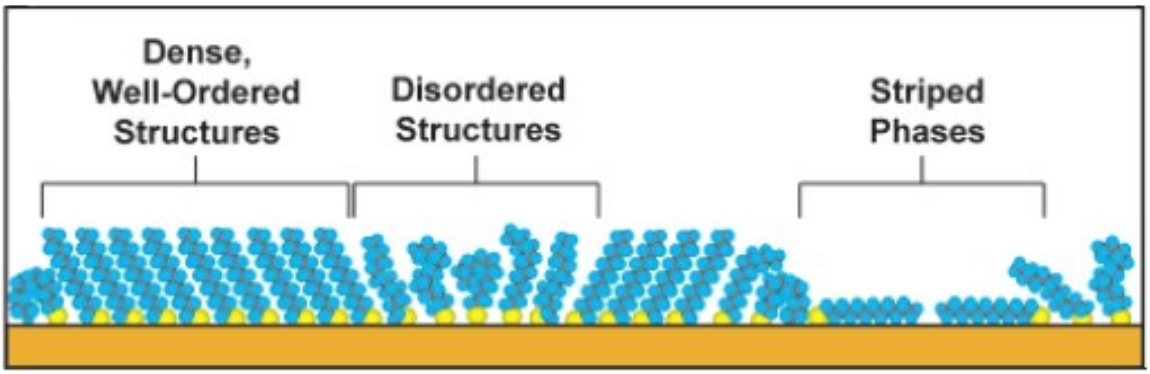

Figure 1.18: Figure adapted from [70], showing broad categorisations of SAM phases. The SAMs can be categorised according to whether the chains are upright and closely packed, or less dense and lying down. Disordered versions of both phases exist.

There are a large number of surface phases of SAMs, but for layers made of long chainlike molecules these usually fall into two broad catagories: 'standing up' phases, where the coverage is high and the molecules are closely packed; and 'lying down' phases, where the coverage is low and the molecules are packed more loosely [73]. When the coverage is very low the molecules lie flat on the surface in order to maximise the Van-der-Waals interaction with the substrate. As the coverage is increased the molecular chains all align pointing outwards in order to minimise their footprint on the surface, allowing a greater number of molecules to bond to the surface, and chain-chain interactions to be maximised. This standing up, maximum coverage phase is the one utilised most often in applications of SAMs as it is typically the most ordered: forming a complete overlayer where the functional groups attached to the chain ends are exposed, and the bare substrate

is covered completely. It is difficult to determine the surface-headgroup bonding in this phase by STM as the interaction between the closely packed chains (typically relatively long) dominates over the surface bonding, and the alkyl chains typically obscure the surface-headgroup bond, forcing a reliance on diffraction based methods to resolve the configuration at the SAM-metal interface [112]. In addition there is some uncertainty about what is being imaged in the STM, especially for longer chains in the standing-up phase [113]. The laying-down phase is typically more illuminating in imaging based methods, such as STM and AFM, as the bonding region is more exposed [114], but is less useful in laboratory applications as it does not present a complete functionalised overlayer as does the dense upright phase.

Full coverage layers of long chains pack in a $\sqrt{3} \times \sqrt{3} - \mathrm{R}30^\circ$ close packed layer [115–117], but in addition were found to exhibit a $c(4 \times 2)$ (or equivalently $3 \times 2\sqrt{3} - \mathrm{rect}$) super lattice by a number of techniques [118], which could be achieved starting from a close packed $\sqrt{3} \times \sqrt{3} - \mathrm{R}30^\circ$ lattice by allowing two distinct sites or chain orientations per unit cell. The $\sqrt{3} \times \sqrt{3} - \mathrm{R}30^\circ$ unit cell would correspond to having the sulfurs in a hexagonal lattice, with the threefold hollow site being the initially proposed bonding geometry [119]. There has been some discussion in the past literature as to whether the sulfur bonding is in fact $\sqrt{3} \times \sqrt{3} - \mathrm{R}30^\circ$, or whether there is some sulfur-sulfur pairing giving rise to the $c(4 \times 2)$ phase [120]. The initial results suggesting this pairing seem to have been refuted [121, 122], and the current model for the $c(4 \times 2)$ is still unsure. Some combination of gold adatoms and vacancies are likely to be involved, for details see [71, section 4.4] and Section 1.6.3. This problem has recently become even more complicated with the discovery that gold adatoms are involved in the bonding [71].

SAMs are attached to the surface by the headgroup-substrate bond. As such it is a key factor in many properties of the SAM, such as the lifetime of the SAM, its conductivity, and its structure. The main source of defects in the SAM is desorption in the long term [70], and the rate of desorption is tied to the strength of the bond which attaches the constituent molecules to the surface. The Au-S bonding therefore determines the length

of time before the SAM forms defects. In addition, the bonding to the substrate can substantially affect conductivity through SAMs [123], which could affect various experimental uses which rely on this property [93, 124, 125]. On surfaces the close proximity of many long alkane chains typically means that Van-der-Waals forces between chains dominate the surface ordering. This changes in low coverage phases, for short chains and on nanoparticles. In low-coverage phases, steric effects play less of a role and the arrangement of the alkanethiol is determined by the headgroup bonding to the surface, and it's interaction with other alkanethiols [126]. Though these low-coverage phases are not the main form of SAMs used experimentally at present, they could have uses in arranging material on a substrate, where the gaps between chains of molecules could be used to control adsorption of another material, or in molecular electronics, where long flat-lying chains have found application [127, 128]. Additionally, in situations where the full coverage phase is desired, the low coverage phase may play an important role as a 'kinetic trap', where the energy barrier to lift the chains from the surface can prevent the formation of the otherwise thermodynamically stable standing-up phase [129, 130]. Indeed, for short alkane chains, there does not appear to be a close packed standing-up phase at all [130, 131]. On nanoparticles the large surface curvature typically increases the space available to the chains [132], reducing chain packing, whilst increasing packing of the binding headgroup [133]. Together, this implies a more important role for the headgroup substrate interaction, as the chains may have less influence on the structure at the nanoparticle surface. As such the bonding between the sulfur and the surface plays an key role in the SAM, yet it is still poorly understood.

1.6.3 Gold adatom models for thiolate bonding

The early interpretation of the bonding of alkylthiolates to gold assumed a direct bond of the sulfur to the gold surface [73, 118]. This could not be reconciled with some results of the time which suggested that the sulfur should be located at gold atom atop sites

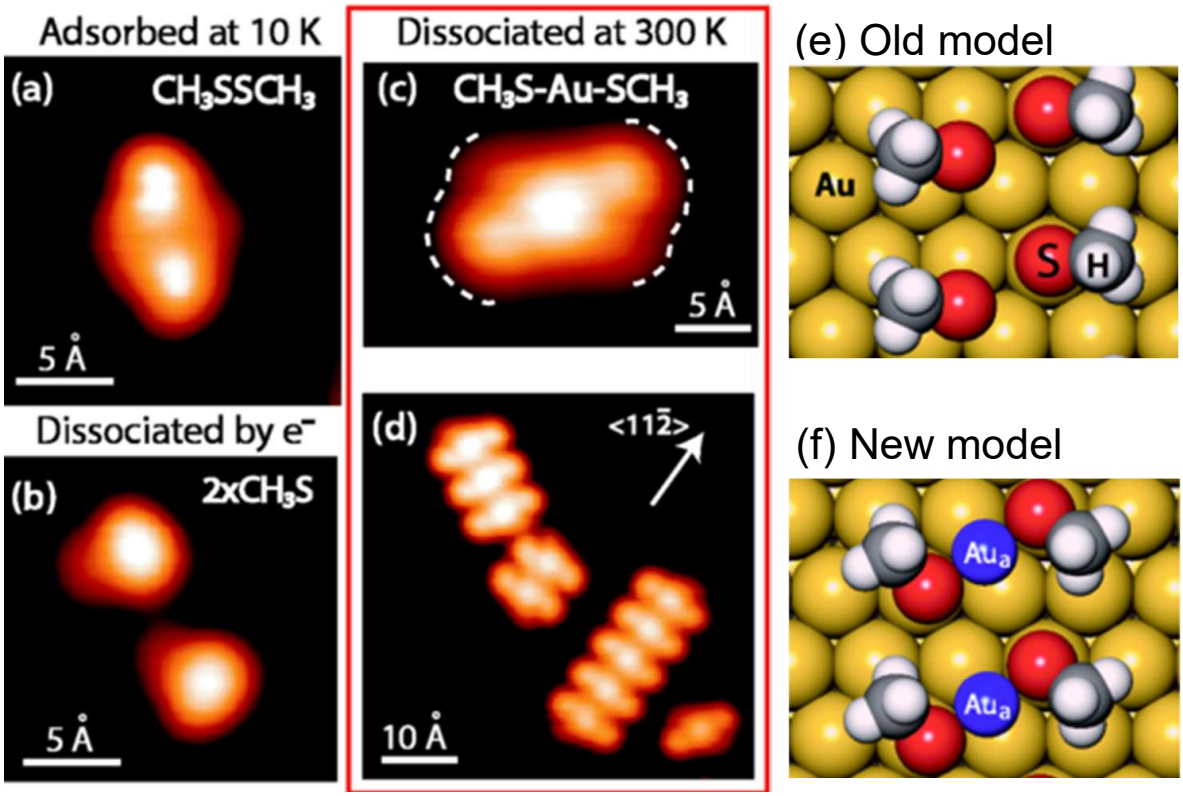

Figure 1.19: Figure adapted from [134] showing evidence for Au-adatom integration into the diemthyl-disulfide molecule on adsorption. Panels a) and b) show the result of electron-induced dissociation by the STM. Panel c) shows the results of dissociative adsorption triggered by raising sample temperature to 300K. The dissociation products self-assemble into the chains shown in d). Panel e) shows the previously assumed model. A new model is proposed in f) to model the result shown in c).

[135, 136], rather than the threefold hollow or twofold bridge sites. Various solutions were proposed, but strong evidence for a new attachment geometry was presented in a paper by Maksymovych *et al.* [134], which used STM imaging of the dissociation of dimethyl-disulfide to show that the base component of the dimethyl-disulfide layer was in fact a $(CH_3)S-Au-S(CH_3)$ moiety. They showed that dissociated physisorbed molecules deposited at 10 K appeared differently in the STM to molecules dissociatively adsorbed by raising the sample temperature from 10 K to 300 K, and proposed that this difference was the result of a gold adatom inserted between the two $S(CH_3)$ groups. In addition they compared the thermal decomposition to that induced by electron injection by the STM

tip and found that the final results were different: the electron-induced mechanism led to the production of two separate $S(CH_3)$ groups as was previously expected; the thermal method led to the incorporation of a gold adatom. The final position of the Au-adatom-dithiolate (AAD) unit was distinguished by using CO molecules to mark the gold lattice position and then triangulating the position of the molecules from these. Examining the registry of the AAD unit suggested that the sulfur would now occupy atop sites in accord with the results of [135, 136]. The AAD unit is imaged as 3 bright features in STM, two possible shapes can be seen depending on whether the AAD unit is in the *cis* or *trans* orientation, these chiral structures will be described in more detail below.

The proposed incorporation of adatoms found further supporting evidence in the known propensity of thiolate based SAMs to lift the herringbone reconstruction [137, 138] and introduce etch pits [139–141] on the surface. These phenomena are now attributed to the need of the thiolate layer to incorporate these gold adatoms into its structure. In the above paper the number of atoms in the reconstruction and in the AAD units was compared to confirm that as the number of chains increased the number of gold atoms involved in the reconstruction decreased; however, the total number of gold adatoms required for saturation coverage is higher than the number released by removing the reconstruction, requiring additional adatoms be removed from step edges and etch pits on the surface. These findings require a reanalysis of previously studied surfaces to determine the range of this new bonding model.

The Au-adatom model has been found to apply to other systems in addition to dimethyl-disulfide, these include longer alkane chains [143] and phenyl groups [144] on gold as well as similar adatom based models on other surfaces [145, 146]. This suggests metal adatoms play an important role in the formation and structure of organic overlayers on a variety of surfaces, but there is still a lot of work to be done in this area. Again, these alterations in the basic structural unit can be particularly important in systems with reduced size, such as gold nanoparticles, where the limited bonding locations on the surface mean small alterations in the bonding could have a substantial effect on the

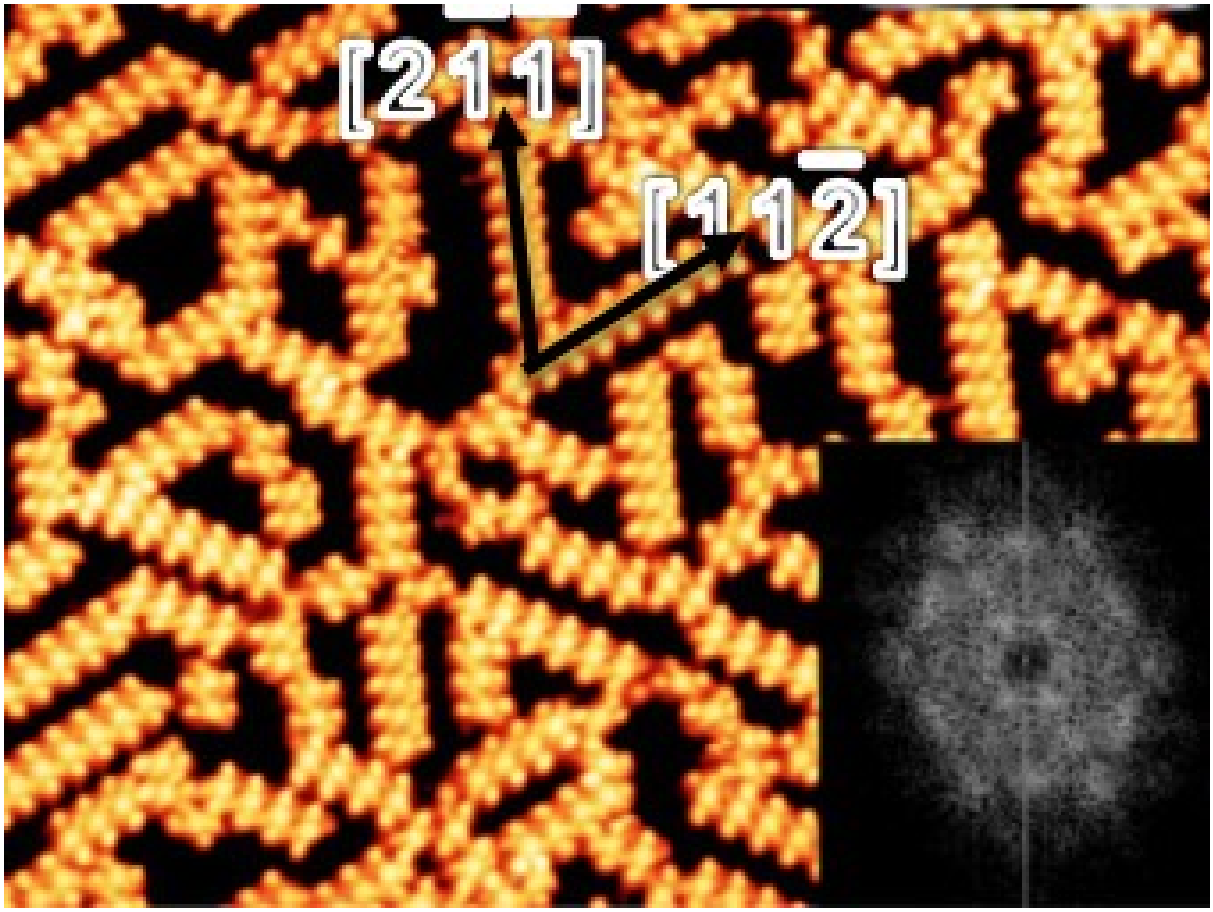

Figure 1.20: Figure from [142] , showing the low coverage phase of the methylthiolate SAM. Chains are formed from the AAD units described in the text. A Fourier transform is also shown as an inset, which shows how the low coverage phase exhibits the same diffraction pattern as a $\sqrt{3} \times \sqrt{3} - R30^{\circ}$ overlayer.

arrangements of the surface overlayer and that, for small nanoparticles, a sizeable fraction of the atoms in the nanoparticle could in fact be located in the ligand coating. This is an important consideration as ligands are frequently used to control the size of nanoparticles formed, so a good understanding of the ligand-particle bonding is important for precise control of the final nanoparticle size distribution. In addition the location of metal atoms in the basic structure of the SAM suggests the possibility of using organic adsorbates to create ordered arrangements of metal adatoms on surfaces, which may have interesting implications, were the atoms magnetic for instance.

For the alkanethiol on gold system the nature of the dominant forces within the SAM depends on the chain length, which may help to explain some of the initial uncertainty

about the bonding. For chains formed of alkanethiols with formula $CH_3-(CH_2)_n-SH$ it is found that the number of carbon units determines whether the substrate-chain or chain-chain interaction dominates the structure. The structure of monolayers formed of chains with $n \leq 2$ is dominated by the Au-S, substrate-chain interaction. In monolayers formed of longer chains the Van-der-Waals interaction between the chains begins to dominate and control the overall structure. This leads to an alteration of the SAM unit cell between propylthiolate and butylthiolate monolayers [131]. For long chains where the Van-der-Waals forces are dominant it may be that the surface bonding plays a less important role. This phenomenon was investigated in [131], where several different chain lengths were investigated using STM. It was found that all chains with $n \leq 2$ could be explained using the AAD bonding motif of [134] being arranged in a 3×4 overlayer. The most commonly observed phases for SAMs with longer chains is a $c(4 \times 2)$, or equivalently $3 \times 2\sqrt{3}-$rect phase. Charge transport through SAMs is usually a function of the length of the alkane chain. If, in addition to chain length, the surface-chain contact alters as the chain length is varied, this would have to be taken into account in these applications.

Another result arising from this new model is that for methylthiolate there does not appear to be a $\sqrt{3} \times \sqrt{3}-\mathrm{R30}^\circ$ phase. A comprehensive study of the phases of methylthiolate SAM is presented in [147], which studies the phase transitions that occur as the coverage of the SAM is varied. At the two extremes are a low coverage striped phase, which was also shown in [134], and the high coverage 3×4 phase. At intermediate coverages two other phases may exist: $7 \times \sqrt{3}-$rect and $3 \times 4\sqrt{3}-$rect. The low coverage phase is formed of AAD units organised into chains, electrostatic interactions between the slightly negative sulfur atoms and the slightly positive gold adatoms drive chain formation. These chains can be thought to build the other phases. Formed of all *trans* isomers, the chains are built by placing an AAD unit on each bridging site along one of the $\{11\bar{2}\}$ directions. The $7 \times \sqrt{3}-$rect phase is the result of stacking the chains side-by-side with an offset as shown in Figure 1.21. To achieve closer packing every other AAD unit in the chain is offset by $\sqrt{3}a$ in the $[\bar{1}2\bar{1}]$ direction (for a chain along $[11\bar{2}]$). This creates

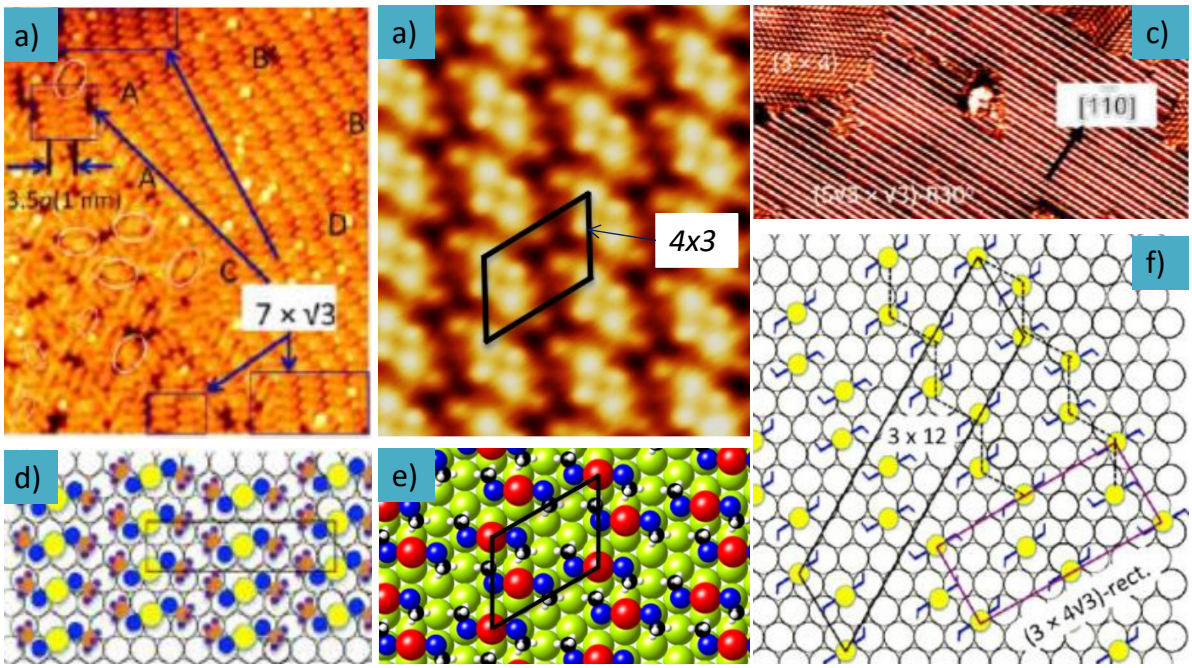

Figure 1.21: Figure collated from [142, 147], showing all phases of the methylthiolate monolayer. Panels a), b) and c) show the phases imaged in STM and d), e) and f) show the deduced structures.

the second basic structural unit, called a 'tetramer' in [134], it is usually present in the low coverage phases as a discontinuity in the chains. This creates zigzag chains which when widely spaced constitute the $3 \times 4\sqrt{3} -$ rect, and when packed as close as possible form the 3×4 phase. When not belonging to one of the above phases, or a variety of domain wall structures between different domains of the above, the molecules form a disordered array over the surface. It is speculated in the paper that previous observations of a $\sqrt{3} \times \sqrt{3} - R30°$ structure in diffraction may have been the result of the chain phase, which presents equivalent spots as a result of the different chain orientations.

As mentioned in the discussion on the discovery of the AAD unit above, the AAD unit can take two conformations on the surface, but there are in fact four possible types of binding. Both sulphur atoms can be considered to be bonded in a tetragonal type geometry, with four bonds comprising one to the substrate, one to the Au adatom, one to a methyl group, and one taken up by a lone pair. As the substrate and adatom bonds are fixed, swapping the positions of the lone pair and the methyl group allows two different

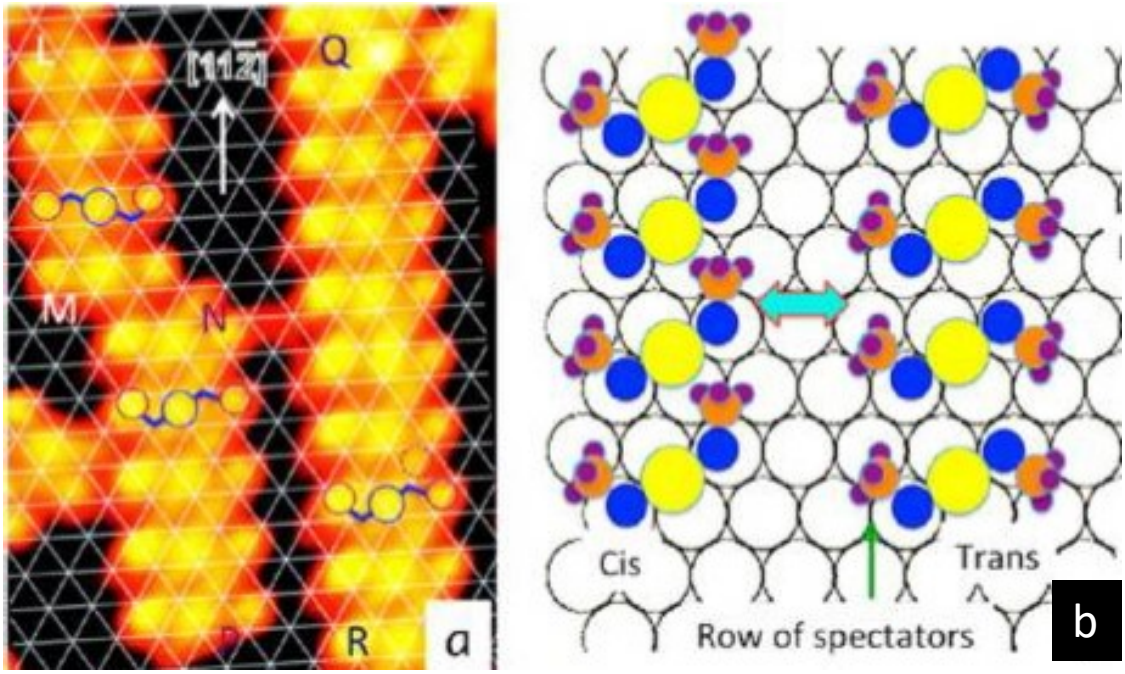

Figure 1.22: Figure from [147], showing *cis-trans* switching in a methanethiolate chain and a simple model. The chain between Q and R shows extra features on the right-hand side when compared to the images shown in Figure 1.19. This is interpreted as a transient switching behaviour under the tip between the *cis* and *trans* forms shown in b) on the right. In the other chains it can be seen that the side that switches varies, this is explored in Chapter 3.

chiral enantiomers, which we label R and S. Both sulfurs can occupy two configurations in this way leading to 4 possible binding configurations: RR, SR, RS and SS. AAD units with the same chiral structure on each side of the adatom (SS or RR) are called the *trans* isomer. A change to SR or RS constitutes a *cis- trans* transformation to the *cis* state. An example of *cis* and *trans* chains are shown in panel b) of Figure 1.22. Chains are usually made up of all *trans* isomers, typically only isolated AAD units or chain end units are found in the *cis* state. In [147] it was found that in addition to the expected three dots, new features are seen when imaging the chains at close tip sample proximity, this is shown in panel a) of Figure 1.22. It was speculated in the paper that this was a result of *cis- trans* transformation induced by the tip in one side of the chain, with one side merely

spectating. In fact, this change was found to be specific to the type of chain being scanned over, with one side of the chain altering for an RR initial state chain, and the other for an SS. The exact reason for this switching was unclear and is one point of investigation of this thesis. The authors speculate that the asymmetry may be a result of the bonding location of the sulfur headgroup, possibly implying another unknown element to the AAD bonding configuration.

In order to better understand the AAD model and the forces involved in the low coverage phase the experiments on the Au(111)-DMDS system in this thesis look at the low temperature phase at a variety of temperatures and under a variety of scanning conditions. Low temperature imaging examines the structure of AAD chains at 77K and further investigates the switching phenomenon described above. A series of other thiolate structures found at step edges or surrounding small gold islands have been imaged, which may be important on nanocluster surfaces. Finally, the study at varied temperature reveals the different dynamical processes which activate as the temperature is increased, and estimates the barriers for these processes.

CHAPTER 2

Methods

2.1 Overview

This chapter describes the experimental methods used in the results chapters to follow. These include working with ultra-high vacuum (UHV) systems, low temperature scanning tunneling microscopy (LT-STM), and the preparation of the surface-molecule systems to be studied.

2.2 Ultra-high vacuum

All experiments in this thesis were conducted under UHV conditions; the attainment and maintenance of these conditions is a challenge in and of itself, and will be described in this section. The description of the UHV apparatus will begin with a description of the chambers which comprise the system, this will then be followed by an explanation of the pumping methods used to achieve and maintain the UHV conditions.

2.2.1 System

The UHV system is composed of two chambers: one for sample preparation (prep chamber), and one containing the STM and cryostat (analysis chamber). In addition to the main chambers, a small loadlock is attached to the prep chamber and can be used to introduce samples to the system without breaking the vacuum. Finally, a gas-line is connected to the system to deliver gas to the chambers for argon sputtering and molecular deposition, this will be described in more detail in Section 2.5. All connections between components of the vacuum chamber are made using CF flanges with oxygen-free copper gaskets, the only exception is the loadlock, which is sealed with a viton gasket due to the high frequency at which it is opened.

The preparation chamber is where sample preparation is performed and has facilities for sample heating and cooling, argon-ion sputtering, and mass spectrometry. Sample heating and cooling takes place on the manipulator arm, which is also used to move

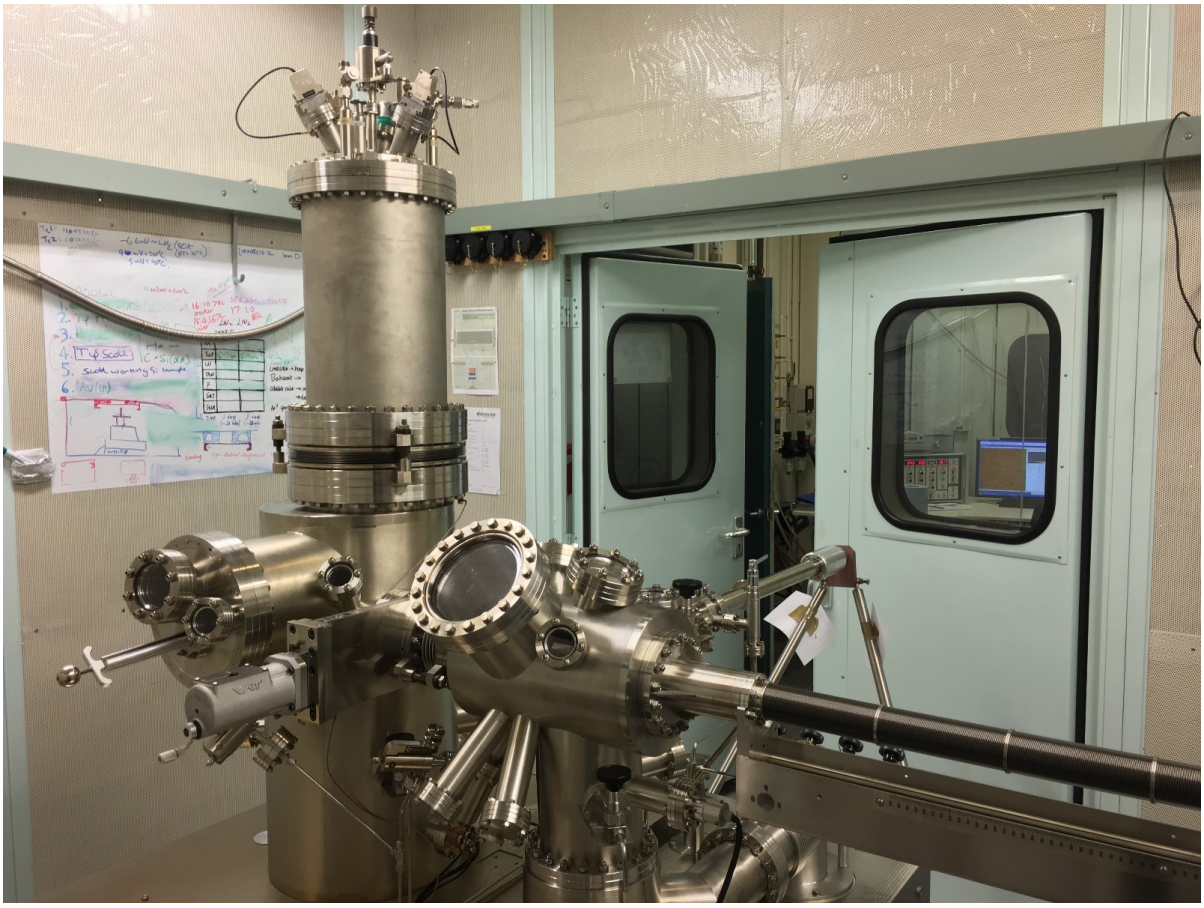

Figure 2.1: A photo of the LT-STM and attendant UHV system. The tall chamber on the left is the analysis chamber, with the cryostat mounted on top via a large bellows. The smaller chamber on the right is the preparation chamber.

samples between prep and analysis chambers. The manipulator arm has two separate stages: one can be used to cool the sample using liquid nitrogen, the other to heat the sample, either via direct-current or resistive heating. Both heating and cooling stages are fitted with thermocouples which allow the temperature to be monitored at the sample stage. Power for both direct-current and resistive heating is supplied by a TDK lambda GEN60/12.5 power supply. Resistive heating is achieved by supplying power to a pyrolitic boron nitride (PBN) heating element, direct current by passing a current through the sample via a contact brush. The temperature can be measured either using a thermocouple

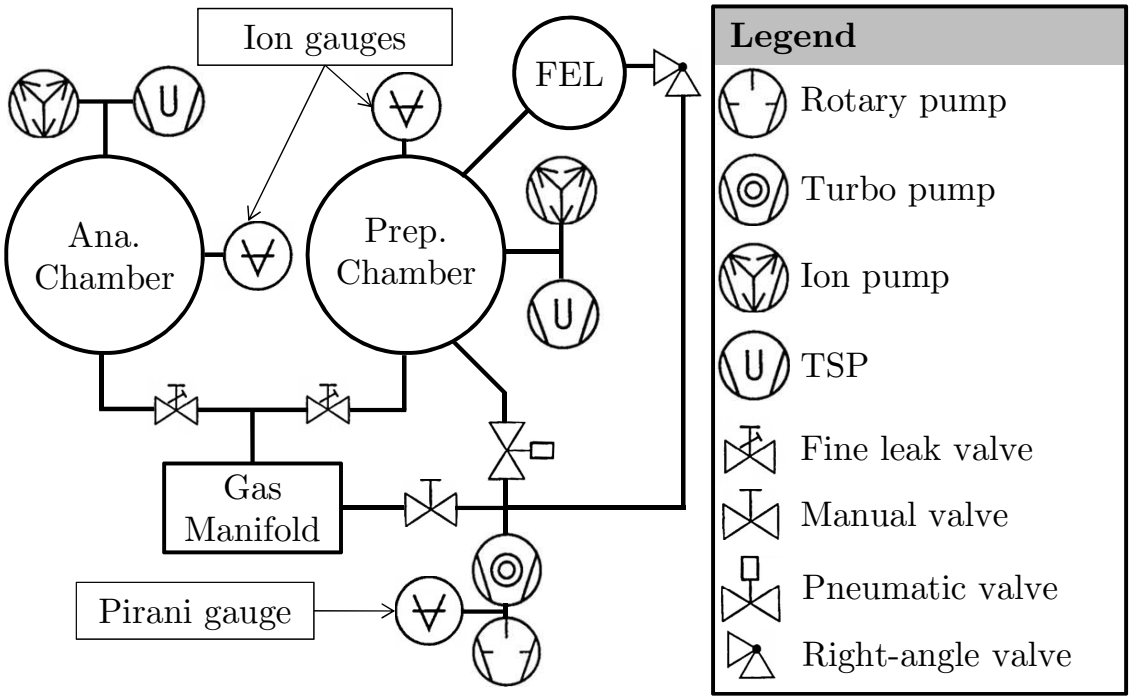

Figure 2.2: A simplified diagram of the LT-STM vacuum system. All of the main pumps, gauges, and chambers are shown. Important valves and connections used in experiments are shown. The gas manifold allows connection of gases and other chemicals to the system for deposition in either chamber. All labelled pumps are discussed in the text.

underneath the sample, or by use of an optical pyrometer mounted near the view port.

2.2.2 Pumping

To attain UHV conditions (starting with all chambers at atmospheric pressure) pumping proceeds via three stages. Initially a rotary-vane pump (rotary pump) is used to *rough out* the chamber, rapidly reducing the pressure from atmospheric pressure to $\sim 10^{-3}$ mbar. Almost simultaneously a turbo-molecular pump (turbo pump) is started, this continues the pumping process, reducing the pressure further, to about $\sim 10^{-7}$ mbar. At this point to achieve a lower pressure it is advantageous to bake the system to remove water from the system (see Section 2.2.3 for further details). Finally, ion-pumps are used to achieve the base pressure of the system, these are assisted by titanium-sublimation pumps (TSPs), which operate on a periodic basis. Using this process it is possible to achieve a base pressure of $\sim 10^{-11}$ mbar in the prep chamber, and $\sim 10^{-12}$ mbar in the analysis chamber.

The whole system is connected to an interlock system, which turns off the power supply to vulnerable components in the event of a significant pressure rise.

The rotary pumps used to initially rough out the chambers also act to *back* the turbo pump: the rotary pump lowers the pressure at the exhaust of the turbo pump such that the pump can work effectively [148]. The rotary pump is a mechanical pump which forces the gas being pumped through a series of compression stages in order to reduce the pressure at the inlet side. Care must be taken to ensure lubricating oil does not enter the vacuum system. Foreline traps between the rotary pump and roughing line act to prevent this. The turbo pump uses a rapidly rotating turbine to pump gas via momentum transfer to particles incident on the turbine blades. The turbine is delicate and will be impeded by the large gas flows at higher pressure, hence the requirement for initial pumping via the rotary pump [148].

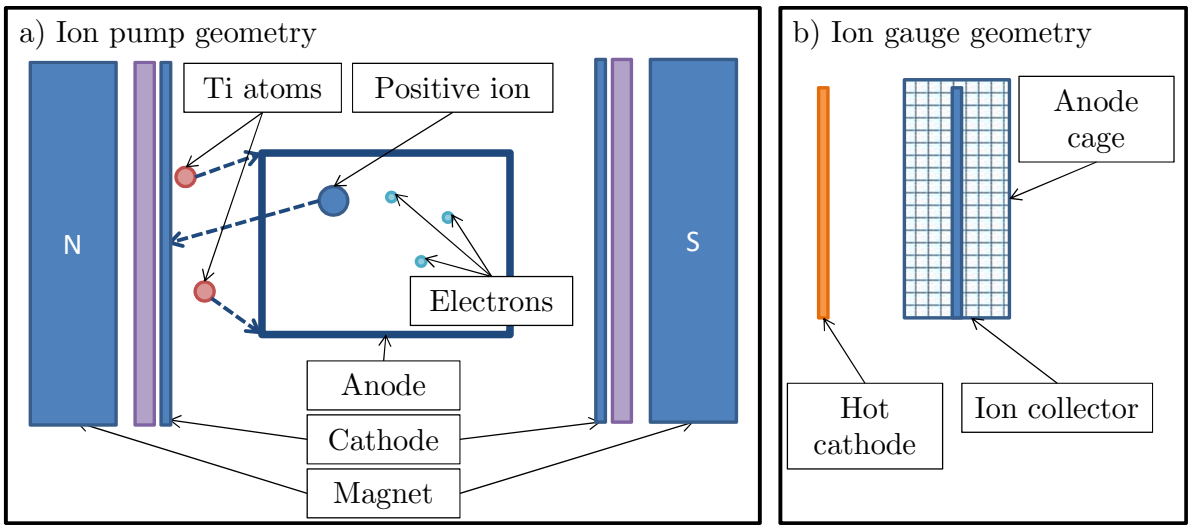

Figure 2.3: Panel a) shows the geometry of an ion pump, panel b) a hot-filament Bayerd-Alpert ion gauge. Their operation is described in the text. In a) the anode is a cylinder, with the cathodes being plates, in b) the anode is a cylindrical cage, and the cathode and ion collector are both thin wires. A diode type ion pump is composed of only the blue elements. In a triode type design the cathode plates are replaced by grids, and the purple features are additional plates behind the cathode grids. The triode geometry helps minimise sputtering of previously buried ions [148].

The ion pump relies on the sputtering of a *getter* substance (usually Ti) to form a

reactive film. Gas present in the chamber can then react with this film and become trapped [149]. Ions and electrons are accelerated by a high-voltage between a cathode and an anode and ionise further gas particles by impact ionisation. It is these ions that sputter the cathode to generate the Ti film. Noble gas atoms are typically trapped by burial in the cathode [150]. A magnet surrounds the electrodes and increases the number of ionisation events by causing electrons to move in long helical paths.

Finally, TSPs work by heating Ti filaments for short periods of time (1 minute). This coats the surfaces around the filament in a reactive Ti film which then traps other particles from the chamber. TSPs are run periodically to replace the reacted Ti with a fresh layer, the lower the pressure the lower the frequency of operation required. At the base pressure of our system it is only necessary to run the TSPs on a weekly schedule.

Pressure is monitored using a hot-cathode Bayerd-Alpert ion gauge with thoria-coated iridium filaments. An ion gauge functions in a similar manner to a redesigned ion pump, where the current of positive ions incident on a collector is used to measure pressure [150]. A hot-cathode gauge uses a heated cathode to generate electrons which are then accelerated to the anode causing the formation of positive ions. These ions are then collected at a collector, at ground potential. The low pressure limit of this detector is due to x-ray emission from electrons striking the anode: the x-rays then cause photo-emission at the collector which is detected as a *positive* current, indistinguishable from that due to ions. The Bayerd-Alpert design rearranges the gauge geometry to minimise this effect [150].

2.2.3 Baking

In Section 2.2.2 it was mentioned that it is necessary to bake the system to remove water and allow the system to reach its base pressure. This water is introduced during exposure of the system to atmosphere. Rather than just opening the system directly to air, nitrogen gas is used to vent the system. Nitrogen gas is pumped away efficiently by the pumps

in use on our system. Venting with nitrogen reduces the presence of other gases which may be harder to pump away. However, whilst carrying out work on the vented system it is impossible to prevent the introduction of some atmospheric gas into the chamber: it is the water vapour introduced here that baking aims to eliminate. Water is particularly troublesome as it degasses at a rate substantial enough to raise the base pressure of the system, but not fast enough to allow all the water to be pumped away quickly. By raising the temperature of the chamber the rate at which the water degasses is increased, thus allowing it to be pumped away over a period of days.

During the baking process the system is surrounded by insulation panels and heated via heating elements, essentially forming an oven around the entire system, which heats the system from the outside. The chamber is baked at 145 °C for 60 hours, a higher temperature would allow a shorter bake but could damage the STM head, the time used is such that the STM head reaches the setpoint temperature during the bake. After baking, the ion pumps are switched back on at high temperatue (around 100 °C) to allow them to release any trapped gas into the turbo pump without it sticking in the chamber. Any hot filaments are also degassed now for the same reason. The gas-line is not pumped during the bake out as there is only one turbo pump for the gas manifold and the prep chamber, using this to pump both would connect the gas-line (which is less well isolated from atmosphere) to the vacuum system, which is preferably avoided. The gas-line is instead evacuated prior to the bake and pumped again whilst the system is still hot, once the ion pumps are pumping the main chamber. If the gas-line is opened to atmosphere, for example whilst making the modifications described in Section 2.5.2, it is baked out separately using heating tape for several days. Otherwise, it is possible to keep the gas-line isolated from atmosphere at all times, meaning that the less thorough baking procedure is acceptable.

2.3 LT-STM

The low-temperature scanning tunneling microscope (LT-STM) is described in this section. In addition information is given on related techniques such as tip preparation and temperature control.

2.3.1 Microscope details

The microscope used for all of the experiments in this thesis was an Omicron LT STM, a commercial device, mounted on an Omicron surface science system, which comprises the preparation and analysis chambers described above. The STM is controlled using a Nanonis control unit (from SPECS Zurich), rather than the SCALA system provided with the microscope. One of the main benefits of this system is the ability to link the system with NI LabView, allowing for automation of some experimental procedures, which is described in detail in Chapter 5. The main components of the STM head are the STM stage, which can be suspended on soft springs to damp out external vibrations; the tube scanner, which moves the tip over the surface in response to an applied voltage; and the coarse motor, which allows the STM tip to be moved towards and away from the sample.

Damping is achieved by four mechanisms, all of which can be understood by considering the response of a harmonic oscillator to external forcing [151]. Firstly, the whole UHV system is situated on a large concrete block mounted on air-legs, which combine to give a very low resonant frequency (2 Hz). For a forced oscillator, vibration above the resonant frequency is suppressed. This very low resonant frequency acts to damp out low frequency vibrations being transmitted through the floor of the building. A secondary system of soft springs within the UHV chamber suspend the STM head, these springs damp out horizontal and vertical vibrations above their natural frequency. Thirdly, when suspended, magnets attached to the stage hang between copper plates on the cups attached to the bottom of the cryostat, these provide damping to the spring system suspending the head.

In a forced oscillator there is a trade-off between suppressing oscillations at the resonant frequency and suppressing those at higher frequencies [4]. The damping of the spring system by the eddy-current dampers is applied such that the resonance is somewhat suppressed, but sufficient high frequency vibration isolation remains. Finally, the STM head must be rigid, this can be understood by considering the STM scanner attached to the sample as an oscillator, where the structure of the STM head is a very stiff spring: in this case, the aim is to have the scanner move with the sample such that their relative displacement does not alter, so a rigid structure with a high resonance frequency is required. In addition to all of the above, the STM is also housed in an acoustic isolation booth, to isolate it from as much of the acoustic noise in the lab as possible (this is the structure seen around the STM in Figure 2.1).

The tube scanner is made of lead-zirconium titanate, or PZT, which is a piezoelectric material that deforms in response to an applied voltage. Voltages can be applied across different quadrants of the scanner to bend the tube in different directions. The whole tube scanner is usually referred to as *the piezos*, with each quadrant being referred to as a separate entity, for example 'the z-piezo'. An important consideration when using the LT-STM is the behaviour of piezoelectrics as a function of temperature: as the temperature decreases the response to a certain applied voltage is much weaker, requiring that the voltage applied to the piezos be recalibrated when the temperature is changed. Usually this is done by inserting a sample with known geometry and altering the calibration until the microscope image matches the ideal image. In practice, the response is almost linear, so by interpolating between calibrations it is possible to generate a good approximation of the calibration to use. As a result of the changing calibrations the piezos also have a resolution and scan range which are dependent on the temperature, as the temperature increases the maximum achievable resolution decreases, but the scan range increases.

In order to image the surface the tip must be brought within the z-piezo range of the surface, this requires a reproducible movement to within $\sim$200 nm of the sample surface, which is achieved using a *slip-stick* coarse motor. This takes advantage of inertia in a

similar way to the magician's trick with glassware and a table cloth: the coarse motor assembly is moved by a rapidly expanding piezo, applying a force greater than the force of friction between two surfaces, the moving part is then held in place by friction as the driving piezo slowly returns to its initial dimensions [152].

The first step in the approach procedure is to bring the tip towards the surface by eye, before activating the automated coarse approach mechanism. On activating the coarse approach, the coarse motor moves forward by one coarse step, pauses, and extends the z-piezo fully; if a setpoint current is sensed then the electronics retracts the z-piezo fully and finishes the coarse approach; otherwise, the cycle is repeated until the setpoint current is sensed. Typically the voltage used for approach is slightly higher, and the current slightly lower, than when scanning the surface of interest under normal imaging conditions, the aim being to keep the tip as far from the surface as possible to prevent crashing the tip on approach. The feedback loop (see Section 2.3.2 for detail) is normally set to operate much faster than when imaging to keep the approach quick.

2.3.2 Electronics

The electronics for the STM consists of three main components: a preamplifier and signal processing, a feedback loop and control software, and a high voltage amplifier. The preamplifier is responsible for recording the tunneling current and performing some initial filtering to remove high frequency noise. The signal from the preamplifier is passed to the Nanonis hardware where it is converted to a digital signal and further processed. The Nanonis hardware downsamples the signal to 14 kHz, the *real-time frequency*, which is the frequency at which the Nanonis real time engine (feedback loop) operates; this rate also determines the maximum speed at which data can be acquired, although for taking precise measurements the data is usually downsampled further to increase the resolution of the measurements. Specifically, this acquisition rate limits the speed at which images may be taken, the time taken to record spectra and the maximum frequency visible in frequency

domain analysis (as it determines the Nyquist frequency). The real-time frequency also places limits on the simulated lock-in amplifier included in the Nanonis hardware: to adequately simulate a sinewave in the software the lock-in frequency must be less than one tenth of the real-time frequency, so $f_{\mathrm{lock-in}} < 1400\,\mathrm{Hz}$. This determines the amount of time required to take scanning-tunneling spectroscopy measurements using the lock-in technique, described in Section 2.3.3.

The Nanonis hardware implements the feedback loop that controls tip position. Deviations of the measured current from a setpoint current are passed to a proportional-integral (PI) control loop, which generates an error signal. This error signal is then used to deduce the voltage that needs to be applied to the z-piezo in order to maintain the setpoint current. The high voltage amplifier takes the $\pm 10\,\mathrm{V}$ control signal generated by the Nanonis hardware and amplifies it to a voltage which can move the piezos. Several levels of amplification are possible: four, seven and fourteen times, yielding a maximum applied voltage of $\pm 140\,\mathrm{V}$. Amplification is chosen according to the desired imaging properties. High amplification gives greater piezo range of motion, allowing for larger scan areas, and greater z-piezo travel. However, noise in the control signal is also amplified, so high amplification gives more noise on small scale measurements. Low amplification reduces this noise allowing for more sensitive measurements. Due to the change of piezo sensitivity with temperature some amplification levels can become unsuitable, for instance at $4\,\mathrm{K}$ the lowest amplification level gives a very small scan range, and so is only practicable for very precise imaging.

2.3.3 Lock-in spectroscopy

The Nanonis hardware integrates a dual phase-locked-loop (PLL), and can be used to perform lock-in amplification of a signal. The principal of lock-in amplification is that only signals that are both at the same frequency and in phase with a control signal are amplified. This drastically improves the signal to noise ratio for the measurement. Having

a dual PLL allows for signals with a specific phase relationship to the control signal to be measured. In STM this technique is typically applied to spectroscopic measurements. In bias-spectroscopy, usually know as scanning-tunneling spectroscopy (STS), the bias is varied with the feedback looped switched off and the change in the current is measured. This provides details on the electronic structure of the sample according to Section 1.2. However, the quantity of interest is the differential of the current with respect to voltage. Differentiation of a noisy signal typically amplifies the noise, as small changes in the signal can create large changes in its gradient. A better technique is to apply a small modulation to the bias, such that $V = V_{\text{Bias}} + \Delta V \cos(\omega t)$, where V is the total bias applied V_{Bias} is the constant component usually varied in the STM, and $\Delta V \cos(\omega t)$ is the lock-in modulation. The lock-in amplifier can then be used to measure the differential directly. This can be understood by noticing that the current, I, is a function of V and can be Taylor expanded for a small modulation voltages:

$$I\left(V_{\text{Bias}} + \Delta V \cos(\omega t)\right) = I(V_{\text{Bias}}) + \frac{\mathrm{d}I}{\mathrm{d}V}(V_{\text{Bias}})\Delta V \cos(\omega t) + \ldots, \tag{2.1}$$

from which is is apparent that the response of I to the modulation of the bias is an additional ΔI that is in phase with the applied bias modulation, and proportional to the required differential.

To measure this quantity experimentally, the tip is withdrawn slightly from the surface until there is no resistive current signal. The bias modulation is then applied at a high frequency $\sim$1000 Hz, which generates a current response from capacitive coupling in the STM. The current response will then be measured 90° out of phase with this signal such that only the resistive component is measured in the experiment. Integer multiples of 50 Hz are avoided when selecting the frequency to minimise any ground noise being measured. The tip is then re-approached and moved to the feature where spectroscopy is required, the current and bias settings used here are known as the stabilisation parameters. When imaging and moving the tip the feedback parameters are set such that the tip

delivers a certain current at a certain voltage, for STS it is desirable for the imaging to take place at a bias where no spectral features are strongly present, such that variation in the tip height with position is as much as possible a result of geometric variation; otherwise, when comparing spectra between two points the tip height at stabilisation parameters may vary as a result of variations in the tunneling probability, not the geometry. Once over the feature to be studied, the tip is allowed to become stable at the stabilisation parameters before switching off the feedback and applying the voltage modulation ($\sim$40 mV, 1012 Hz). The bias is then swept over the range where spectral information is required (typically -2 V to 2 V), and both I and the resistive component of the lock-in signal are measured. The quantities I, V and $\mathrm{d}I/\mathrm{d}V$ are recorded simultaneously.

One final improvement is known as the Feenstra, or variable-gap technique. Because the current already typically increases rapidly with bias, the spectroscopic features at smaller biases can be hard to distinguish – STS has a low dynamic range. In order to increase the dynamic range, the tip can be approached to the surface in a linear way during the measurement, at the same time as sweeping the voltage. This acts to increase the measured signal at lower bias, allowing for better resolved spectra at these voltages, particularly important in semiconductors where the feature could be in the bulk bandgap. As the position of spectral features with energy is usually the desired quantity, the change to the amplitude of the signal is not a major issue.

2.3.4 Tip preparation

The STM tip is arguably the most crucial part of the STM, unfortunately it is also the most difficult to control. The quality of an STM image is entirely dependent upon the electronic states presented by the apex atom (or atoms) of the tip, as such no matter how good the control of the tip formation mechanism there will always be some element of chance involved in the imaging process. The aim of tip preparation is to give the user the best chances of getting a so-called 'good tip' in later in-situ tip treatments. A

good tip is largely determined by the user, and unfortunately introduces an element of subjectivity and irreproducibility into the imaging process. This section describes the entire tip preparation process, first giving a description of the process and the reasons for each step, then giving the detailed procedure followed.

Tips are produced via electrochemical etching of tungsten in sodium-hydroxide. Etching results in a nicely formed tip because of the preferential etching near the surface of the sodium hydroxide, which forms a 'neck' in the wire that gradually narrows as etching continues; eventually the bottom part of the tip drops off into the sodium hydroxide and the etching voltage is rapidly switched off. The aim of the tip preparation procedure is to produce a sharp tip which is mechanically stable. Wrongly chosen etch parameters, or vibrations disturbing the meniscus during etching can lead to malformed tips. Common problems are tips that are highly asymmetric; tips that etch in multiple stages, leaving steps down the edges; and tips that are too long. A one-to-one aspect ratio of tip length to tip diameter is desirable: tips that are too long tend to be unstable mechanically when scanning, introducing noise into scans; tips which are too short tend to not be very sharp.

The first step in making a tip is to cut a length of tungsten wire (diameter 0.25 mm, 99.95% purity), which is significantly longer than the final tip required. This wire will be electrochemically etched in 2 $\mathrm{mol/dm^3}$ sodium hydroxide to form the tip. For the tips used in the experiments in this thesis a two stage etching process was used: the first etch removes the damaged and deformed material near where the wire was cut, the second etch forms the tip itself (details are below). Before etching, the majority of the tip is immersed in the sodium hydroxide and electropolished by applying 9 V for around 10 seconds, this cleans the length of wire to be used.

Various parameters have an effect on the drop-off that terminates the etching process. The voltage applied to the tip to induce etching must be cut off as soon as possible after the drop-off, this prevents etching continuing after drop-off and blunting the tip. To control this a differential cut-off power supply is used, which cuts the supplied power very rapidly after a rapid decrease in the current (this happens on drop-off as the amount

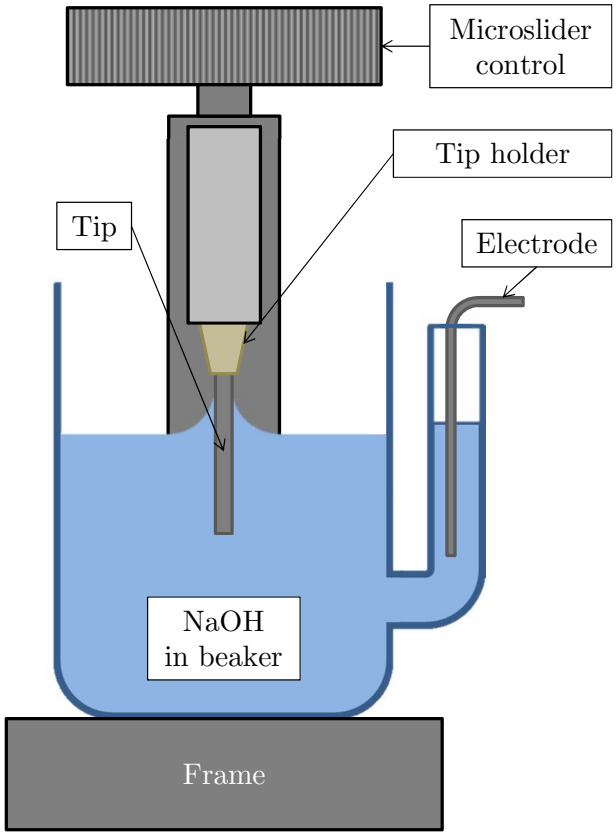

Figure 2.4: The tip etching station used to prepare tips in this thesis. The blue feature is a special glass beaker with a spout on the side, filled with NaOH. The design minimises issues as a result of bubble formation at the electrodes. The grey structure is a frame which support the tip holder via a microslider, allowing for precise control of immersion depth via the top dial. The meniscus is important in tip formation, and is shown where the tip meets the etchant. The tip acts as one electrode in the electrochemical process, the other electrode is inserted into the etchant via the spout.

of tungsten wire in the solution rapidly decreases). The amount of tip material initially inserted into the sodium hydroxide determines the geometry of the tip by altering the force on the neck during etching. A microslider is used to finely control the length of tip initially inserted ($\pm 0.05\,\mathrm{mm}$). Finally, the applied voltage affects the etch rate and tip shape formed. A high voltage etches faster and gives a tip with a smaller aspect ratio, a low voltage etches slower and gives a larger aspect ratio [153]. Moreover, higher voltages produce more oxidised material [154], and cause greater etching during the short time a voltage is still applied after the drop-off before the power supply cuts out. A high voltage

was used for the majority of the etch, reducing the applied voltage just before the drop-off. This process aims to create a low aspect ratio tip with minimal post-etch blunting and oxide growth.

After etching and rinsing, the tip is examined in an optical microscope at two hundred times magnification to check its macroscopic structure. If the tip looks reasonable, with no obvious deformities, it is then annealed before placing it into the vacuum chamber. After etching a large quantity of tungsten oxide coats the tip, and further oxide growth can occur in atmosphere; the purpose of annealing is to remove as much of this tungsten oxide as possible before the tip is used, without blunting the tip [155]. Ideally this would be performed in the vacuum chamber in which the tip is to be used, the LT-STM has no facility for this at present, however, so the anneal is performed in the loadlock of another vacuum system. After the anneal the tip is transferred to a tip holder and inserted into the LT-STM loadlock within 20 minutes, preventing substantial oxide regrowth. This process has been found to give tips of acceptable quality, with good imaging capabilities after a small amount of in-situ tip treatment. The applied currents for the tip anneal are judged based on the colour of the hot tungsten tip (bright orange $\sim$1300 K [156]), as the exact value of the required current can vary depending on the length of the tip and how it is attached to the annealing station.

The full tip-etch procedure is as follows:

1. *Electropolish* - immerse full length into 2 mol/dm^3 NaOH and apply 10 V for 10 s.
2. *Etch 1* - immerse 4 mm of W wire and etch at 9 V until drop-off.
3. *Etch 2* - immerse 1.5 mm of W wire and etch at 9 V until the current drops to 5 mA, then reduce voltage to 3 V and leave until drop-off.
4. *Rinse* - rinse the tip by immersing 10 times in each of three separate beakers of deionised water, store in isopropanol until the next steps.
5. *Check* - check for defects in microscope at 200$\times$ magnification.

6. *Anneal* - anneal in vacuum by applying direct current to heat the tip apex to a bright white (about 5 A) for 5 s. Then degas for 5 minutes at a dim-orange (about 3 A), allow to cool for 10 minutes then vent and transfer as quickly as possible to LT-STM.

7. *Degas* - heat to 140 °C for an hour in the LT-STM prep chamber[1].

Once in the LT-STM system the tip is transferred to the STM head where it can be used in experiments. A tip is rarely suitable for experiments just after etching, in-situ tip preparation procedures are required. A number of techniques can be applied, bias pulses and controlled crashing are amongst the most commonly used, but the results can vary depending on the parameters used, the surface being studied and the tip condition itself. Usually I applied a moderately high bias of 3 V to 4 V and left the STM scanning for at least a day to remove residual oxide contamination from the tip apex, this could be seen as deposits in the STM. Bias pulses, $|V| \gtrsim 4\,\mathrm{V}$, were then applied to try and generate atomic resolution images (if they were not already obtained). This step has to be performed on a surface known to the experimenter.

Once atomic resolution has been obtained, spontaneous tip changes can still alter the images. Bias pulsing was typically used to change the tip state until desirable image qualities were attained. Large bias pulses will result in large changes to the tip apex structure, depositing material to the surface in large amounts, sometimes spanning 10 nm to 100 nm. Smaller pulses yield more subtle changes to the imaging characteristics. Controlled crashing was usually used on soft metal surfaces, where the tip is harder than the material being indented into. The tip was brought toward the surface until contact was achieved then pushed further in, before being withdrawn slowly at a high bias, this was found to sometimes yield a good tip state. On silicon, controlled crashing was found to be more unpredictable, as at the atomic scale the silicon is harder than the tungsten, crashing frequently distorts the tip; however, sometimes a silicon cluster will be attached

[1]The maximum degas temperature is 140 °C to avoid de-magnetising magnets on the tip transfer plate.

to the apex and provide exceptional images [4].

2.3.5 Temperature control in the LT-STM

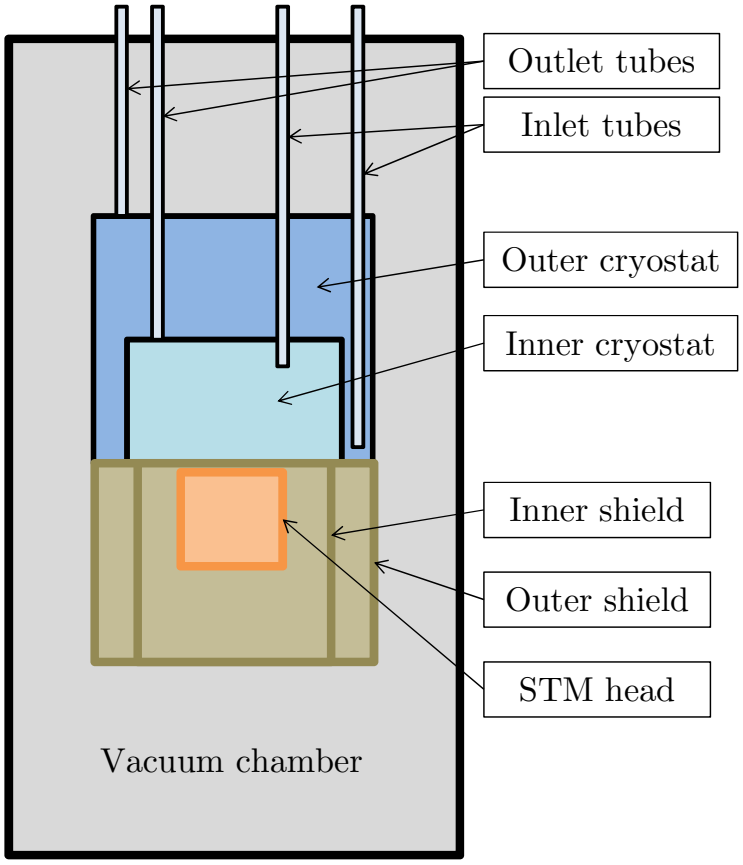

Figure 2.5: The geometry of the cryostat which cools the STM head. The entire cryostat is suspended inside a vacuum chamber shown in grey. The gold squares represent cylindrical shields enclosing the STM head to prevent radiative heating of the sample, these have doors to allow access to the sample stage. Inlets and outlets for the cryogens and their boil-off are indicated. Two additional access points for sensing equipment are not indicated for clarity.

The STM head of the LT-STM is located on the bottom of a cryostat. The cryostat is vacuum insulated and consists of an inner and an outer cryostat. The outer crysotat insulates the inner cryostat to conserve the cryogen inside for a long period. Operating the STM with no cryogen allows imaging at room temperature. Filling both chambers with liquid nitrogen allows imaging at 77 K, this is the temperature used as a base for most

of the work in this thesis. Filling the inner cryostat with liquid helium allows imaging at 4.6 K. Lower temperatures can be achieved by pumping the cryostats, this facility was not used for any of the work in this thesis. Advantages of imaging at lower temperatures are greater tip stability and the reduction of molecular diffusion and other thermal processes that can disturb imaging.

A small heating element on the STM stage allows resistive counter-heating of the sample to any temperature above these base temperatures (and below room temperature, above which the STM is not intended to operate). By using the counter-heating facility it is possible to study a process at a wide variety of temperatures. A silicon diode is used to measure the temperature. The signal from the silicon diode is used as the control signal to a proportional-integral-derivative (PID) controller, which controls the current supplied to the heater. As stated previously, counter-heating allows access to temperatures between the base temperature and room temperature, but in practice temperature near room temperatures can be quite inconvenient due to the time taken for the system to reach the temperature and equilibrate. Temperatures between 4.6 K and 77 K are also inconvenient as the counter heating will accelerate helium boil-off.

2.4 Surface preparation

The work in this thesis was performed on two surfaces, Si(111) $-$ 7$\times$7 and Au(111). The preparation methods for these two surfaces are described in detail in this section.

2.4.1 Silicon

In this thesis boron doped, p-type silicon was used. It was produced using the Czochralski process by Siltronix, and supplied in polished wafers of resistivity 0.01 Ω cm to 0.02 Ω cm. The first step in sample preparation is to cut a section of the wafer to the correct size for the sample plate. This is achieved using a diamond tipped knife to scratch a line into the surface, along which the wafer can then be carefully broken. Care is taken to

not come into contact with the surface to be imaged at any point, apart from with lint-free tissue. The sample is then blown with nitrogen gas to remove any lint that may be on the surface. Standard Omicron direct-current-heating sample plates are used for silicon, these allow for direct-current heating in the preparation chamber: a requirement for silicon sample preparation as some preparation steps require very short heating cycles. These are difficult to achieve when heating the sample via an external resistive heating element, which has a slow response to changes in the heating current applied. It is crucial that the sample does not come into contact with any stainless steel, as nickel will readily contaminate the sample and prevent the observation of any reconstruction. No further ex-situ cleaning is applied.

Once the silicon sample is attached to the sample plate it is transferred to the manipulator arm via the loadlock. The next stage in sample preparation is to degas the sample and sample plate to remove adsorbed material before further preparation steps. In previous experiments on boron doped silicon in our group it was found that dopant segregation to the surface on heating can be a problem, introducing substantial numbers of defects. To avoid this issue any heating processes are kept to a minimum, whilst still achieving the desired surface reconstruction. The first step is to degas the sample and sample plate resistively for 1 hour. Next, the sample is degassed via direct current heating at 500 °C for around 4 hours, just below the temperature at which the native oxide is removed. The sample is brought up to temperature very slowly to maintain a low pressure (below 10^{-8} mbar) in the vacuum chamber. This procedure attempts to remove contaminants whilst still maintaining the protective oxide coating. Once the sample is degassed it can be reconstructed into the Si(111) $-$ 7$\times$7 reconstruction desired for experiments.

The reconstruction process used for the silicon studied in this thesis is described below:

1. *Flash* the sample using direct current heating at 1100 °C for 5 seconds,

2. *Anneal* the sample at 700 °C for 120 seconds by reducing the current,

3. *Cool* the sample slowly to room temperature by reducing the current at a constant

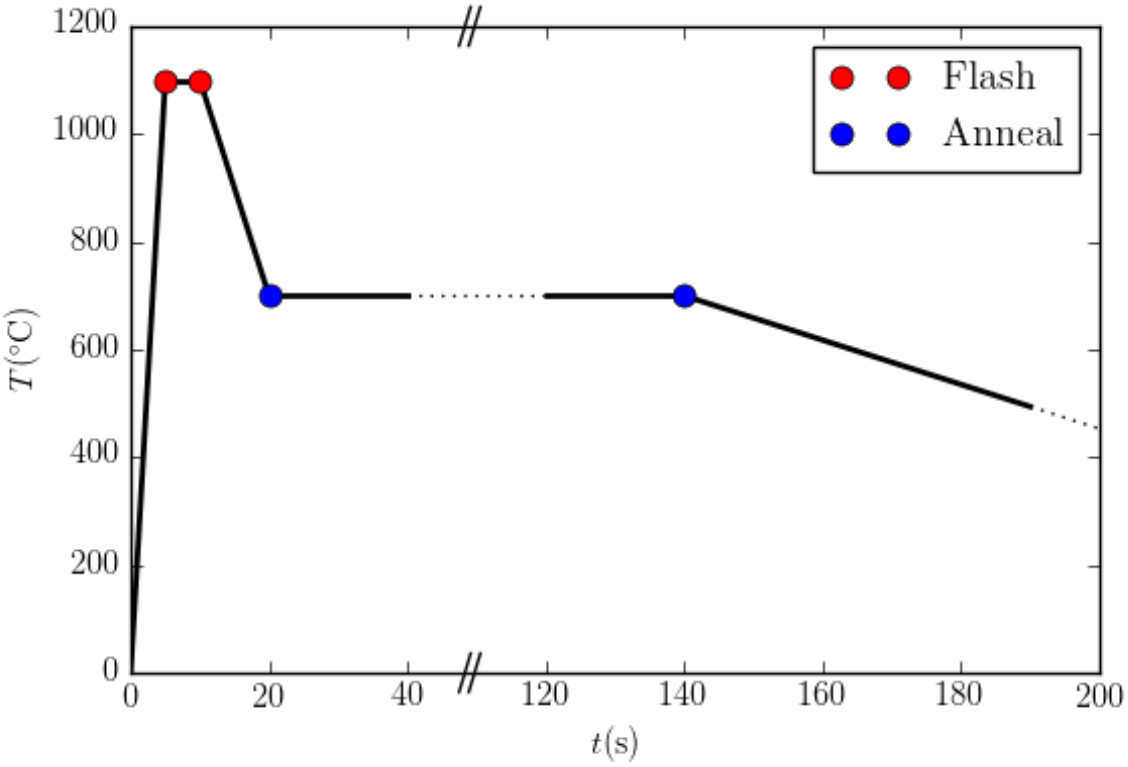

Figure 2.6: Temperature against time in the silicon reconstruction process described in the text. The points shown with red and blue markers indicate the endpoints of the flash and anneal respectively. The dotted line at the right of the graph indicates that the sloped line continues until the applied power is zero, around 3 minutes.

rate.

The reasoning behind each step will be described in more detail in the remainder of this subsection. The exact temperatures and times used were chosen to give domains with desired properties for the experiments performed upon molecule deposition, though it was found that the sample preparation was not overly sensitive to small variations in the preparation parameters. For each new sample, a pyrometer is used to deduce the applied current corresponding to the required temperatures. As the applied current is controlled manually, the final cooling from 700 °C is achieved by reducing the current at a constant rate to 0 A. After reconstruction, when the current is reduced to 0 A, the temperature is typically ∼140 °C as measured at the thermocouple. The anneal current is reduced in 0.1 A increments every 10 s, giving an average cooling rate of 3 °Cs^{-1} for a typical sample.

The flashing stage is particularly important for two reasons. Firstly, it removes contaminants that build up on the surface during imaging; secondly, it raises the sample temperature above the temperature at which the transition to the 7×7 phase occurs. During scanning, various contaminants from the vacuum chamber will build up on the sample surface. Heating the sample to a high temperature causes them to coalesce into islands before desorbing [157]. Empirically, it was found that samples prepared in our chamber remained relatively clean in the analysis chamber for a period of several days at 77 K and 5×10^{-12} mbar. The usual flashing schedule was to flash a sample then image for the remainder of that day and the next, before flashing again. The crucial factor in achieving a 7×7 reconstruction is how the sample is cooled after the high temperature flash. Many methods of doing this are reported in the literature but all essentially follow a high temperature flash with a fairly slow cooling. The high temperature phase of silicon(111) is a 1×1 reconstruction, at 1100 K this undergoes a reversible phase transition to the 7×7 reconstruction that we desire [158]. The aim of the reconstruction process is to cool the sample from the flashing temperature down to room temperature whilst allowing the 7×7 domains to grow.

In the process described above, step two provides a long period for the 7×7 domains to grow. This was particularly important due to the presence of the boron dopants, which tend to form their own domains. Boron has a long diffusion length at high temperature, and also a lower rate of evaporation from the surface than silicon (about 1% of the silicon rate), so heating the sample tends to cause segregation of the boron to the surface [159]. In [159] they study the effects of various anneals on the amount of boron segregated into separate surface domains. They find that above $\sim$800 °C the segregation of boron is significant, but below this temperature annealing tends to grow 7×7 domains at the expense of boron domains. This step was added to my procedure to encourage larger 7×7 domains.

In practice, it was found that removing step two of the preparation process, and cooling slowly from the transition temperature, led to smaller 7×7 domains with apparently fewer

dopants within them. The large number of domain walls made subsequent non-local experiments difficult as an area of Si(111) $-$ 7$\times$7 of at least (50 nm $\times$ 50 nm) is required for an experiment. On the molecule covered surface distinguishing a domain wall can be a difficult task, so minimizing their presence is an important part of the reconstruction process. Adding the additional two minute anneal provided generally larger domains of 7×7, with more widely spaced domain walls, facilitating non-local experiments on the molecule covered surface.

2.4.2 Gold

All experiments on the gold surface in this thesis were performed on a gold single crystal. The gold single crystal has been in use for a number of years and is attached to a standard omicron sample plate, via tantalum strips spot welded to the sample plate. Cleaning the sample requires two steps:

1. *Sputter* the sample with argon ions for a period of at least 5 minutes, 1 kV and 14 µA.

2. *Anneal* the sample at ∼750 °C for at least 15 minutes.

The times here are very flexible, the main rule being that the anneal time should be longer than the sputtering time.

The first step of the preparation procedure, argon-ion sputtering, fulfils a similar role to the flashing stage in the silicon preparation procedure described in Section 2.4.1. Instead of evaporating material from the hot sample surface, the impact of the argon ions removes material via high-energy collisions, stripping away layers of material from the surface of the sample. This sputtering process results in a heavily pitted surface, with significant impact damage. The aim of the second step is to raise the surface temperature and allow the diffusion of the gold atoms to 'heal' the surface, providing a flat surface on which to do experiments. Similarly to silicon, the longer the anneal the larger the terraces

produced. Initially the gold sample contains impurities which will be visible in STM. In addition to smoothing out the surface, each anneal cycle causes impurities to segregate to the surface, these are then stripped away by the subsequent sputter cycle, purifying the sample further. Many sputter-anneal cycles are necessary to clean the sample when it is first inserted into the vacuum, but once purified the sample remains pure and only requires sputter-cycles to remove material deposited in experiments, for example to remove the SAMs described in Section 2.5.3. Due to it's unreactive nature the gold surface remains clean for a very long time in the analysis chamber, the main contaminants being highly mobile physisorbed species which stick on the cold surface. When covered completely with a SAM the surface is even more unreactive. During my experiments I found it was only necessary to remove the sample from the cryostat periodically to desorb physisorbed species; otherwise, the low coverage SAMs I was primarily focussed upon were stable for long periods of time, with little need for frequent sample cleaning.

2.5 Molecular deposition

All of the studies in this thesis rely upon the deposition of molecules onto a clean reconstructed surface, for the study of physisorbed chlorobenzene on silicon it was necessary to deposit molcules in-situ directly onto the STM stage. This section describes the methods by which molecules were deposited, both at room temperature in the prep chamber, and at low temperature onto the STM stage. In addition, the methods by which the deposited substances are prepared prior to deposition are also described.

2.5.1 Room temperature deposition

Room temperature deposition is achieved through use of a fine leak valve pointed at the manipulator arm in the preparation chamber. This valve is connected to a gas-line leading to a manifold, upon which two chemicals can be attached. The gas-line also provides the supply of argon gas to the ion-gun for sputtering. Both chemicals used in

the experiments in this thesis are liquid at room temperature, meaning they can be stored in glass vials connected to the manifold via a CF to Swagelok adaptor. Each chemical is individually isolated from the manifold via Swagelok bellow-valves. Both chemicals used in my experiments are liquids with fairly high vapour pressures (in both cases over 10 mbar at room temperature [160, 161]) making them very easy to deposit via the mechanism described above: all that is required is to allow the vapour formed above the liquid phase material to enter the evacuated gas-line up to the leak valve, providing a store of gas that will allow depositions for several months.

Prior to storing the gas in the gas-line it is first necessary to purify both the chemical and the gas-line as much as possible. Argon gas is used to flush the gas-line and help remove impurities. The chemical to be deposited is then purified through vacuum-distillation, otherwise known as freeze-pump-thaw, which describes the method concisely [162]. First, the sample is cooled using liquid nitrogen until it is completely solid. Then the vial is evacuated using the turbo pump, which is connected to the gas manifold, this pumps away any gas not dissolved in the chemical of interest. When the chemical is thawed, impurities (and some of the solvent) will leave the solution into the space above the liquid until the pressure reaches the vapour pressure of the chemical, this can be seen as an evolution of bubbles in the liquid chemical. The solubility of gases in organic solvents is lower at lower temperature, which tends to force impurity gases out of the chlorobenzene. On the second freezing cycle the number of impurities trapped in the frozen liquid is much lower as they have moved into the gas phase above the chemical, far fewer impurities will dissolve before the chemical freezes, so this gas remains to be pumped away in the next pumping cycle. This process is repeated until no bubbles are seen during the thaw stage, typically this is after one or two cycles, though for the experiments of this thesis the process was repeated three times to be consistent.

Once purified and allowed to fill the gas-line the gas is admitted to the prep chamber and allowed to raise the chamber pressure to that usually used for deposition ($\sim 10^{-8}$ mbar), a residual gas analyser (RGA) is then used to check the composition of the gas. An ex-

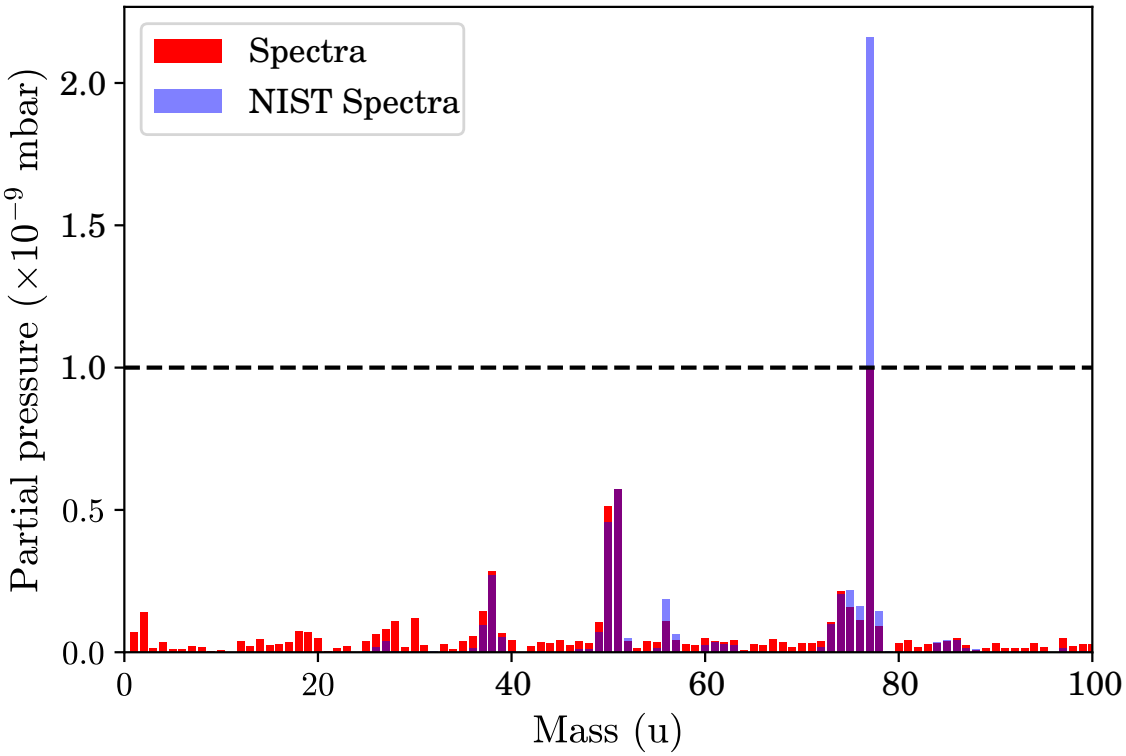

Figure 2.7: Comparison of a recorded mass spectra (red) and one taken from the NIST database [163] (transparent blue). The overlap between the two appears purple. The dashed line indicates where the recorded spectrum is artificially truncated due to the RGA settings. The NIST spectrum is rescaled such that the peak at 51 u matches the same peak in the recorded spectra (the original NIST spectra is given with relative intensities).

ample for chlorobenzene is shown in Figure 2.7. Note the presence of certain signature peaks: these are characteristic patterns in the mass spectrum due to fragments formed in the spectrometer. These peaks can be compared to a reference spectra to determine the gas present. The recorded spectrum is shown in red with a transparent blue overlay of a spectra taken from NIST, as a result the signature peaks are shown in purple. The RGA used here was not capable to recording the full chlorobenzene mass peak as the maximum recordable mass was 100 u (compared to the total chlorobenzene mass of 112 u/114 u). In addition, the peak at 77 u was artificially truncated by the RGA software in order to display sufficient detail on the smaller peaks whilst using a linear scale. If a setting was used which allowed the full 77 u peak intensity to be measured it was typically difficult to examine the smaller peaks when recording the spectra. In reality this peak should cor-

respond to a larger partial pressure. A background spectrum is recorded before allowing the chemical of interest into the chamber. This is subtracted from the spectra taken after allowing the chemical into the chamber, leaving primarily peaks that occur as a result of the gas from the gas-line. To better examine the full spectra a higher sensitivity recording could be made, this was not performed in these experiments as quicker scans were found to be sufficient to check that the gas was mainly chlorobenzene.

In the spectrum shown the sum of partial pressures not accounted for by the chlorobenzene peaks in the mass range shown is $\sim 2 \times 10^{-9}$ mbar, compared to the total chamber pressure of $\sim 2 \times 10^{-8}$ mbar, indicating that $\sim 90\%$ of the chamber pressure is contributed by the chlorobenzene. For the purposes of the experiments in Chapter 4 this is not an issue as deposition is performed at room temperature, where only molecules that chemisorb to the surface will remain throughout the experiments and the large quantities of molecules investigated in the non-local experiments help to average away the results of any contaminants. For the experiments of Chapter 5 a better investigation of these background gases may be necessary, given the ease with which molecules will physisorb at 4 K. This will be discussed further in Chapter 5.

Taking the background spectra also presents an opportunity to check that the vacuum conditions in the chamber are normal and that no unexpected peaks appear. At low pressures, expected peaks are at 2 u for H_2 and 28 u for CO. Just after venting (or in the presence of a leak) water and air may be present, giving peaks at the atomic masses of water, nitrogen and oxygen (nitrogen and oxygen appear in the ratio appropriate for air). In the spectra shown in Figure 2.7 some water peaks appear, possibly suggesting small amounts of water in the gas-line.

2.5.2 Low temperature deposition

To deposit molecules at low temperature requires them to be deposited directly on to the cooled sample on the STM sample stage. Depositing on a sample cooled on the

manipulator is not viable as the sample would still need to be moved to the STM head: at this point the temperature rises, desorbing any molecules successfully deposited. To allow for deposition in the analysis chamber three main modifications were required: Firstly, a leak valve was added to the chamber; secondly, this valve was connected to the existing gas-line system; finally, the doors around the cryostat have windows in their default configuration (see Section 2.3 for details), these were removed to allow the material being deposited to reach the sample.

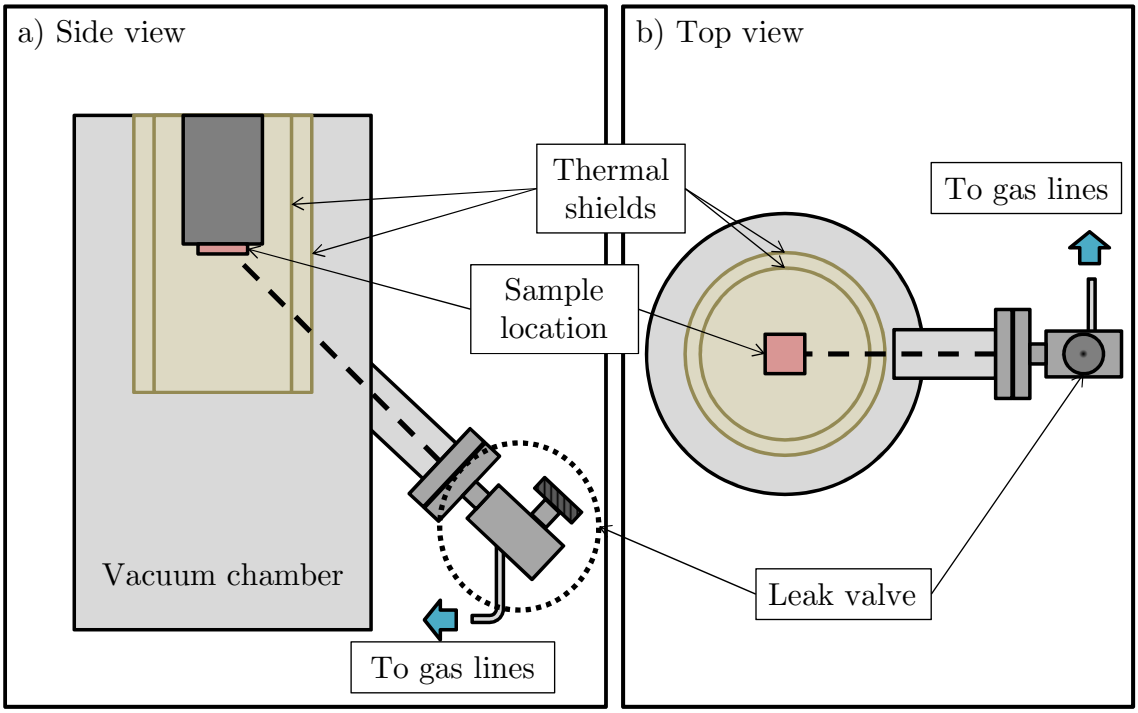

Figure 2.8: The figure shows a schematic of the low temperature deposition facility added to the LT-STM during this PhD. The thermal shields indicated in gold enclose the STM head to prevent radiative heating of the sample. They have small ports in the sides to allow for deposition onto the sample stage along the path shown by the dotted line. A leak valve was added as shown to allow gas to be admitted to the chamber.

A fine leak-valve from the company VG was connected to the analysis chamber via a flange oriented towards the sample stage. The valve was then connected to the existing gasline via a union-T. Both leak valves now share the same supply of gas. One benefit of this is that the same gas can be deposited in both chambers, allowing for mass-spectrometry on the gas using the mass-spectrometer in the prep chamber. Once

the gas-line modification was complete the entire gas-line was baked for several days at >100 °C. The gas deposition was then calibrated by first allowing argon gas into the chamber to deduce how the valves dial corresponds to pressure rises in the chamber. This was performed at room temperature, then with the crysostats at 77 K to see whether the additional cryopumping affected the deposition rate. Finally, chlorobenzene was deposited using the valve, and the results compared with that using the prep chamber valve.

Caution is required when using the deposition valve in the analysis chamber, as the large amounts of chlorobenzene physisorbed to the cold cryostat will be released when the cryostat warms up, this occurs as a pressure burst whenever the liquid nitrogen in the outer cryostat runs out. More care must be taken to ensure that this material doesn't contaminate samples, or reach unacceptable levels, necessitating more attention be paid to the fill level of the outer cryostat, which normally has little effect on the sample. Periodic baking is also a necessity to ensure that excessive amounts of material don't build up in the chamber.

2.5.3 Self assembly

The SAMs in this thesis were based on dimethyl-disulfide (DMDS), the details of the SAM and its structure are given in Section 1.6. Here I describe the process used to produce the SAM. The SAM phase to be studied is the low temperature chain phase. An easy way to make this is to first deposit substantial amounts of material to fully cover the surface. The coverage can then be reduced by annealing the sample, which causes some of the molecules to desorb. The chain phase then forms upon cooling to 77 K[2]. The exact parameters are chosen depending on how low a coverage is desired. It is recommended that the sample be checked by STM imaging after the initial deposition to determine the coverage before the anneal. In this thesis the coverage was gradually reduced over a series of anneals, checking the coverage after each one.

[2]At room temperature the low coverage phase essentially forms a liquid on the surface see Chapter 3.

1. *Deposit* the DMDS on clean reconstructed gold by using the leak valve to raise the chamber pressure to 5×10^{-8} mbar for 10 minutes to produce the full coverage layer.

2. *Anneal* the sample at $\sim$100 °C for 15 minutes, check coverage in STM and repeat as required.

CHAPTER 3

Self-assembly of Dimethyl-Disulfide on Au(111): Dynamics of Dimethyl-Disulfide on the Au(111) Surface

3.1 Motivation

On adsorption of dimethyl-disulfide (DMDS) molecules on the Au(111) surface, a gold adatom can be incorporated into the molecule to form an Au-adatom-dithiolate (AAD) moiety, as described in Section 1.6.3. These AAD groups seem to be the building blocks of all of the phases of methanethiolate found on gold [147]. But although the basic structural motif now seems to be determined, there are still some features in the STM images of [147] which have not been fully explained. These have been studied further in the work of this chapter. In the paper by Tang et al. [147] AAD units were found to consist of extra spots when imaged in STM at high current and low bias. It was speculated that these were the result of *cis-trans* switching of the AAD units under the tip. This suggestion was motivated by the position of the spots as seen by the STM, but there were a number of areas that required further investigation. Firstly, it was possible that the observed effect was artefactual, as it was only observed for methanethiolate AAD over a short series of images on a single day with a single tip. Secondly, only the effect of bias was probed systematically, motivating systematic studies of the effect of setpoint current and scan direction relative to the chains. Finally, though a physical mechanism was suspected, it was unknown whether thermal energy played a role in the switching process. The low temperature study presented here consists of systematic studies of the effect of bias, setpoint current and scan-direction on the switching process. It was found that the switching was a common feature, but seemed to depend strongly on the tip condition, making it difficult to observe. However, with a suitable tip the switching appears to occur for both the forwards and backwards fast scan directions, and up and down slow scanning motion. In addition, the switching was transient and it was not generally possible to observe the molecules remain in their switched position, apart from one case where very strong interactions with the tip were present. Finally, the study of conformational change as a function of temperature confirms that the switching could not be thermal in nature,

and thus is most likely induced by a physical interaction with the tip.

All data presented in this chapter was recorded by myself apart from that presented in panels c) and d) of figure 3.3 and the image shown in 3.7 (recorded by Lin Tang). The data presented in figure 3.3 showed clear examples of individual AAD units switching, which can be harder to observe due to the rarity of suitably isolated single AAD. Single AAD are commonly found directly adjacent to AAD chains and switching is sterically hindered. The data presented in figure 3.3 shows a very clear example of several adjacent chains of different chirality, making it a good example of the effect of chirality on the switching process.

Methanethiolate is the simplest example of an alkanethiolate that can be deposited on gold, and its adsorption is primarily dictated by the headgroup, as interactions between the single carbon chains are too weak to dominate over the interactions with the surface. As such it is the simplest model system for studying the sulfur-gold bonding, which plays an important role in all alkanethiolate self-assembled monolayers, but is still poorly understood. A number of studies proposing the gold adatom model also suggest a dynamic nature to the SAM at room temperature. At low temperatures, dynamic processes are frozen out by the lack of thermal energy, and at room temperature most SAMs studied are in the high coverage phase, or the dynamics are too fast to follow (except in some cases of video STM). As a result there are few atomic scale studies of the dynamic processes that occur in these low coverage SAMs, which could provide insight into the types of behaviour that the gold adatoms are involved in beneath the layer of alkane chains. This information could be important in the ongoing debates about the structures of the room temperature phases, which appear to be quite dynamic. The temperature dependence study of this chapter, presented in 3.3, comprises a detailed analysis of STM images over a wide temperature range. A number of thermally activated processes were found including diffusion of AAD units, thermally induced switching of the AAD, and thermal decomposition of AAD chains. In particular, it was found that the barriers to surface diffusion and conformational change are lower than expected from DFT, but that the

energy binding an AAD unit to a chain of other AAD units is higher. These results suggest that at room temperature the thiolate-gold interface could in fact be quite dynamic.

The final studies presented here are of a number of unusual thiolate species, trimers and bridge-bonded step edge structures. As these both seem to involve lower coordinated gold atoms, it suggests they may be important in the field of gold nanoparticles, where lower coordinated atoms are more common than on surfaces. Alkanethiolates are usually assumed to bond to nanoparticle surfaces in similar AAD structures to those found on the Au surface, but if alkanethiolates bond differently to steps, these species could be common features on nanoparticles.

The results of the study of the switching process at 77 K are presented first, as it provides a perfect opportunity to introduce the AAD structure in detail. The temperature dependent dynamics study follows. Finally, step-edge and trimer structures are investigated.

3.2 Switching of Au-adatom-dithiolate on gold

The appearance of the low coverage phase of DMDS on gold has been described in detail in Section 1.6.3. The AAD units usually appear as a series of three dots along an axis perpendicular to the chain direction. However, under imaging conditions where the tip is very close to the sample the imaging properties can change in a subtle manner. When the chain is imaged at very high current and low voltage, the AAD units show extra spots in the STM image. These extra spots also appear in ethyl-thiolate chains under similar conditions.

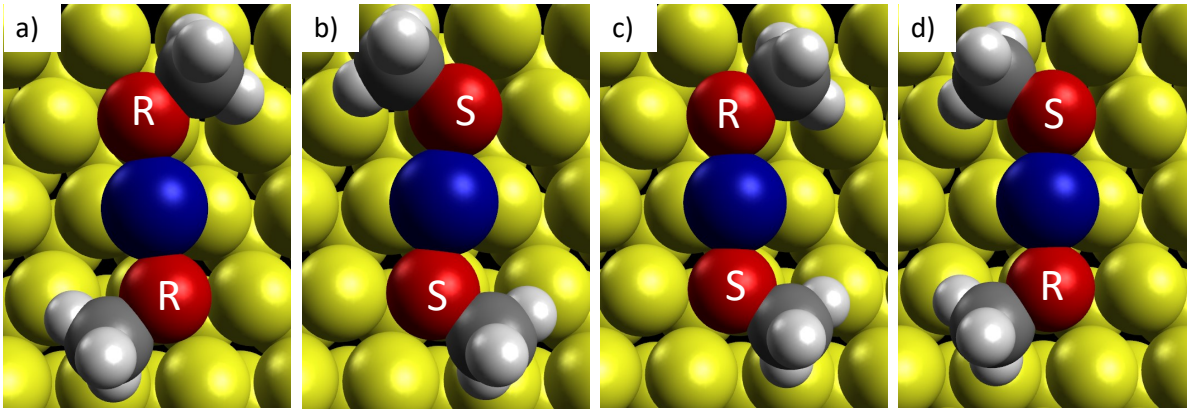

Figure 3.1: Possible chiral enantiomers of the AAD unit. Panels a) and b) show the R-R and S-S *trans* forms, and c) and d) show the R-S and S-R *cis* forms.

3.2.1 Structure of Au-adatom-dithiolate and symmetric switching

Both sulfurs of the AAD unit are chiral centres, and can take left and right handed forms. This allows for four possible chiral enantiomers of the AAD unit, two of which can be called *cis*, two *trans*, which are shown as they appear in STM in Figure 3.1. In the STM both the Au-adatom and the methyl groups appear as bright spots, the sulfur atoms are not visible, so the AAD unit appears as three spots. For the *trans* form, the spots are arranged in a line, for the *cis* form they are arranged in a wide 'v' shape. The dominant form in the low coverage chain phase is the *trans* form, as the chains are made up of *trans* AAD centred on neighbouring Au bridge sites. However, the *cis* form is also sometimes visible on the surface, either on the ends of the chains or as isolated units, and most commonly where crowding forces the AAD unit to take the *cis* form for steric reasons.

Figure 3.2 shows the expected *cis* and *trans* forms as imaged in STM in the absence of switching. In the figure the end of an R-R *trans* chain is shown, where a methyl group of the last AAD unit is flipped outwards so that it takes the S-R *cis* form. An individual R-R *trans* unit sandwiched between a chain and another AAD unit is also highlighted. The image was recorded at -70 mV bias, and 1 nA current but no significant switching behaviour was seen in this case. However, there was some distortion around the edge of

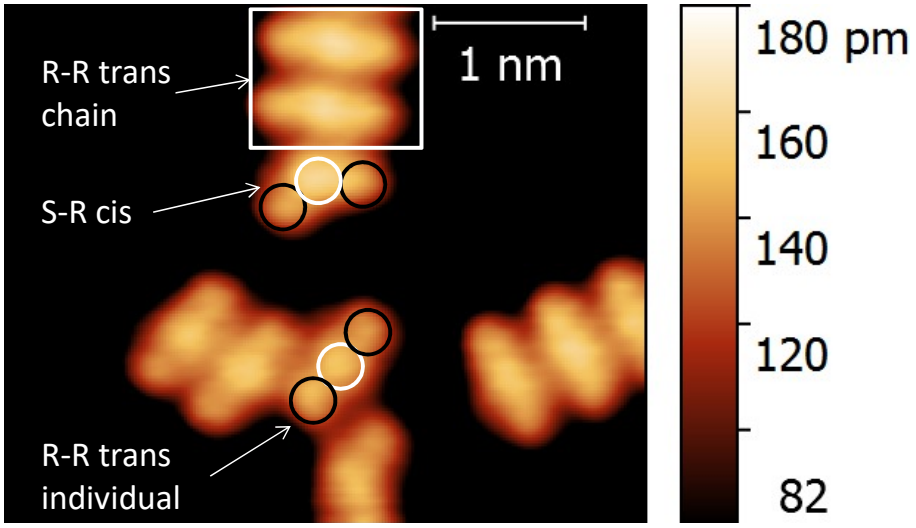

Figure 3.2: An image of several AAD units recorded at −70 mV bias, 1 nA setpoint current. An R-R chain is highlighted, where the unit at the end of the chain is in the stable S-R *cis* form. An R-R *trans* individual is also highlighted.

some molecules which may suggest a somewhat flexible tip apex.

Figure 3.3 shows a *cis* AAD unit imaged at −0.6 V and −0.01 V bias, panels c) and d), respectively. Both images are recorded at 1 nA setpoint current. Notice how the molecule develops extra features in the low bias image, imaging as five spots, rather than three. At −0.6 V the image contains a *cis* form molecule, circled in white, corresponding to the R-S *cis* form in panel a), indicated by the arrow. At −0.01 V the *cis* form AAD shows extra features that lie in the same position as would be expected of the methyl groups of a *trans* molecule in the same location. This leads us to speculate that the new spots are a result of a temporary conformational change induced by the proximity of the tip to the AAD unit. This will be termed *symmetric switching* of the AAD unit, and is shown schematically in Figure 3.3 panel b). This effect can also be seen in chains, where an extra spot appears only on one side of the chains (explored in Section 3.2.2).

This conformational change could be induced through a number of physical mechanisms: an electronic mechanism, the tip electric field or a physical mechanism. An electronic mechanism seems unlikely as the switching dominates at small bias, whereas electronic mechanisms typically require the voltage to be above some threshold. The

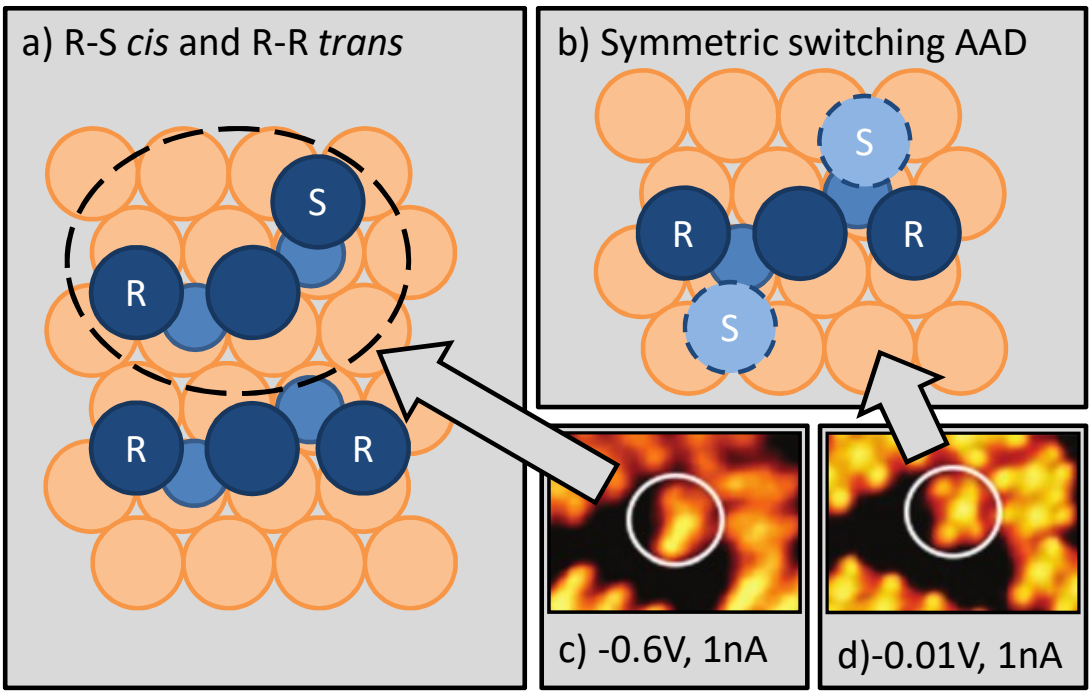

Figure 3.3: A model for switching to explain additional STM spots is presented here. Panel a) shows *cis* and *trans* forms of an AAD unit, panel b) shows how they can be combined to give a five feature unit. Panels c) and d) show the STM realisation of this phenomenon. The STM data used in this figure was recorded by a previous student Lin Tang, and is presented in [164]

.

switching is seen independent of bias polarity and primarily at low bias, which suggests the field of the tip is not the main cause of the switching (though it may contribute, see below). Altering the bias typically alters the tip-sample separation in a sublinear fashion: for example, during injection experiments from Chapter 5 it was found that a fourfold increase in voltage yields only a 3 Å change in the separation, which is an $\sim 30\%$ increase given a typical separation of $\sim$10 Å. If a simple V/d model of the electric field is used, this suggests that increasing the bias increases the field, and so the low bias condition of our experiments should decrease the applied electric field in the junction, though it may be that in the near vicinity of the tip apex the field exhibits a more complex dependence on tip-sample separation. This suggests that a general wide ranging switching induced by the field in the junction is unlikely to result from the low bias conditions, but a localised

interaction with the field of the tip near the apex may occur. In addition, given the dipolar nature of the $S - CH_3$ pair a significant polarity dependence may be expected, which is not seen. The remaining option is a physical mechanism arising from a combination of Van-der-Waals and dipolar interactions with the field of the tip, a hypothesis which is supported by the occurrence of switching mainly at small tip sample separation, as both contributions to the physical interaction will be stronger closer to the tip

The AAD units image the same way when scanned twice under the same conditions. They do not appear as purely *cis* enantiomers on a second scan, suggesting the switch is only a temporary change, and that the AAD units must switch back from the *cis* form to the *trans* form, either between scans or upon the tip passing over them again. The scans in both backward and forward directions along the fast scan axis show the same switching behaviour, and the molecule does not appear streaky, or with a distinct cut as can be the case when imaging thermal motion occuring on timescales faster than time per scanline. The above points all reinforce the idea of an attractive tip-AAD interaction: an attractive interaction would pull the methyl group towards the present tip location at all times so should always image the methyl group when over both possible sites.

Figure 3.4 shows a schematic of how the symmetric switching process might arise. The pictograms show various phases of the tips motion over an AAD unit, scanning upwards. Only the forward scans are shown, but it is assumed that the same occurs on the backward scan (explored in Section 3.2.2). In image 1, the tip approaches scanning from the bottom, as it nears the methyl group an attractive interaction pulls the methyl group towards the tip location. Image 2 shows this attraction holding the methyl group in place whilst the tip passes over it, imaging it in the S conformation. In images 3 and 4 the tip passes over the AAD unit normally imaging both groups in the R conformation. In images 5 and 6 the same process occurs as shown in images 1 and 2, but this time for the opposite methyl group. The result and its experimental realisation are shown in Figure 3.3.

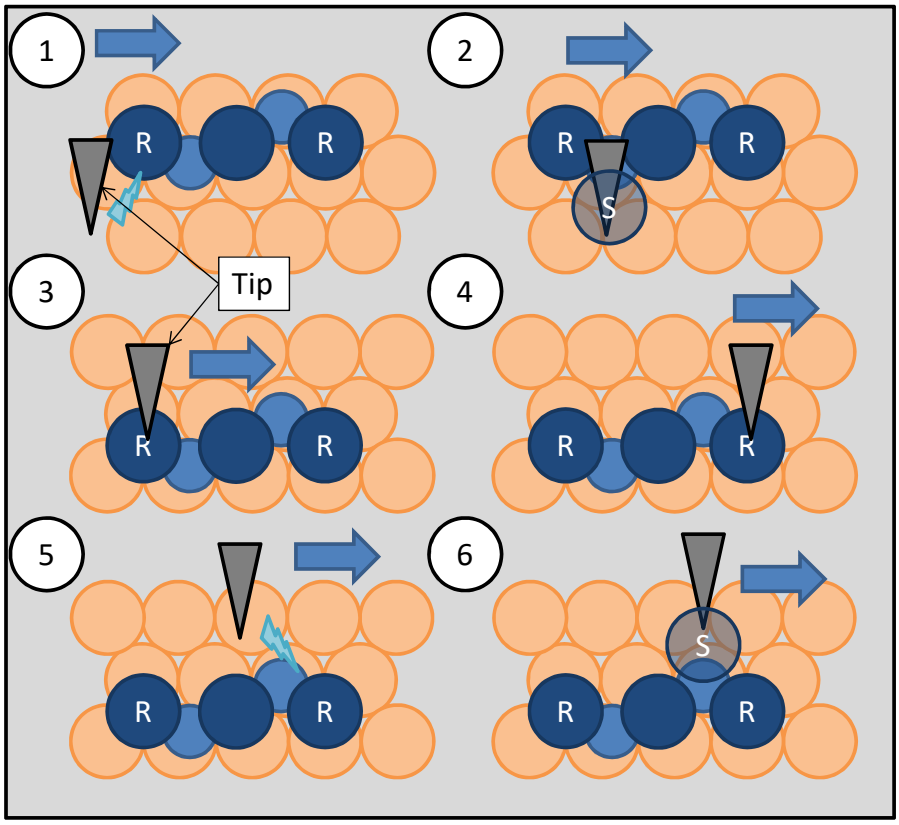

Figure 3.4: Schematic of the proposed mechanism behind the symmetric switching process, a discussion of which is given in the text. The blue arrow represents the fast scan direction along which the tip is moving. The individual diagrams are in chronological order. The slow scan direction is vertically upwards.

3.2.2 Asymmetric switching of Au-adatom-dithiolate chains

In AAD chains the switching behaviour seems to be dominant on one side of the chain, the side depending on which enantiomer is being scanned, and shows variation in the switching depending on the alignment with the slow scan direction. This would be the case if one side of the chain switched as shown in Figure 3.5. This leads to several further questions. Why is only one side involved when the bonding environment of both sides of the chain should be identical? Do the AAD remain switched once scanned in this mode? Is the switching a collective phenomenon, or do individual AAD switch independently?

Determining whether two types of molecule have the same chirality is possible by

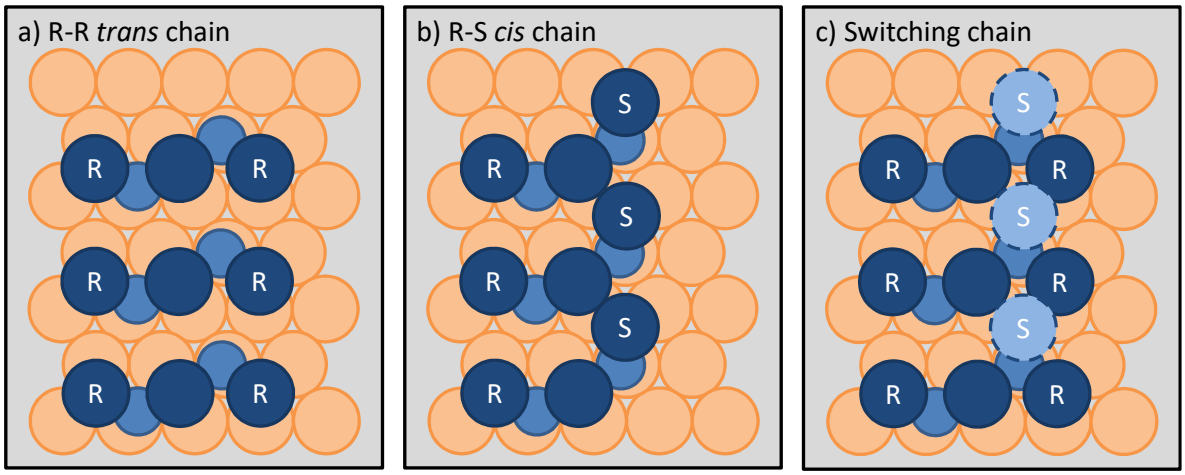

Figure 3.5: Model for switching chains showing the same phenomenon as in Figure 3.3, but now isolated to one side of the chain.

looking at their spacing. This makes it possible to investigate whether the side of a chain which switches is related to the chirality of the chain. The registration of the chains with the underlying lattice implies that a chain translated along the direction perpendicular to the chains by an integer number of the gold lattice spacing, na, will be situated on the same lattice sites. The same is true if the chain is translated by an integer times the spacing between AAD units, $n\sqrt{3}a$, parallel to the chain. If on the other hand the chain is moved in the direction perpendicular to the chains by a distance equal to $(n + 1/2)a$, or parallel to the chains by $(n + 1/2)\sqrt{3}a$ then the chirality of the chain switches. As the spacing between chain elements is $\sqrt{3}a$ it is possible to calculate an a for each image independent of the quality of the calibration. The origin of these rules is shown in Figure 3.6. The figure shows how the four gold atoms beneath the gold adatom and sulfurs can be used as a footprint. The change in chirality after translating an adatom to a new bridge site can be determined by seeing whether the footprint at the new bridge site is the same or different. Note that this model only works for translations of the Au adatoms[1], but the rules derived from it allow the chirality of any parallel chain to be compared quickly.

[1]The footprint does not possess the same chirality as the full AAD, and can be changed into the other footprint by rotation. To make it have the same chirality as the full AAD it is necessary to draw an oriented pattern such as an arrow on one of the atoms of the footprint.

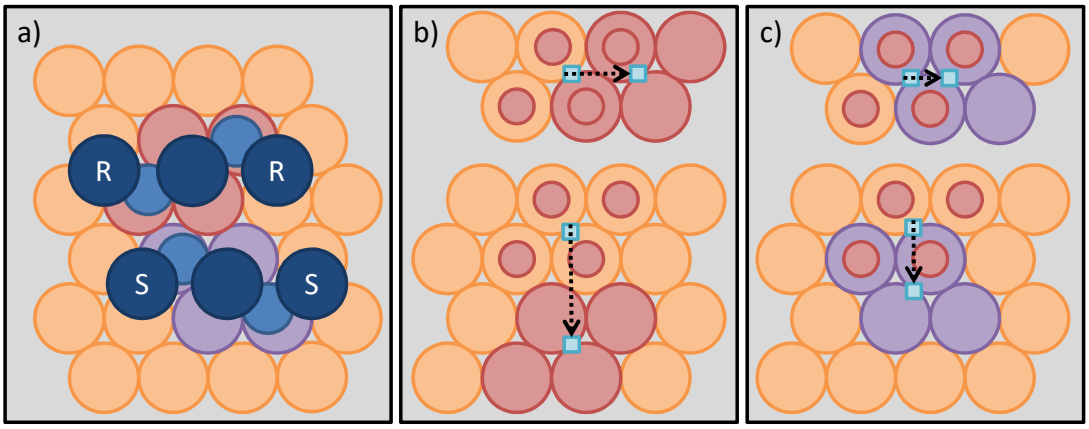

Figure 3.6: Panel a) shows schematics of the two types of *trans* AAD units, and their footprints assigned according to the four gold atoms underneath. Panels b) and c) assess the effect of translating an adatom on the chirality of the AAD based on it. The initial and final locations of the adatom are indicated by small blue squares connected by dotted arrows. Its initial footprint is indicated by the overlay of smaller circles. The final footprint is shown according to its chirality. Panel b) shows translation perpendicular to the chain direction by a and parallel to it by $\sqrt{3}a$ (top and bottom respectively). Panel c) shows the same but this time for $a/2$ and $\sqrt{3}a/2$.

An example of the application of these rules to a set of switching chains is shown in Figure 3.7. The chains under the lines labelled 1,2 and 4 are parallel. The chains under 1 and 4 are separated by $6a$, the chains under 1 and 2 by $4.5a$. However, in both cases the chains are shifted relative to the chain under 1 by $(\sqrt{3}/2)a$. As such the chirality of the chain under 2 is the same as that under 1, whereas the chirality of the chain under 4 is different. It is found that chains of a certain chirality all switch on the same side, but that the side that flips is different for R-R and S-S chains.

It was also found that both upwards and downwards slow scan directions relative to the chains do not alter the side which flips, this rules out the scan direction (an obvious experimental asymmetry) being the cause of the asymmetry in the switching. Figure 3.8 shows a series of four images of the same set of chains taken at 50 mV bias and 1 nA setpoint current. The top two images show an upwards slow scan direction, the bottom two downwards. In each case the right image shows the scan recorded whilst the tip travels right to left (forward), the left image shows left to right (backward). Apart from

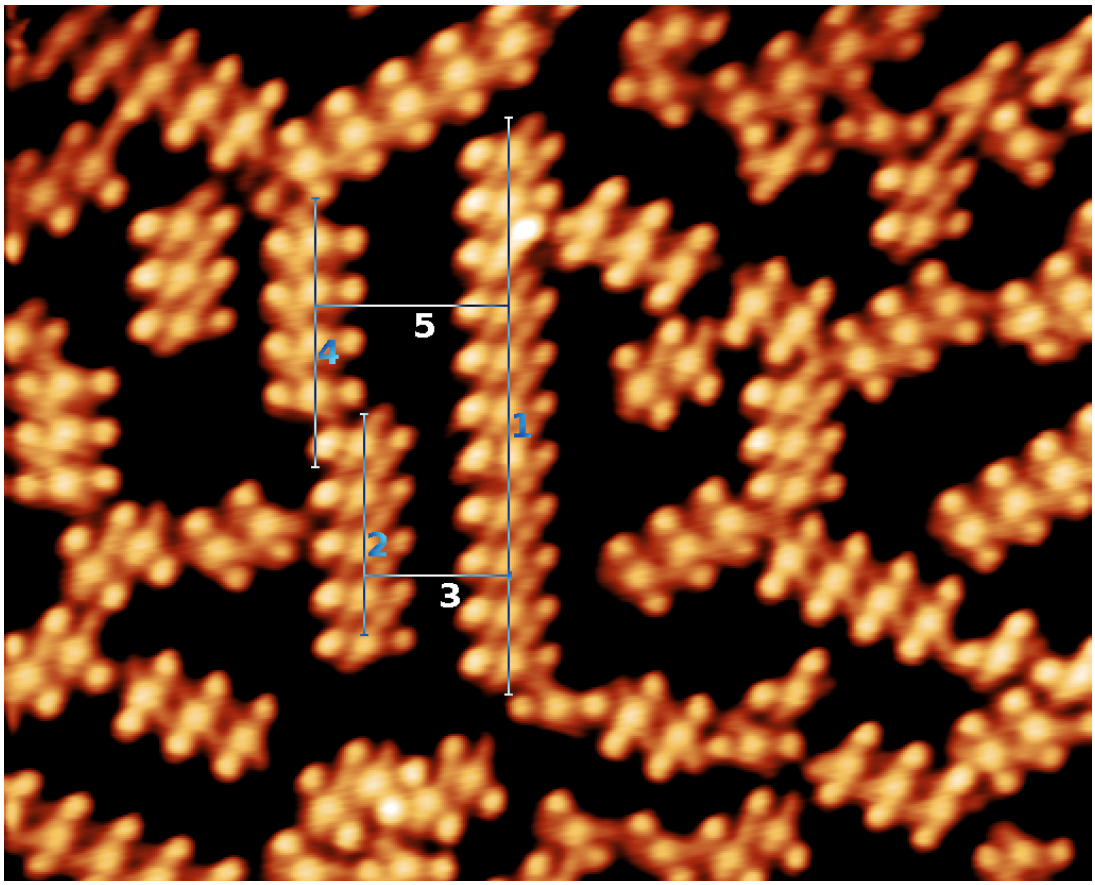

Figure 3.7: Asymmetric switching at 10 mV and 1 nA. The numbered lines can be used as discussed in the text to determine the relative chirality of the chains. The data used in this figure was recorded by a previous student Lin Tang, and is presented in [164]

.

some slight differences in the imaging on each side of the chain the images show identical switching processes. The small differences are probably a result of the imperfect response of the feedback to the sharp vertical gradient at the edge of a chain, which will cause the edge that tip approaches the chain from to image slightly differently to the edge the tip leaves from.

To investigate the switching process further the system was scanned once under parameters that induce the switching, before returning to a passive voltage where the switching is not triggered. The resulting images showed that the AAD units do not remain switched. A series of images were taken in 50 mV steps from 500 mV to 50 mV to determine when

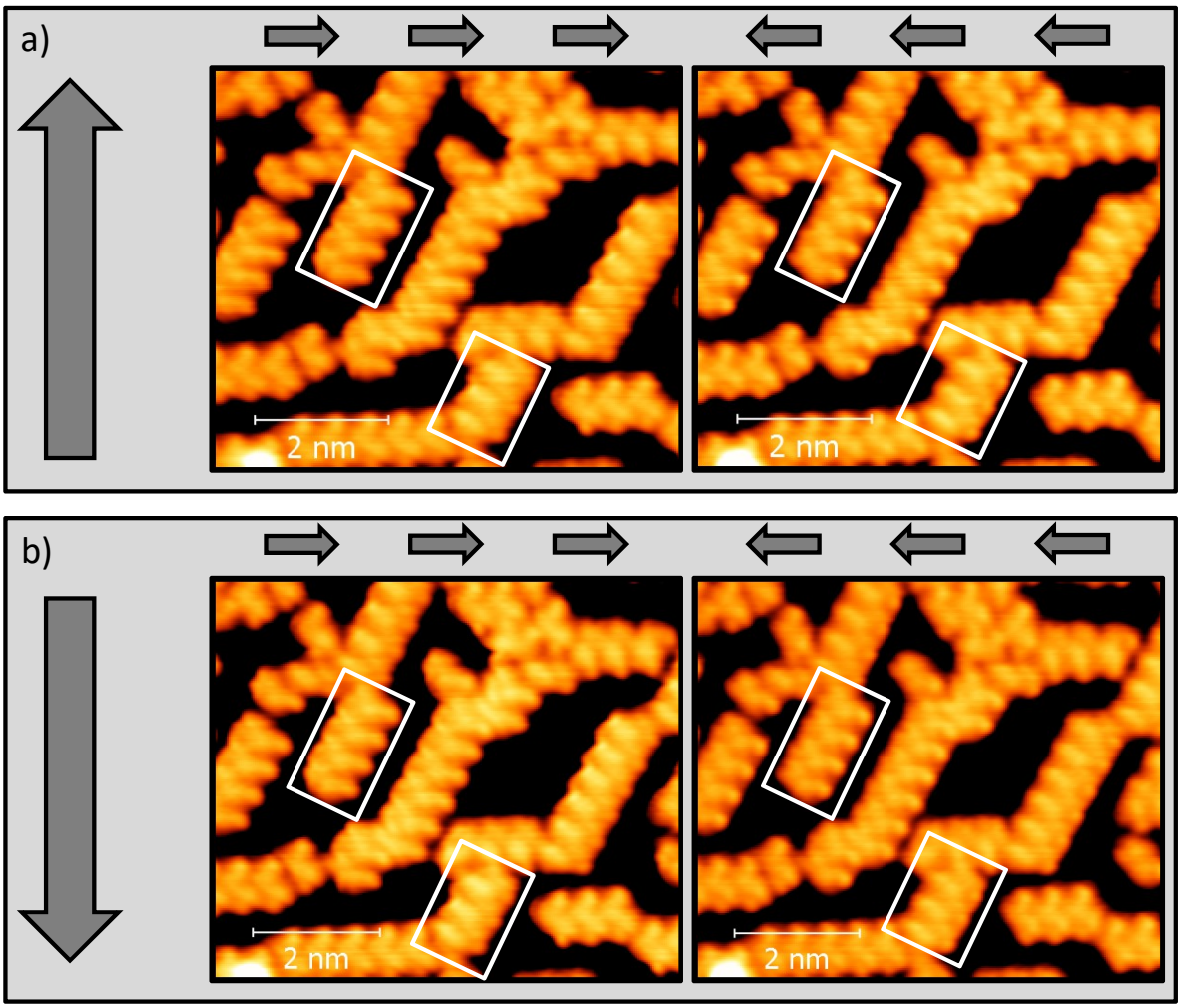

Figure 3.8: Images taken at 50mV bias an 1 nA setpoint current. Panels a) and b) show upward and downward slow scan directions respectively. The triplet of arrows above each image represents the fast scan direction. There appears to be no significant difference between the switching in the images.

switching occurred; For the tip used it was found that biases $V \gtrsim 400\,\mathrm{mV}$ were passive, but that below this the asymmetric switching behaviour gradually increased in intensity. There did not appear to be a distinct threshold voltage, rather switching was initiated in a smooth manner. After a downward 50 mV scan the bias was increased to $\sim$0.6 V and an upward scan commenced. This scan showed no noticeable alterations to the molecules when compared to an initial scan at 0.4 V. This process is shown in Figure 3.9. There are no observable alterations to the forms of the chains between the initial and final image in the chain, suggesting no permanent switching is induced by the low bias scan.

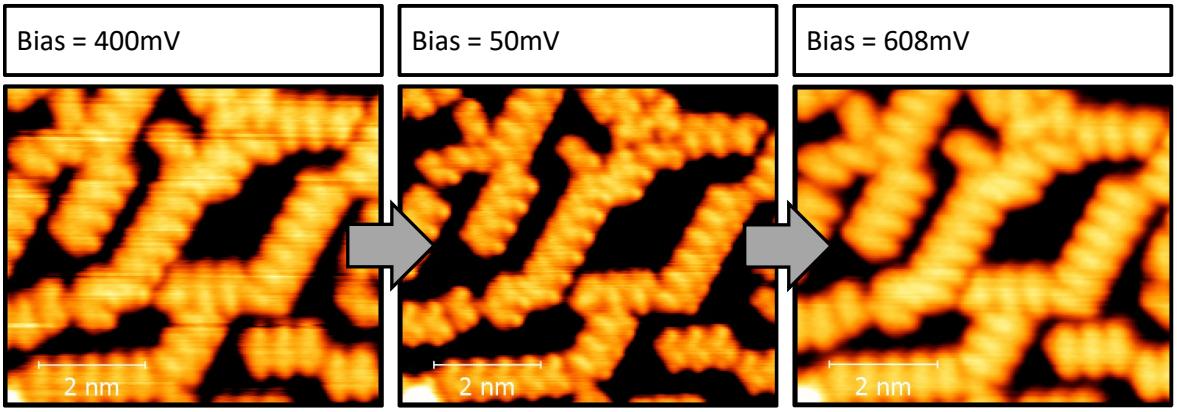

Figure 3.9: Images taken at 1 nA setpoint current. Each image was recorded at the bias given above it. In the 50 mV image there is a clear asymmetric switching behaviour in the chains. In the images taken at high bias there is not. The 608 mV image was recorded directly after the 50 mV image as described in the text.

Stable *cis* and *trans* form molecules exist at 77 K and thermal switching was found to be very rare even at higher temperatures (investigated in more detail in Section 3.3.4) so it can be assumed that the switching is not thermal in either direction. In order for the molecules to not remain permanently switched the *cis* form imaged must either be switched back whenever the tip approaches it again, or not be moved to a stable position. One possibility is that the *cis* form is less stable than the trans, and thus can be switched back even by the passive voltage. Another possibility is that the switched form is only held in place by the presence of the tip, and rapidly relaxes to the *trans* form after the tip moves on. The STM is not capable of imaging the other units in the chain at the same time as the one directly under the tip, so can not determine whether only one methyl group switches, or whether all the methyl groups on each side collectively switch back and forth during a scan. If only one methyl groups switches it may be that tip holds it in the *cis* position against the steric interaction with the next chain element, which remains in the *trans* form, and that when the tip moves further away the methyl group may then switch back. Switching of single methyl-groups seems more likely than concerted switching of the whole chain as the energy cost should be lower, especially for long chains.

A final experiment consisted of a series of images, first at steadily decreasing bias, with

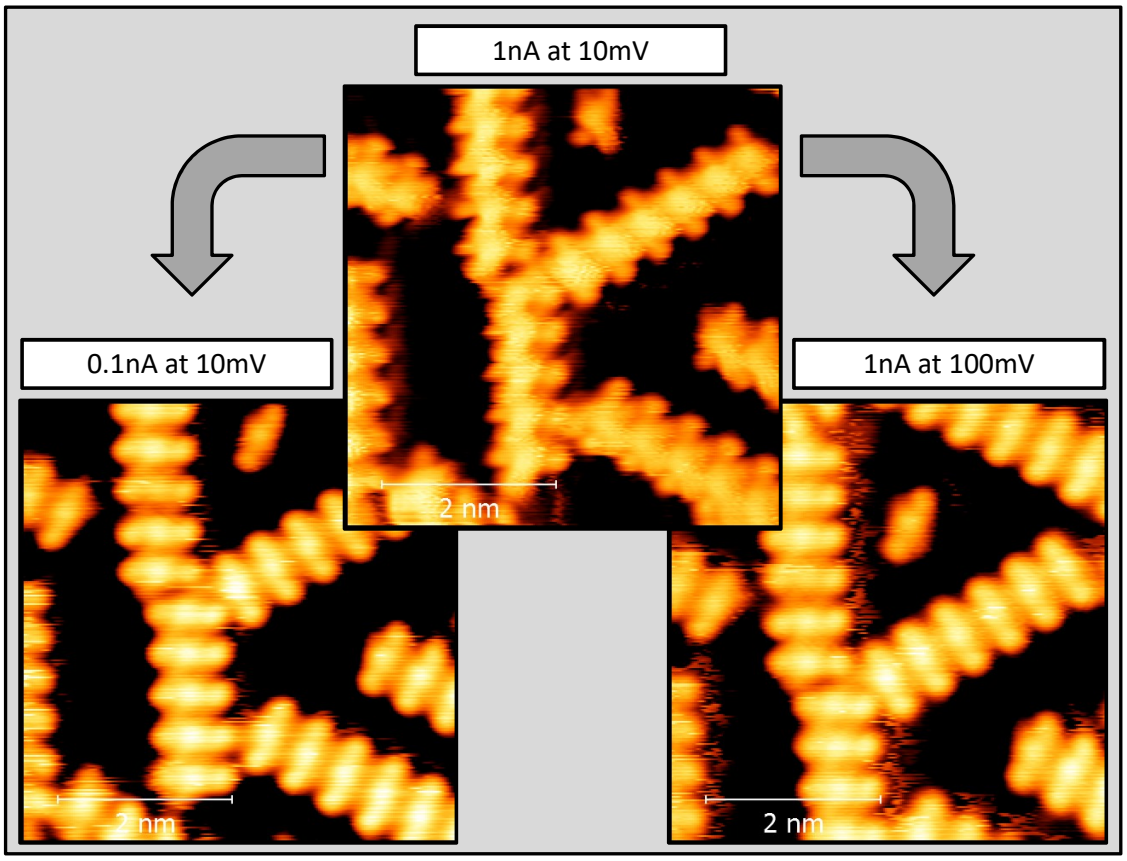

Figure 3.10: The top image is recorded under conditions that induce asymmetric switching in the chain. The bottom images show the results of reducing current and increasing bias, left and right respectively, both of which stop the switching behaviour. The imaging conditions are shown in the boxes above the images.

constant current, then at steadily decreasing current, with constant bias. This compares two methods of altering the tip-sample separation, to see whether both methods have the same effect on the switching process. The sequence of applied biases was 100mV, 50mV, 30mV, then 10mV. The current setpoints used were 1nA, 600pA, 300pA and 100pA. It was found that both means of increasing the tip-sample separation stop the switching behaviour. For the particular tip used it was found that biases below $\sim$ 100mV were required to switch, with the switching intensity increasing strongly for the 30mV and 10mV images. When altering the current, it was found that the switching intensity decreased sharply between 600pA and 300pA. Figure 3.10 shows an image taken at low bias and high current, where switching is obvious, and compares it to two images, one of which is

taken with a reduced current, the other with a raised bias; both parameter changes can be seen to stop the switching process.

The transition from switching in the current sequence seemed sharper, but it is uncertain whether this is a result of the spacing between parameters chosen. Potentially, current variation is better than bias variation to alter the tip-sample separation for these experiments as varying the bias can also alter the states being tunnelled into on the chain/surface, whereas altering the setpoint current only alters the distance. This is apparent when looking at the average tip sample separation over an image for these sequences of images. The bias variation sequence has largely unpredictable variations in tip-sample separation, whereas the current reduction leads to a systematic increase in the tip-sample separation. This may explain the clearer transition to and from switching.

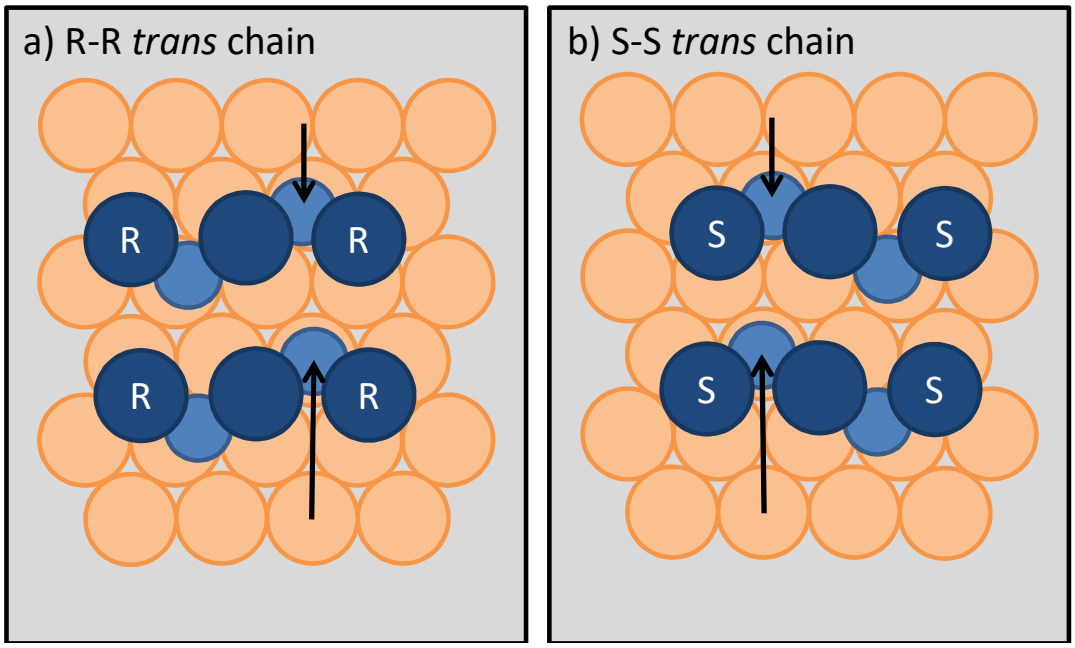

Figure 3.11: Panel a) shows an R-R chain, panel b) an S-S chain. The top AAD unit is the usually assumed bonding in each case, the bottom is with a small shift towards the nearest fcc site. The black arrows indicate how the sulfurs are now in subtly different bonding locations.

The reasons behind the asymmetry of the switching are not entirely clear, as for the normal AAD there is no difference in the bonding environments of the sulfurs on either side of the chain. The only difference lies in the second layer down, where for both types of

chain each side of the chain lies over a different hollow site, the left hand side of S-S chain will be over the same hollow site to the right hand side of the R-R chain. This may be enough to create the asymmetry in the switching, perhaps through some difference in the interaction with the methyl group. This could be supported by DFT of single methane thiolates which finds that the strength of the interaction between a methanethiolate and the two types of hollow site differs. Alternatively it may be that the AAD units that form the chain are offset slightly towards either the fcc or hcp site of the substrate as shown in Figure 3.11, which compares this shift for R-R and S-S chains, and finds it would generate the required broken symmetry. This would then create different bonding environments for the sulfurs as shown in Figure 3.12, which also shows the second layer gold atoms underneath. The driving force for this offset would probably be induced by interactions within the chain. This idea of a shift is supported by absence of asymmetry in the switching of single AAD, which would be expected to also switch in an asymmetric manner were the shift not required.

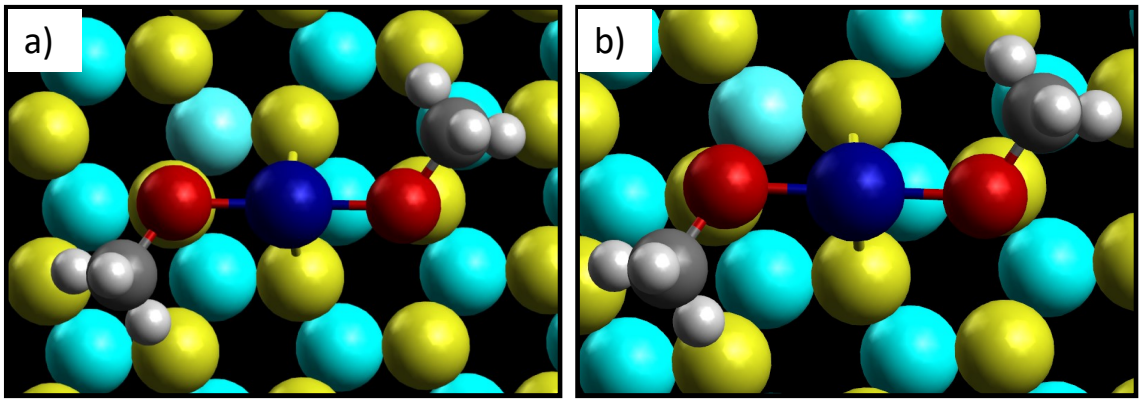

Figure 3.12: Comparison of the shifted AAD, in panel a), to the normal AAD in panel b). Gold atoms in the top layer are coloured gold, those underneath are coloured light blue.

3.3 Dynamics of AAD units as a function of temperature

To look in detail at the dynamic processes possible in the self-assembled layer a thorough study was conducted at a number of temperatures between 77 K and 200 K. The intention of this study was twofold, to experimentally determine whether conformational change was viable at 77 K and to determine the structural stability of the chains, together with the paths by which they break up. By performing these experiments at a range of temperatures it is possible to identify thermally activated processes and then extract activation energies by fitting increases in the number of events to an Arrhenius type expression. This then indicates the relative ease of each process occurring.

Several thermally activated processes are found to occur in the AAD chain phase: At 77 K no processes occur frequently, the system is largely stable with very rare diffusion events. Between 90 K and 130 K single AAD units diffuse over the surface. Next, above 130 K small chains of AAD appear to diffuse over the surface as units and conformational changes of single molecules and chain end units can occur. Finally larger chains can diffuse, and chains can break up into smaller chains, at these temperatures single AAD diffusion is facile, and occurs too quickly to be seen by the STM, only noticing the times when the AAD units remain still long enough to be imaged.

The simple qualitative ordering of events tells us several things about the system. Firstly, the AAD unit appears to prefer to diffuse together as a unit. If this were not the case, then in order to diffuse the AAD unit would have to break up and recombine elsewhere. Single thiolates are not seen breaking off of AAD units, apart from possibly at high temperatures, arguing against a mechanism where the AADs units fragment to diffuse. Secondly, small chains of AAD also appeared to diffuse as units, this tells us that it is easier to move multiple AAD over the surface than to break the chain, which indicates that the intrachain bonds are stronger than the barrier for surface diffusion. By looking

at when the chains began to break up, and comparing this to the length of chains that can diffuse as a unit, it is possible to estimate the strength of the intrachain bonding. Finally, thermally activated conformational change occurred, but not at the lowest temperatures, indicating that the energy required to thermally switch the molecule is higher than that to cause diffusion. This is particularly relevant to the switching behaviour observed due to the tip at low temperatures, as it suggests that it could not be a thermal process.

The DMDS system studied in this chapter is produced by first creating a full coverage layer by depositing molecules from the gas phase over an extended period, before reducing the coverage by heating the gold surface to desorb some of the molecules. At room temperature and reduced coverage the molecules are not stably arranged on the surface, and instead form a kind of 2D gas phase. When cooling to 77 K to perform the experiments of the previous section this gas of molecules on the surface condenses to form the AAD chains. This process is achieved very rapidly on contact with the cryostat, held at 77 K. By studying the system at a variety of temperatures it is possible to determine the processes that can take place during this rapid cool down, and how they could potentially affect the final system arrived at. A rapid cool down essentially freezes the AAD chains after a short formation time, resulting in only the short chains that form before the diffusion rate drops significantly. The formation of long range ordered structures is kinetically hindered. The formation of the chain phase is in some ways analogous to the formation of islands on metal surfaces, where island size is a sensitive function of deposition rate and temperature [165, 166].

In order to study these processes in detail a series of images were taken of several surface areas every in 10 K increments between 90 K and 190 K. The series of images was then aligned to a high precision using an algorithm, allowing for comparisons of sequential pairs of images in the series and highlighting any changes, which were then labelled. An attempt was made to identify the initial and final positions of all AAD units that were involved in a thermally triggered event. To avoid the STM tip having an influence on the thermal processes imaging was conducted at low currents and reasonably high bias.

The parameters used were 500 mV and 50 pA. These parameters do not permit very high resolution images, but the image quality is sufficient to identify motion of the AADs and *cis-trans* switching at chain ends.

If the probability of a process happening is very large, then it will happen many times during a single STM image. This typically appears as streaking or blurring of features in the STM image, as the species being imaged moves under the tip between scanlines, or even within them. On the other hand, if the probability of a process occurring is very small, then the process will only occur very rarely and may not be seen by the experimenter during the timeframe of the experiment. In between these extremes the number of events which happen during an image can be counted. This leads to a histogram of events against time, where the bin size is given by the length of time taken to record the STM image ($\sim$ 5 minutes). In order to normalise the probability it is necessary to have an estimate of the number of AAD units that could undergo each process in an image; for instance single AAD diffusion needs a count of single AAD units which could diffuse in order to determine how probable diffusion is. To determine the AAD chain populations, all of the chains on the initial image of the series were labelled by their endpoints to provide an estimate of the initial population of chains and their length distribution. This population was then adjusted by taking into account the measured alterations in chain lengths over the series to give a population for each image in the series. The time between images is used, together with the initial populations, to generate a probability per unit time of a single AAD unit undergoing some process. The details are given in their relevant sections below.

3.3.1 Single AAD diffusion ($T \lesssim 130$ K)

At temperatures below 130 K the diffusive behaviour is uncomplicated. Most AAD units are stable and do not move. Isolated AAD units are capable of diffusion over the surface, usually to the nearest unoccupied bonding location on the gold lattice. The gold lattice

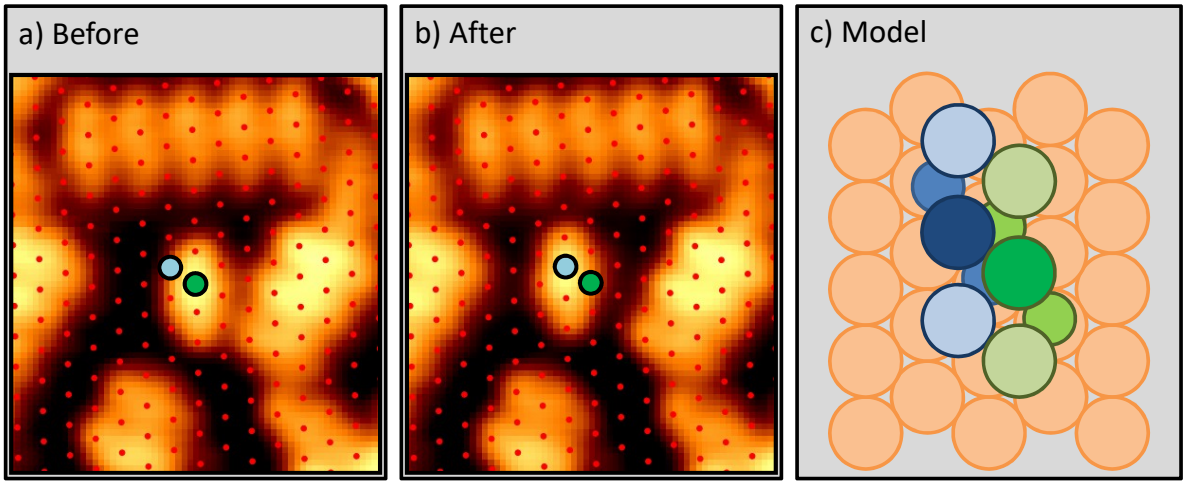

Figure 3.13: Panels a) and b) show a single AAD unit in two consecutive STM images. The initial and final Au-adatom locations are marked in green and blue, respectively. The red dots in both images mark the locations of bridge sites in the underlying Au lattice, deduced from the positions of the AAD units. Panel c) shows a ball model for the process. The chains are shown in the same colours as their markers on the STM image, with the shades being used to distinguish the Au-adatom, sulfurs, and methyl groups (darkest to lightest, respectively).

vectors are deduced by using the lattice vectors of the AAD chains, together with the structural model of the AAD bonding location. Using this derived lattice it is possible to determine where the AAD unit diffuses to relative to its initial position. This also allows the number of diffusive hops to be estimated. If multiple hops occur during the time taken to record an image, only the final location will be seen. It is assumed that the AAD unit travelled in a straight line between initial and final location, so the length of the vector between these two points is used to calculate whether the complex moved to its nearest neighbour site or next nearest, and so on. This is only an estimate as it is possible that the AAD unit took a more complicated path between the two locations. However, it is likely that the shortest distance is a good estimate of the path taken as the diffusion rate is not very high (lots of AAD units do not diffuse) and the number of hops made is usually only one or two, suggesting that a more complicated path is unlikely. At very high temperatures, single unit diffusion occurs at such a high rate that the diffusion can not be quantified accurately, this is discussed below.

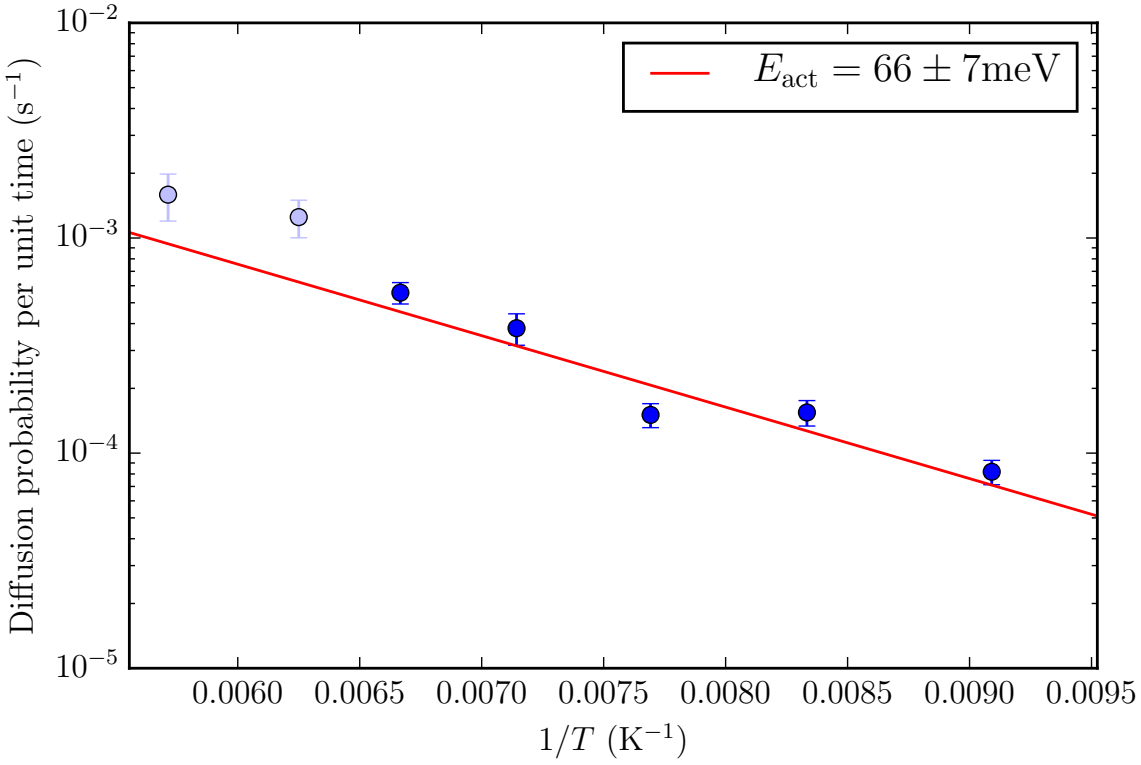

Figure 3.14: Graph showing the diffusion probability for single AAD units per unit time plotted for a range of temperatures. Each point is the average of the measured values over ~ 10 images, errors are the standard error on that mean. The points in lighter blue on the left are excluded from the fit, as rapid diffusion of single AAD makes the diffusion difficult to quantify accurately (see text). The red line is an exponential fit, giving the activation energy shown.

To normalise the diffusion probability the number of single molecules available to diffuse has been counted. This can be used, together with the time taken between images, to provide a diffusion probability per unit time. Several series of images were taken, and for each image the total number of diffusive hops (calculated as described in the previous paragraph) was normalised against the population of single AAD over the image, before dividing by the total imaged time to give a probability per unit time. This is shown plotted on a semi-log plot against $1/T$ over the full range of temperatures in Figure 3.14. The value plotted for a temperature is the mean of all of the values measured from the images at that temperature, the errors are the standard error on that mean. The two points in a lighter blue colour on the upper left were not taken into account for the exponential fit

as diffusion rates are difficult to quantify at high temperature. One reason for this is that at high temperature diffusion is facile, this is evident from the appearance of the AAD units in STM, where they often move multiple times within the same scan. The initial population of AAD measured is therefore a significant underestimate of the number of AAD units available to diffuse, as single AAD can not always be unambiguously identified. This leads to the apparent increase in the diffusion probability at these temperatures (in excess of what would be expected from the trend). In addition, the sample of single AAD is reduced as the rapid diffusion allows them to travel until they reach the end of an AAD chain, which they subsequently join to. Finally, because of their highly mobile nature, the assumption of short diffusive paths begins to break down and a more complicated model involved random walks would need to be developed.

The activation barrier for the diffusive process was found to be $(66 \pm 7)\,\mathrm{meV}$. This barrier is much lower than those calculated by DFT of 0.5 eV [167] and 0.37 eV [168]. There are two possible sources for this difference: Firstly, DFT is known to give inaccurate binding energies, especially at the level of theory used in the two papers above; secondly, the diffusion barrier measured in STM could be altered by the presence of the tip. A more detailed comparison to theory is left to Section 3.4.

An interesting point to note is that the thermal energy required to break a bond between the methanethiolate groups and the gold of the AAD units is evidently much higher than the diffusion barrier on the surface, as the AAD units appear to diffuse as a whole unit. The AAD unit is usually considered to by bonded to the surface in multiple locations (both sulfur headgroups and the Au-adatom are bonded to the gold surface underneath), but diffuses strictly in the *trans* form between nearest neighbour bonding locations at low temperature (at elevated temperatures more exotic motion is possible). This provides an interesting example of a structure which has incorporated a surface atom, but behaves like a single molecule-like unit. Similar behaviour has also been proposed to explain the motion of thiolate covered steps on gold [169] and oxygen on copper [170]. Both of these systems suggest interesting theoretical treatments. It was also noticed

that quite often once an AAD unit had diffused it would often diffuse again. This could be a result of interactions with nearby chains, which may present a slightly asymmetric potential, leading to an enhanced probability to return to the initial site (rather than continuing in one direction). This mechanism has been proposed in video STM studies of diffusion in electrochemical systems [171, 172].

3.3.2 Small chain diffusion ($130\,\mathrm{K} \lesssim T \lesssim 150\,\mathrm{K}$)

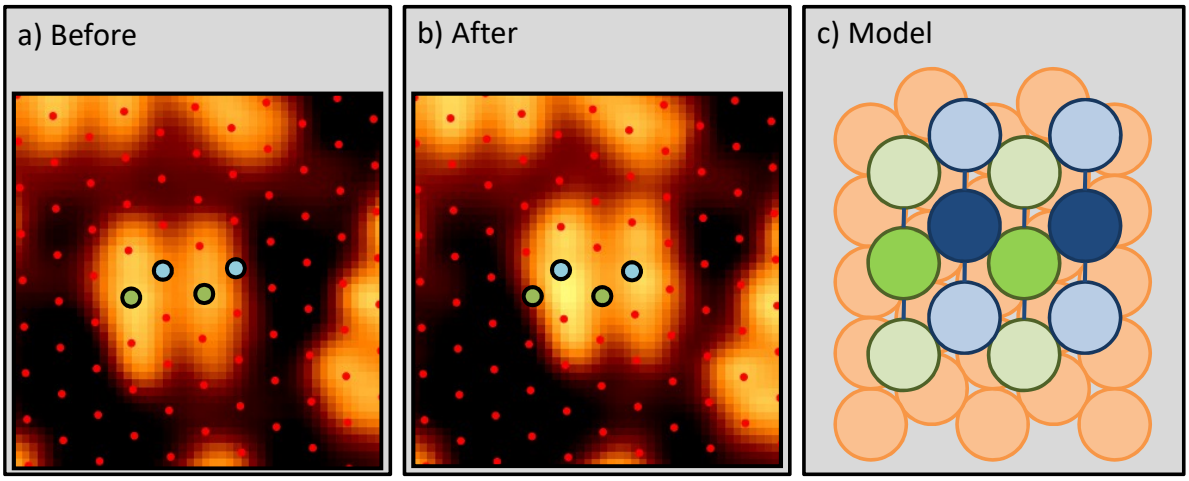

Figure 3.15: Panels a) and b) show a two unit AAD in two consecutive STM images. The initial and final Au-adatom locations are marked in green and blue, respectively. Panel c) shows a ball model for the process, where the sulfurs are not shown for simplicity. The chains are shown in the same colors as their markers on the STM image, with the shades being used to distinguish the AU-adatom and methyl groups (dark and light, respectively).

An extension of the previous section's experiments to slightly higher temperature exhibits further interesting behaviour. Again the AAD units only diffuse as units, however now longer chains can diffuse. In this case small chains of two units can diffuse to their nearest neighbour locations. This suggests a qualitative measure of the intrachain bond strength: if diffusion of chains occurs often, the intrachain bonding is greater than the diffusion barrier. At higher temperatures even longer chains can diffuse, but it becomes more difficult to ascertain whether the chain moved as a unit.

The diffusion probability for a chain of two AAD units is plotted in Figure 3.16,

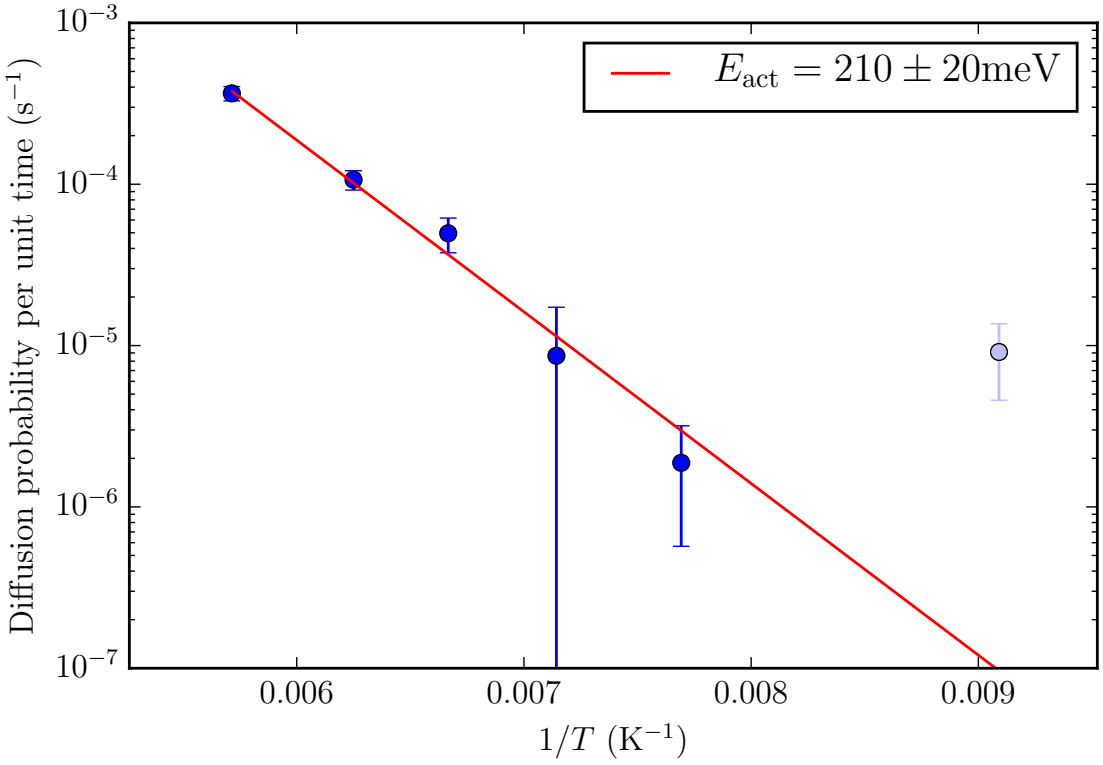

Figure 3.16: Diffusion probability for a chain of two AAD units per unit time, plotted for a range of temperatures. Each point is the average of the measured values over ~ 10 images, errors are the standard error on that mean. Lighter points are excluded from the fit for reasons given in the text, temperatures with no measured events are ignored. The red line is an exponential fit, giving the activation energy shown.

yielding an activation energy of (210 ± 20) meV. The measured activation energy is over twice the energy required for single unit diffusion, suggesting that the process of moving two AAD units coupled together is more difficult than just moving two individual AAD units[2].

The relative strengths of diffusion barriers and the intrachain bonding have interesting implications for chain formation. At room temperature the AAD units form a liquid phase on the surface, as the temperature is reduced this liquid condenses to form the AAD chains. If the intrachain bonding is stronger than the diffusion barrier, then under a given set of formation conditions longer chains will be formed, if the converse is true,

[2]A number of two-unit chains appeared to diffuse at 110 K. On re-examining the images, all of the events were from one series where it appears that a double tip may have given single units the appearance of double ones, so the values were added to the single diffusion counts instead.

then shorter chains, or possibly no chains, will be formed. In this system the intrachain bonding is significantly stronger than the diffusion barrier, so reasonably long chains are formed. Potentially this quality could be tailored to promote longer chains. The non-linear increase of chain stability against diffusion with the number of units in the chain may also impact on the formation of the layer, making chains become stable much more rapidly than would be expected from a linear model.

3.3.3 Chain breakage ($140\,\mathrm{K} \lesssim T \lesssim 160\,\mathrm{K}$)

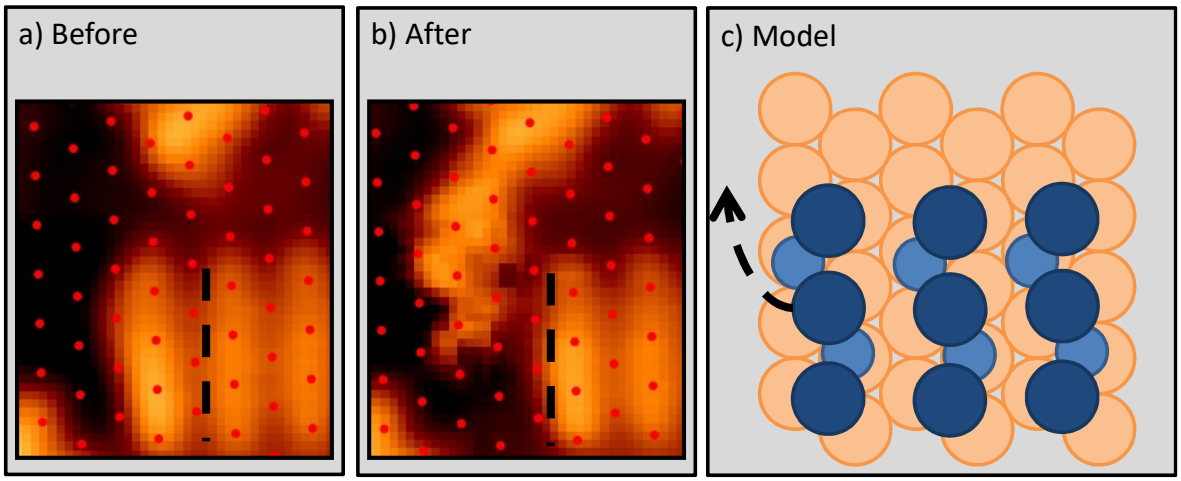

Figure 3.17: Panel a) and b) show the final AAD unit breaking off of a chain between two consecutive STM images. Panel c) shows a ball model of this process.

At the highest temperatures chains can split into smaller chains. In order for a chain to break, at least one of the remnants of the chain must diffuse. The energy requirement for chain breakage is dominated by the energy required to leave the chain, after which diffusion over the surface is facile at the temperatures involved. There are several interesting quantities that can be studied for this process.

Firstly, chain breakage begins to be measurable at around 140 K. At this temperature chains up to two units can diffuse, and single molecules can diffuse over a few nearest neighbour sites. Chain breakage is more complicated to extract an energy for, as at higher temperature chains can break at any point into varied lengths of fragments, with

the viability of the process being a complex interplay of the energy to break the chain and the energy required for the fragments to diffuse. For $140\,\mathrm{K} \leq T \leq 160\,\mathrm{K}$ chain breakage is dominated by events where one AAD unit breaks off of a chain (making up all of the measured events). At 175 K around a third of the chain breaks are more complicated. For complicated breaks it is not possible to tell whether a chain immediately breaks into the fragments seen, or whether a small section breaks off before being joined by further elements. The difficulty of breaking the chains may argue for a single break, but it is also possible that the proximity of a nearby AAD may make it easier for an AAD unit to leave a chain if there are longer range interactions present in the system.

For single unit chain breaks the rate limiting step is the energy required to initially leave the chain. Normalising the number of single unit breaks to the number of chain ends (twice the number of chains), gives the probability of a single AAD unit breaking off the end of a chain. This is a worse normalisation than for single molecule diffusion as quite often chains can end at other chains and the close packing at these junctions may hamper the breaking process, implying that the normalisation overestimates the number of molecules which could diffuse, thus leading to an underestimate of the absolute probability of diffusion. However, this shouldn't affect the variation of the rate with temperature, unless the number of chains ending at other chains changes significantly. Plotting this value against temperature and fitting an exponential allows an energy barrier to be extracted.

Figure 3.18 shows the probability of chain breakage plotted as a function of $1/T$. The leftmost point corresponds to 175 K and is ignored as a substantial number of chain breaks involve many small chains, so it is not possible to unambiguously determine what happened in the break up. At the three temperatures fitted the only breakage process occurring is single unit breaks, thus it is possible to easily distinguish the events and normalise them. The extracted activation energy is $(320 \pm 80)\,\mathrm{meV}$, which makes chain breakage the most costly of the dynamical processes being investigated in this section,with trans-to-*cis* switching being a close second. This is significantly higher than the value

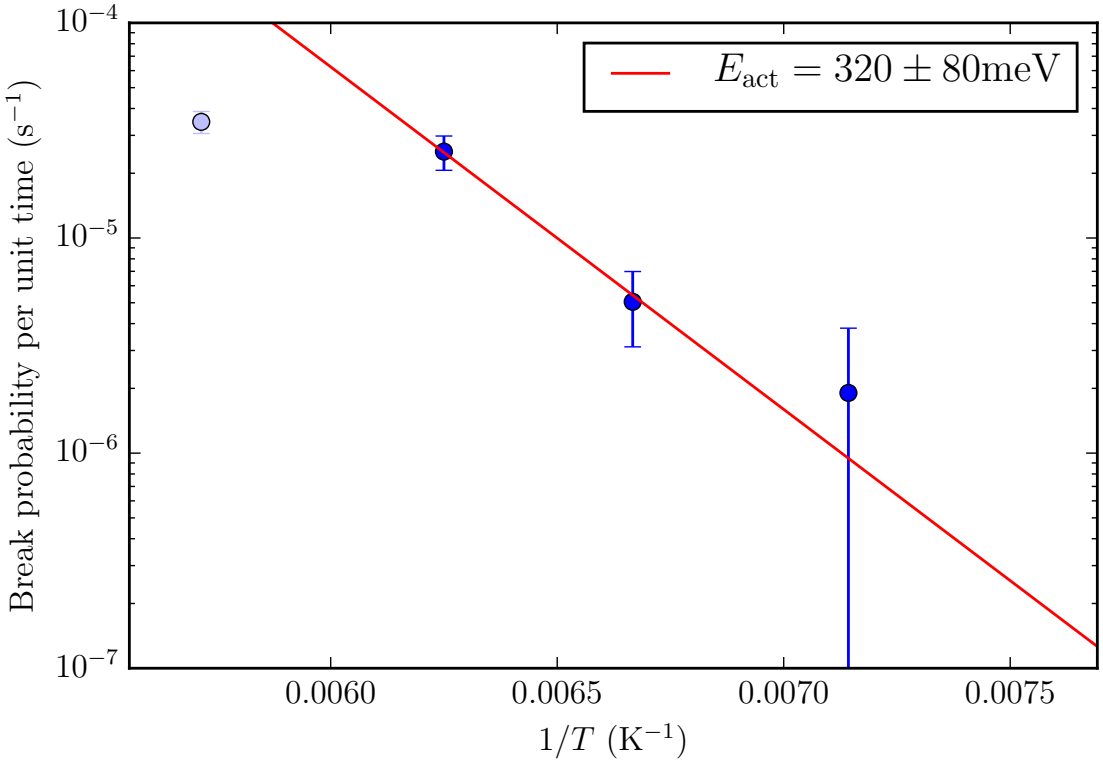

Figure 3.18: Probability for an AAD unit to break from a chain per unit time, plotted for a range of temperatures. Each point is the average of the measured values over ~ 10 images, errors are the standard error on that mean. Lighter points are excluded from the fit for reasons given in the text, temperatures with no measured events are ignored. The red line is an exponential fit, giving the activation energy shown.

quoted in [173] of 0.09 eV, suggesting that a major part of the intrachain interactions is missing from the DFT simulations reported there.

Secondly, processes in which chains coalesce can also occur. Energetically, this is permissible at lower temperatures, but is suppressed by the lack of mobility of smaller chains. At the temperatures where breakage becomes common, coalescence also becomes more probable as a result of the higher frequency of diffusion. The net changes in chain length are then interesting, as they determine whether chains tend to grow or shrink at these temperatures. This can be determined by comparing each chain length altering event and looking at whether the average chain length after the event is larger or smaller than before the event. It was found that in general chains get longer rather than shorter. This was also found to be noticeable when examining samples that had been held at

elevated temperatures for extended periods. The extended gentle anneal favours long chains, and this is evident to the eye when looking at images taken after such a period.

3.3.4 Conformational change

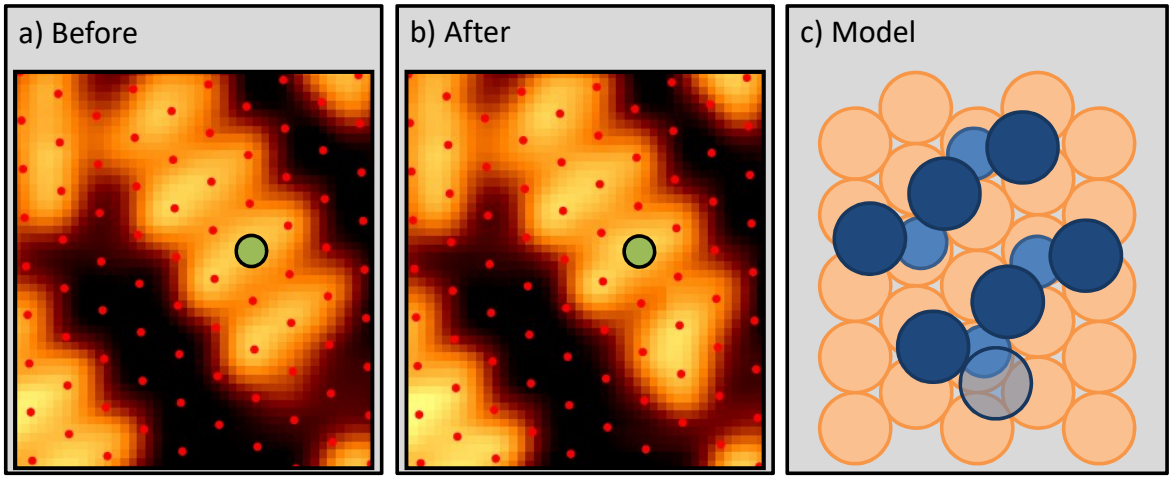

Figure 3.19: Conformational change to the last AAD unit in a chain. Panels a) and b) show the same chain imaged in two consecutive STM images at 150 K. A green dot marks the same AAD unit on both images to guide the eye, whilst not obscuring switching. Panel c) shows a ball model of this event. Note that this thermal switching process is imaged at low current and high bias (50 pA and 1 V, respectively), and differs from the asymmetric switching observed in Section 3.2.2.

Conformational changes take place at fairly high temperatures compared to diffusion of AAD units; moreover, they are only observable in a small temperature range, because at higher temperature chain breakage competes with conformational change. The occurrence of *cis-trans* switching events is constrained to chain ends and isolated molecules, as steric hindrance prevents thermal switching within chains. Single molecules are much more likely to diffuse than to switch because of the low diffusive energy barrier, so switching is most commonly observed at chain ends. However, chain breakage followed by diffusion is dominant at chain ends, as every chain can break in multiple locations, but can only switch at its very end. In an intermediate temperature range $140\,\mathrm{K} \leq T \leq 160\,\mathrm{K}$ (similar to single AAD chain breaks) *cis-trans* switching is quantifiable.

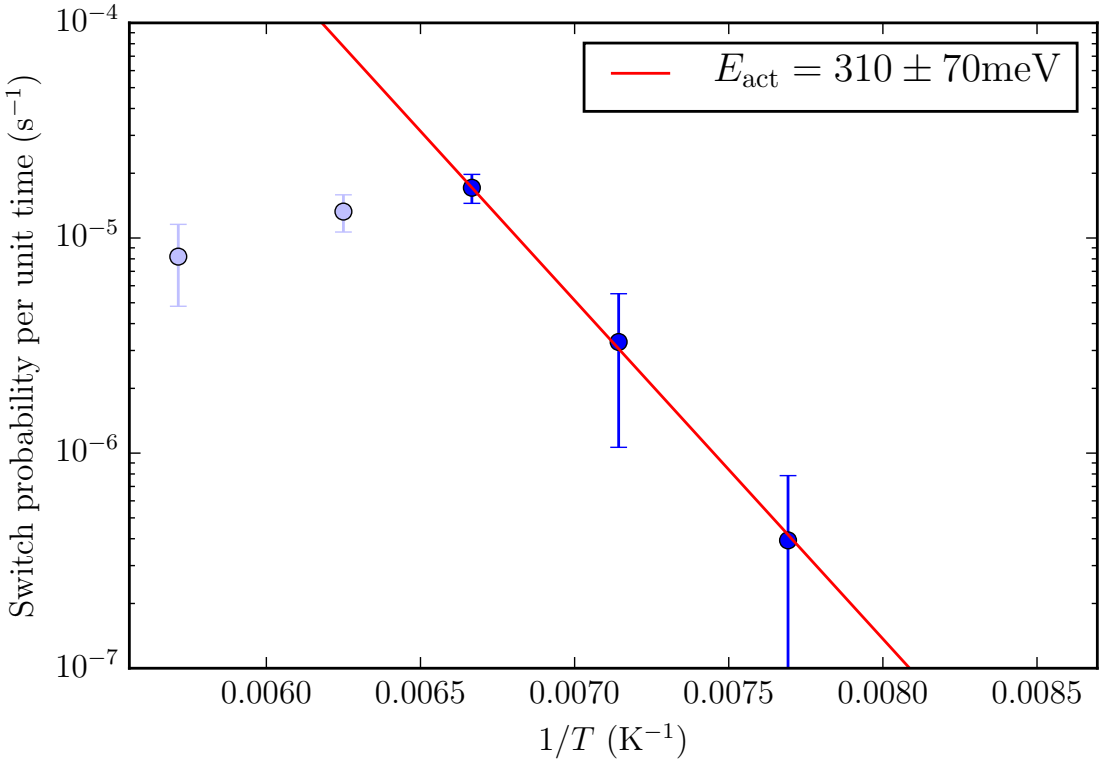

Figure 3.20: Probability for a conformational change to the *cis* form, plotted for a range of temperatures. Each point is the average of the measured values over $\sim$ 10 images, errors are the standard error on that mean. Lighter points are excluded from the fit for reasons given in the text, temperatures with no measured events are ignored. The red line is an exponential fit, giving the activation energy shown.

An additional complication with conformational switching is that it can occur in both directions with different rates, complicating normalisation. For switching to the *cis* form, switching events can be normalised to twice the number of chains, as this estimates the number of chain ends (see discussion in Section 3.3.3). However, for switching from *cis* to *trans* the normalisation relies on a count of the number of *cis* form AADs. This count is achieved in the same manner as for the chain populations, measuring the number of *cis* AAD units then keeping track of the net change over the series of images.

The two graphs of this section, Figure 3.20 and Figure 3.21, show the activation energies for switching from the *trans* form to the *cis* form, and vice-versa. It is found that switching back to the *trans* form appears to be marginally easier, though the errors do allow for the possibility that the two have similar activation energies. More observations

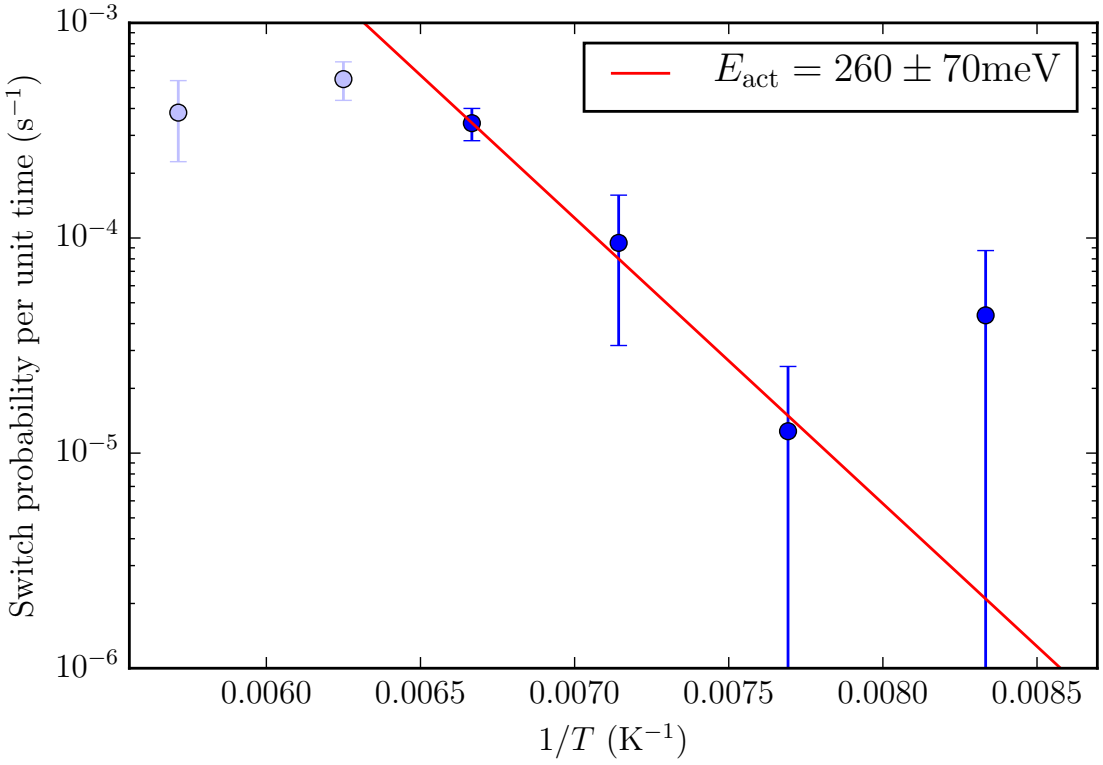

Figure 3.21: Probability for a conformational change from the *cis* form, plotted for a range of temperatures. Each point is the average of the measured values over ~ 10 images, errors are the standard error on that mean. Lighter points are excluded from the fit for reasons given in the text, temperatures with no measured events are ignored. The red line is an exponential fit, giving the activation energy shown.

at 120 K would reduce the errors, as no *trans*-*cis* events were observed, and only one *cis*-*trans* event, unfortunately the low frequency of the events at this temperature would make that experiment time-consuming. Both energies measured here are less than the 0.5 eV predicted by DFT studies [173, 174], but the ordering matches the prediction of a slightly higher barrier for transformation from *trans* form to *cis* form given in [174].

The larger energy requirements for *trans* to *cis* switching are interesting when considering the low temperature tip-activated switching process. The size of the energy barriers suggest switching can not be a thermal process in either direction, and is triggered solely by the presence of the tip. However, the easier transformation from the *cis* form back to the *trans* form may be part of the reason that a later scan at passive voltages does not find all the molecules remaining in their switched positions.

3.3.5 High T behaviour ($T \gtrsim 190\,\mathrm{K}$)

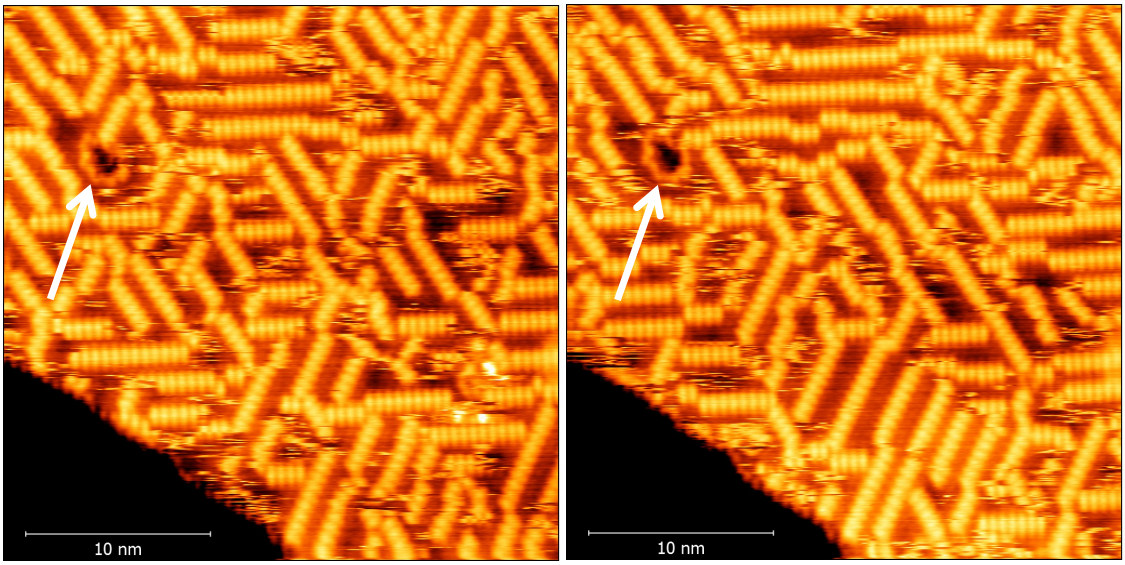

Figure 3.22: The chain phase at 190 K. The chains rapidly change orientations in the time between the two consecutive images (about 5 minutes). A feature is highlighted in white to guide the eye. It can be seen that below and to the right there is an area of chains that has changed orientation by 60°. The hazy areas between chains are rapidly diffusing AAD units. The bias was 0.5 V, current 100 pA.

At the very highest temperatures studied (190 K) the chains form an interesting ordered liquid phase. AAD units still exist and form chains, but the chains are constantly changing length and orientation. There is a complex interplay of attractive and repulsive interactions in this situation. Attractive interactions exist between AAD units in the chains, but between chains there seems to be a repulsive interaction, evident from the tendency of the chains to space out. Rows of chains can create interesting diffusive environments, where single molecules can diffuse onto and off of chain ends, but AAD units in the middle of the chains can not move easily due to the packing of the chains. Eventually (200 K and above), no chains or AAD units exist. This liquid phase is likely composed of methanethiolate groups and gold atoms diffusing freely over the surface. It may be of interest to examine this transition in greater detail, as it may be that the liquid transition occurs when the AAD units themselves begin to break up.

3.4 Comparison to theory

The AAD units studied in this chapter present several areas of theoretical interest: firstly, the diffusing species are attached to the surface at multiple locations, opening up the possibility for complex diffusive motion; secondly, the AAD units are capable of internal conformational change, whilst still remaining relatively simple; and finally, the diffusion is constrained and takes place in an interesting potential landscape generated by the chains. Few experimental systems allow for the study of all three areas described above, addressing them all in one experimental scenario allows for detailed comparison with theory. This section compares the experimental results for all processes with a number of theoretical studies on the AAD system and other similar systems exhibiting diffusion of complex entities.

The AAD molecules of this chapter appear to behave as single units with two points of contact to the underlying Au(111) surface. Diffusion of complex units on surfaces can exhibit a number of interesting effects not present in diffusion of single atoms. These effects arise from the need to satisfy multiple molecule-surface bonds during the motion of the molecule. A number of systems have been studied in the literature and exhibit unusual phenomenon. One of the most interesting of these is directed diffusion on an isotropic surface [175, 176]. Typically this is a result of a molecule with two molecule-surface bonds 'walking' parallel to some axis. Firstly, one of the molecule-surface bonds breaks, before a slight motion of the molecule allows the bond to reform at an adjacent site, with the molecule left in a unstable position. The other molecule-surface bond then breaks, allowing the molecule to relax over a new location on the surface before it reforms. Because only one bond is broken at a given time the molecule is forced to move along a constrained path parallel to its axis. Two examples of this behaviour are 9,10-dithioanthracene [175] and anthraquinone [176] on Cu(111). Another consequence of the requirement to fulfil multiple molecule-surface bonds simultaneously is that the minimum hop distance may be

several unit cells over the surface, rather than nearest neighbour [177, 178]. In addition, there may be differences between motion along a molecular axis and rotation even when the molecule is not so constrained as the walking molecules detailed above [178, 179]. This is the case for alkanes on Pt(111) [178], where rotational motion over the surface about the end of the molecule (a 'swing' mode) is far easier than direct translation, particularly for long chains. This is a consequence of the molecule traversing a path between global energy minima that passes through various local energy minima. The 'swing' mode was found to allow the molecule to maintain a larger fraction of the chain in energy minima compared to direct translation where all chain atoms have to pass over energy barriers at the same time. Changes in molecular orientation were found to have particularly high barriers, so molecular orientation remains fixed over long times. In the case of some porphyrin species on Cu(111) Marbach and Steinrück [179] found that molecules diffuse primarily in a straight line, with rotation between different symmetry directions having a higher energy barrier.

In addition to directing motion over the surface, the presence of a backbone linking two molecule-surface bonds can affect surface diffusion in other ways. For instance, a molecule consisting of several identical constituents linked by a molecular backbone above the surface may be more strongly bound to the surface overall than its constituents would be individually, but have a lower barrier to diffusion. Geometrical constraints lead to local minima in configuration space around the global energy minima, if these are very close in energy to the global minima then diffusion can be easier for the full molecule than it is for the individual constituents. This can lead to a molecule having a lower diffusion coefficient than would be expected. An example of this is given by Franke and Pehlke [180], where a 1,4-butanedithiol molecule is found to diffuse far more easily than two methanethiolate molecules bound separately without the connecting carbon backbone, despite being more strongly bound to the surface overall. In the paper by Raut and Fichthorn [178] it was found that as alkane chain length increases the diffusion barrier grows, but for long chains the barrier starts to decrease again. This is because the large number of surface bonds

essentially starts to smear out the potential energy landscape in the plane parallel to the surface: some parts of the molecule are always in areas of high potential energy due to an inability to match all of the molecular constituents to minima in the surface potential. The authors compare diffusion barriers for a perfectly matched molecule (for which all molecular constituents lie over surface minima) and the real alkanes, and find that the real diffusion barrier is significantly lower, particularly for long chains.

There are a number of theoretical studies on the AAD system, though few study diffusion of the complexes. Two studies of the diffusion of AAD complexes [167, 168] will be used for comparison to the experimental results presented earlier in the chapter. In both cases the ground state bonding geometry is determined through DFT using the generalized gradient approximation for the exchange functionals, and the projector augmented plane-wave method. In both papers a number of trial geometries were relaxed to local energy minima. To treat diffusion it is necessary to study the evolution of the binding energy as the AAD complex traverses some path over the surface. To do this the climbing image nudged elastic band scheme is used. In this scheme a number of configurations of the AAD unit between two symmetry equivalent locations are taken to form an initial guess of a reaction path. These are then relaxed to give a minimum energy path (MEP) between initial and final configurations. As such, the derived diffusion barriers are dependent upon the specific MEP traversed. This is evident when comparing the results of the two papers on AAD diffusion by Jiang and Dai [167] and Franke and Pehlke [168], and is important to bear in mind when comparing with experimental results. The highest point on the MEP is a configuration labelled as the transition state, and the energy difference between this state and the ground state configuration is the energy barrier that must be overcome for the process to occur.

The measured diffusion barrier of (0.066 ± 0.007) eV is far smaller than those presented in both papers cited above, which were 0.37 eV [168] and 0.5 eV [167]. [168] suggest an approximate error of $\sim$0.1 eV on their calculations. There are a number of possible reasons for these differences. Firstly, the DFT results are heavily dependent upon the experimental

path proscribed as described later in this section, and also will not account for Van-der-Waals energies. Secondly it is possible that the presence of the STM tip reduces the diffusion barrier locally when scanning (as seen in [181]). Finally, surrounding AAD units will create a complex potential landscape across the surface that may affect the diffusion. This is not expected to be a strong effect here given the tunneling parameters used (10 GΩ gap resistance), which have been found in other studies to have no significant effect [179, 182]. Although parameters were chosen to try to minimise any effect of the tip a systematic study would be required to rule out any energy offsets as a result of the chosen scanning parameters. A possible systematic study would count diffusive events at a high and low temperature (where accurate event counting was still possible) for a variety of scan parameters and compare them to look for systematic shifts. Despite the difficulties matching the absolute values of the energies there are still a number of experimental results to compare to theoretical calculations.

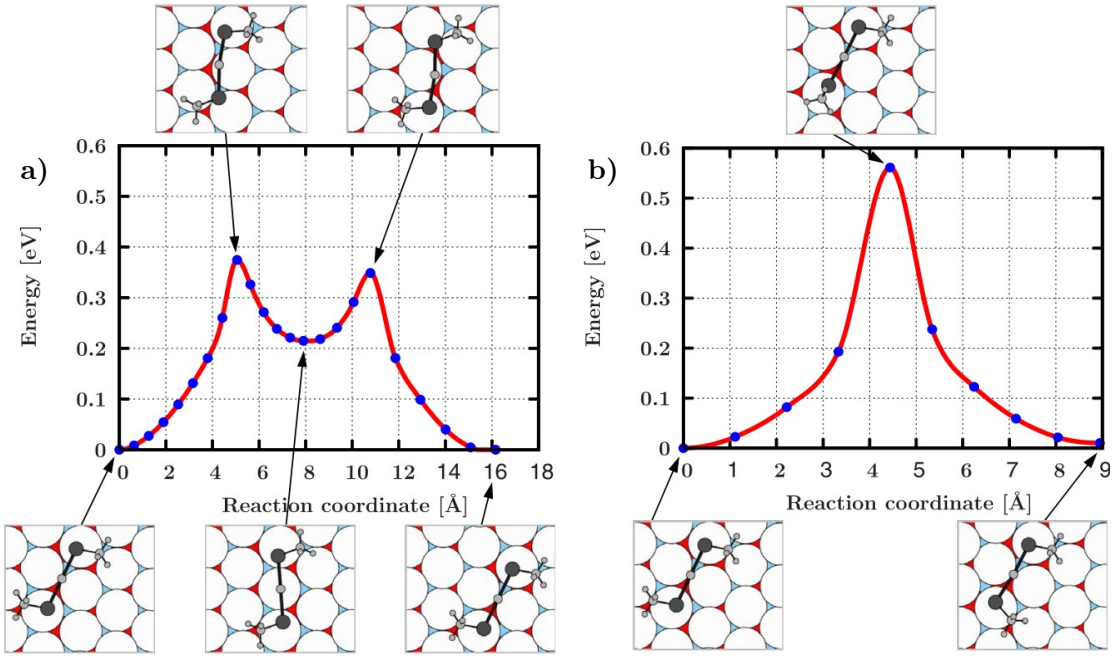

Figure 3.23: Diffusion MEP and isomerization MEP. Panel a) shows the MEP for diffusion, which can be seen to proceed through rotation about each Au-sulfur bond in a method that leads to net translation. The barrier for the process is 0.37 eV. Panel b) shows the MEP for isomerization, with a higher barrier of 0.56 eV. Figure adapted from [168].

The diffusive path followed determines the diffusion barrier calculated by theory, but is dependent on the initially guessed path. Experimentally the initial and final positions for a single diffusion event are easily accessible. This narrows down the space of possible paths by fixing the end points experimentally. The results given by Franke and Pehlke [168] are a much better fit for the observed initial and final positions shown in Figure 3.13. In the paper by Franke and Pehlke [168] the diffusive processes considered consist of a sequence of rotations about each Au-sulfur bond, resulting in a net translation. This is shown in Figure 3.23, panel a), and the overall motion is a good match to experiment (see Figure 3.13) In the paper by Jiang and Dai [167] a path consisting a combined rotation and translation of the AAD is considered. The motion described in Jiang and Dai [167] does not fit the majority of experimentally observed diffusion events, suggesting that the initial path chosen does not match the real path traversed. Franke and Pehlke [168] provide an explanation for this: they study translation and rotation of the AAD complex separately, finding that diffusion where the initial and final state correspond to a pure translation involves a lower diffusion barrier than when the final state is also rotated compared to the initial state. This is corroborated by the higher energy barrier for diffusion found by Jiang and Dai [167]. If the diffusion data set presented in Section 3.3 is broken down into diffusion involving rotation and diffusion without rotation, it should be possible to probe the respective barriers and compare further to the theoretical results. This would be an interesting area for future study.

The arguments of the previous paragraph all assume diffusion of the AAD unit as a coherent whole. Another possibility is that a single methanethiolate group leaves the AAD unit and diffuses before being followed by the rest of the unit. Experimentally this does not appear to occur, though it would not be visible if such a process only occurred on very short timescales. Several pieces of evidence argue against break up of the AAD units. Firstly, no single methanethiolate units are seen to break off of the chains at very low temperatures. If single $S - CH_3$ groups were constantly breaking off and reattaching at a high rate (with diffusion occurring if the remaining components followed), then at low

temperature it could be expected that this process would slow enough to be seen. On the contrary, $S-CH_3$ groups are only seen to diffuse away separately at high temperatures where diffusion is facile, suggesting tightly bound AAD units. Constant rapid diffusion would also lead to poor quality STM images with a lot of streaking suggesting motion, this was not seen apart from at high temperatures. This is supported by the theoretical calculations by Franke and Pehlke [168], who found that the barrier to a single $S-CH_3$ leaving the AAD was larger than any of their studied barriers to diffusion. Interestingly, the AAD system exhibits an increased barrier to diffusion relative to that for individual $S-CH_3$ radicals [168]. There may be interesting consequences for diffusion rates once significant numbers of $S-CH_3$ can break free of AAD units. It is possible that this is the reason for the rapid rearrangement of chains possible at 190 K, or even for the transition to the liquid phase above ∼200 K. This may an interesting area for future experimental and theoretical study.

In addition to diffusion there are a number of theoretical studies of *cis-trans* isomerization in AAD units [168, 173, 174]. All of these studies find the barrier to *cis-trans* isomerization to be ∼0.5 eV, again this is larger than my experimental result of (310 ± 70) meV, but these values are closer to being the same within error. An example MEP from the paper by Franke and Pehlke [168] is shown in Figure 3.23, panel b). The experimental results further support the energy ordering suggested by [168]: diffusion followed by rotation then isomerization, in order of increasing energy barrier. The difference between diffusion barrier and isomerization barrier measured in [168] is the same as that measured in this chapter, within error, with an experimentally measured difference of (240 ± 70) meV, compared to the theoretical (190 ± 100) meV (error approximate). This supports the possibility of a constant energy offset between the DFT and experimental results, whether a theoretical or experimental offset.

Finally, the forces holding the AAD chains together have not been systematically investigated theoretically and should prove a fascinating area for future study. The energy decrease on adding an AAD must be substantial given the barrier to single AADs leaving

chains. One theoretical paper suggests an attractive interaction which reduces the energy by 0.09 eV per AAD unit in the chain [173], together with a repulsive interaction between the stripes. This is likely a result of electrostatic effects, as the AAD units have areas of slightly positive and slightly negative charge, with the sulfur atoms being negatively charged by about $-0.16\,e$ and the gold positively charged by about $0.14\,e$ [146]. It is likely that the intrachain interactions are complex, potentially being a function of chain length. The experimental analysis could be extended by studying the rate of single AAD breaks as a function of chain length, to determine whether non-nearest-neighbour interactions are present. If present, these could have a significant effect on the formation of the self-assembled layers. In addition, interactions between AAD chains and single AAD units may affect diffusion. This could be investigated by studying diffusion as a function of position relative to the surrounding AAD chains.

3.5 Step-edge species

The AAD chains are not the only structures formed after deposition of dimethyl-disulfide on the gold surface. Alternative bonding types can occur at step edges and other locations where an excess of gold atoms are present. Decoration of step edges by thiolate species can take two forms in this system, depending on both the type of step edge and the coverage of thiolate species on the surface. The simplest decoration is an AAD chain along the step edge, which is common for steps aligned along one of the directions which the chains can take; this occurs most often at high coverage. The second form of decoration is a row of what appear to be single methanethiolates which are packed along the step edge.

The decoration of step edges by thiolates has particularly interesting implications for the structure of monolayer protected gold nanoclusters. At present it is largely assumed that alkylthiolate capping layers bond using the AAD 'staple' motif. However, it is difficult if not impossible to image the surfaces of capped nanoclusters at present, so most of the structural models are theoretical in nature. The lower coordination of atoms at

steps on the gold surface may more closely model a high curvature surface like that of a nanocluster, where a large proportion of sites can be of low coordination. Therefore, different bonding configurations that occur at steps could play a major role in nanoparticle capping layers.

In this section the decoration of step edges in the dimethyl-disulfide on gold system is investigated. A structural model is proposed for the apparent single thiolate species, and its thermal stability is described.

3.5.1 Structural model

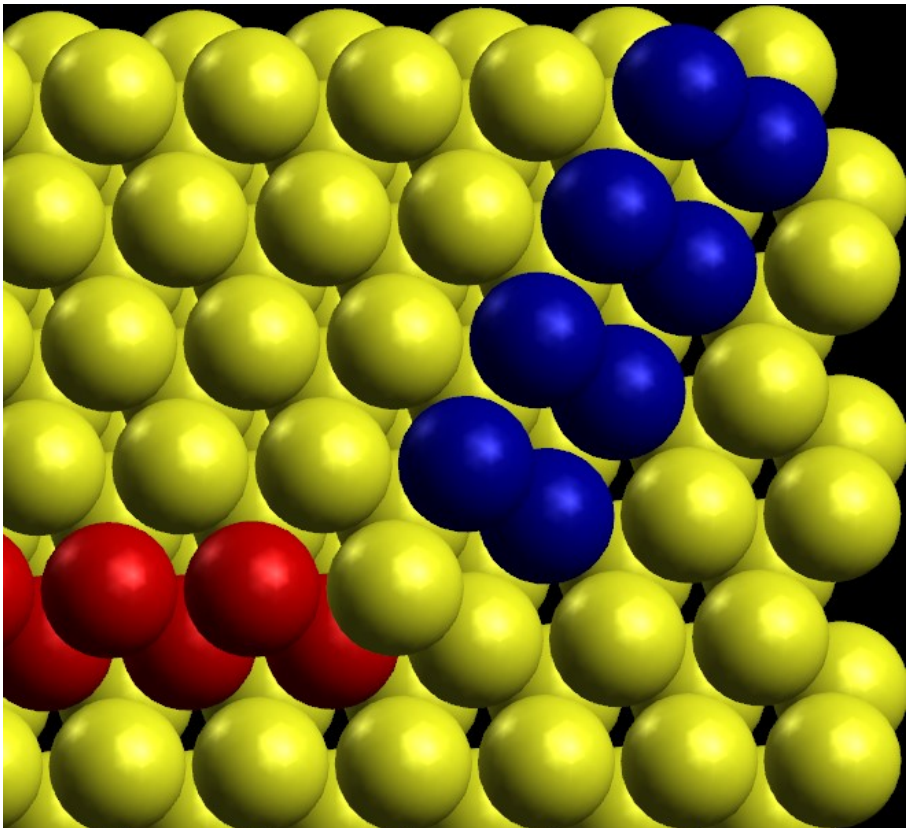

Figure 3.24: Ball model showing the two type of step on the gold surface. The atoms coloured blue show a 100 microfacet, the atoms coloured red a 111 microfacet.

On the gold surface, steps fall into two categories: those normal to the $[\bar{2}11]$ direction, and those rotated by 60° running normal to the $[0\bar{1}1]$ direction. The two types of step reveal two different microfacets corresponding to the (111) and (100) surfaces of gold.

On the bare surface, steps descending along the [$\bar{2}$11] direction expose {111} microfacets, ascending steps {100} microfacets. Steps of the {111} type are typically more stable, with steps of the other type being much less common and typically existing in short fragmented zig-zag steps between regions of the {111} type.

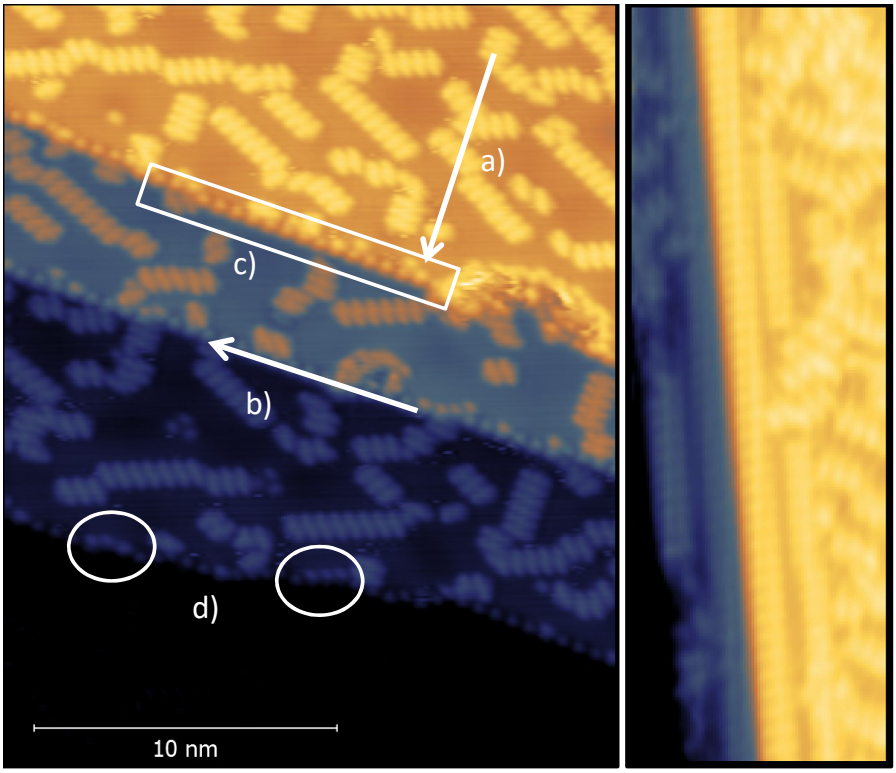

Figure 3.25: STM image showing step edge decoration for steps normal to the [$\bar{2}$11] direction. The white arrow labelled a) indicates the [$\bar{2}$11] direction, b) labels the [0$\bar{1}$1] direction. The image on the right shows step edge decoration at much higher coverages, where a step is decorated along the [$\bar{2}$11] direction. The vertical extent of the image is 20 nm. Images were recorded at 0.1 V, 100 pA and 790 mV, 800 pA.

On deposition of dimethyl-disulfide different steps can be stabilised depending on the thiolate coverage. At high coverage, steps running parallel to the [$\bar{2}$11] direction are stabilised. These are typically decorated by a chain of AAD units in their typical staple form. These type of steps are not stable on the bare surface, marking a significant impact as a result of the molecular bonding. At lower coverage this is not the case, instead the two usual types of gold step exist but with small differences in stability as a result of decoration by single methanethiolate groups. Now the steps are a combination of the usual

more stable {111} type steps, decorated with regularly spaced methanethiolate groups, and lengths of irregular steps decorated in a disordered manner by methanethiolate. As a results of the methanethiolate bonding large regions of the {100} type step can occur.

The appearance of the regular {111} step-edge species suggests that they are single methanethiolate species. The ubiquity of the step-edge decoration, and its absence on a clean surface argues against it being a result of contamination from the vacuum, implying that the decoration is formed of some fragment of a DMDS molecule. On terraces, combinations of two methanethiolate groups form the usual AAD units and image as multiple dots, AAD units decorating steps also clearly image in this manner. The features imaged are the gold adatom, and the methyl groups, suggesting the sulfur is not imaged. As the sulfur is responsible for bonding the methyl group to the surface this leaves a single methanethiolate unit as the only viable candidate.

The regular spacing of the spots which decorate the {111} type steps at low coverage suggests that the species being imaged are in registry with the gold lattice at the edge of the step. The spacing between the step edge features is measured to be (0.592 ± 0.007) nm from a line profile, approximately twice the gold lattice spacing, which was deduced to be (0.277 ± 0.005) nm on this image. The height of the features as measured by STM is less than that of the methyl groups on the upper terrace, but more than that of those on the lower terrace. This is shown in Figure 3.26, which shows line profiles through the methyl groups of two chains, one on the upper and one on the lower terrace, in addition to a line profile taken normal to the step through one of the step-edge species. The points on the curve highlighted by circular markers were used to deduce the apparent heights of each feature (where more than one was used an average was taken). The offset between curves beginning on the upper terrace and that on the lower terrace was used to measure the step height, and the data shown is scaled such that the step-height is correct. Methyl groups were measured to have heights (0.186 ± 0.006) nm and (0.170 ± 0.004) nm on upper and lower terraces respectively. The difference in these values is likely the result of different lateral positioning of the line profiles. The step-edge species was found to

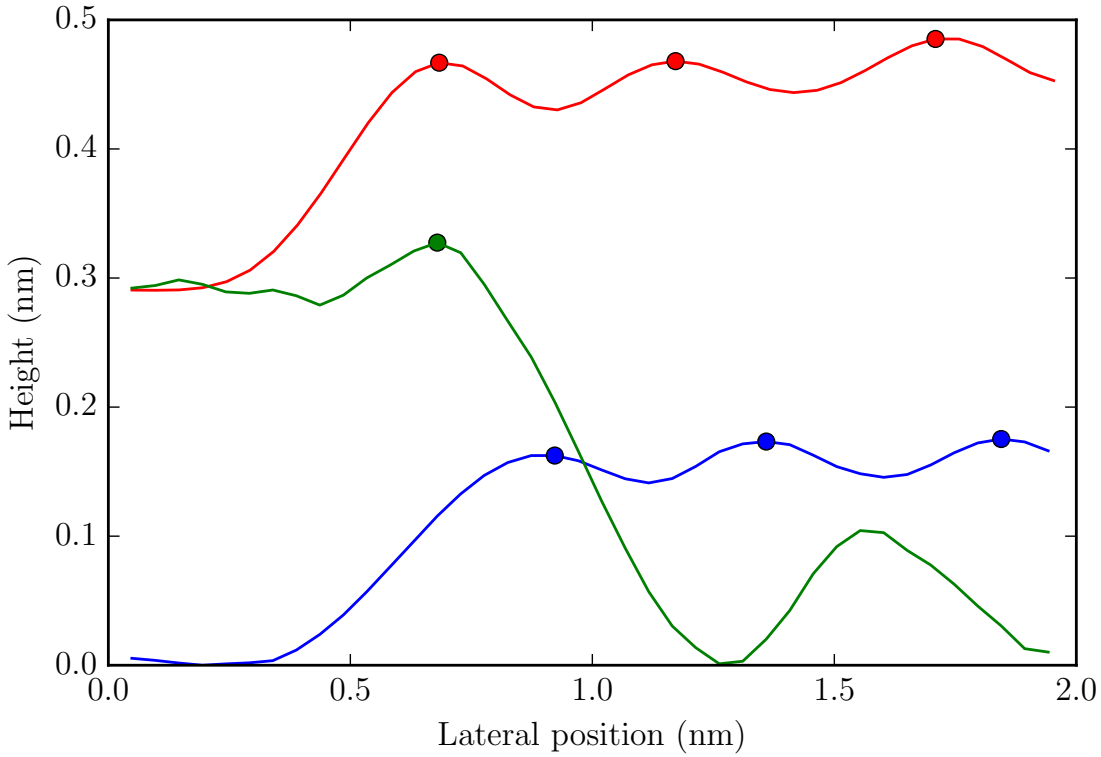

Figure 3.26: Line profiles through several surface features. The red and blue lines are taken through the methyl groups of AAD units on the terrace. The green line is through a step-edge feature. The coloured markers indicate peak positions to derive the heights given in the text. Two of the maxima appear slightly offset, this is an optical artifact, as the peaks are flat.

extend ∼0.04 nm above the upper terrace, and thus ∼0.33 nm above the lower terrace. The values found only rule out bonding solely on top of the terrace, as it is known from [134] that single methanethiolates image as taller than the methyl groups of an AAD. However, the paper does not present the measured height of methanethiolate (only a comparison image), without which it isn't possible to tell whether the step edge species is different in apparent height to an isolated methanethiolate.

The data described above suggests a bridging arrangement, where each thiolate bonds between two gold atoms of the step edge. Figure 3.27 shows a close up of a section of step edge near conveniently placed AAD units, together with a model showing the locations with respect to the underlying lattice. The step edge is indicated in red, with the gold lattice shown in orange. AAD units are shown in dark blue, and the bridging

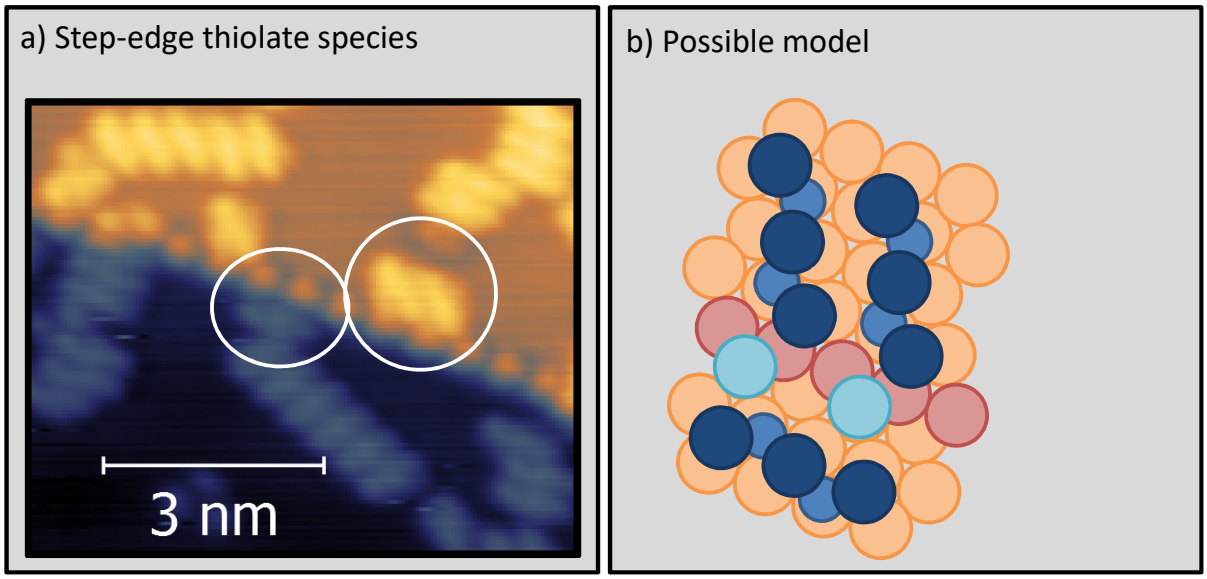

Figure 3.27: Panel a) shows a close up of the step-edge species cut from the image of Figure 3.25, two interesting features are hightlighted with white circles. A proposed model for these features is shown in b). The step edge is shown as red circles, gold atoms as orange circle, the AAD units are shown in dark blue, and the step edge species in a light blue. Apart from its positioning parallel to the step, the location of the methanethiolate bonded to the step is uncertain.

methanethiolates are shown in light blue. The positions shown appear to match those in STM, though the exact location of the bonding in the direction normal to the step is unknown. It would seem reasonable that the sulfur is bonded in a location vertically above the last gold atom of the lower terrace (as shown in the model) as this would closely mimic the bonding environment in the AAD units, where the sulfur is bonded to two gold atoms, the adatom and a substrate atom.

3.5.2 Thermal stability

The step edge species were found to be very stable, usually much more so than the chain phase located on the terraces. This may be attributable to the close packing along the step edge, which suppresses the usually facile diffusive dynamics. The energy to remove a thiolate unit from the step edge must be fairly high, as they are stable and present even in the completely disordered AAD phase at 210 K. Some can be seen in the images of

Figure 3.22.

A thermally activated process was found to take place at 170 K for the thiolate species on step edges parallel to the $[\bar{2}11]$ direction, but is unclear what exactly is happening. There appear to be two forms of the step edge decoration which fluctuate between images, this is primarily observed on the step edges parallel to $\{\bar{2}11\}$ directions, which at this temperature are decorated by AAD chains on the lower terrace, and single bright spots on the upper terrace, which are assumed to be single methane thiolates. The thiolate decoration on the top step edge can display two intensities in the STM image, and fluctuates between these two brightnesses between images. The decoration by AAD on the lower terrace may result from the rapid diffusion on the terraces, where the steps act to capture diffusing AAD units into a more stable position. Potentially, this could be another switching mechanism that could merit further study.

3.6 Trimer species

In addition to the step edge species described in the previous section, a three-lobed *trimer* feature is also sometimes found on the surface. The trimer species seems to be another thiolate bonding configuration that forms on terraces. Two possible configurations are three methanethiolate arranged in a triangular fashion, with the methyl groups pointing out, or a similar configuration of methanethiolate around a small gold island. Both are a possibility, and are difficult to distinguish in the STM without theoretical input. This section will describe possible model structures, and compare them with experimental results. Again, these structures may be of interest in the nanocluster field. If a gold island is present in the trimer it would exactly match a model for a capped Au_3 cluster presented in [183].

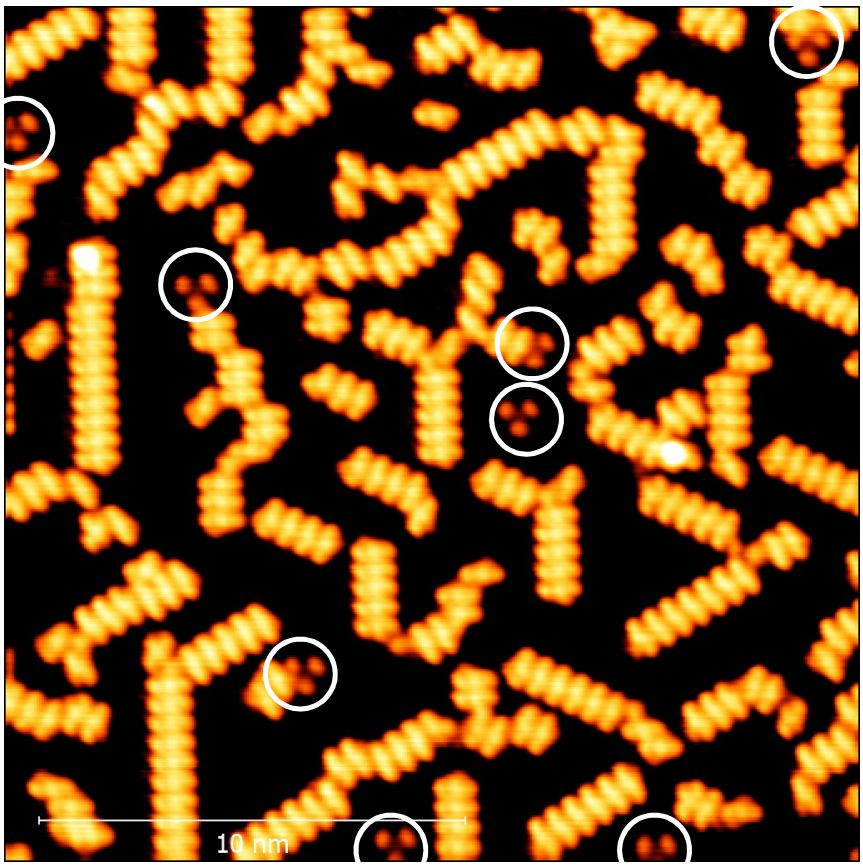

Figure 3.28: Shows a number of trimers decorating the surface between chains (indicated by white circles). Notice how the trimers only show one orientation. The image was recorded at 50 mV, 1 nA.

3.6.1 Structural model

The trimer species are not seen on the clean surface, but only after deposition of DMDS and heating to produce the low coverage phase. They occur in sufficient numbers, at least one or two per image but sometimes much higher, to indicate that they are likely to not be a contaminant, and again suggesting an alternative methanethiolate based structure.

Interestingly the orientation of the trimer features is fixed, they are only ever observed with one orientation. As the feature is threefold rotationally symmetric there are two possible commensurate orientations on the surface lattice. The presence of only one orientation suggests a mechanism which preferentially selects for this orientation. On the clean surface the only possibility is that the structure is sensitive to the difference between

fcc and hcp hollow sites.

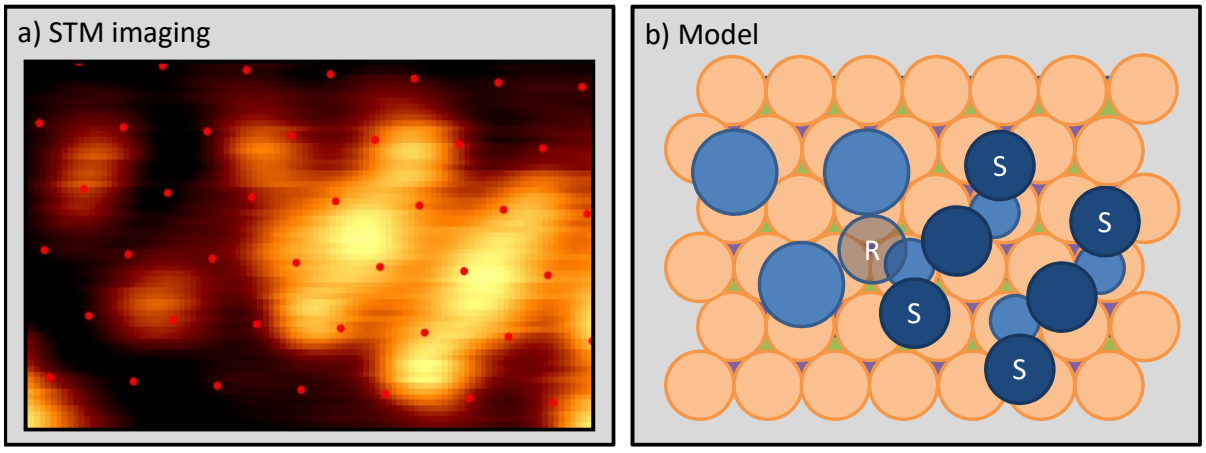

Figure 3.29: Panel a) shows a close up image of a trimer directly adjacent to a two AAD chain. Overlaying a lattice with the periodicity of the gold atoms underneath enables the position of the trimer to be deduced. Panel b) shows how a model can be constructed around the 'ghosting' which occurs at the chain end. This ghosting happens only on the side of chains that can switch to cis form. This then allows the footprint of the AAD to be correctly matched to the chain. The image is recorded at $-0.3\,\mathrm{V}$, $500\,\mathrm{pA}$

It is possible to use the locations of nearby AAD chains to calculate the bonding location of the trimer species. This is shown in Figure 3.29, the red spots indicate the position of surface gold atoms. The alignment can only be trusted for very nearby AAD as the vectors were hand calculated, and as a results small errors build into reasonable offsets over distances greater than a few unit cells. From this image it can be seen that the methyl groups are situated over hollow sites of the surface, it is uncertain which hollow site is preferred, but the hollow sites are all of one kind. This is a similar phenomenon to the asymmetric switching, where methyl groups were found to switch above one type of hollow site, but not the other. There are two possible ways of connecting three hollow sites. Each hollow site is a triangle, if three are put together to form a large triangle, they can all either point in the same direction as the triangle, or opposite to this direction. The arrangement that is found is formed of triangles pointing in the same direction as the large triangle, responsible for the hexagonal arrangement of atoms centred around a single atom.

It is possible that the trimer is built around a gold island. This trapping of gold atoms by adsorbates is a common feature on this surface, occurring in the AAD units of this system, and in the formation of C60 magic-number clusters [184]. In this case the addition of a gold island may provide a means for selection of one particular hollow site over the other, as a gold trimer will present different microfacets depending on the location of the gold trimer on the surface. A small gold island placed atop the hexagonal arrangement of atoms shown can present either {111} or {100} microfacets at the hollow sites where the methyl groups are located, depending on the island placement. The type of facet is then correlated to the type of hollow site the methyl groups lie over, the {111} microfacets lie adjacent to fcc hollow sites, the {100} adjacent to hcp ones. Adding a gold island would therefore select one hollow site.

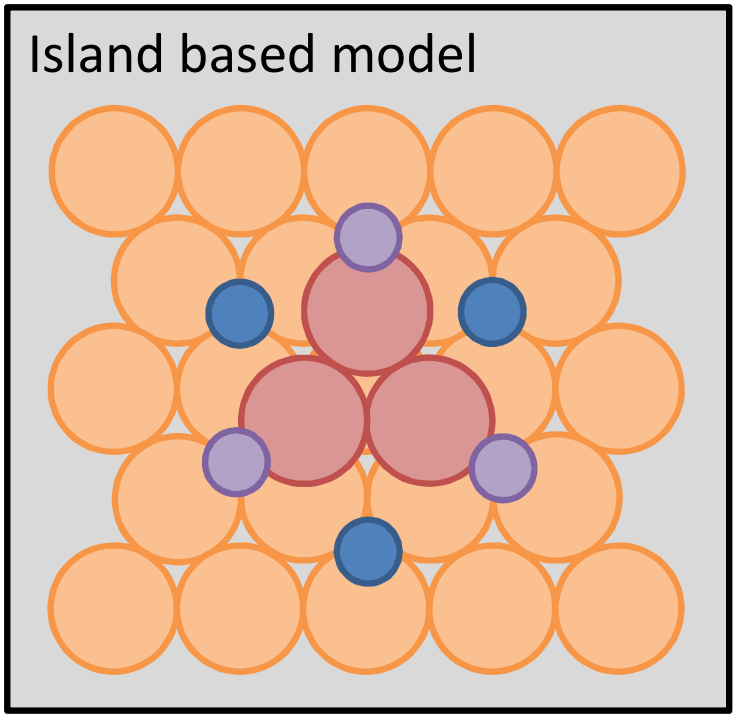

Figure 3.30: Possible gold island structures. Gold atoms in the surface are in orange, the triangle of gold atoms in red is the gold island. The positions of methyl groups measured by STM are shown in two possible orientations in purple and blue.

The appearance of the trimers after heating the surface to reduce the coverage of

the molecules may support the inclusion of a gold island: on heating the AAD units will breakdown such that the methanethiolate can desorb. This will release a number of gold atoms on to the surface. It may be that on subsequent cooling this excess of gold atoms are hindered from reaching stepedges by the thiolates diffusing over the surface, and subsequently become trapped in the layer. This would then favour the production of new thiolate bonding configurations with a lower ratio of thiolate to gold atoms; such as the trimer with a ratio of one Au-adatom to one methanethiolate.

3.6.2 Thermal stability

The trimer structures appear very stable compared to the AAD units. They exhibit no thermally induced processes until around 170 K where one trimer was observed to diffuse. This low measured activity may in part be a result of sample size, with only 1 or 2 trimers being observed per image during the dynamics study, making it difficult to make quantitative statements about the stability. However, at this temperature, diffusion of single AAD occurs at a very rapid rate, whereas the trimer diffusion event only occurred after many images, suggesting a much higher stability.

3.7 Summary and outlook

In summary, a number of interesting dynamical processes have been studied in the low coverage AAD chain phase formed by depositing DMDS on the Au(111) surface. These include diffusion, *cis*-*trans* switching, and chain breaking.

All of the dynamical processes studied were found to be thermally activated between 77 K and 200 K, and would all be facile at room temperature. It was found that the largest energy barrier was for break-up of the chains, (320 ± 80) meV, followed by *trans*-to-*cis* switching, (310 ± 70) meV, *cis*-to-*trans* switching, (260 ± 70) meV, and finally diffusion (66 ± 7) meV. These energy barriers are all substantially lower than predicted through DFT models, apart from the barrier to break a chain, which is larger. This may suggest

a missing component in the DFT simulations, whether this be substantial contributions from Van-der-Waals forces, or long range cooperative interactions between elements of the chains.

Diffusion was found to occur mainly in the AAD complexes (apart from possibly at the highest temperatures studied), which also appeared capable of diffusing collectively in small groups. These may be interesting systems to study theoretically, as they are complex structures composed of adsorbed molecules with incorporated surface atoms. The ability of the AAD complexes to travel in small chains may be particularly interesting, as the interactions with the substrate that permit this are presumably complicated.

The presence of long chains impacts the diffusive motion of single AAD. Long AAD chains are stabilised by attractive forces within the chain, and provide barriers to the diffusion of AAD units, creating an interesting diffusive environment. The outcome of this is that chains tend to grow in length when held at intermediate temperatures, where the chains do not break up rapidly, but single AAD diffusion is relatively rapid. Single units can diffuse onto and off of the ends of chains, but there is an energy barrier to leaving the chain that is not present for attachment to the end of the chain. Overall, this favours chain growth. This implies annealing could be used to create a layer of long chains that can guide deposition of other adsorbates into lines on the surface.

The ease with which all of the above thermal processes occur suggests that the sulfur gold interface could be highly dynamic beneath the alkane chains in long alkane chain SAMs at room temperature. This kind of proposal has been made before in the literature, with several instances of experimental detection of coexistent phases [122, 146], and complicated adatom-vacancy models [185]. The experimental study of the dynamics of the sulfur headgroup when unencumbered by a long alkane chain may help to refine these models.

It was also found that the STM tip was capable of initiating *cis*-to-*trans* switching of both single AAD units, and AAD units within chains. This process was found to be most likely a result of a physical interaction with the STM tip. The switching was initiated

at very low bias, and high currents, conditions under which the tip-sample separation is small, with the intensity being a fairly smooth function of the applied parameters. The switching appeared to be somewhat dependent on the orientation of the slow scan-direction with respect to the chains, but was found to be insensitive to whether the tip was scanning up or down along this direction. It was also found to occur in both backwards and forwards fast scan-directions.

Switching within AAD chains was particularly interesting as only one side of the chains was found to switch, with the side being dependent on the chirality of the chain. The only possible reasons for this are a particularly strong influence of the presence of the gold atom in the subsurface layer at hcp sites, or an unexpected offset in the adatom bonding, such that each side of the chain is in a subtly different bonding environment. The surface introduces an element of asymmetry that would otherwise not be present.

Finally a series of other Au-adatom based structures were described, which were methanethiolates in a trimer or bridge-bonded geometry. The bridge-bonded species were found on step edges and may play an important role on highly curved surface such as those of gold nanoclusters. The trimer is a highly oriented structure, that only points in one direction with regards to the surface lattice, making it a useful marker species. In addition, if it follows the usual trend of including gold adatoms into its structure, it may contain a small gold island. This would make it an experimental realisation of a thiolate-capped Au_3 nanocluster.

3.7.1 Future work

The experimental studies here could be extended in several ways. These include more work on the dynamics using new experimental and theoretical techniques, further systematic study of the switching behaviour, or further investigation of the more novel methanthiolate structures. Many of these could also be studied with longer chain alkanethiolates to determine the impact of chain length.

It would interesting to apply video rate STM to the diffusion system, which would allow for better study of the higher temperature regime where our traditional STM does not have the temporal resolution to resolve single AAD diffusion. This would also allow it to be determined when the AAD units themselves begin to break up, though this was hinted at in my high temperature images, it was not possible to quantify. Single methanthiolate motion is important as it may be the dominant form at room temperature.

The dynamics studies described here could be combined with a theoretical study using more modern DFT techniques that incorporate Van-der-Waals in a more rigorous manner, to try to improve models of the sulfur gold interface. Several studies have been presented [167, 173, 174, 186], but many of these predict incorrect energy barriers for processes, and even incorrect orderings. There is also the option to perform molecular dynamics to investigate the diffusive motion and look at how these AAD complexes move over the surface. The interplay between stable long chains and mobile short chains could be an interesting problem in this context.

An extension using our equipment would be to look at the dynamics of ethanethiolate. The effect of increasing alkane chain length on the diffusion could then be quantified. For instance does this have a stronger effect on diffusion than it does on chain breaking, in which case it would be possible to increase the diffusive barrier relative to that of breaking the chains. How would this then affect the large scale structures formed?

This extension has been studied already for the switching behaviour, where similar behaviour was found to occur, but it was found that symmetric switching could also be triggered in chains [164]. This could obviously be further extended to propanethiolate.

The realisation that the asymmetric switching is more easily controlled by current variation may suggest I-Z spectroscopy as a technique to investigate the switching. It might be that this would provide a quantitative measure of a threshold. In addition, AFM would be an interesting technique to apply to the system as the force applied to the chains could be measured directly, this could also help eliminate the issue of electronic structure convolution into the imaging.

To extend the study of the more novel methanethiolate structures, it may be possible to tailor the formation parameters to favour formation of trimer structures. For instance, by allowing very slow desorption from the full coverage layer, formation of structures with more adatoms per methanethiolate may be preferred; or, codeposition of gold atoms could favour these structures. This would give more insight into the reasons for their formation. Codeposition is appealing, as it would also allow for different adatoms to be deposited, these could have interesting effects on the SAM structures if they are incorporated.

Finally, the bridge-bonded thiolates could be modelled in a nanocluster context, to see what impact they have on their capping. This would be particularly interesting for small structures where the ratio of steps to terrace is high, though it may also be interesting for large clusters where it has been predicted that surface would be induced to form steps [187]. A more detailed study of the other step directions could also be undertaken.

CHAPTER 4

Non-local Manipulation of Chlorobenzene on Si(111) – 7 × 7: Temperature Dependence of Non-Local Desorption

4.1 Motivation

Prior work by our group and collaborators has established the existence of a non-local manipulation mechanism for aromatic molecules on the Si(111) $-$ 7×7 surface due to electrons from the STM tip [36, 40, 42, 43]. These non-local experiments are of interest as they probe the interaction of low-energy electrons and holes with molecules at the atomic scale. Other techniques, such as electron-stimulated desorption (ESD) or photostimulated desorption (PSD), use large electron (or photon) doses over large areas, and although they provide a great deal of information on the surface-molecule system they do not provide the same atomically resolved data as STM can. Earlier experiments in the STM mimicked these other experiments closely by scanning the tip over the surface [16], essentially simulating a homogeneous electron dose over an area of the sample. However, it was found that molecules distant from an area of injection also respond to the electrons (see discussion in Section 1.3). It is important to note that the lifetimes of carriers in surface states are very important in a non-local process. If the interpretation of a scanning-style experiment (see Section 1.3) assumes only direct interactions of the injected electrons with the molecules, it will underestimate the number of electrons involved. Many electrons will tunnel to the substrate, where they persist for a certain lifetime before potentially interacting with an adsorbate. If these electrons are not accounted for then calculated reaction probabilities per electron will be too high. The non-local mechanism is therefore of great interest as it allows for the study of carrier transport and energy dissipation in surface states, and the effect of these phenomena on the interactions of surface state carriers with adsorbates.

If the molecule attached to the surface is well understood, then the molecule can act as a marker for surface transport at the atomic scale, signalling locations of high electron density by undergoing some reaction. This marking capability has been used to great effect in [40], and could be particularly interesting on novel surfaces which exhibit quantum effects. Were it possible to control these non-local processes in a precise manner,

they could be exploited to interface with multiple adsorbates in a parallel manner. An area of research where these processes may be exploited, or become a hindrance, is molecular electronics. When aiming to investigate a potential molecular device with the STM it is important to investigate where the electrons doing the manipulation are coming from – is the electron delivered directly from the tip or is it from the substrate? More pertinently, does this vary with temperature – will a process that works at 4 K also work in the same way at 295 K? This could be a particularly interesting problem if trying to investigate a molecular 'wire', where it would be important to confirm that the wire is the charge transport route, not the substrate, and that the route of charge transport is controlled; on the other hand, this also perhaps suggests surface states as useful charge transport channels if they can be controlled adequately.

Previous experiments on electron-induced non-local manipulation of the Si(111) – 7×7: PhCl system found that desorption was thermally activated [42]. An increase in desorption activity around room temperature ($T \gtrsim 230\,\mathrm{K}$) was explained by electronic excitation followed by thermal desorption. At low temperature ($77\,\mathrm{K} \lesssim T \lesssim 230\,\mathrm{K}$), another thermally activated process was found to be dominant. The associated activation energy suggested the process could be related to either surface phonons or molecular vibrational modes.

In order to further investigate this process, I have investigated hole-induced desorption over the same temperature range as the electron-induced process. It was speculated that altering the charge carrier could potentially lead to different temperature dependent behaviour, and that this might provide insight into the mechanisms at play. If the thermal activation is a result of a molecular mode, it might be expected that transient excited states formed by capturing an electron or a hole may be affected differently by the activation of the molecular mode, so the electron and hole attachment processes may exhibit different behaviour. Alternatively, the mechanism by which the charge triggers desorption could be substantially different depending on the sign of the captured charge, and thus be affected differently by different surface or molecular vibrational modes.

This chapter details the experiments performed on hole-induced non-local manipulation on the Si(111) $-$ 7$\times$7 surface, and compares them to the relevant experiments with electrons. To start, an introduction to the experimental methods are given. This is followed by a description of the analytical methods used to extract quantitative information from the STM images. The rest of this chapter discusses the experiments performed with 2 eV holes over the temperature range of 77 K to 295 K, beginning with a description of the phenomena observed and ending with a quantitative analysis of the non-local desorption process as a function of temperature. These results are compared with the electron-mediated process. I performed all of the experiments on holes, along with contributing some of the data comprising one of the data points in the electron data set. The electron data set was initially recorded by Tianluo Pan prior to my period of study. Two of the points were added to the initial set to provide more information over certain temperature ranges. These were recorded immediately prior to me beginning my experiments, one at 260 K, one at 95 K. I was involved in the recording of two of the ten data sets comprising the 95 K point as training on the apparatus. I later re-analysed the electron data taking into account thermal desorption, defects and the radial decay of the current in a manner consistent with the latest results on this system. This allowed for a comparison with my hole data, which was analysed in the same manner.

4.2 Experimental procedure

Before discussing the experimental results and analysis in detail, a quick overview of the terminology describing a non-local experiment will be given here, together with a description of the experimental method. In a non-local experiment charge is injected from the STM tip into a point on the sample and the resulting effects on nearby molecules are studied. Two images are used to observe the results of the experiment, one is taken before the injection and one afterwards. These images are recorded at parameters that are known to not affect the molecules (passive parameters) and are referred to as the before

a) Before injection b) After injection

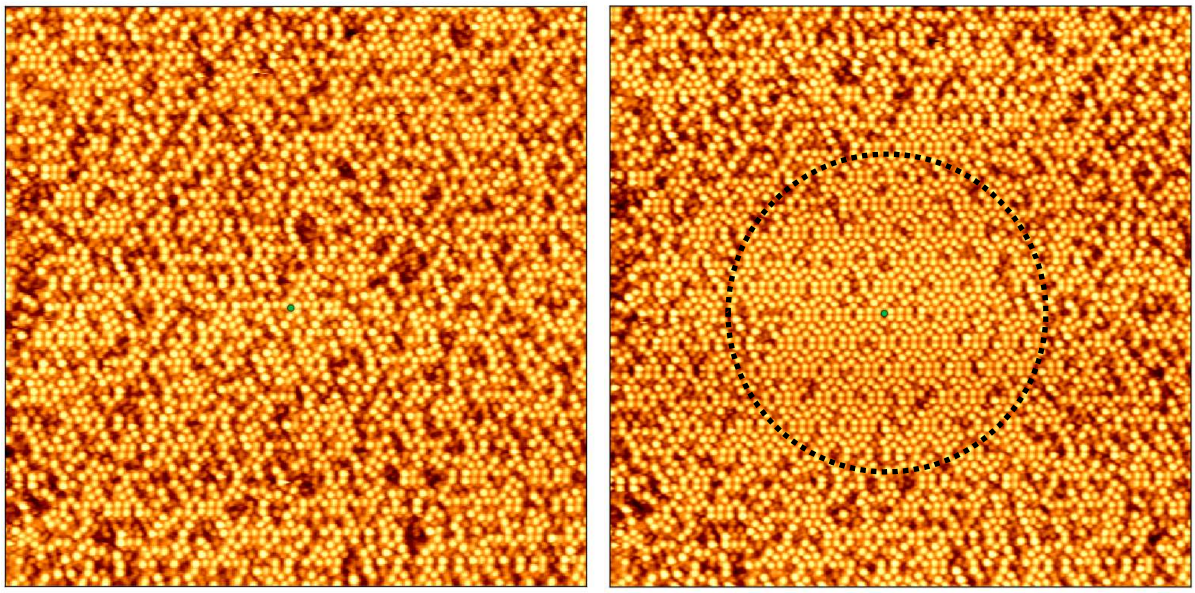

Figure 4.1: Two STM images of Si(111) − 7×7: PhCl showing the surface before and after an injection at 260 K with parameters −2.0 V, 800 pA, 80 s. In both images the silicon adatoms appear as bright features. The darker features obscuring the unit cell are chemisorbed chlorobenzene molecules. The injection was performed at the corner hole labelled by a green dot near the centre of the image. Notice how in b) there is a large area of silicon adatoms that have been cleared (highlighted with a black dotted circle). The images both show a 51.2 nm by 51.2 nm area.

and after images. The charge injection is described by three parameters: the sample bias, which sets the carrier energy (positive bias for electrons, negative for holes); the tunneling current, which sets the carrier injection rate; and the injection time, which simply describes how long the injection parameters are applied for. In the experiments of this section, the sample temperature is also varied. The injection location used in this section is always a corner hole of the Si(111) − 7×7 surface. The results of an injection performed at 260 K with parameters −2.0 V, 800 pA, and 80 s are shown in Figure 4.1, in this case the results of the injection are clearly visible to the eye.

Experimentally, the non-local experiments are performed by scanning the surface at passive imaging parameters until a suitable area free of steps is found, this is then checked to ensure no domain walls cross the image, as the associated disorder could affect the non-local process. The area is then scanned to form the before-image. Following this, the scan

size is reduced so that scans are very quick, and the tip is moved to scan over an area around the centre of the image. This is done to ensure that the injection proceeds in the desired location, and avoids misalignment as a result of piezo creep or thermal drift. The scanning is then stopped and the tip moved over a corner hole. The current is increased and the bias is then raised to the injection bias for the injection time. The feedback is left on so that a measured dose of electrons can be delivered. After the injection, the parameters are returned to their passive scan values and another set of small images recorded to check the tip did not drift out of the corner hole during the injection. The after-image is then recorded. Experiments are spaced out by at least 100 nm and are not conducted near areas where the tip has been processed.

The non-local mode was previously observed at room temperature as a result of both electron and hole injection, but was studied in greater detail for electrons. Scanning-style experiments suggested a similar desorption behaviour for holes and electrons as a function of voltage and current, so the first experimental question to be answered here was whether the hole-induced process would also exhibit a similar temperature dependence. Figure 4.2 shows an image comparing the results of a hole injection of 800 pA for 80 s at −2.7 V and 77 K to an electron injection with the same parameters at the opposite polarity (800 pA for 80 s at 2.7 V), a substantially larger area of desorbed molecules is visible after the hole injection. It is obvious that the hole-induced process is more efficient than an electron injection of the same energy. This makes sense if we assume the previous results for the voltage thresholds at room temperature also hold at the lower temperature: the −2.7 V injection is much further above threshold. The large number of desorbed molecules causes issues with quantitative analysis as it prevents a good analysis of the radial decay of the process by saturating the desorption over the image. The electron injection bias was chosen to be just above the threshold for non-local desorption. In order to prevent these saturation effects a bias of −2.0 V was selected for further hole experiments, which is a similar distance above threshold to the bias used in the electron experiments. The negative bias after-image of Figure 4.2 is not very useful for quantitative analysis, but

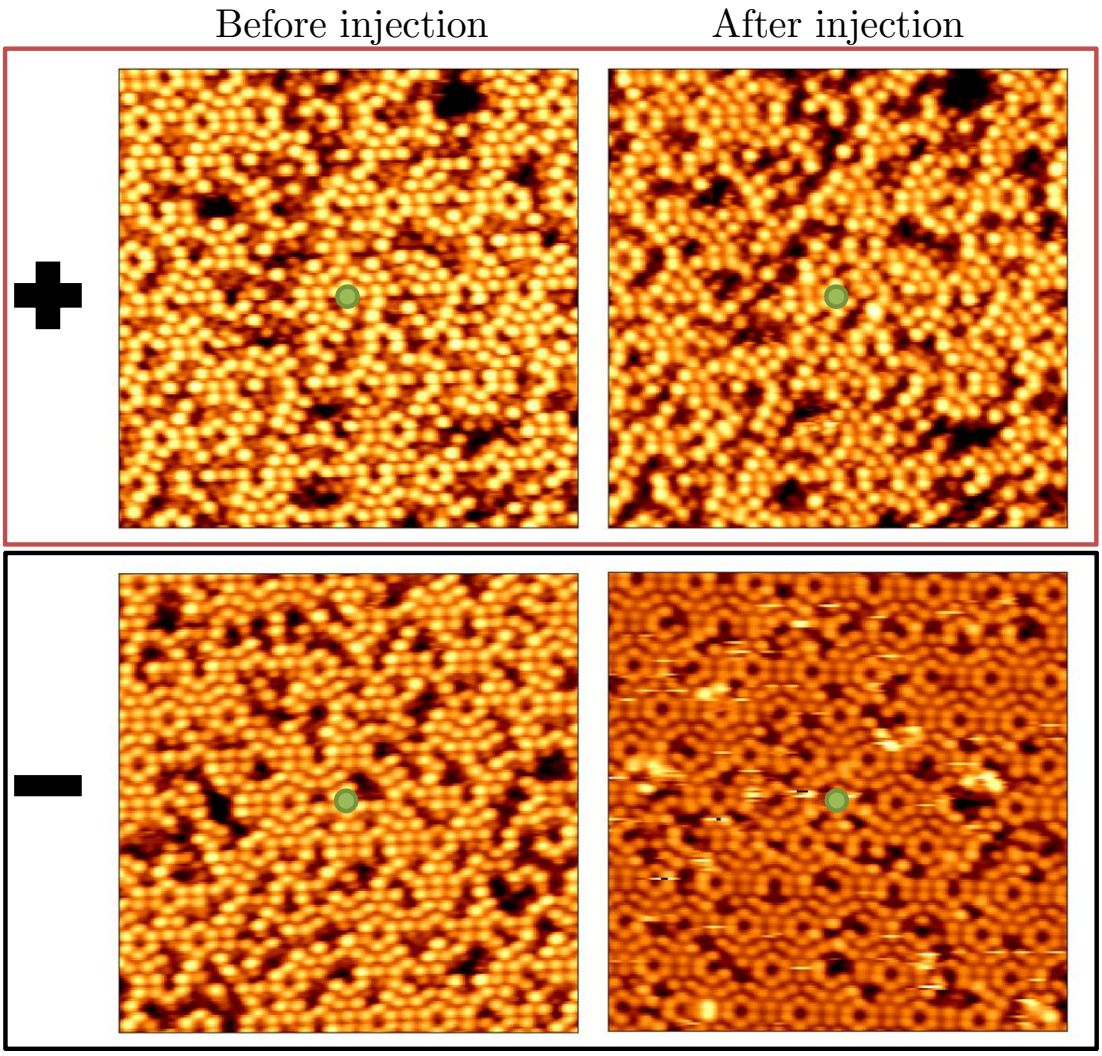

Figure 4.2: Comparing the results of hole and electron injections with exactly the same injection parameters. The red box marked with a plus shows a before-after image pair from an injection at 2.7 V bias (2.7 eV electrons), the black box marked with a minus shows the same for an injection at −2.7 V (2.7 eV holes). For both injections the setpoint current was 800 pA and the injection time was 80 s. Notice how there is little evident desorption for the positive bias electron injection, whereas at negative bias a significant number of molecules are desorbed. The images are 20 nm by 20 nm subsections taken from larger images, centred on the injection site (green spot), so that the behaviour is clearer to the eye.

there are many interesting qualitative features: in particular, the area of dark features at the injection site, and the bright speckles that are distributed over the image. Both of these phenomena have become more clearly understood following the experiments of Chapter 5.

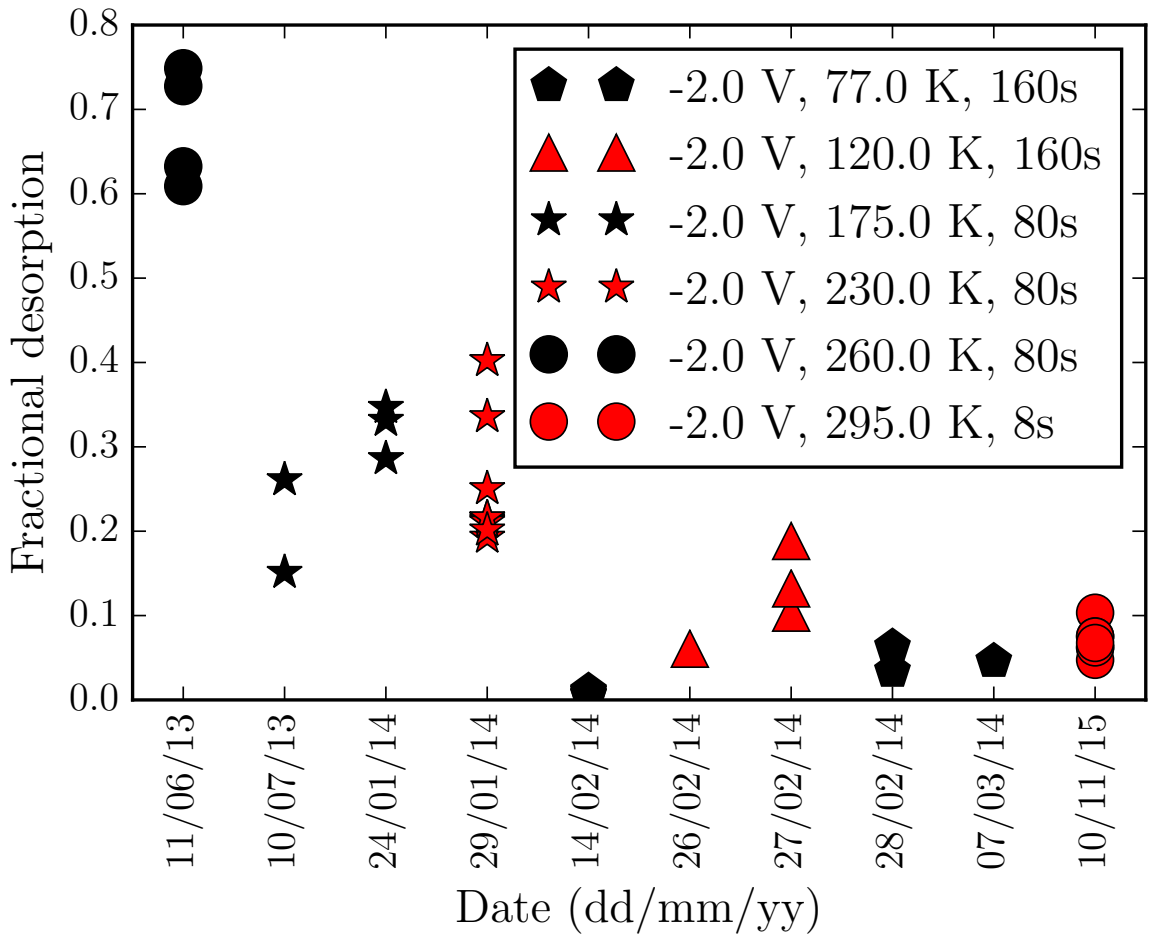

Figure 4.3: Variation in fractional desorption over all experiments. Fractional desorption was measured over a 20 nm circle centred on the injection location. The injections were all performed at the parameters given in the legend. It can be seen that the variation over short time scales is typically larger than that over long periods. Some datasets look like they may separate into subsets possibly representing different tip-states (for instance the 260 K dataset).

The experiments of this chapter were performed over the course of a year on a number of different samples with a number of different tips. Figure 4.3 shows the variation in desorption seen in individual non-local experiments over the full course of the experiments. The fractional desorption over a 20 nm circle centred on the injection location is used as a metric to look for any obvious systematic variation over the course of experiments. It can be seen that the variation in factional desorption within a day as a result of changes between tip-states is often equal to, or larger than, the variation over longer time periods.

One sequence of hole injections at 120 K was conducted on various days over the course of eight months [1]. This sequence was performed on several silicon samples, after multiple reconstruction procedures, with multiple tips and is shown in Figure 4.4. As such any systematic errors should be clear. It is found that the fractional desorption remains relatively constant over the long period, with larger variations occurring between experiments conducted over short periods. There are no obvious trends or shifts in the data. This suggests that the effect of tip-state is likely the dominant contribution to systematic variation in the experimental results, unfortunately this is also the least controllable aspect of the experiments. As there are no known significant effects of performing the experiments on different silicon samples with different tips, it is assumed that the various experiments are comparable to each other. It should be reiterated that the tip state can affect experiments in a significant way; however, this is independent of the macroscopic tip used, being purely related to the atomic states at the tip apex. The results in this chapter are derived from averages over all experiments performed with a certain parameter set. As such they average over experiments performed with a number of different tip-states, with the aim of removing systematic effects that are the result of different tip-states. It is desirable to perform experiments with a variety of tip states to ensure the measured phenomena is not just specific to a certain tip-state. The tip-state is highly subjective, and hence it was not attempted to divide experiments into sets by tip-state here, though some datasets shown in Figure 4.3 suggest possible subsets, such as the 260 K dataset, which divides into two.

One particularly unfortunate side effect of the unpredictable nature of the STM tip is that it is difficult to cross-link experiments. The large bias changes during injections increase the chances of tip change, which can lead to a loss of image quality and significant time being required to return the tip to a good imaging state. Repeating experiments is

[1] This sequence is not shown in Figure 4.3 as it was found necessary to perform longer injections to get good curves for fitting the radial behaviour (see later in the chapter); however, this sequence spans the longest time period, making it a good candidate for examining the effects of changes in the sample and tip.

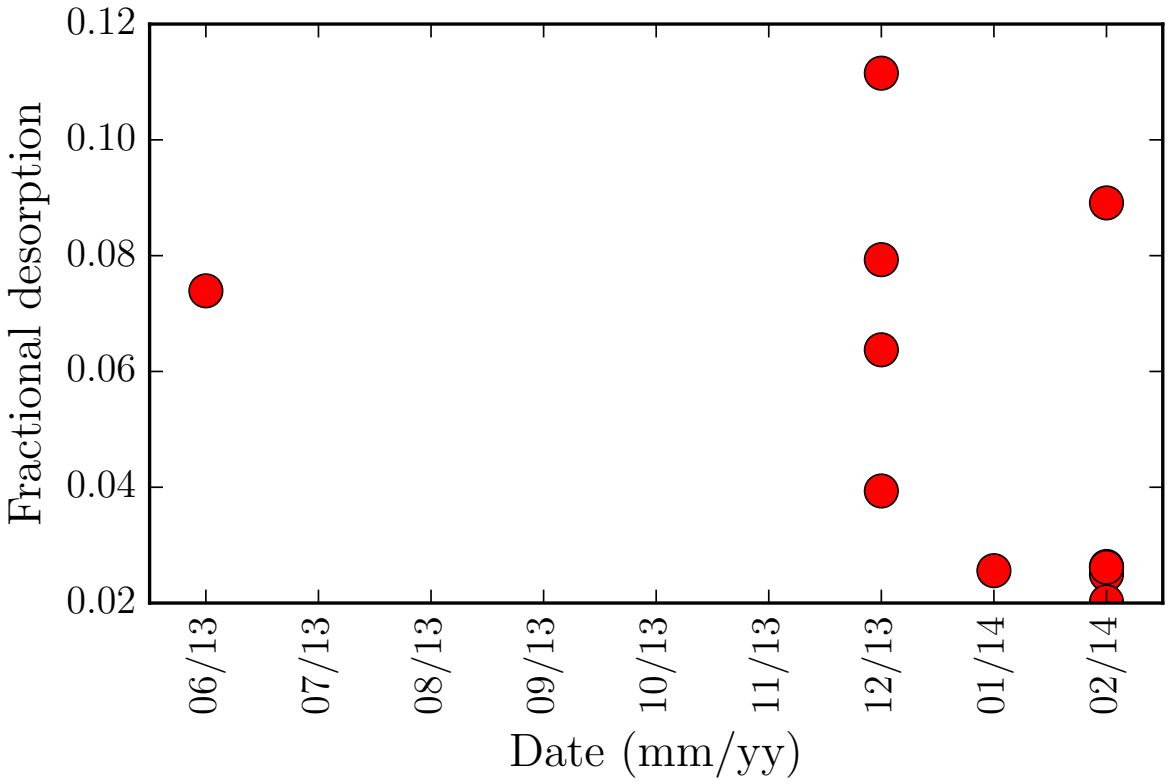

Figure 4.4: Variation in fractional desorption for a series of experiments performed at 120 K. Fractional desorption was measured over a 20 nm circle centred on the injection location. The injections were all performed at −2.0 V, 800 pA for 80 s. It can be seen that the variation over short time scales is typically larger than that over long periods. These experiments are not used in the remainder of the chapter as insufficient desorption was measured to fit good radial curves.

therefore difficult as it can significantly increase the amount of time required to perform the experiments. For example, to get the most direct comparison of the electron and hole-induced processes it would be desirable to repeat the previously performed electron-induced desorption experiments, performing hole injections followed by electron injections on the same sample one after the other in order to directly compare the two processes. However, this doubles the chances of changing the tip, and may prevent the acquisition of sufficient data for either charge carrier. This is particularly true when changing sample temperature as there are significant periods of time required to allow the STM to stabilise after temperature changes, so it is necessary to try and perform experiments as efficiently

as possible. With the implementation of the automated injection procedure described in Section 5.2.1 it is more feasible to perform experiments relying on more injections, which could improve the quality of the data gathered in future experiments.

4.3 Quantitative analysis methods

In order to quantitatively analyse the results of a non-local desorption experiment it is necessary to be able to compare a specific atomic site on an image before and after an injection experiment. STM images can be distorted by a number of processes such as thermal drift, piezo creep and hysteresis, so it is not as simple as just subtracting the two image intensities from one another pixel by pixel. In addition, when measuring the position of an atomic site relative to the tip, these image distortions can lead to inaccurate values for distances and angles. This necessitates an image processing scheme whereby each point on an image is mapped to an ideal silicon lattice site as indicated schematically in Figure 4.5. Any distances can then be computed from this lattice position, completely avoiding errors due to image distortion. Moreover, sites with the same label can be compared on multiple images.

Image analysis of past experiments was achieved by software provided by a group alumnus, Peter A Sloan. However, the site recognition of this software often failed when presented with strongly distorted images, which arise more frequently when altering the sample temperature significantly due to the greater thermal drift. In order to solve this problem I developed a more advanced algorithm which was more robust to image distortion. In addition it does not require guesses of the lattice vectors on a case-by-case basis (a requirement of the previous software), but only a global set of guesses, which need only be approximate. Both my algorithm and the previous one rely on feature recognition.

The older algorithm relies on searching for easily recognised corner hole features on the surface using cross-correlation based template matching to a library of corner hole templates. These sites are used to refine an initial guess of the surface lattice. As corner

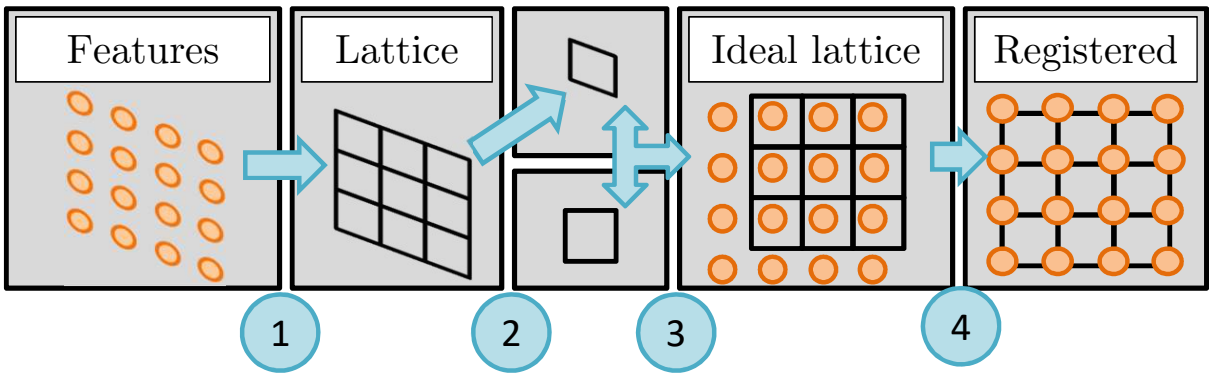

Figure 4.5: Schematic of the lattice recognition described in detail in the text. The box labelled 'features' shows a set of features on the surface arranged periodically, these might be corner holes of the silicon unit cell. In the next box, labelled 'lattice', a lattice determined by fourier methods is shown. This is used to deduce the unit cell in the top small box to the right, which is compared with the ideal unit cell below to generate an affine transform to the ideal lattice. Finally, this lattice is registered with the surface features. Each blue arrow is labelled underneath and referred to in the text.

holes can easily be distorted (for instance if one of the adatom sites appears dark as a result of a defect) not all corner holes will be found, so the lattice must be reconstructed from the arbitrarily spaced corner holes that are found. In the presence of molecules this problem is exacerbated. Because the grid is only fitted to a subset of corner holes, large distortions in the image are sometimes not accounted for properly leading to a mismatch between the identified lattice and the real lattice.

In my algorithm the auto-correlation of the image is used to deduce the lattice vectors of repeating structures in the image. These are used to transform the image to remove thermal drift, before repeating the lattice recognition process to extract the surface lattice. The surface lattice is transformed back to the original image coordinates, such that any measurements of the image intensity can be made on the initial image. Because the autocorrelation detects periodic features over the whole image, it is much less susceptible to errors from defects and molecules obscuring atoms allowing for a more robust lattice matching process. A further benefit of this method is that the substrate need not be silicon, with some small modifications any substrate with a periodic crystal structure

visible in the STM can be analysed in this manner[2]. Figure 4.5 shows a schematic of this process, details of the numbered steps are given below.

4.3.1 Template matching details

As the auto-correlation,and cross-correlation are used so often in this section a quick overview is given here. The cross-correlation of two functions is defined by

$$(f \star g)(x, y) = \int_{-\infty}^{+\infty} \int_{-\infty}^{+\infty} f^*(\mu, \nu) g(x + \mu, y + \nu) \mathrm{d}\mu \mathrm{d}\nu \tag{4.1}$$

which can be applied in a normalised form to discretized images as

$$(f \star g)[x, y] = \sum_{\mu} \sum_{\nu} \frac{(f[\mu, \nu] - \langle f \rangle)\,(g[x + \mu, y + \nu] - \langle g \rangle)}{\sigma_f \sigma_g} \tag{4.2}$$

where $\sigma_{f/g}$ is the standard deviation of the respective function, and angled brackets represent the mean of a function. The normalised cross-correlation gives a measure of the overlap of two images at a point x, y for different relative offsets μ, ν between them, peaks are located at offsets where the two images overlap the most. Algorithmically, cross-correlation can be implemented either by performing the sums numerically, or by exploiting fourier methods for better performance on larger images [188]. Normalisation is particularly important, as otherwise areas of high intensity on one image will also generate peaks in the cross-correlation. The analysis programs used in this thesis were written in both Python and Matlab. Efficient cross-correlation is implemented using either the function `match_template` from the scikit-image `feature` module for Python [189], or the function `xcorr2` from the image processing toolkit for Matlab [190].

The algorithm used for lattice recognition in this thesis, and the older algorithm described in 4.3 are both based on the idea of template matching, however the size of the template determines how robust the process is to defects and noise. A template of a single

[2]Though any substrate could be analysed, the correct surface lattice vectors must be known in order to give correct distance and angle measurements.

corner hole will give a very strong cross-correlation signal on a perfect corner hole, but is very sensitive to defects, such as a missing adatom from the corner hole. As a result the algorithm can only find with certainty those corner holes which are complete. Essentially, this template gives the most precise result, but is likely to fail to find a match. This leads to the lattice being deduced from strongly identified lattice sites which can be distributed quite unevenly over the surface. As the size of the template increases the correlation becomes more robust to errors from defects, essentially sampling many corner holes at once, so being less sensitive to each individual one; however, larger features are more likely to be distorted by piezo creep and drift, which can lead to mismatches between the template lattice and the image lattice, depending on where the template is being compared to the image. This can lead to small errors in lattice locations. So a larger template gives more consistent, if slightly less precise results. The upper limit to template size is to use a template which is the same size as the image itself, the auto-correlation of an image. As it is most robust to defects, the autocorrelation is used to get an estimate of the lattice vectors of the crystal in the image, in a similar manner to [191]. These lattice vectors together with the ideal surface lattice vectors can the be used to generate an affine transform that maps the measured lattice to an ideal lattice, removing most thermal drift from the image.

4.3.2 Affine transformations to remove thermal drift

An affine transformation maps a triangle into another triangle, combining rotation, scaling and skewing operations. It is most easily expressed using an augmented matrix:

$$\begin{pmatrix} x_2 \\ y_2 \\ 1 \end{pmatrix} = \begin{pmatrix} a & b & p_1 \\ c & d & p_2 \\ 0 & 0 & 1 \end{pmatrix} \begin{pmatrix} x_1 \\ y_1 \\ 1 \end{pmatrix}, \tag{4.3}$$

where x_i and y_i are sets of x, y coordinates in two images, the quantities a, b, c, and d are coefficients of a combined rotation and scaling matrix, and the p_i are x and y components of a translation vector. Affine transformations can be used to remove the effect of thermal drift in a manner similar to that described in [192]. Thermal drift typically results in constant velocity drift of the sample with respect to the tip, meaning that relative positions as measured on an image (ideal coordinates) differ from their relative positions in reality (sample coordinates). This leads to a map from ideal coordinates to sample coordinates given by

$$\begin{pmatrix} 1 + v_x/u_f & v_x/u_s & 0 \\ v_y/u_f & 1 + v_y/u_s & 0 \\ 0 & 0 & 1 \end{pmatrix}, \tag{4.4}$$

where $\vec{v}$ is the sample drift velocity, u_f is the fast scan speed, and u_s is the slow scan speed. Starting from the corner where scanning commences, x is measured along the fast scan direction, y along the slow. Subsequent images will also have a a translation vector $\vec{p} = \vec{v}t_{\text{scan}}$ added to the matrix, where t_{scan} is the time taken to complete a scan. For the lattice recognition algorithm the measured points on the surface lattice and their ideal positions suffice to solve for the six unknowns in a general affine transformation, and generate a map from the measured coordinates to the ideal surface lattice. Easy generation of affine transforms was provided by the `transform` module of scikit-image for Python.

4.3.3 Lattice alignment

Peaks in the autocorrelation only identify the surface lattice periodicity, not the location of specific points in the unit cell (template matching does identify specific points, but does not identify the periodicity). In order to get a reproducible reference the deduced lattice must by referred to a specific point in the unit cell. To do this a sample of the image, several unit cells in size, is taken around each lattice point found in the image. This

generates a correlation averaged image of the unit cell, which should strongly resemble the ideal silicon surface. The lowest point in the ideal unit cell is a corner hole, so measuring the distance between the lowest point and the centre of the correlation averaged image allows the lattice to be mapped onto a corner hole of each unit cell.

The affine transform removes most of the thermal drift, but additional distortions may still be present as a result of piezo creep and other non-linear processes. To account for these a second lattice recognition step is performed. In the second recognition step the lattice recognition procedure is performed on several smaller subsections of the image centred on lattice sites found in the first lattice recognition. In essence, this measures local distortions of the lattice on top of the global variation as a result of thermal drift. These sub images are overlapped slightly so that most points are found in multiple sub-images and their positions then averaged to provide a best estimate of the actual lattice locations. The result of this step is a lattice of corner hole locations over the entire image. A final alignment step takes this lattice row-by-row and shifts each row to maximise overlap with corner holes. The lattice sites are taken row-by-row as additional distortion on top of the thermal drift is greater between rows than within rows: this being a result of the greater time between rows given the slower scanning speed in this direction.

In order to ensure that the measured intensities of the locations are not affected by any interpolation processes, required in applying a transformation to an image, the deduced corner hole sites are then transformed back to the original image coordinate system to give the final set of corner hole coordinates. These coordinates can be used to measure properties of the image, but are all labelled in terms of the real lattice vectors. The final result is that each point in the image is directly referred to the tip location in the basis of the real world silicon lattice vectors, allowing for accurate distance measurement and site-by-site comparisons over multiple images. Adatom locations are then deduced by using the lattice coordinates given in [54] together with the lattice vectors measured in the above lattice recognition.

4.4 Non-local desorption from 77 K to 295 K

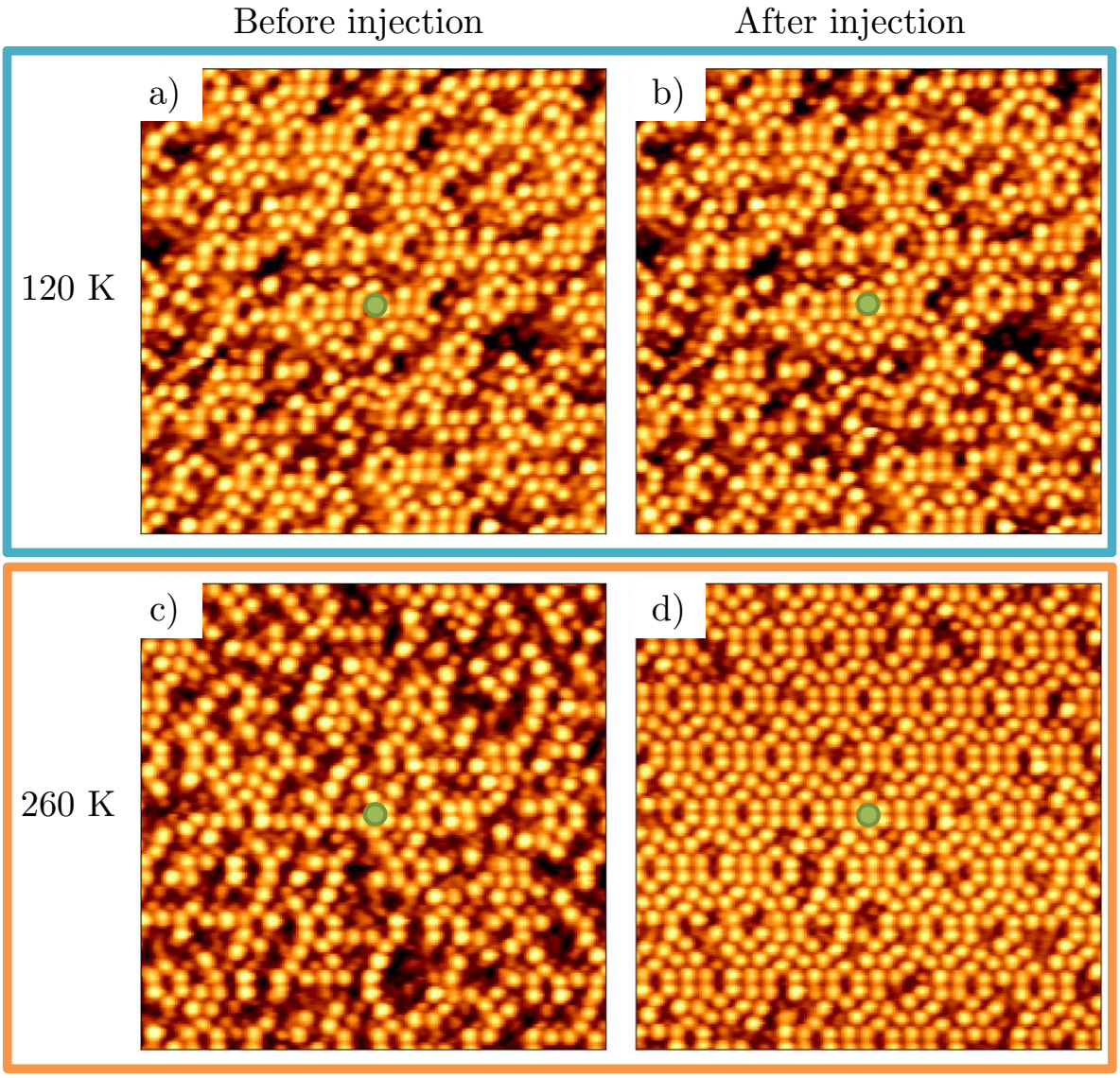

Figure 4.6: Two sets of before and after images showing the results of a non-local desorption experiment at 120 K and 260 K. Panels a) and b) in the blue box show the results of an injection at 120 K with parameters −2.0 V, 800 pA, 80 s. Panels c) and d) in the orange box show the results of an injection at 260 K with all other parameters the same. It is clear by eye that the desorption process is more efficient at the higher temperature. The images are 20 nm by 20 nm subsections taken from larger images, centred on the injection site (green spot), so that the behaviour is clearer to the eye.

Figure 4.6 shows an example of the experimental data that forms the basis of this chapter, clearly illustrating the increase in the number of desorbed molecules with tem-

perature. Qualitatively this is the same general trend as for electron injections. The quantitative analysis of this chapter will examine the two manipulation modes in order to determine whether there are any differences in the physics at play. In order to study the temperature dependence of the hole-induced process, a number of non-local experiments have been performed at several temperatures between 77 K and room temperature (77 K, 120 K, 175 K,230 K, 260 K, and 295 K) at −2.0 V bias and 800 pA setpoint current. The injection time was adjusted so that reasonable numbers of molecules would desorb: the default injection time was 80 s, reduced to 8 s at room temperature, and increased to 160 s for $T \leq 120$ K.

As mentioned above, Figure 4.6 shows the result of the same injection at 120 K (top two images) and 260 K (bottom two images). Both injections were performed with identical parameters (−2.0 V, 800 pA, 80 s), but the results of the injections are very different. In panel b) desorption is almost invisible to the naked eye, whereas in d) there is an obvious area of desorption. In order to quantify this change with temperature, the analysis program described in Section 4.3 is used to compare each atomic site before and after the injection.

4.4.1 Radial behaviour

To connect the changes in the number of adsorbed molecules to the properties of the molecule-surface complex a simple rate equation model is used in the manner of [36, 40, 42, 43]:

$$\frac{\mathrm{d}N(r,t)}{\mathrm{d}t} = -\sigma(r,t)N(r,t), \tag{4.5}$$

where $N(r,t)$ is the number of molecules at radius r and time t, σ represents the probability per unit time of a molecule desorbing as a result of an interaction with the injected electrons. This equation can be integrated to give

$$\frac{N(r,t_{\mathrm{inj}})}{N(r,0)} = \exp\left(-\int_0^{t_{\mathrm{inj}}} \sigma(r,t)\mathrm{d}t\right), \tag{4.6}$$

relating the experimentally measurable molecular populations to the desorption probability σ. The quantity σ can be further broken down into parts resulting from the transport and from the molecule:

$$\sigma = \sigma_{mol}(T, V) n_e(I, T, V, r, t)^g, \tag{4.7}$$

where σ_{mol} is a cross-section for desorption per unit time, and n_e is the number of electrons that reach a radius, r, per unit area. The index g represents the number of electrons required to trigger the process, and the arguments of the two functions show which parameters affect which component of the desorption probability, where V is injection bias, I setpoint current, and T sample temperature. The quantity g was found to be unity at room temperature for electron and hole-induced desorption, and is assumed to take the same value at low temperature. The cross-section is assumed to be independent of radius, with all the radial dependence of the desorption probability coming from the transport. In reality there is the possibility of small shifts in the capture cross-section as a function of radius as a result of the inhomogeneous electric field over the sample due to the tip. Resulting stark shifts in the molecular levels could affect the capture probability, this effect is assumed to be negligible.

The quantity $n_e(I, T, V, r, t)$ deserves further consideration. It represents all of the transport behaviour of the surface, hence the dependence on the various parameters. Some of the parameters enter trivially, others in a slightly more complex manner. The effect of variation in current is most easily understood. Because the currents used are so low, it can be assumed that there is a very low density of electrons in the sample (effectively only individual electrons at a time), therefore the main role played by the current is merely to define the number of electrons delivered according to I/e, where e is the electron charge. The bias voltage dependence arises because it determines which surface state the electrons tunnel into, giving rise to the voltage thresholds for non-local manipulation. Below the threshold no state is available to transport the electron to the molecule with sufficient energy to cause desorption, whereas above the threshold the

electron can travel through the surface to the molecule and potentially be captured. Bias plays a particularly important role for hole driven processes as there are a variety of filled surface states to tunnel into. The main effect of tunneling into different surface states is to alter the decay length of the process, though there are also more subtle effects such as variations in the suppressed region near the injection location with increasing energy above the bottom of the surface state band. In addition, the surface state the charge carrier is in also plays a role in the electron/hole capture at the molecule in a way that is not entirely understood, leading to variations in desorption probability with bias on top of the general thresholding behaviour. From the work discussed in Section 1.3 it is known that above threshold the electron transport consists of two parts, a short-lived ballistic transport phase near the tip [40], and a more long-lived diffusive transport regime, where the charge carriers undergo diffusive motion within the surface state [43]. This diffusive regime is responsible for the majority of the desorption events as the charge carriers spend a far longer time undergoing diffusive motion in the surface state. Charge carriers which scatter into the bulk leave the surface state and can no longer trigger desorption. This is represented by introducing a loss channel into the diffusion model. The resulting radial probability distribution for the charge carriers is described by a modified bessel-function of the second kind $K_0(r/\lambda)$. Combining all of these facts with Equation (4.6) gives the following (for $g = 1$):

$$\frac{N(r, t_{\text{inj}})}{N(r, 0)} = \exp\left(-A \cdot K_0(r/\lambda) \cdot \frac{I}{e} \cdot t_{\text{inj}}\right), \tag{4.8}$$

$$A(T, V) = \frac{s}{2\pi D(T, V)} \cdot \sigma_{\text{mol}}(T, V), \tag{4.9}$$

$$\lambda(T, V) = \sqrt{D(T, V)\tau_{\text{out}}(T, V)}, \tag{4.10}$$

where s is the fraction of charge carriers that enter the surface state from the tip (rather than directly entering the bulk), assumed to be one; D is the diffusion coefficient for the surface state, which obeys the usual Einstein relation $D = \tau_{\text{col}} k_{\text{B}} T/m^*$, and is a

function of the scattering time for the charge within the surface state τ_{col} (analogous to the relaxation time in bulk semiconductor physics); and τ_{out} is the lifetime of the charge carrier within the surface state. The combined quantity $AK_0(r/\lambda)$ is the probability per injected electron that a molecule desorbs at a radius r. The life time of the surface state and the scattering time for the carriers within it differ, though it was proposed in [43] that they are both a result of phonon scattering. To remove an electron from the surface state requires it to scatter out of the surface state, which presumably leads to more constraints on the energy and momentum change of the scattering carrier, and hence $\tau_{\text{out}} > \tau_{\text{col}}$. Thermal desorption, diffusion and defects all affect the accurate determination of molecular populations, as well as the counting of desorption events. This is discussed in the following paragraphs[3].

Diffusion events occur as a result of thermal [46, 49, 61] or electron-induced processes (found in the experiments of this work) over the full temperature range studied. Because diffusion can potentially occur between radial bins on the surface and alter the populations of bins in the absence of desorption, the raw molecular populations can sometimes lead to erroneous desorption counts, and are not used directly in Equation (4.8). Instead, changes in adatom intensity are classified into dark-to-bright (DB) and bright-to-dark (BD) events, corresponding to a molecule leaving from and arriving to an adatom site, respectively. When a molecule diffuses, a BD event should occur with a corresponding DB event nearby. By pairing BD events with nearby DB events this allows desorption and diffusion events to be separated and counted individually. The number of diffusion events is small compared to desorption so can be neglected here.

Defects present on the image, such as missing adatoms or boron-dopants, typically image as dark features and can not be distinguished from the molecules. To account for these defects, the number of molecules is assumed to be some fraction of the number of the dark features observed experimentally, $N(r,0) = \gamma N_D(r,0)$. The quantity γ is deduced

[3]Functional parameters are only written out explicitly when being varied from this point onwards for notational simplicity.

by studying defect populations measured over 43 scans of the clean surface on different samples at various times. These defect populations are compared with the measured number of dark features to determine how many dark features are molecules. There is also an additional statistical error taken into account for $N(r,0)$, as there is a variation in the number of defect features found on different areas of the surface. Experimental determination of the scaling factor and error is presented in the Appendix B. The scaling factor used here is $\gamma = 0.85$, with an associated statistical error of 0.02.

The above ideas can be incorporated into Equation (4.8) as follows:

$$\begin{aligned} N(r,t_{\text{inj}}) &= N_{\text{des}}(r,t_{\text{inj}}) + N(r,0), \\ N(r,0) &= \gamma N_{\text{D}}(r,0), \\ \Rightarrow D(r) \equiv \frac{N_{\text{des}}(r,t_{\text{inj}})}{\gamma N_D(r,0)} &= 1 - \exp\left(-A \cdot K_0(r/\lambda) \cdot \frac{I t_{\text{inj}}}{e}\right), \end{aligned} \tag{4.11}$$

where N_{des} is the number of desorption events (DB events with no neighbouring BD event) and $N_D(r,0)$ is the initial population of dark features observed experimentally. The quantity $D(r)$ is the fractional desorption as a function of radius from the injection site. Rephrasing the equation in terms of desorption events and the initial molecular population removes errors that arise as a result of processes like diffusion or adsorption of contaminants during the experiment, which both alter the populations of dark features in the annular bins in the absence of desorption.

Figure 4.7 shows three example plots of the radial variation in the fractional desorption $D(r)$ (defined in Equation (4.11) above). These are fitted to the model described in Equation (4.11) to obtain values for A and λ. The data is based on the aggregate desorption counts and molecular populations over several before-after image pairs, the errors are given by whichever is larger out of the statistical counting error, or the standard error on the mean deduced from the standard deviation of fractional desorption values measured over all images at a temperature. There are a number of experimental subtleties which need to be taken into account when fitting the above data: hot-carrier ballistic transport,

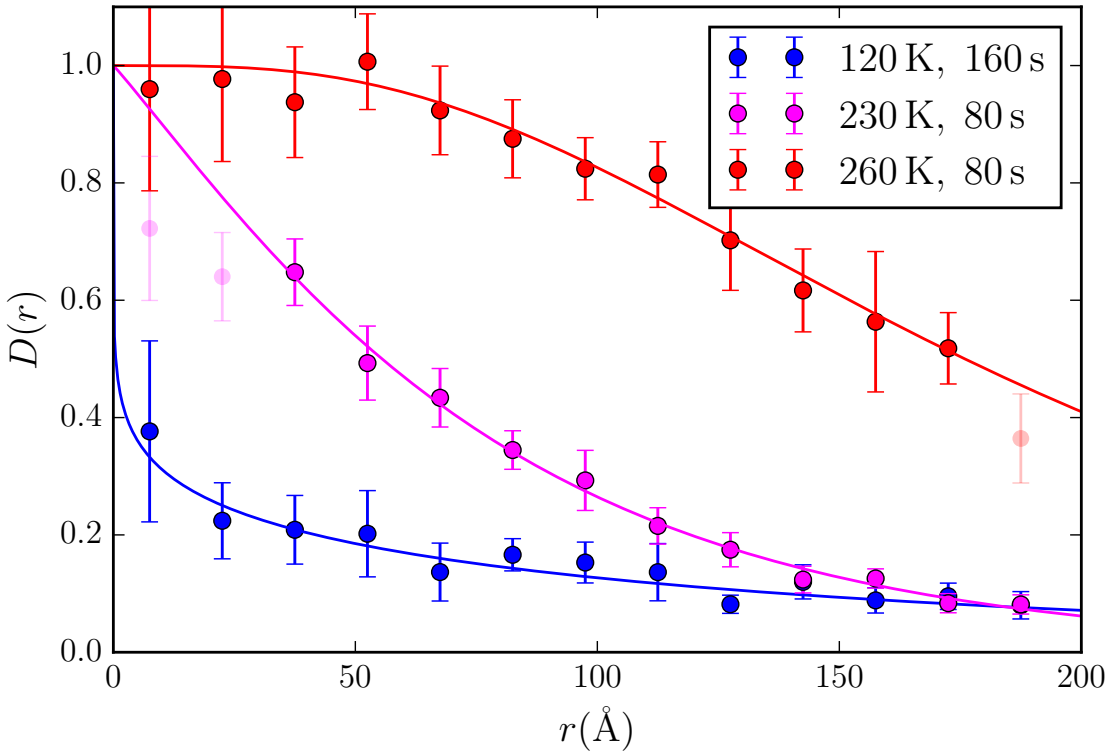

Figure 4.7: Comparing the radial distributions for injections of 2eV holes at three different temperatures. The injection parameters are identical (800pA,-2V) apart from the injection time and sample temperature (shown in legend). The solid lines are fits to the model given in Equation (4.8). For the 120 K data, $\lambda = (300 \pm 100)$ Å and $A = (1.3 \pm 0.4) \times 10^{-13}$. For the 230 K data, $\lambda = (80 \pm 7) \times 10^{1}$ Å and $A = (2.6 \pm 0.4) \times 10^{-12}$. For the 260 K data, $\lambda = (110 \pm 30)$ Å and $A = (9 \pm 4) \times 10^{-12}$. Transparent points are ignored in the fit for reasons discussed in the text. It should be noted that the fitted function always passes through one.

the maximum measurable area, surface defects, and thermal desorption.

The suppression region arising from ballistic transport, described in [40], gives reduced desorption near the origin. To account for this, the data is fitted multiple times gradually excluding points up to 50 Å from the origin. Data at high radii is not affected by the suppression, so fits that don't include the data near the origin give similar trends. As points near the origin are added to the fit it alters gradually, if the fit is depressed significantly near the origin then those points are excluded. It should be noted that the fitted function always passes through one on the ordinate axis. For example, in the 230 K curve in Figure 4.7 if the suppression region is not excluded the fit will typically

overshoot the data at larger radii, leading to worse overall fit. At most two points were excluded, which is in agreement with [40], where a maximum suppression region of 10 nm is measured at −2.0 V at room temperature.

Desorption events can be detected to the very corners of the image, but at these points most of the annular bin being studied will lie outside the image, increasing the errors in the measurement. Annuli where the number of initial molecules stop increasing with radius are ignored. Largely, the data in these regions follows the trend established at inner radii, but sometimes it begins to systematically overestimate desorption.

Finally, at room temperature significant amounts of thermal desorption can occur [46, 49], leading to a constant background desorption probability. The measured population in the first image will have decreased by the time the injection is carried out meaning the measured $N(r, 0)$ will overestimate the actual populations at the time of the experiment. Similarly, the final measured population is reduced compared to that after the injection This is taken into account by using arrhenius expressions studied in [46] to correct the populations for the changes that take place during the entire experimental procedure, again details are left to the Appendix B. The effect is only really significant at room temperature and above, as the thermal desorption is suppressed very rapidly with reduction of the sample temperature.

The decay lengths extracted from the fits are presented in Figure 4.8. The graph shows $\Lambda \equiv \lambda^2/T$, this is proportional to $\tau_{\mathrm{col}}\tau_{\mathrm{out}}$, as can be seen from Equation (4.10), together with the discussion below. The quantity Λ essentially indicates the strength of the scattering processes responsible for both diffusion within the surface state, and scattering out of it. For electrons it can be seen that the quantity $\sqrt{\tau_{\mathrm{col}}\tau_{\mathrm{out}}}$ varies little with temperature, whereas for holes it appears to increase with decreasing temperature. The behaviour seen for holes might be expected for phonon scattering, where the scattering time would decrease as the temperature increased due to the increasing populations of phonons. Though interesting, this behaviour will not be studied in detail in this chapter for several reasons. Firstly, the decay length for holes has been found to be a sensitive

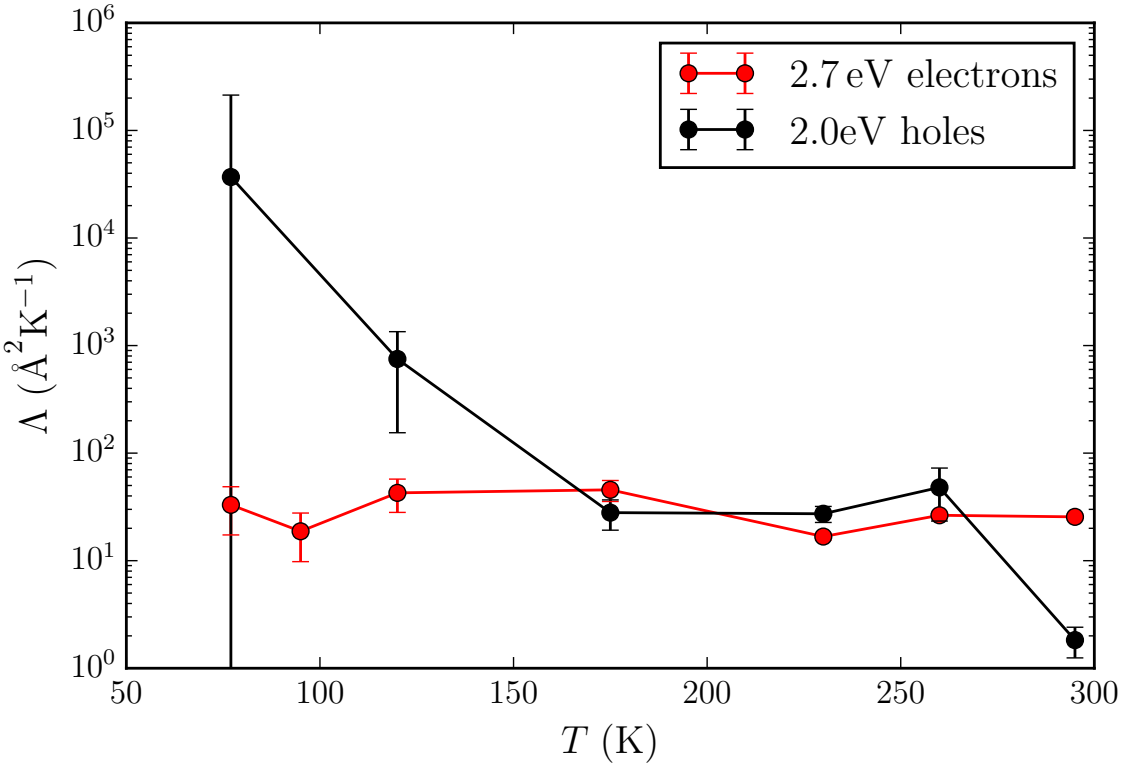

Figure 4.8: Variation of the parameter $\Lambda \equiv \lambda^2/T$ with temperature. This shows that for holes the product $\tau_{\text{col}}\tau_{\text{out}}$ grows with decreasing temperature as would be expected of phonon scattering. For electrons the scattering seems to be almost constant, with perhaps a slight increase with decreasing temperature. Electron data recorded by Tianluo Pan and published in [42], re-analysed by myself as described in the text.

function of both injection and manipulation site, so it is necessary to inject into an adatom site such that the surface state being populated is well-defined [40], otherwise there is potential to be measuring different decay lengths from several surface states. Secondly, the errors in the decay length at low T are quite large as the small amount of desorption makes extracting an accurate decay length particularly difficult. This could be solved by using a higher injection bias than that used here to cause more desorption. Finally, without some extra insight into the lifetimes for both surface states at these temperatures it isn't possible to separate the surface state lifetime and the scattering time within the surface states, so it is difficult to determine further details of the physics.

4.4.2 Temperature dependence

Temperature dependence enters into the above arguments in two main ways, by altering the transport properties of the surface, and by altering the molecular cross-sections to desorption. As the temperature changes, the scattering probabilities for carriers in the surface state change also, which causes the decay length to vary with temperature by altering both the diffusion coefficient and lifetime of the surface state. Changes in the molecular cross-section could be a result of an alteration of the probability of the molecule capturing the charge carrier with temperature, or a result of an alteration in the probability of desorption following charge capture, for instance as a result of increased molecular lifetime. In order to extract properties of the molecule correctly it is necessary to remove as much as possible of the transport process' temperature dependence. The previous results in [42] use the integrated populations of large annuli near the centre of the image to detect the variation in reaction probability. This can convolute the temperature dependence of the transport into the molecular cross-section. The results of [43] show that the decay length of the process varies significantly with temperature, decreasing as the temperature is decreased. As a result, the integral method overestimates the decrease in desorption probability with temperature, adding the effects of thermal variation in molecular cross sections to the effects of a reduction in the number of electrons incident on an annulus distant from the tip as temperature increases. Further to this, there is no guarantee that the dependence of the transport on temperature is the same for electrons and holes, so including it could lead to errors when comparing desorption induced by the two carriers.

To avoid the above problem, the method used in the analysis of this section is to look at the variation of A extracted by fitting the radial dependences shown in the previous subsection (Section 4.4.1). This method removes the influence of the variation in the radial decay of the transport process with temperature. Given the Arrhenius type behaviours exhibited in [42, 46], and the similar rapid increase in desorption probability

with temperature seen in the hole-induced processes shown in Figure 4.6, the molecular cross-section is assumed to have an exponential temperature dependence. This gives σ, from Equation (4.8), of the form

$$\sigma_{\text{mol}} = B_{\text{mol}} \exp\left(\frac{-E_a}{k_B T}\right), \tag{4.12}$$

where E_a is an activation energy derived from the mechanism providing the thermal enhancement to the desorption, and B_{mol} is a constant. Substituting this σ_{mol} into Equation (4.9) implies A is of the form

$$A = \frac{s}{2\pi D} \cdot B_{\text{mol}} \exp\left(\frac{-E_a}{k_B T}\right). \tag{4.13}$$

All of the terms in the prefactor are assumed temperature independent for the remainder of the analysis. This is not strictly correct for D, which has a weak dependence on temperature. From the discussion following Equation (4.8) we recall that $D = \tau_{\text{col}} k_{\text{B}} T/m^*$. The temperature dependence of τ_{col} for the hot electron in our surface state is unknown but in the semiconductor bulk it typically varies in a polynomial fashion with temperature. For instance, scattering from phonons usually leads to $\tau_{\text{col}} \propto T^{-\frac{2}{3}}$ [193], which would give $D \propto T^{-\frac{1}{2}}$. Using this relationship in the fits performed below leads to only small changes in the low temperature activation energies. Scattering from phonons is typically the dominant scattering mechanism at these temperatures, but if a similar relationship for impurity scattering is used the effect is also not significant. For the remainder of the discussion the exponential term is assumed to dominate over the polynomial temperature dependence of the diffusion coefficient, and the additional temperature dependence of D is ignored.

Figure 4.9 shows the variation in the quantity A with temperature for both electrons and holes, fitted to the sum of two Arrhenius expressions of the type given in Equation (4.13). The electron data used is the same raw data as that used in [42], but here the

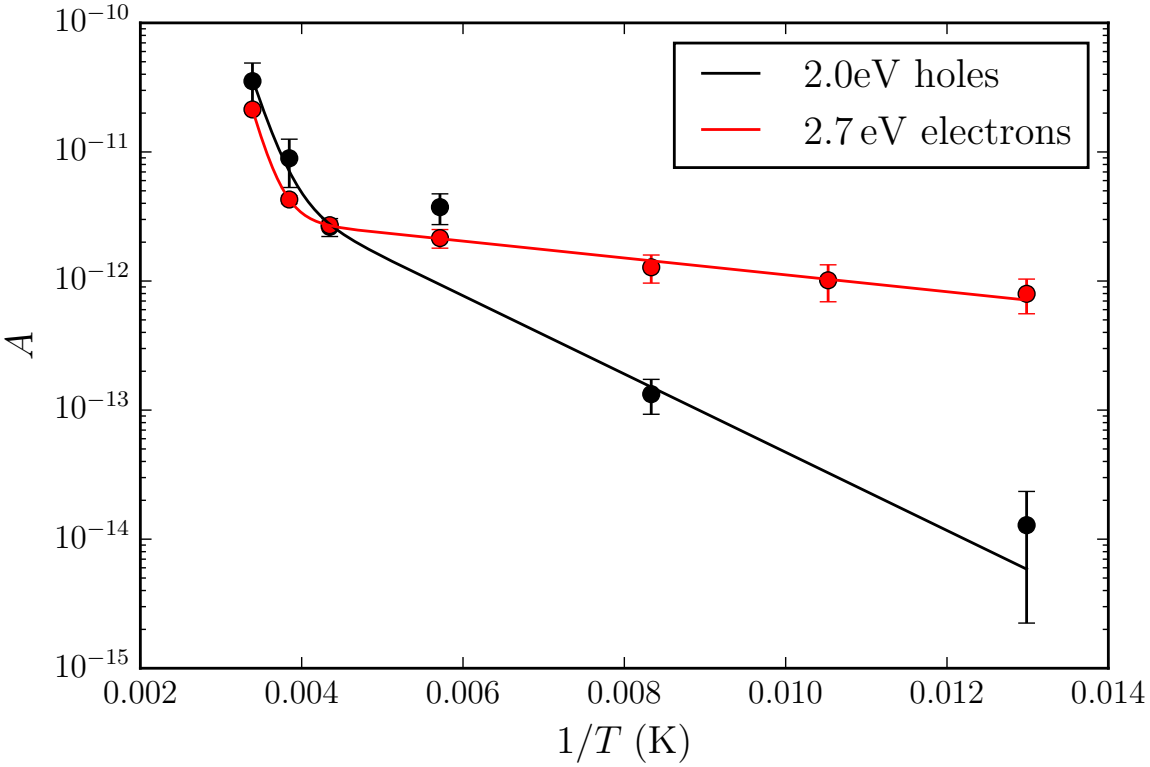

Figure 4.9: Temperature dependence of A from Equation (4.6) for electrons and holes. The leftmost three points are used to fit the higher temperature activation, and the rightmost four to fit the low temperature activation. The third point from the left is used in both fits, and the high temperature fit subtracted from the full range before fitting the low temperature regime. Electron data recorded by Tianluo Pan and published in [42], re-analysed by myself as described in the text.

radial dependence, thermal desorption, and defects are fully accounted for. The second point from the right and the second point from the left, at 95 K and 260 K respectively, were recorded significantly after the rest of the electron data set, and hence provide a consistency check indicating the results do not vary over time in an unpredictable manner. Both curves appear to be combinations of two exponentially activated processes, so a sum of two exponential functions is fitted over the full range of temperatures. The overall behaviour is qualitatively similar, with a term with a large activation energy that dominates at high temperature, and one with a small activation energy that dominates in the low temperature regime. The activation energies found in this analysis for electron-induced desorption are (13 ± 3) meV and (47 ± 50) meV. For hole-induced desorption the

values are (60 ± 10) meV and (400 ± 300) meV.

In [42] it was reported that the desorption probability was enhanced thermally by two different processes. At higher temperatures, the desorption enhancement was dominated by a process which showed a thermal activation energy of (450 ± 170) meV. At low temperatures, the desorption was still found to be thermally activated, but with a much smaller activation energy of (21 ± 4) meV. The high temperature regime was associated with the transfer of the molecule to the physisorbed state followed by thermal desorption, the activation energy closely matching the barrier between physisorbed state and gas phase quoted in a previous paper [46] for chlorobenzene on Si(111) − 7×7. The low temperature regime was tentatively proposed to be related to excitations of surface phonons assisting in the desorption. These values are similar to, but still slightly different from the values deduced for the electron-induced process in the new analysis presented here.

The first result of this new analysis combined with the new hole-induced desorption data is that at room temperature the desorption mechanism is similar for both charge carriers. For both carriers desorption appears to occur via the physisorbed state. The barrier from physisorbed to chemisorbed state was measured for benzene in [69] to be (0.30 ± 0.03) eV. Recently, the difference between the barrier from chemisorbed to physisorbed state, and the barrier from chemisorbed state to vacuum has been measured to be (0.19 ± 0.05) eV in [61]. This is the same as the difference between the barrier from physisorbed to chemisorbed state, and the barrier from physisorbed state to vacuum. This suggests a total barrier to gas phase of $\sim$0.49 eV, if the physisorbed state of chlorobenzene has a similar physisorbed well depth. The bonding of chlorobenzene and benzene are very similar [58, 194], with chemisorption taking place in a similar geometry, and both molecules having a physisorbed state that is stable at low temperatures [69, 195]. Binding of chlorobenzene is typically slightly stronger as evidenced in the higher thermal desorption peaks in TPD [58, 194]. This is supported by recent DFT simulations with corrections for Van-der-Waals forces, which suggest that the physisorbed state has a binding energy of 0.6 eV. So it may be that the physisorbed well depth is slightly deeper

than ∼0.49 eV, but it still remains as the most likely candidate for the high temperature activation energies measured here. The similar results for both hole- and electron-induced desorption suggest that both molecules also desorb on the same path, via the physisorbed state. This similarity may rule out desorption in the ionic form, as the anion and cation would likely experience different interactions with the surface, subsequently affecting the attraction between substrate and physisorbed molecule.

The new low temperature analysis of the electrons gives a similar activation energy to that previously attained, but rules out the transport as a potential mechanism for the low temperature activation. In the previous results, which did not account for variation of the decay length of the transport process with temperature, it was possible that the desorption probability could appear to increase as the range of the transport increased, as more molecules would be affected for the same electron dose without any alteration of the molecular cross section. This increase could have been misinterpreted as a small variation of the molecular cross-section with temperature. Removal of the transport related thermal variation is likely the reason for the reduction of the activation energy for electron-induced desorption. However, a small thermal activation still remains, suggesting that some thermally activated process still affects the desorption process in addition to any effects of the transport phenomena.

The low temperature activation energy does appear to differ between the electron- and hole-induced process. In both cases the order of magnitude of the activation energy suggests vibrational modes of the molecule-substrate complex. For the surface, these would be phonons; for the molecule, low energy vibrational modes. For a vibrational mode to play a role in the desorption process it would be one that affects the molecule substrate bond, suggesting modes which results in motion of the adatom, or alteration of the Si-C bond between the molecule and substrate as possible candidates.

In the gas phase, vibrational modes can play a role in dissociative processes, so it might be expected that similar mechanisms may play a role in surface bond cleavage. A specific example would be dissociative electron attachment to chlorobenzene, where the

dissociation takes place in σ^* states associated with the chlorine atom, but the capture of the electron occurs in π^* states which lie lower in energy. To couple these two states of different symmetry, a vibrational mechanism or distortion of the anion is necessary [196]. More relevant to the experiments here is the observation of Arrhenius type expressions for dissociative electron attachment to a wide variety of molecules in the gas phase. This paper by Fabrikant and Hotop [197] summarises a number of mechanisms that can lead to barriers in DEA, and considers the validity of the application of Arrhenius type expressions to dissociation rates; finding that they are typically applicable over a range of temperatures, which depend on the dissociation mechanisms, but that they underestimate the theoretical energy barriers. The processes are typically thermally activated either as a result of requiring a certain vibrational excitation of the neutral molecule in order to efficiently capture electrons and form the anion state in which dissociation occurs, or as a result of a barrier to dissociation once in the anion state.

There are also a number of theoretical studies investigating the effect of vibrational pre-excitation via laser irradiation on photodesorption that suggest vibrational excitation of the substrate-adsorbate bond could increase desorption yields [198]. In these models it is proposed that an IR laser is used to pre-excite the adsorbate substrate bond, a second UV laser pulse is used to electronically excite the adsorbate. In a semi-classical model, enhanced desorption can be understood to take place as a result if the electronic excitation from the vibrationally excited ground state places the excited state wavepacket on an area of the excited state PES that is very steep. If, when the wave-packet decays it has generated significant kinetic energy, it can then desorb on the ground-state PES. These models have been applied to Cs on Cu(111) [199], and to H_2 on Ru(1000) [198]. The degree of control over the vibrational and electronic excitation is very high in the theoretical studies so they are not directly comparable to the system studied here, but it does show that such mechanisms are in theory possible.

A number of surface phonons can be associated with the $Si(111)-7\times7$ reconstruction. These exist in addition to the usual bulk phonons of silicon, and arise as a result of

the differing bonding geometries at the surface. Typically, the higher frequency modes can be associated with features of the reconstruction, whereas lower frequency modes are associated with movement of large areas of the reconstructed unit cell [200–202]. The observed excitation energy for the electronic process of (13 ± 3) meV is too low to be a molecular vibrational mode (see below), so if it is related to any vibrational feature it must be a surface phonon. Even so, most of the surface phonon features seen in EELS [203], HAS [202] and theoretical calculations [200, 201] lie above this in energy, leaving only a small set of options. The lowest resolved peak in EELS lies at 40meV, so is not a viable candidate. HAS resolves peaks at 10meV and 15meV, the first is a comparatively long wavelength surface oscillation involving many atoms (surface Rayleigh wave), the latter is associated with adatoms of the unit cell. This assignation is corroborated by the theoretical results of Štich [201], who attribute this higher frequency mode to an energetic adatom wagging motion. This would seem to be a reasonable candidate to assist the desorption process, as it has some component along the molecule substrate bond. In addition, the observed electron-induced adatom hopping seems to suggest that electronic excitation and adatom movement are connected in some way. It may be possible that prior thermal excitation of this vibrational mode facilitates desorption when an electron arrives at the site.

Support for the role of an adatom in the desorption process comes from a recent paper by Rusimova and Sloan [204] implicating the adatom in the manipulation process. In this paper it is found that local injection can induce desorption either through direct capture of the electron to the molecule, or through injection into the adatom followed by desorption by excitation of the adatom. The experimental signal for this was two different rates for desorption, depending on whether the injection was directly into the molecule or into the adatom. These were a fast rate for direct injection into the molecule, and a slow rate for injection into the adatom. The second rate directly matched that for adatom hopping in the absence of a molecule, a process whereby the adatom hops out of the surface due to an electronic excitation (see Section 1.3.1 for an earlier example). It was suggested that

the adatom plays a crucial role in the non-local process.

Molecular vibrations of chlorobenzene on Si(111) $-$ 7×7 have been observed using EELS [58]. The lowest three modes for chemisorbed chlorobenzene are 39 meV, 61 meV and 72 meV rounded to the nearest meV. These correspond to a ring deform mode, the C-Cl wag mode, and the C-Si stretch mode. Of these, the C-Cl wag best matches the smaller activation energy for the hole-induced process, but the C-Si stretch would seem more related to the desorption process. Though a theoretical study of benzene desorption from Si(100) found that ring deformation played an important role in desorption from that surface, so it may be that the prior vibrational excitation of the ring bending mode can facilitate different dynamics on the excited state PES. At the resolution of our experiment it is not possible to distinguish which molecular mode plays the main role. In addition, further silicon-surface phonons exist in this higher energy regime, the closest being at 66meV. For the hole-induced process molecular modes appear to be more relevant, as the only phonon mode in the energy range is suggested to have a weak effect on the adatoms [201], so it is difficult to see why it would play a role in the desorption process.

Support for the possibility of two different desorption mechanisms comes from a theory collaboration [205], whose work suggests that the adatom plays an important role in electron stimulated desorption, but not hole stimulated desorption. This matches the above results remarkably well.

One other possibility for the larger activation energy for hole-induced desorption is a shift in the energetic position of surface states with temperature. There are reports that features in the surface electronic structure are observed to have higher energies in low temperature STS than would be expected from room temperature measurements [206–208]. This would imply that for a non-local process the injection would actually provide charge carriers at lower energy than expected given the bias, a shift of $\sim$0.5 eV between room temperature and 77 K. This effect was found at the bias corresponding to the majority carriers on n-type, P-doped silicon [208], with a smaller shift occurring for the bias corresponding to the minority carriers ($\sim$0.2 eV between room temperature and 77 K).

The authors proposed non-equilibrium charging of the surface states as a mechanism. However, there is also the possibility these shifts result from the finite resistance of the sample [209]. Unfortunately the data for p-type silicon is less conclusive [210]. Shifts in carrier energy are important, as lower energy carriers have a lower probability of causing desorption, meaning that these shifts would lead to a suppression of desorption at low temperature, and give an increase in the probability of desorption with temperature. It is not believed that this is the reason for the observed energy barrier in this chapter, because if the injected energy was smaller than the applied bias by an amount significant enough to reduce the desorption probability significantly, it should also reduce the decay length of the non-local process [40]. If the shift is small, it should only reduce the desorption probability slightly, and may not have a significant effect. The decay length is not seen to decrease in the above experiments suggesting that the injection bias is not reduced significantly. The only way to unambiguously confirm this would be to record STS spectra at each temperature on the *p*-doped sample studied here, and determine whether or not the injected carrier energy differs from what is expected.

4.5 Summary and outlook

In summary, non-local desorption of chlorobenzene from the Si(111) − 7×7 surface by hole injection has been studied at a variety of temperatures between 77 K and 295 K. These results were compared to a re-analysis of electron-induced desorption over the same temperature range. It was found that in both cases the physisorbed molecular state plays a key role in desorption at room temperature. This is apparent as an Arrhenius behaviour of the desorption probability with activation energy of (470 ± 50) meV for electrons and (400 ± 300) meV for holes, both of which compare well to the established value of 0.5eV. At low temperatures the process is still temperature dependent but with much smaller activation energies: (13 ± 3) meV for electrons and (60 ± 10) meV for holes. The new analysis method rules out convolution of the temperature dependence of surface carrier

transport into the desorption data as a mechanism. It is suggested that the low temperature activation is a result of vibrational excitation in the molecule-substrate complex increasing either the probability of electron-capture or of subsequent desorption. It is not known at present what the mechanism for this vibrational enhancement is, but effects which are similar in principle occur in gas-phase systems, and also on surfaces. These non-local effects may play an important role in electron-irradiation of surfaces more generally.

4.5.1 Future work

A number of areas of the Si(111) − 7×7: PhCl study could be improved upon or explored further. The new automated experimental methods described in Section 5.2.1 permit more efficient experiments. This enhanced efficiency would allow for a better designed experiment where electron- and hole-induced desorption experiments are alternated to ensure any impact from different samples or molecular coverages is minimised. Redoing the electron-induced experiments in this manner was infeasible using the manual methods of this chapter due to the amounts of time required. In addition, it would be possible to perform enough experiments to study desorption from specific adatom sites, rather than averaging over all adatom sites. STS measurements across the full temperature range could ensure that the injection energy is as expected, and that no band-bending effects are present.

Altering the molecule adsorbed may provide further insights, for instance a similar study with benzene, or another benzene based molecule with a different functional group, could look for an effect on the hole-induced activation energy, which might be expected if the barrier is related to a molecular vibrational mode. The molecule chosen would have to have sufficiently different mass that the vibrational modes were substantially different. Further theoretical input may help to explain differences in the thermal activation energy, or shed further light on the role of adatoms in the desorption process. Finally, a laser-

assisted STM manipulation process could be envisaged, where IR excitation is used to try and pre-excite vibrational modes at the measured energies, as suggested in [198, 199]. The effect on the non-local process could then be analysed. It may be that the atomic scale insights from such an experiment could contribute to further development of the field of photo-controlled chemistry, which has so far been difficult to realise experimentally.

CHAPTER 5

Non-local Manipulation of Chlorobenzene on Si(111) – 7 × 7: Non-Local Manipulation of the Physisorbed State

5.1 Motivation

Previous results on concerted thermal and electron-induced non-local desorption [42], and bond selective dissociation by thermally assisted electron attachment [46], together with the results of the previous chapter, all show the dramatic effects of temperature on non-local manipulation with the STM. This chapter explores the application of these ideas to open up a new manipulation channel in our Si(111) − 7×7: PhCl model system.

At room temperature, dissociation is primarily a two electron process, thought to proceed through the physisorbed state. This requires that a second electron is incident on the molecule after its promotion to the physisorbed state, but before it desorbs thermally [45, 46]. In the non-local geometry, the probability of a molecule interacting with two electrons is far lower than that for interaction with a single electron. A one-electron process is thus much more efficient than a two-electron one, which favours non-local desorption over dissociation at room temperature.

At higher temperature dissociation becomes a one-electron process. Molecules thermally excited to the physisorbed state can dissociate as a result of an interaction with a single electron. Potentially, this would allow for non-local dissociation at elevated temperature. However, at elevated temperature thermal desorption is constantly reducing the molecular populations, and the dissociative process is always in competition with desorption.

For chlorobenzene on Si(111) − 7 × 7 there is a barrier between physisorbed and chemisorbed state. At low temperatures, molecules in the physisorbed state do not have enough thermal energy to overcome this barrier and chemisorb, leading to a stable physisorbed species. This state has been investigated for chlorobenzene [195] (and the similar molecules benzene [69] and toluene [195]) on the silicon surface previously, and has been found to be stable at liquid nitrogen temperatures and slightly above (60K-110K). The physisorbed molecules can be produced by depositing molecules at low temperatures,

where a thermal transition to the chemisorbed state is not possible. The vanishingly small probability of thermal desorption at these low temperatures favours one-electron dissociation, and may allow for non-local dissociation.

This chapter exhibits the realisation of the scheme described above on Si(111) − 7×7 at 4.6 K, constituting the first use of temperature to open a new molecular manipulation channel, and not just to control an already existing one. First, the imaging characteristics of the system are described, followed by the methods for extracting quantitative information. A number of non-local processes are found, and their likely origins discussed. A promising candidate for a dissociation product is found, and its spatial distribution relative to the parent molecule is examined in detail to compare with room temperature dissociation experiments. Finally, suggestions are made for future experiments.

5.2 Imaging characteristics at 4.6 K

Initial experiments were conducted at 77 K motivated by the experiments of Lu et al. [195]. At 77 K, low diffusion barriers between the atomic sites mean that the molecules are free to move over the surface at low coverage. The molecules are more likely to be located over certain atomic sites as a result of variations in surface-molecule interaction over the unit cell. In STM images this shows up as a characteristic pattern. However, because the molecules do not remain localised above specific adatom sites for a long period of time detection and characterisation of a non-local process is difficult. In order to reduce the ease of diffusive motion over the surface, the system temperature was reduced to 4.6 K, at which temperature the motion of the molecules is greatly suppressed.

The imaging process at 4.6 K is similar to that at 77 K with a few minor differences. To image the system in STM at 4.6 K requires sufficient bulk-carriers to propagate a current through the sample. When there is insufficient thermal energy to excite significant numbers of carriers from the dopant bands to the bulk bands, freeze-out of free carriers will occur. To avoid this situation, a highly doped boron sample is used, providing sufficient

conductivity for imaging even at 4.6 K. Another complication is that piezo sensitivity is greatly reduced, meaning that the maximum achievable scan range is much smaller.

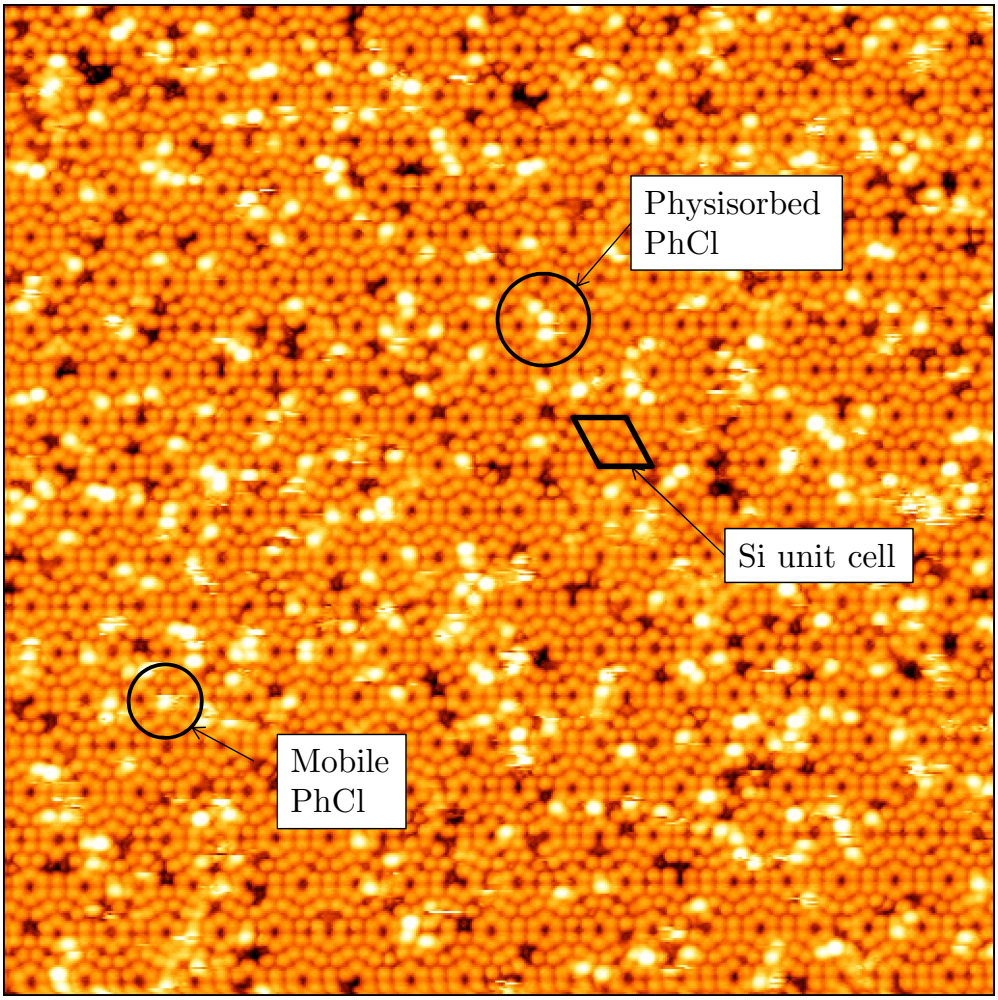

Figure 5.1: An image of the Si(111) − 7×7 surface decorated with physisorbed chlorobenzene molecules. The molecules are the bright features, three are highlighted by a circle. The adatoms appear in the characteristic 7×7 pattern at intermediate brightness, a unit cell is highlighted. A mobile molecule is highlighted, distinguishable by streaking. The dark features are defects. The image was recorded at 1V, 10pA. The image dimensions are 51.2 nm by 51.2 nm.

The physisorbed chlorobenzene molecules are shown Si(111) − 7×7 in Figure 5.1. A current of 10 pA was used to record the image at a bias of 1 V, with the intention of minimising tip-molecule interactions by maximising tip-sample separation. It was found whilst scanning that higher voltages seemed to cause more molecular motion, despite the increased tip-sample separation. This could be a result of stronger interactions between

the higher field of the tip and the polar chlorobenzene molecules. As usual the silicon adatoms are visible as bright features in the characteristic 7×7 pattern. In addition, a number of brighter features are visible. These brighter features result from the physisorbed chlorobenzene molecules deposited at 4.6 K. In contrast to experiments at 77 K, at 4.6 K molecules remain localised during imaging. Some streaking of molecular features is visible, which implies motion under the tip whilst scanning that area. In addition, molecular motion is also evident between images. These diffusion events are likely induced by the tip, given the low probability of thermal events at this temperature. Quantitative analysis of these images required several modifications to the analysis scheme described in Section 4.3. These are described below. In addition, a new automated experimental procedure was employed to enhance the reproducibility of the experiments.

5.2.1 Experimental and analytical methods

To conduct the experiments at 4.6 K a new automated non-local manipulation process was implemented in a similar manner to those used in [40, 43]. The ideas used are similar to those used in the manual experiments of 4. Two modification are taken from the methods of [40, 43]. Firstly the tip is retracted whilst parameters are changed, avoiding current spikes, and secondly a specific number of electrons is delivered, rather than applying a certain setpoint for a certain time. Both of these are described in more detail below. The implementation used is all developed by myself, and relies on my image analysis algorithms to control tip positioning.

LabView is used to control the Nanonis hardware which in turn controls the STM. Firstly, a before image is recorded with dimensions 51.2 nm by 51.2 nm. This is followed by a sequence of smaller images over the centre corner hole of the image. Correlation based pattern matching is used to ensure that the small images are centred on the desired corner hole, correcting for piezo creep as a result of the large changes in tip position. After these a further small image is recorded. This image pauses half-way through with the tip over

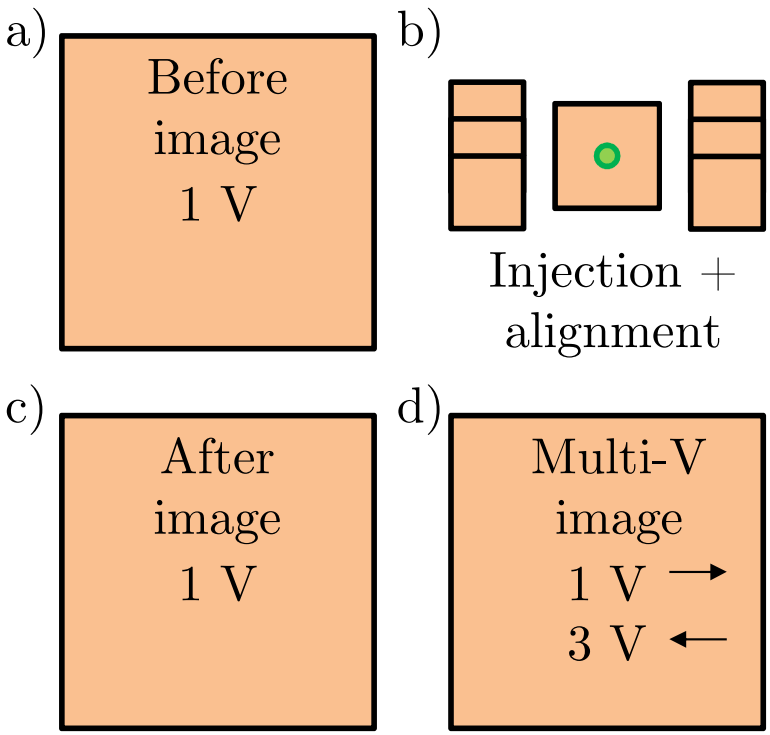

Figure 5.2: A schematic of a full injection experiment. Panel a) is the before image, recorded at 1 V. Panel b) shows the multiple small images used to correct the tip location for drift and other distortions, before and after the injection. The injection is performed halfway through an image as described in the text, its location is indicated with a green dot. Panel c) is the after image with the same dimensions as the before image, recorded at 1 V. Panel d) is the multi-V image, which is recorded at 1 V in the forward scan direction, and 3 V in the backward scan direction. All images are recorded at 10 pA setpoint current.

a corner hole, at which point an injection is performed. For the injection, the tip is first retracted ∼10 nm from the surface (where the current is essentially 0) to set the injection parameters, before re-approaching and performing the injection with the feedback on until a set electron dose is delivered. Retracting the tip prevents current spikes that occur after a large change in bias due to the imperfect feedback response. The electron dose is derived by integrating the actual delivered current over the experiment, which usually fluctuates slightly about the setpoint current due to small shifts in tip-sample separation. Using the integrated electron dose rather than the ideal dose (derived by multiplying injection time by setpoint current) does not significantly affect the injection time as the fluctuations in the current are quite small. After the injection, several small images are recorded so

that the injection location on the after image is recognisable. These are followed by an after image with the same dimensions as the before image. The small images before and after the injection can be used to find the injection location using a template matching algorithm. No compensation for thermal drift was required at 4.6 K as the STM was found to be stable over an atomic site for far longer than an injection period. In addition to the above images it was found that some reaction products were easier to identify in 3 V scans, as in [41, 45], so each non-local experiment requires a further after image (the multi-V image). A schematic of the full procedure is shown in Figure 5.2.

To minimise tip-molecule interactions during the imaging parts of the experiments a setpoint of 10 pA was used, giving a large tip-sample separation. A further benefit of the low setpoint is that it reduces the probability of inducing further reactions when scanning at 3 V, as the electron dose is ten times lower than the lowest injection current used. However, as a result of the low setpoint current the tip cannot follow the atomic contours closely and gives little contrast, making it hard to ascertain the adatom-site on which reaction products are located. When recording the 3 V multi-V image a 1 V image is recorded in parallel, using the backward and forward scan directions, respectively. In this image the adatom-sites are clearly visible. It is not possible to just overlay the forward and backward scans, as small shifts are always present between the two that cause a lattice mismatch. These shifts could be a result of small hysteretic effects in the piezos, or arise from the combination of the tip velocity with the sample drift velocity, which leads to a doppler-shift like effect on the spatial-frequency of features in the images. To relate the location of the reaction products to specific adatom-sites the after image of the series is used together with the multi-V image in an image processing routine. In this routine the after image, in which both forward and backward scans are recorded at 1V, is used to generate a map of the small distortions arising between the forward and backwards images. These distortions are assumed to be similar for two images recorded consecutively, so the map between forward and backwards scans is assumed to apply equally to the after and the multi-V image. Applying the map to the multi-V image

allows the reactants to be accurately associated with the nearest lattice location, and hence their coordinates deduced relative to the injection location. The data in the after image and the forward scan of the multi-V image are essentially interchangeable. However, the after image is important, both for the alignment reasons described above and other experimental reasons, such as recording the positions of dark features to ensure that they were not produced during the 3 V scan of the multi-V image. The after image is also important as it provides information on the physisorbed populations soonest after the injection, as the multi-V image introduces a further time delay, and the molecules will have experienced further sweeping during the after image (see Section 5.2.2).

In order to analyse the behaviour of the molecules in more detail and with a view to future quantitative analysis of injection experiments, some modifications were required to the analysis methods described in Chapter 4. Specifically, the program described therein used the separation of the adatom intensities into two gaussians to determine the threshold used to label sites bright or dark. This was particularly easy for the given molecular coverage as the population of adatoms with bright (usual adatom) intensity was similar to that of those with darker (molecules) intensity. Because the physisorbed molecule coverage is much lower, this process becomes much more difficult. A new scheme is applied where the adatom-site intensities are measured over the whole image and aggregated in a histogram. These adatom-site intensities fall into three broad categories, bright, normal, and dark corresponding to physisorbed molecules, clean adatoms, and defects, respectively. The peak of this intensity distribution is very sharp and corresponds to the average clean adatom height as measured by the STM. This adatom height is then used as the zero of intensity, such that defects and possible chemisorbed molecules (which appear dark) have negative intensity, and physisorbed molecules (which appear brighter than the adatoms) have positive. Finally, the entire intensity scale is renormalised to the standard deviation of the adatom-site intensities. The clean adatom peak dominates the distribution and is roughly gaussian. After rescaling clean adatoms have zero intensity, and any adatom-site where the modulus of the intensity is larger than one is classified as a

feature – physisorbed molecule if positive, and defect if negative. This scheme was found to be more reliable than trying to find three peaks in the distribution, as sometimes there would be a wide distribution of physisorbed intensities, making it difficult to identify an associated peak.

These techniques constitute a full experimental and analytical suite for non-local experiments at 4.6 K, with the capability of analysing reaction products at low current and high voltage.

5.2.2 Sweeping

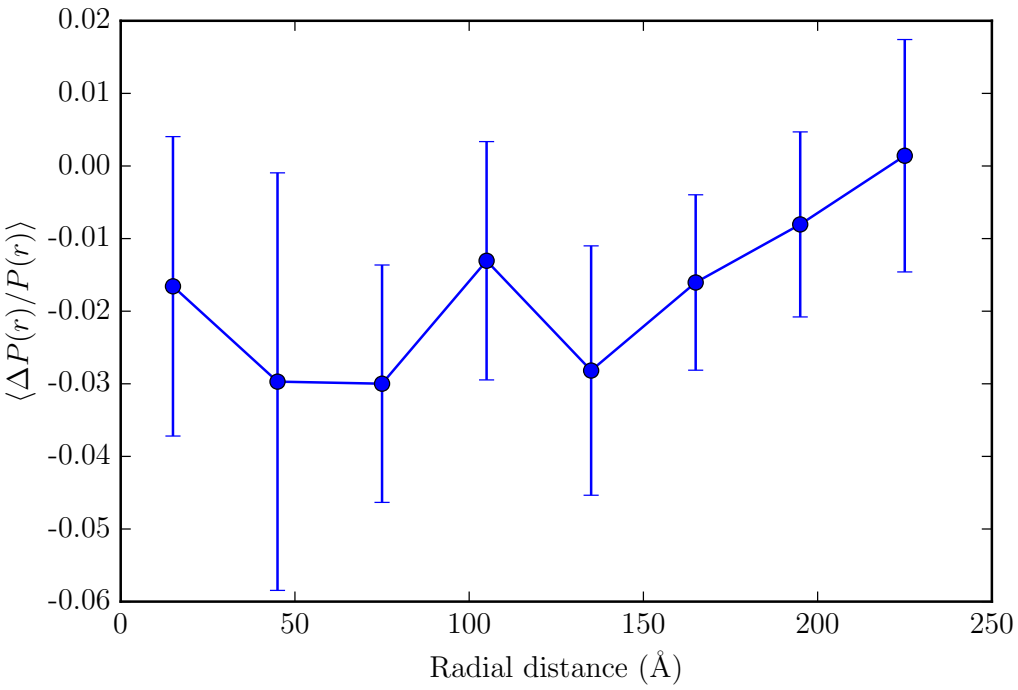

Figure 5.3: Fractional changes in the populations of physisorbed molecules in 30 Å annular bins around the injection site. The plotted values are the average of the mean fractional changes from three series of images, weighted by the error in those means. The errors are combined accordingly.

As the physisorbed molecules are more weakly bound than the chemisorbed species they sometimes move between images. This is likely a result of sweeping by the STM tip. Sweeping can alter the positions of molecules, and affect normalisation of radial probability

distributions by introducing uncertainty in the molecular populations of annular bins ($P(r)$). Sweeping was investigated by recording three long series of images (at least 20 images) at passive imaging parameters. In each image the physisorbed molecular populations were recorded to determine how the tip affects the molecules. The overall population of molecules in an image was found to decay on long timescales, until it reaches a plateau (described in Appendix C). The changes in populations of annular bins ($\Delta P(r)$) between consecutive images are more important for the non-local experiments than long term behaviour of the populations over the entire image. These changes can be subtracted from the change that occurs during an injection, such that only changes in the molecular population as a result of the injected electrons are attributed to the injection. As the changes in the positions of molecules during the scan are unlikely to be thermal it is assumed that the number of molecules that move between annular bins is a function of the number of times an area was scanned. One set of images was recorded at half the scan speed, but showed no significant differences in the sweeping. This supports the argument that the effect is tip-induced, as a thermal phenomena should exhibit a larger effect when imaged for a longer time.

The mean fractional change ($\langle \Delta P(r)/P(r) \rangle$) in the populations is shown as a function of radius in Figure 5.3. It was found that on average the molecular populations decreased slightly between consecutive images, but that there was significant variation between image pairs. This is because molecules swept from one annular bin must enter another, so when some bins lose molecules some must gain molecules. The values shown in the graph can be used to correct the initial and final physisorbed populations of the non-local experiments by assuming half of the sweeping occurs before and half after the injection, and rescaling the before and after $P(r)$ accordingly.

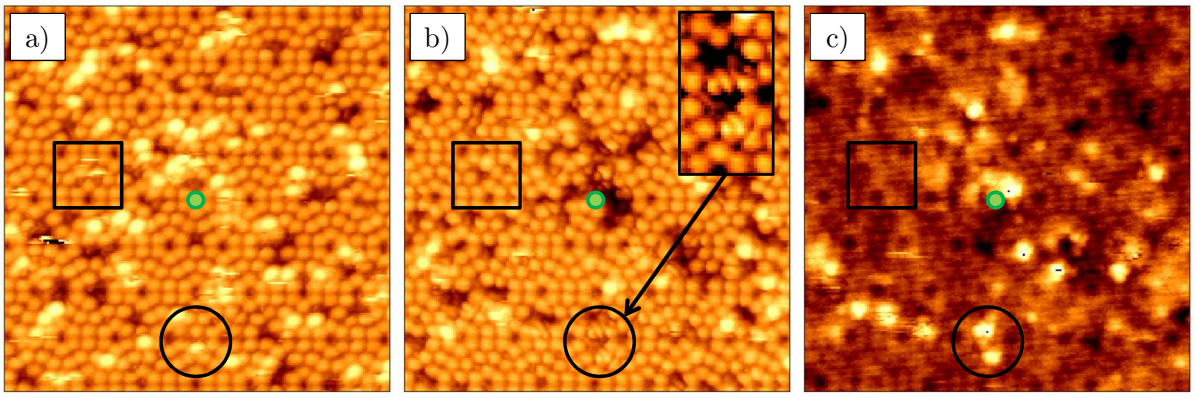

Figure 5.4: Sections from STM images taken during a non-local injection at 4.6 K (injection parameters: 4.0 V, 400 pA, 80 s). Each image shows a 20 nm by 20 nm area centred on the injection site (green dot). Image a) is from the 1 V before image, image b) from the 1 V multi-V image, and image c) from the 3 V multi-V image. All images are recorded at a setpoint of 10 pA. Image c) is recorded at the same time as b) by switching the bias between the forwards and backwards scans. In the centre of b) new dark features are observed together with a depletion of the physisorbed features compared to a). In c) an abundance of bright features can be seen, these can be correlated with new features appearing at 1 V in b). An example is shown by a black circle: in a) there is a physisorbed molecule, in b) there are two dark features and two 'dumb-bell' like features (magnified in the inset), in c) there are two bright features.

5.3 Identification of non-local manipulation products

The result of a non-local injection at 4.6 K are shown in Figure 5.4, where a) shows the before image, and b) and c) show the forward and backward scans of the multi-V image, respectively. For the physisorbed molecular system the behaviour is more complicated than the corresponding chemisorbed system. A number of new dark features (D1 features) can be observed around the injection location (green dot), together with depletion of the initial physisorbed population. In addition, a new reaction is highlighted with a circle, which results in a 'dumb-bell' like feature situated on an adatom. The same feature appears bright in the 3 V scan of the multi-V image (B3 feature).

In addition to molecular processes, adatoms can hop. This behaviour is well known on silicon [32], and results in a new dark feature and a slightly brighter neighbouring adatom. This process is examined in detail below, in order to avoid misinterpreting it as

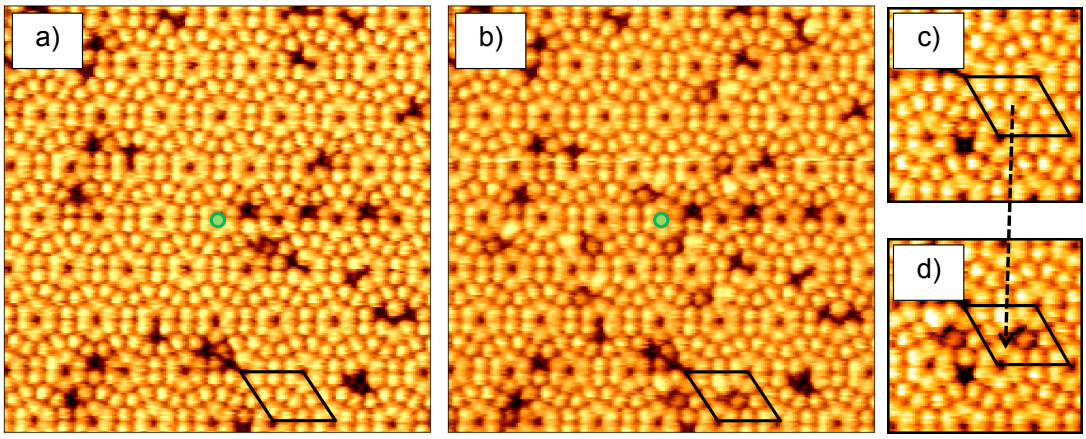

Figure 5.5: Panel a) shows the clean silicon surface (apart from defects). Panel b) shows the result of an injection performed at the green dot (injection parameters: 4.0 V, 800 pA, 80 s). Both images are 20 nm by 20 nm areas centred on the injection site taken from the full before and after images, and were recorded at 1 V, 10 pA. Several adatoms have hopped as a result of this injection, a unit cell containing an example is highlighted in all of the images. Panels c) and d) are 75 Å by 75 Å subsections taken from the before and after images, respectively. In the central two unit cells adatom hops can be seen, described in detail in the text. A black arrow indicates the adatom that has hopped and its final position.

a molecular event.

5.4 Adatom hopping

The appearance of adatom hops in STM is shown in Figure 5.5, depicting a clean Si(111)−7×7 surface. Panels a) and b) are 20 nm by 20 nm areas centred on the injection site taken from before and after images respectively (both recorded at 1 V, 10 pA). The injection parameters were 4.0 V bias, 800 pA injection current, for 80 s. Panels c) and d) are 75 Å by 75 Å subsections taken from the before and after images. They show magnified views of adatoms hops. Note how the adatoms that move are always middle adatoms (see discussion of Section 1.4.1), and hop onto adjacent middle adatoms. A barely seen dark area is left at their initial location, and an adjacent middle adatom in the other half of the unit cell changes intensity slightly. This behaviour is identical to that described in [32].

The adatom hops only appear in one half of the unit cell. This is also remarked upon in [32], where it is noted that this is the faulted half of the unit cell. The darker feature in the adjacent half-unit-cell is not present for some tip states.

Here we are mainly concerned with ensuring that an adatom hop is not mistaken for a feature produced as a result of a molecular reaction. No B3 features are observed after an injection on the clean surface for any parameter set chosen, implying that the molecules are required for the formation of B3 features to occur. Hopped adatoms do appear slightly brighter than the surrounding adatoms at 3 V, but only by (40 ± 5) pm as opposed to (105 ± 5) pm for the B3 feature. In addition, B3 features are seen on all adatom sites, whereas hopped adatoms are always located over FM adatoms[1]. The above considerations rule out hopped adatoms as possible candidates for the B3 features. The hole left by the hopped adatom may be mistaken for a D1 feature, but this will be taken into account in Section 5.7.

To further characterise adatom hopping, injections were performed on the clean surface at similar bias and current as was used in the main experimental series and the results analysed to determine the hopping behaviour. The fraction of unit-cells in which an adatom hops (hopping-fraction) is shown in Figure 5.6 for a variety of currents at 4.0 V, and also for 400 pA at 4.5 V. The hopping-fraction is broadly similar for the parameters used, exhibiting a decay similar to that observed for our non-local process. The adatom hopping process is thought to originate from a similar mechanism to the non-local process, so this would be expected. There is a slight increase in hopping-fraction with increasing current, and a more significant increase with increasing voltage. Hopping was seen at biases as low as 2.5 V.

Interestingly, the hopping behaviour does not show the current dependence we would expect. Based on a rate equation formalism similar to that in Equation (4.6), we would expect the radially integrated hopping probability to be proportional to I^g, where g is the number of electrons required to cause a hop. In this case, fitting I^g to the above

[1]Faulted middle adatom. Refer to the discussion of Section 1.4.1 for more information

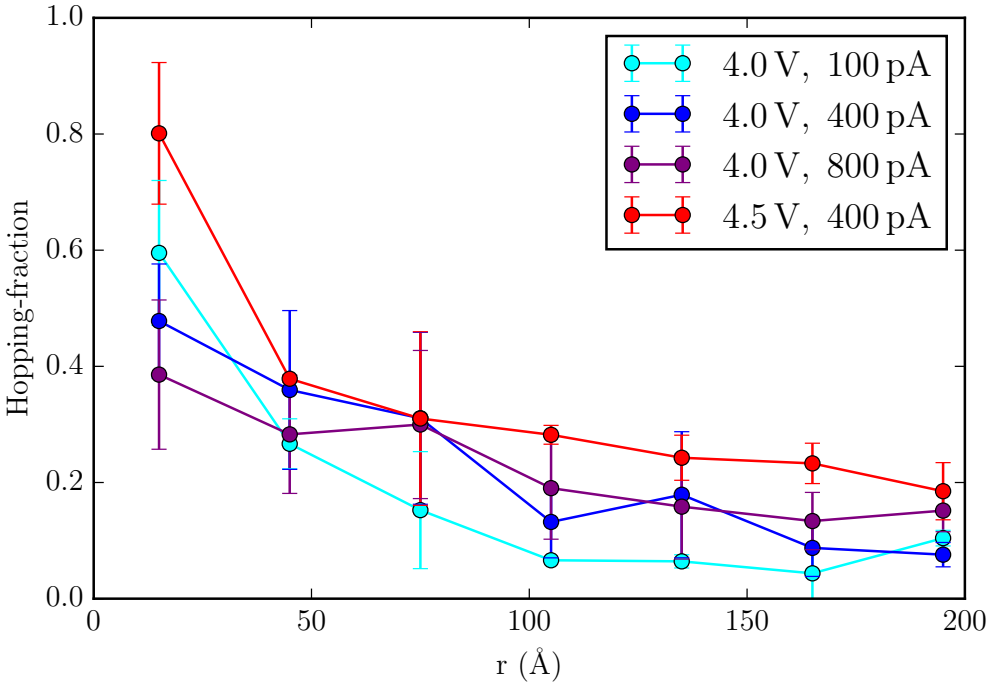

Figure 5.6: Fraction of unit-cells in which an adatom hops as a function of radial distance from injection site for various injection parameters. Generally the hopping-fraction increases with current and with voltage.

yields $g = 0.1 \pm 0.2$, which does not seem physical, especially as the hopping process is known to be one electron. In Stipe et al. [32] it was noted that sometimes the apparent number of electrons found using this method could appear less than one as a result of additional voltage drops present in the sample: these would reduce the effective energy of the electrons as the current increased hence reducing the hopping yield below what would be expected. Modelling the gap as a series resistance, and assuming the resistance of silicon is small yields

$$V_{\text{gap}} \approx V_{\text{bias}} \left(1 - \frac{R_{\text{Si}}}{R_{\text{gap}}}\right), \tag{5.1}$$

where V_{gap} is the voltage dropped across the vacuum gap, which determines the injected carriers' energy, and V_{bias} is the bias applied. The quantities R_{Si} and R_{gap} are the resistances of the sample and vacuum gap respectively. At low temperature the resistance of the sample can be higher than at higher temperature, either due to restricted carrier transport from the surface [208] or through the bulk [32, 209]. In this simplified model, as

the gap resistance is decreased by increasing the current (reducing tip-sample separation), the effective injection voltage is decreased. In the bias range probed, the hopping probability is a sensitive function of bias. This reduction in the effective injection voltage with increasing current can therefore reduce the yield below what would be expected given the rise in current. This phenomena also appears in the response of the physisorbed species to the injection.

5.5 Physisorbed depletion

If the B3 and D1 features arise from the molecules, then their appearance would be expected to be related to the depletion of physisorbed molecules. Starting from an adapted Equation (4.6) the molecular populations as a function of radius would be expected to follow

$$\frac{P(r, t_{\text{inj}})}{P(r, 0)} = \exp\left(-\sigma_{\text{tot}}(r, I, V) t_{\text{inj}}\right), \tag{5.2}$$

$$\sigma_{\text{tot}}(r, I, V) = -\frac{1}{t_{\text{inj}}} \ln\left(1 - \frac{\Delta P(r)}{P(r, 0)}\right), \tag{5.3}$$

where $\sigma_{\text{tot}}(r, I, V)$ is the probability of a molecule undergoing any reaction which removes it from the physisorbed state. The ratio of a product to ΔP should then be equal to the ratio of that product's reaction probability to the total reaction probability, $\sigma_{\text{prod}}/\sigma_{\text{tot}}$. This approach was found to yield reasonable results for the B3 features (see Section 5.6), but D1 features were created in quantities greater than the number of molecules lost (see Section 5.7). There are a number of possible reaction products. In the event of dissociation of the molecule a chlorine atom and a phenyl radical will have to attach to the surface. At room temperature this yields two dark features. Another possibility would be an electron-induced conversion of the physisorbed molecule to the chemisorbed form. This would create the usual dark chemisorbed chlorobenzene feature. Finally, the physisorbed molecule could desorb. More exotic processes such as breaking of the benzene ring and

dehydrogenation have been seen in benzene on other surfaces [211, 212], but haven't been seen before in the Si(111) − 7×7: PhCl system.

5.5.1 Radial dependence

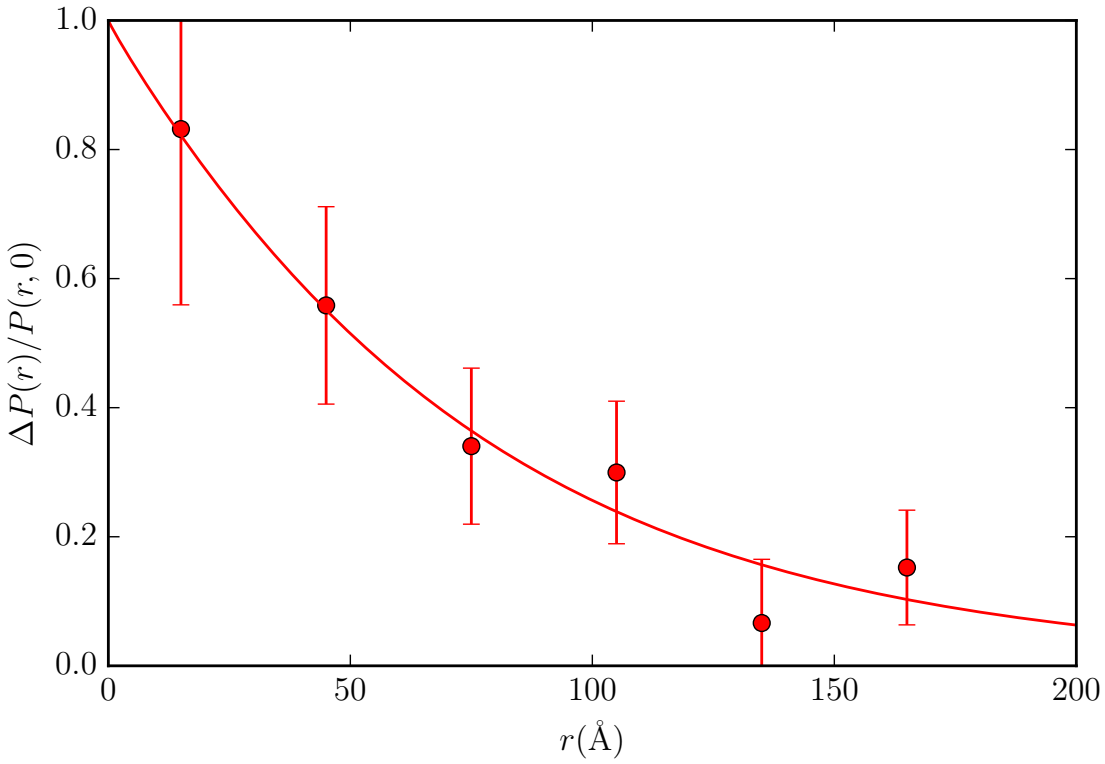

Figure 5.7: Fraction of physisorbed molecules which are manipulated during an injection as a function of radius. The fit is to the radial transport model defined in Equation (4.8). Extracted fit parameters are $A = 4 \pm 3 \times 10^{-12}$ and $\lambda = (80 \pm 40)$ Å. Wider bins are required both because there are fewer studied molecules than in the chemisorbed case, and because diffusion between bins is far more common in the physisorbed state.

The radial distribution of the fractional decrease of physisorbed populations is shown in Figure 5.7 for an injection at 4.0 V bias and 400 pA setpoint current for 80 s, the results are similar to that found for other non-local processes described in Section 4.4.1 and elsewhere [40, 43]. The data is presented in wider bins to reduce the probability of diffusion altering the populations of the bins. The mean change in populations as a result of sweeping is added[2] and the errors assume statistical errors on the before and after

[2]The change is negative, such that the decrease attributed to the injection is less that the total

populations, and also on the number of molecules that are swept. The fit to the data uses the Bessel equation fit described in Equation (4.8), and give a similar decay length to the other electron experiments, though the errors are very large as a result of the uncertainty in the data (200 ± 200) Å at 4 V and (200 ± 100) Å at 4.5 V. Both data sets are averaged over four currents, which could increase the uncertainty here, as the decrease in injection bias with current postulated for adatom hopping is also likely present here (see Section 5.5.3).

5.5.2 Bias dependence

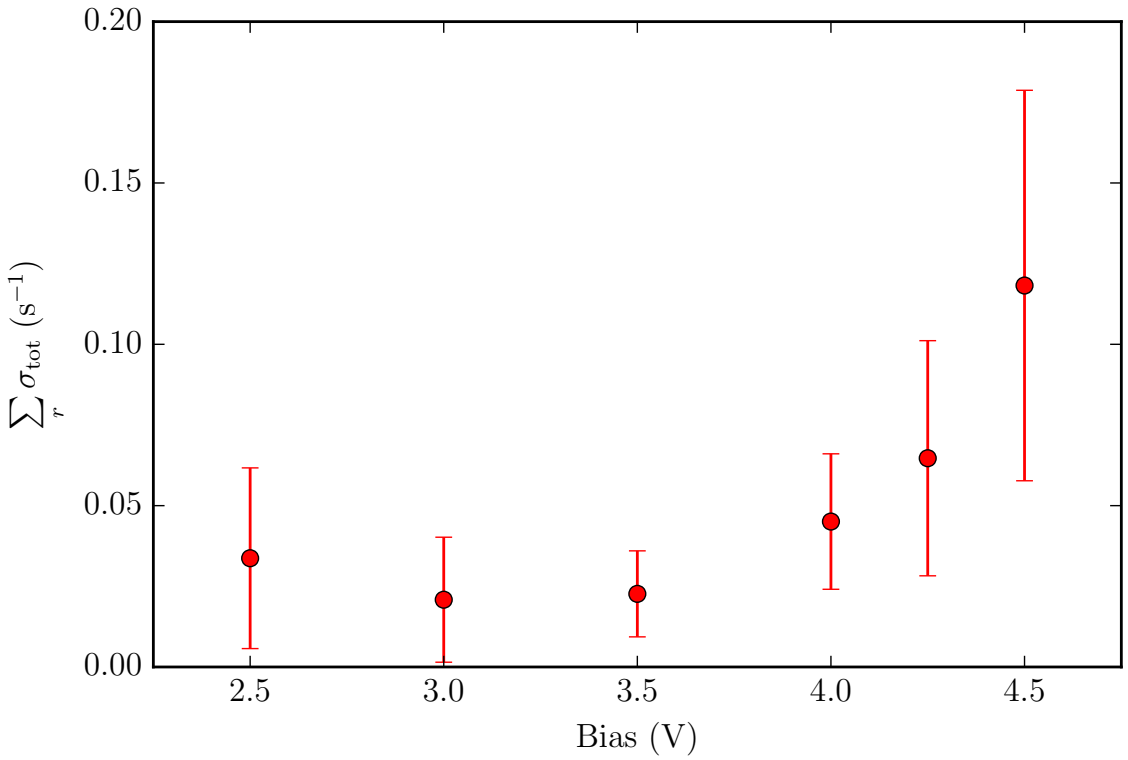

Figure 5.8: Fraction of physisorbed molecules which are manipulated integrated over all radii as a function of bias. Relatively flat at low bias, with an increase in reaction probability above 3.5 V. All injections were performed at 400 pA for 80 s.

The probability of loss of molecules to any reaction channel as calculated using Equation (5.3) and integrated over all radii, is shown as a function of injection bias in Figure

decrease.

5.8. The injections were all performed at the same current and for the same length of time (400 pA, 80 s). The reaction probability increases rapidly above 3.5 V. The main cause of this appears to be the onset of B3 production at a similar bias.

5.5.3 Current dependence

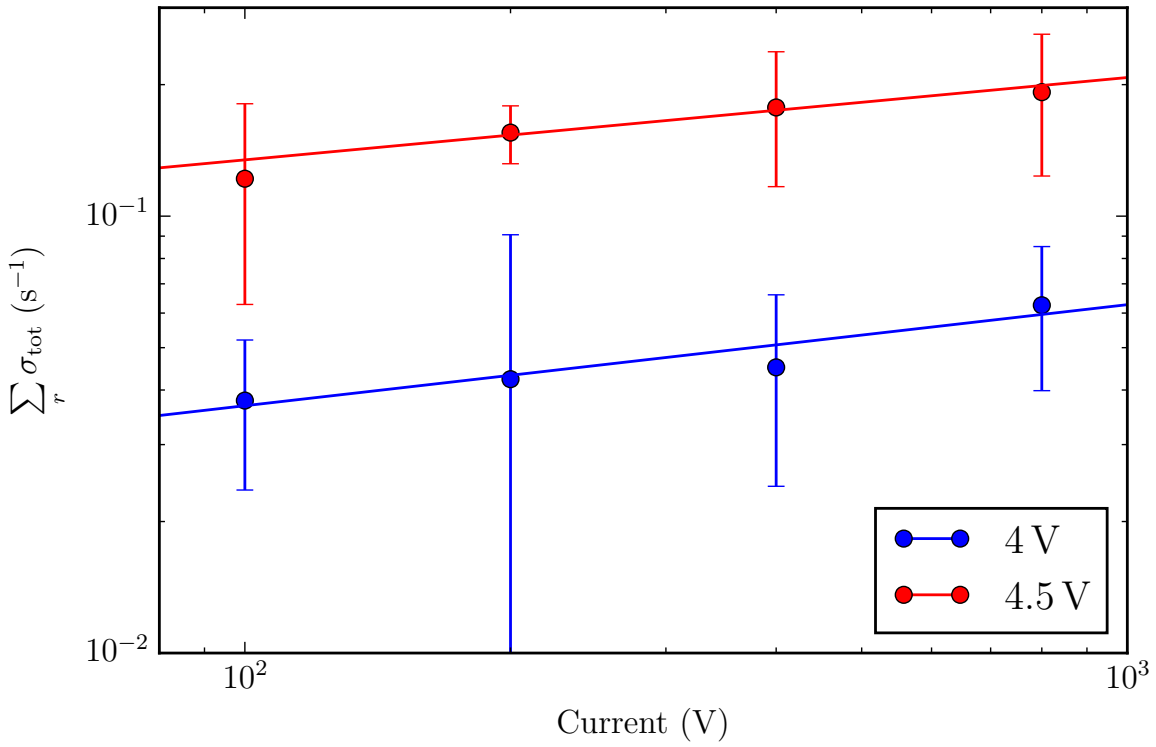

Figure 5.9: Fraction of physisorbed molecules which are manipulated integrated over all radii as a function of current for injections at 4.0 V bias and 4.5 V bias. The fits are to AI^g, where g should be the number of electrons required for a reaction. It is found that for 4.0 V electrons $g = 0.2 \pm 0.2$, and for 4.5 V electrons $g = 0.2 \pm 0.4$. Both values of g are unphysical, as described in the text.

Figure 5.9 shows the current dependence of the integrated reaction probability. The graph is shown as a log-log plot as $\sum_r \sigma_{\mathrm{tot}} \propto I^g$ should yield straight lines that can be fitted to extract g. The injections were all performed for the same length of time (80 s) and biases used are shown in the figure. In both cases the reaction probability increased sub-linearly, with $g = 0.2 \pm 0.2$ for 4.0 V electrons and $g = 0.2 \pm 0.4$ for 4.5 V electrons. It

appears that at the low temperature used, all of the non-local processes studied here are affected in a similar way to the adatom hopping. This fits with the assumed mechanism, as at both biases studied the reaction probability is increasing rapidly, so a small decrease in the effective bias would suppress the expected rise from the rising number of injected electrons. Unfortunately, this prevents an unambiguous determination of the number of electrons required for the studied reactions.

5.6 B3 features

The B3 features are likely either to reflect single or multiple chlorine atoms. There are three main pieces of evidence for this: the bias dependence of the STM imaging, the bias dependence of the yield, and the spatial distribution of the B3 features relative to the initial molecule. These are discussed in the following subsections.

5.6.1 Imaging characteristics

As noted above in Section 5.3 the B3 features appear bright at 3 V, and as a distorted adatom feature at 1 V. This bright appearance is similar to that observed when imaging chlorine atoms resulting from dissociation starting from the chemisorbed state [41, 45]. The appearance at 1 V is not the same as that of room temperature chlorine atoms, which image as a reduction in intensity at an adatom site. In contrast, images of B3 features exhibit substructure, and do not appear dark at 1 V.

The appearance and DOS intensity at 1 V and 3 V closely resemble dichloride species described in [213], which have a larger density of states between the Fermi-level and 1 eV, and exhibit high electronic state density symmetrically on either side of the adatom location. A number of chloride species are possible on silicon, ranging from SiCl to $SiCl_3$. Formation of these species could be possible at the studied coverages, especially given the tendency of the physisorbed chlorobenzene to cluster. This is supported somewhat by imaging, where B3 features can sometimes appear to have more than two lobes. However,

it is uncertain why the dichloride features would be the dominant reaction product over the monochloride. It is possible that the single chloride is more difficult to identify at 3 V as there are a number of bright features at this bias (physisorbed molecules and B3 features both appear bright); whereas, the B3 feature is particularly intense, and also clearly visible at 1 V.

5.6.2 Bias and current dependence of yield

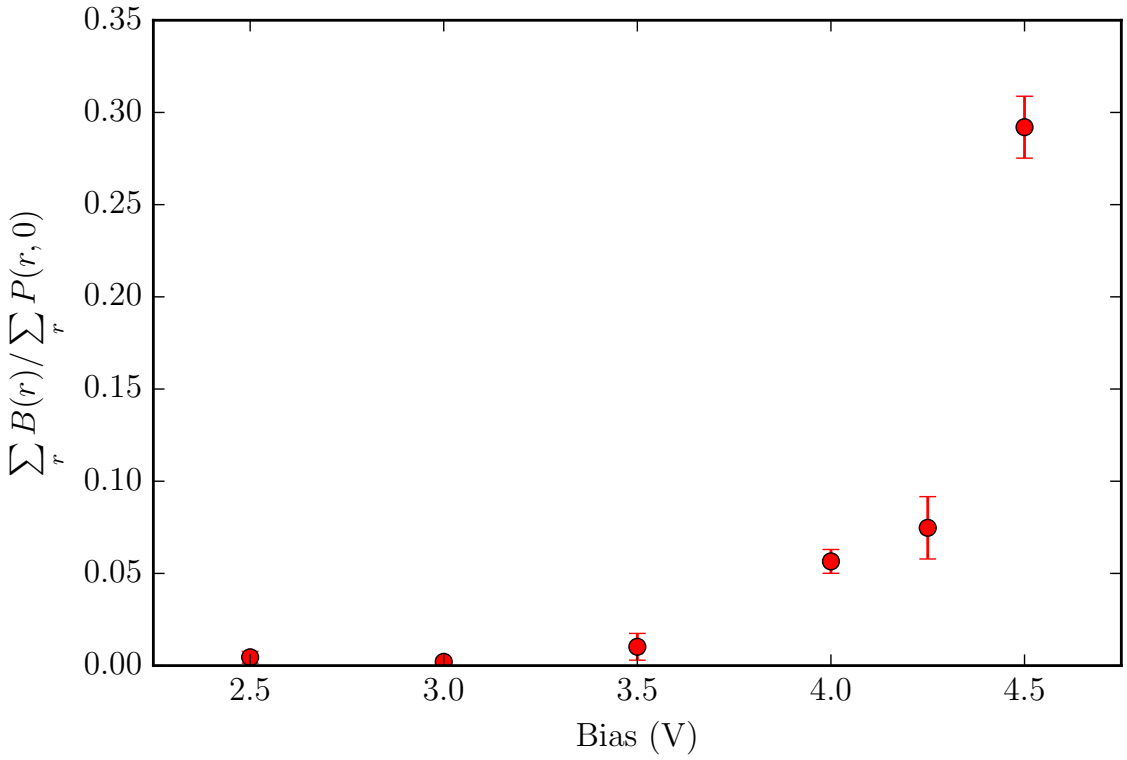

Figure 5.10: Number of B3 products formed per initial physisorbed molecule as a function of bias. Notice that the process shows a threshold at around 3.5 V.

The bias dependence of B3 formation is shown in Figure 5.10. The total number of B3 features is normalised to the initial number of physisorbed molecules. Though this is not a direct measure of σ_{B3} it indicates the threshold for the process, and can be compared with similar measurements in [44], where a similar yield is used to determine the bias threshold for dissociation. There it was found that dissociation showed a sharp onset

near 3 V. Here, dissociation begins to increase just above 3 V, with a slightly slower onset than that found in [44]. Slight differences in the threshold could be the results of the bias shifts mentioned in Section 5.5.3. If multiple chlorines are necessary to form the B3 features it may also be that the bias dependence is complicated by a requirement for multiple dissociation events in the near vicinity.

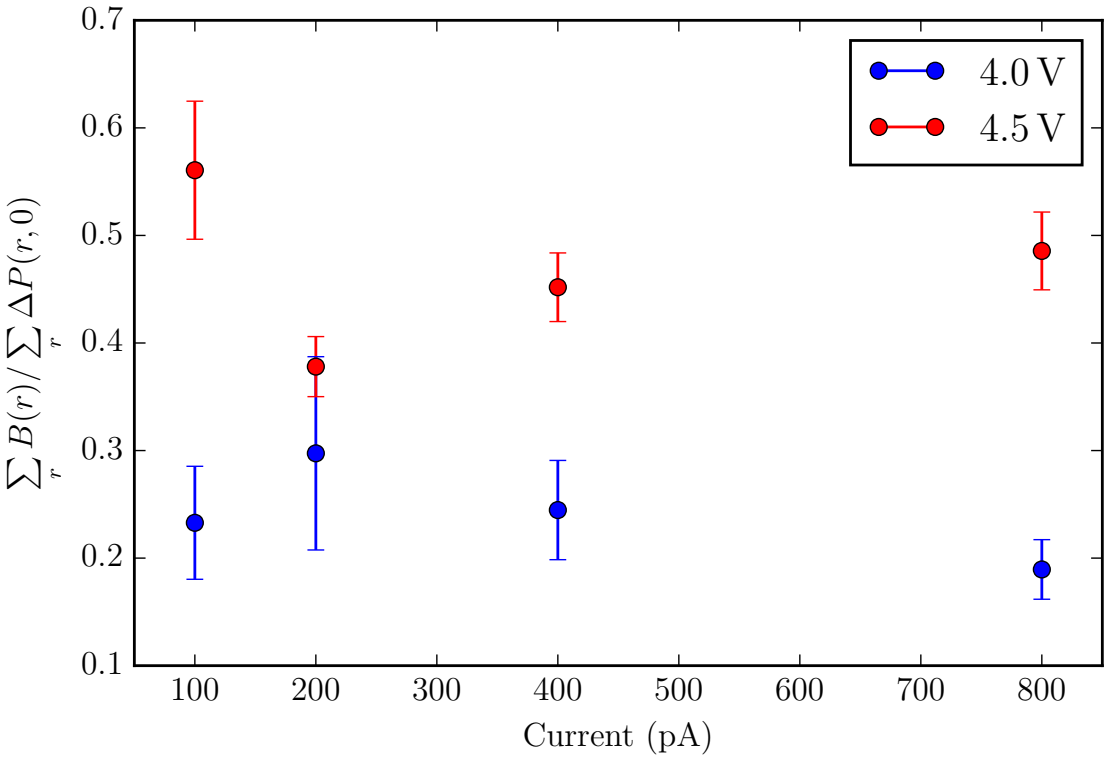

Figure 5.11: Ratio of total number of B3 features produced to change in physisorbed features as a function of current for the biases shown in the legend.

The ratio of B3 products to total lost physisorbed molecules was not found to vary significantly with current, this suggests that both processes have the same g. This is shown in Figure 5.11. Following the discussion below Equation (5.3) at the beginning of Section 5.5 it would be expected that $B(r)/\Delta P(r) = \sigma_{\mathrm{B3}}/\sigma_{\mathrm{tot}}$. If both processes are dependent on the same number of electrons then the ratio should be constant as a function of current. Summing over the image neglects the radial dependence of the probabilities but as that should not be affected by the injection current, this is a reasonable approach.

5.6.3 Spatial distribution of products

A strong piece of evidence supporting the assignment of the B3 features as chlorine atoms is their spatial location relative to the physisorbed species. If the event is dissociation, a phenyl radical would also be produced. This phenyl radical would likely bond to the nearest bonding site due to its relatively large size (compared to the chlorine atom) and highly reactive nature. At room temperature, phenyl groups bonded to silicon image as dark features. The separation between each B3 feature and its nearest-neighbour dark feature can be measured and compared to a test distribution of separations assuming the dark features are randomly located on the surface. The test distribution is selected in such a manner that the distribution of dark features over the four distinct adatom sites matches the measured distribution of the real dark features. In addition, the dark features are not allowed to populate a site populated by a B3. This ensures that possible correlations from site-specific bonding of the dark features is taken into account. For instance if both B3 and dark features are only formed on UM adatom sites, then there may be a stronger correlation between their locations than if the dark features are uniformly distributed. By correctly distributing the dark features, it is possible to measure additional correlation on top of this base correlation.

Figure 5.12 shows the distribution of B3 features relative to their parent phenyl for injections at 4 V, the distributions for all currents were summed as there did not appear to be a systematic variation in the distribution with current (discussed below). The small peak located at 0 is for B3 found at the same site as phenyl, these data points may be in part be erroneous labelling of a B3 adatom as a dark feature. However, some B3 features did appear to be formed on dark areas of the surface. It is possible that they are bonded in an unusual geometry such as to a rest-atom (as was mentioned to occur in [45]). In the real distribution the majority of B3 features are found on nearest neighbour adatoms to the phenyl groups (between 6 Å to 7 Å), whereas for the test distribution the separations are more uniformly distributed. This behaviour is different to that observed

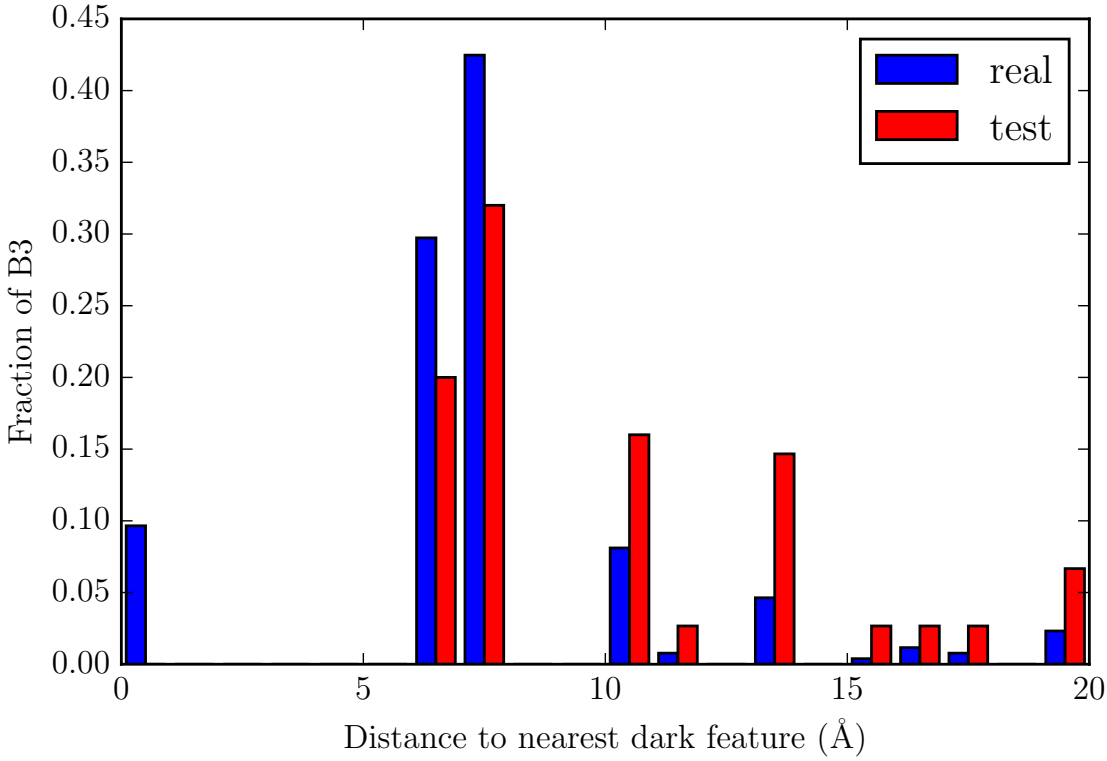

Figure 5.12: The graph shows the distribution of the separations of B3 features and their nearest dark feature neighbours. It is found that in the majority of the 266 B3-phenyl pairs analysed the B3 features and phenyl features are situated on nearest-neighbour adatom sites (6 Å to 8 Å). This data is for 4 V, 80 s injections over a range of currents (the injection current did not affect the distribution significantly).

at room temperature in [45], where it was found that the chlorine could be located on more distant neighbouring adatoms. At 4.5 V this pairing is less obvious, but this is in part because the coverage of dark features is so high that the average nearest neighbour distance is already very small. Out of the 1707 dark features now labelled phenyl groups, it was found that 1238 were located within 15 nm of a physisorbed molecule. To confirm that defects on the surface were not the source of the B3 features this procedure was also performed for initially dark adatoms. It was found that only 950 phenyl features were located within 15 nm of these initial dark features, suggesting that the molecules are more likely to be the source of the phenyl and B3 features.

Figure 5.13 shows the distribution relative to the nearest physisorbed molecule binned in the same manner as the data in [45]. Interestingly this is very similar to the room

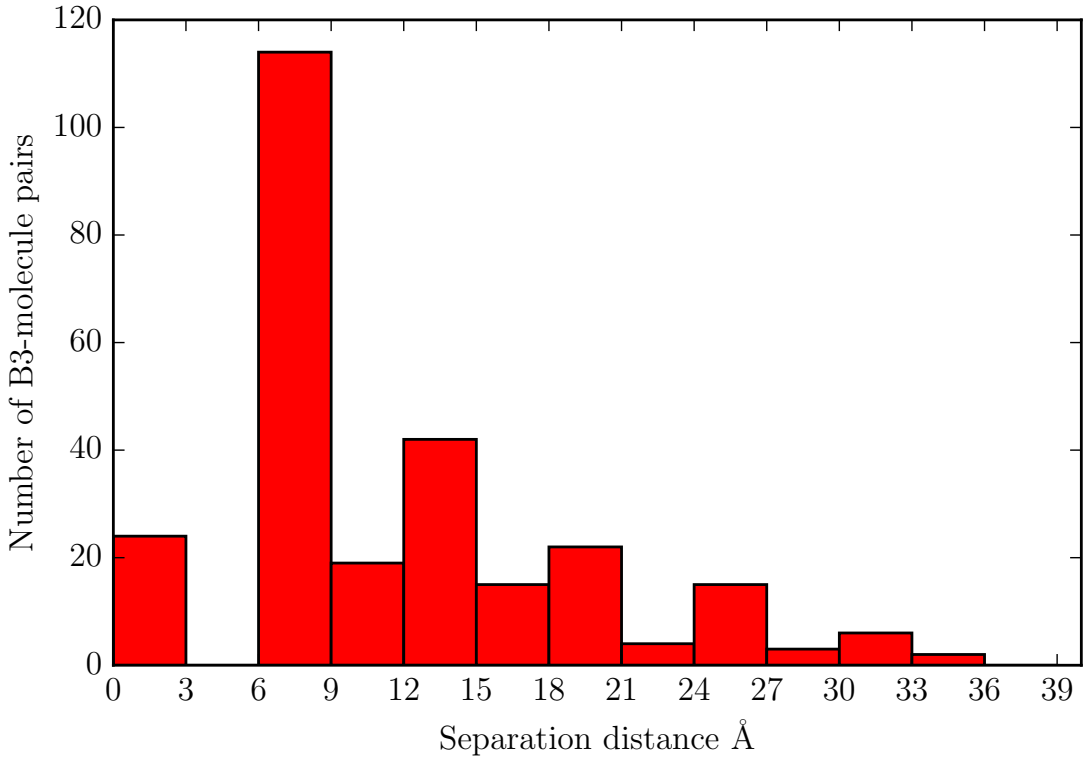

Figure 5.13: The graph shows the distribution of the separations of B3 features and nearest-neighbour initial physisorbed molecules. The distribution is found to resemble that found for 4.0 V, 100 pA injections at room temperature. The data presented is from 4 V, 80 s injections over a range of currents (the injection current did not affect the distribution significantly).

temperature distribution. Because the positions of both molecules and B3 features are determined by the nearest adatom location only adatom-adatom distances can occur. This discretises the distribution. For both unfaulted and faulted halves of the unit cell the spatial locations of the adatoms are identical so the possible separations are determined by the relative locations of other adatoms relative to either a middle or a corner adatom (see Section 1.4.1 for an explanation). The nearest neighbour distances are then 6.6 Å and 6.7 Å to the equivalent adatoms in the other half of the unit cell, and 7.7 Å to the adjacent adatoms in the same half of the unit cell. The exact proportional filling of the various bins is then dependent on the motion of the physisorbed molecules between being recorded in the before image, and dissociating during the injection. This leads to the oscillatory filling shown. As can be seen from the figure, most of the B3 features are found on a

nearest neighbour to the initial physisorbed molecule, with decreasing numbers at larger distances. Some B3s are found on the same adatom site, this is likely a result of the physisorbed molecule moving to an adjacent site before the injection, so these events will be added to the nearest neighbour peak in the discussion below.

To compare the data here to that in [45] it is necessary to determine the likely corresponding peaks. The data presented in [45] has some dissociation products between 3 Å to 6 Å from the initial molecule. This suggests the coordinate system is labelled relative to the initial molecule (as these distances are shorter than the shortest distance between adatoms), this would potentially offset the coordinates by 3 Å. If we assume that the two initial peaks in the data presented in figure 2 b) of the paper correspond to nearest neighbour separations in the data presented here, then the distribution has three main peaks. When the data in Figure 5.13 is renormalised to account for the sample size in [45] the distribution of separations is very similar, as shown in the table below.

Source	Peak 1	Peak 2	Peak 3
Data in Figure 5.13	13 ± 1	4.1 ± 0.6	2.1 ± 0.5
Sloan *et al.* 2005[45]	18 ± 4	5 ± 2	1 ± 1

Table 5.1: Comparison of peak heights in distribution of separations between initial molecules and their dissociation products (shown in Figure 5.13). Peak 1 corresponds to 6 Å to 9 Å, peak 2 to 12 Å to 15 Å, and peak 3 to 18 Å to 21 Å. In [45] similar peaks are visible but offset slightly due to differences in measurement.

The above similarity may provide a route to explaining the increase in average separation observed in [45], where the explanation was not based on the physisorbed dissociation model. As can be seen above the chlorines from the physisorbed molecules are distributed over a greater range of sites relative to the molecule than relative to the phenyl. This is a result of the motion of the physisorbed molecule between being imaged and its dissociation. It is likely that a similar process occurs at room temperature after the initial electronic excitation. The transient physisorbed molecule may move over the surface until it is hit by a second electron and dissociates. As the process is always competing with thermal desorption of the physisorbed state, a longer delay between electrons would favour

dissociation from more long-lived physisorbed molecules. Molecules which were initially more highly excited and mobile are also more likely to thermally desorb, so would be less long-lived. Together this would suggest that low currents would favour desorption from less mobile physisorbed transients, and hence populate only the nearest neighbour sites; whereas higher currents could also dissociate the shorter lived, more excited physisorbed transients distributing chlorine more widely over the surface. In the work here, the dissociation is likely not dependent on a second electron and hence the distribution does not depend on current. The position of the phenyl group is not discussed in [45], so it is unknown whether the separations between phenyl group and chlorine measured in that work would support such a model.

5.7 D1 features

In addition to the dark features labelled as phenyl groups above, there are a large number of other dark features formed during the injection. These could be a result of adatom hopping, which creates a dark feature, or they may be another product produced from the physisorbed molecules. In addition, some dark features were found to vanish during the injection and may simply have moved to a different site, leading to the appearance of a new dark feature.

The ratio of dark features of unknown origin (U) to their possible sources (S) is given by

$$\frac{U}{S} = \frac{D - B - H}{\Delta P + L - B},$$

where D denotes new dark features, H dark features associated with hopping, L lost initial dark features, B dissociation events and ΔP lost physisorbed molecules. This is shown quantitatively as a function of bias in Figure 5.14. Hopping was only measured in detail at 2.5 V, 4.0 V, and 4.5 V so was interpolated for the other biases. The hopping-fraction used in the discussion in Section 5.4 is not used directly. Instead the hopping data is used

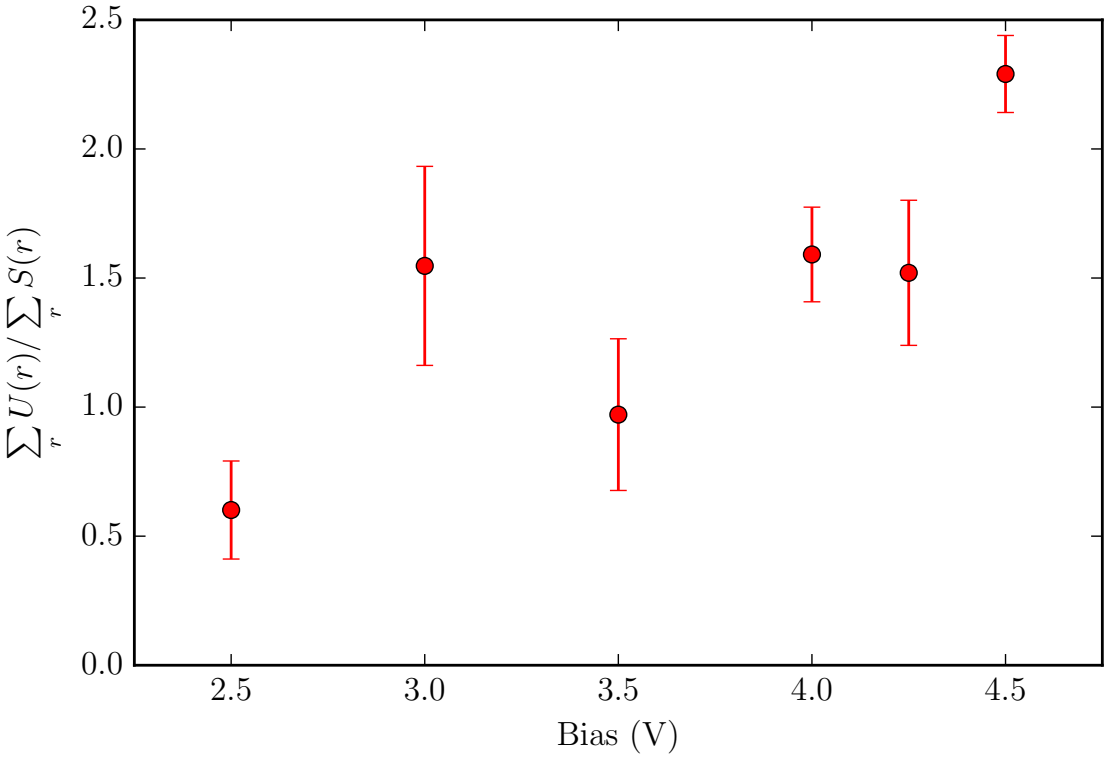

Figure 5.14: Ratio of all unknown dark features (D1 features minus the estimated number of hops minus phenyl groups) to possible sources (lost physisorbed molecules minus those lost to dissociation, plus lost dark features). It can be seen that more dark features are produced than can be accounted for, particularly at higher bias.

to determine the probability of an adatom going dark as a result of hopping, and this is then used to determine the expected number of dark features as a result of hopping for each non-local experiment. It can be seen that the number of unidentified dark features is often significantly greater than the number of possible sources. There are three possible sources for the unidentified dark features, firstly a molecule could form multiple dark features, secondly there could be a significant number of unaccounted for molecules or contaminants, or finally hopping may not have been accounted for accurately.

It is possible that the phenyl groups could dissociate further, either dehydrogenating or breaking up the carbon ring once adsorbed to the silicon. These processes are known to happen on some metal surfaces, though it is likely the surface plays an important role in these processes. Benzene has been observed to both dehydrogenate, and dissociate

further subsequent to dehydrogenation (3.75 V on Cu(001) at 8 K). Although the exact reaction products were not determined, a break up of the carbon ring was speculated [211, 214]. Similarly in electron impact experiments on Ag(111) it was found to be possible to break up the carbon ring, but this required far higher electron energies of 12 eV, further suggesting the surface plays an important role.

If a single physisorbed molecule forms a single dark feature (that does not dissociate), and hopping is correctly accounted for, then there must be a population of unidentified molecules on the surface. Streaking and part-imaged molecules are often seen, suggesting some molecules may not have been accounted for because of their motion. In addition, there are sometimes features that could be adsorbates, but do not image exactly the same as the physisorbed species. These may be other adsorbates which have physisorbed during the course of experiments, or contaminant molecules deposited together with the chlorobenzene during deposition. Given that contaminants are expected to contribute $\sim$ 10% of the deposition, it is unlikely that they account for all of the dark features produced during injections. However, it is possible that a contaminant molecule could dissociate or interact in a different manner to chlorobenzene and hence may produce multiple dark features during the injection. Finally, the height distribution of the physisorbed molecules shows two peaks when analysed in detail. It is possible that some of the chlorobenzene molecules could be pi-pi stacked. In the gas phase, chlorobenzene clusters held together by pi-pi stacking can be formed [215]. It may be that on the surface or during deposition some chlorobenzene dimers are formed, giving the extra peak in the height distribution. Again this peak could be a result of contamination, further exploration is necessary.

In addition to molecular processes, it is possible that the surface plays a role in the dark feature formation. Hopping was studied at 2.5 V, 3.5 V, 4.0 V, and 4.5 V, with at least two injections performed at 4.5 V and for all injection currents at 4.0 V (11 injections total, 100 pA, 400 pA, 800 pA). The data set at 3.5 V was neglected because of unusually high hopping, but it may be that the hopping process is highly dependent on the tip-state when performing the injections, as noticed in [44] for chlorobenzene manipulation. If

this is the case a more detailed study may have to be performed to account for the dark features properly, though the hopping studies have ruled out adatom hopping as a source of the B3 features.

A thorough study of the dark feature production is infeasible with the current experimental data. The above uncertainties all need to be investigated in more detail. A number of experiments will be proposed in the outlook to address this.

5.8 Summary and outlook

In summary, it has been found that reducing the temperature to 4.6 K and depositing chlorobenzene directly onto the cold sample results in stable physisorbed species. Non-local manipulation experiments performed on these molecules reduce the physisorbed populations and yield a number of interesting products. The loss of physisorbed molecules is found to increase with both injection bias and injection current. A threshold was found at around 3.5 V, above which the reaction rate increased rapidly. The reaction probability was found to increase with current sub-linearly with an order of electrons $g = 0.2 \pm 0.2$ for 4.0 V bias, and $g = 0.2 \pm 0.4$ for 4.5 V bias. Both are unphysical and suggest a decrease in effective injection energy with increasing current, this was also found to affect adatom hopping which is known to be a one electron process.

The features labelled B3 imaged as bright features at 3 V and exhibited a threshold for production at 3.5 V. Both traits are shared by chlorine production from dissociation at room temperature. In addition, 91% of B3 features were found to occur within 15 Å of a new dark feature, which was not present before the injection. It was proposed that this was the phenyl radical produced in the dissociation process newly bonded to the surface. The B3 features imaged differently at 1 V to chlorine at room temperature, showing a two-lobed, 'dumb-bell' like feature. The reason for this is uncertain, but it is possible that multiple-chlorine features have been produced. Further work would be needed to confirm the reasons for the different appearance.

In addition to the B3 features, a large number of features which image as darkened adatoms at 1 V were produced. These dark features were found in addition to the phenyl groups produced in the B3 process, and could not be accounted for by adatom hopping or diffusion of already extant dark features. There were more unidentified new dark features than molecules lost, suggesting that either not all the molecules are accounted for, or a single molecule can form multiple dark features. Reasons for this were discussed, and could include molecules not imaged by the STM, multiple chlorobenzene molecules imaging as a single molecule, further dissociation of the phenyl groups, or errors in the treatment of adatom hopping.

Future experiments should aim to address the current dependence, to unambiguously confirm the process is one-electron; the unidentified dark features and the reasons for the different low bias imaging of the B3 features. To address the first point a spectroscopic study could be conducted over the current and bias range probed and the peak locations compared to results at higher temperature when any transport limitations are lifted. This should allow for the calibration of the applied bias to the effective bias. The dark features and the nature of the B3 features could be addressed by a local manipulation study of the physisorbed system at low coverage, such that the reaction products could be unambiguously identified. An effort could be made to better determine the contents of the gasline, and reduce any contamination present. In particular, it could be tested whether the B3 products look different as a result of the lower production rate of Cl, and whether it is possible to further dissociate the phenyl ring. A further simple experiment would be to perform injections on benzene and see whether the production of B3 features is suppressed. If the B3 features do involve multiple Cl features, it may be interesting to investigate the mechanisms by which the multiple atoms come together on a single site, and the coverage dependence of this phenomena.

Bibliography

[1] J. Binney and D. Skinner, *The Physics of Quantum Mechanics* (Oxford University Press, 2013), ISBN 978-0-19-968857-9.

[2] J. Bardeen, Phys. Rev. Lett. **6**, 57 (1961), ISSN 0031-9007, URL http://link.aps.org/doi/10.1103/PhysRevLett.6.57.

[3] A. D. Gottlieb and L. Wesoloski, Nanotechnology **17**, R57 (2006), ISSN 0957-4484, URL http://stacks.iop.org/0957-4484/17/i=8/a=R01?key=crossref.bc22daa1f15b42589baa336aa2aefaf8.

[4] C. J. Chen, *Introduction to Scanning Tunneling Microscopy* (Oxford University Press, 2007), 2nd ed., ISBN 9780199211500.

[5] C. J. Chen, Ultramicroscopy **42-44**, 147 (1992), ISSN 03043991, URL http://linkinghub.elsevier.com/retrieve/pii/030439919290259M.

[6] J. Tersoff and D. R. Hamann, Phys. Rev. B **31**, 805 (1985), ISSN 0163-1829, URL http://link.aps.org/doi/10.1103/PhysRevB.31.805.

[7] L. Gross, N. Moll, F. Mohn, A. Curioni, G. Meyer, F. Hanke, and M. Persson, Phys. Rev. Lett. **107**, 086101 (2011), ISSN 0031-9007, URL http://link.aps.org/doi/10.1103/PhysRevLett.107.086101.

[8] K. Sattler, *Fundamentals of Picoscience* (CRC Press, 2013), ISBN 978-1-4665-0509-4.

[9] W. Krenner, D. Kühne, F. Klappenberger, and J. V. Barth, Sci. Rep. **3**, 1454 (2013), ISSN 2045-2322, URL http://www.nature.com/articles/srep01454.

[10] P. N. Nirmalraj, D. Thompson, and H. E. Riel, Sci. Rep. **5**, 10116 (2015), ISSN 2045-2322, URL http://www.nature.com/articles/srep10116.

[11] S. A. Contera, H. Iwasaki, and S. Suzuki, Ultramicroscopy **97**, 65 (2003), ISSN 03043991, URL http://linkinghub.elsevier.com/retrieve/pii/S0304399103000305.

[12] I. Ekvall, E. Wahlström, D. Claesson, H. Olin, and E. Olsson, Meas. Sci. Technol. **10**, 11 (1999), ISSN 0957-0233, URL http://stacks.iop.org/0957-0233/10/i=1/a=006?key=crossref.7ef376e4bf06d48dafc48b7c2d466208.

[13] A. Heinrich, C. Lutz, S. Baumann, and I. Rau, *IBM Research: A Boy And His Atom* (2013), URL http://www.research.ibm.com/articles/madewithatoms.shtml{#}fbid=ynJHj1f5cSR.

[14] F. E. Kalff, M. P. Rebergen, E. Fahrenfort, J. Girovsky, R. Toskovic, J. L. Lado, J. Fernández-Rossier, and A. F. Otte, Nat. Nanotechnol. **11**, 926 (2016), ISSN 1748-3387, 1604.02265, URL http://dx.doi.org/10.1038/nnano.2016.131.

[15] D. M. Eigler and E. K. Schweizer, Nature **344**, 524 (1990), ISSN 0028-0836, URL http://www.nature.com/doifinder/10.1038/344524a0.

[16] G. DUJARDIN, R. E. WALKUP, and P. AVOURIS, Science (80-.). **255**, 1232 (1992), ISSN 0036-8075, URL http://www.sciencemag.org/cgi/doi/10.1126/science.255.5049.1232.

[17] K. Stokbro, C. Thirstrup, M. Sakurai, U. Quaade, B. Y.-K. Hu, F. Perez-Murano, and F. Grey, Phys. Rev. Lett. **80**, 2618 (1998), ISSN 0031-9007, URL http://link.aps.org/doi/10.1103/PhysRevLett.80.2618.

[18] S.-W. Hla, L. Bartels, G. Meyer, and K.-H. Rieder, Phys. Rev. Lett. **85**, 2777 (2000), ISSN 0031-9007, URL http://link.aps.org/doi/10.1103/PhysRevLett.85.2777.

[19] S.-W. Hla, G. Meyer, and K.-H. Rieder, Chem. Phys. Lett. **370**, 431

(2003), ISSN 00092614, URL http://linkinghub.elsevier.com/retrieve/pii/S0009261403000174.

[20] J. L. Zhang, J. Q. Zhong, J. D. Lin, W. P. Hu, K. Wu, G. Q. Xu, A. T. S. Wee, and W. Chen, Chem. Soc. Rev. **44**, 2998 (2015), ISSN 0306-0012, URL http://dx.doi.org/10.1039/C4CS00377B.

[21] H. L. Tierney, C. J. Murphy, A. D. Jewell, A. E. Baber, E. V. Iski, H. Y. Khodaverdian, A. F. McGuire, N. Klebanov, and E. C. H. Sykes, Nat. Nanotechnol. **6**, 625 (2011), ISSN 1748-3387, URL http://www.nature.com/doifinder/10.1038/nnano.2011.142.

[22] Y. Nakamura, Y. Mera, and K. Maeda, Surf. Sci. **601**, 2189 (2007), ISSN 00396028, URL http://linkinghub.elsevier.com/retrieve/pii/S0039602807001975.

[23] B.-Y. Choi, S.-J. Kahng, S. Kim, H. Kim, H. W. Kim, Y. J. Song, J. Ihm, and Y. Kuk, Phys. Rev. Lett. **96**, 156106 (2006), ISSN 0031-9007, URL http://link.aps.org/doi/10.1103/PhysRevLett.96.156106.

[24] Y. Okawa and M. Aono, Nature **409**, 683 (2001), ISSN 00280836, URL http://www.nature.com/doifinder/10.1038/35055625.

[25] Y. Okawa and M. Aono, J. Chem. Phys. **115**, 2317 (2001), ISSN 0021-9606, URL http://aip.scitation.org/doi/10.1063/1.1384554.

[26] P. Maksymovych, D. C. Sorescu, K. D. Jordan, and J. T. Yates, Science (80-.). **322**, 1664 (2008), ISSN 0036-8075, URL http://www.sciencemag.org/cgi/doi/10.1126/science.1165291.

[27] D. R. Belcher, M. W. Radny, S. R. Schofield, P. V. Smith, and O. Warschkow, J. Am. Chem. Soc. **134**, 15312 (2012), ISSN 0002-7863, URL http://pubs.acs.org/doi/abs/10.1021/ja3026399.

[28] D. Menzel, J. Chem. Phys. **091702** (2012), URL http://link.aip.org/link/?JCPSA6/137/091702/1.

[29] P. Saalfrank, Chem. Rev. **106**, 4116 (2006), ISSN 0009-2665, URL http://pubs.acs.org/doi/abs/10.1021/cr0501691.

[30] K. Morgenstern, N. Lorente, and K.-H. Rieder, Phys. status solidi **250**, 1671 (2013), ISSN 03701972, URL http://doi.wiley.com/10.1002/pssb.201248392.

[31] Y. Nakamura, Y. Mera, and K. Maeda, Phys. Rev. Lett. **89**, 266805 (2002), ISSN 0031-9007, URL http://link.aps.org/doi/10.1103/PhysRevLett.89.266805.

[32] B. C. Stipe, M. A. Rezaei, and W. Ho, Phys. Rev. Lett. **79**, 4397 (1997), ISSN 0031-9007, URL http://link.aps.org/doi/10.1103/PhysRevLett.79.4397.

[33] A. Bellec, D. Riedel, G. Dujardin, O. Boudrioua, L. Chaput, L. Stauffer, and P. Sonnet, Phys. Rev. Lett. **105**, 048302 (2010), ISSN 0031-9007, URL http://link.aps.org/doi/10.1103/PhysRevLett.105.048302.

[34] R. Nouchi, K. Masunari, T. Ohta, Y. Kubozono, and Y. Iwasa, Phys. Rev. Lett. **97**, 196101 (2006), ISSN 0031-9007, URL http://link.aps.org/doi/10.1103/PhysRevLett.97.196101.

[35] P. Maksymovych, D. B. Dougherty, X.-Y. Zhu, and J. T. Yates, Phys. Rev. Lett. **99**, 016101 (2007), ISSN 0031-9007, URL http://link.aps.org/doi/10.1103/PhysRevLett.99.016101.

[36] P. A. Sloan, S. Sakulsermsuk, and R. E. Palmer, Phys. Rev. Lett. **105**, 048301 (2010), ISSN 0031-9007, URL http://link.aps.org/doi/10.1103/PhysRevLett.105.048301.

[37] L. Chen, H. Li, and A. T. S. Wee, ACS Nano **3**, 3684 (2009), ISSN 1936-086X, URL http://www.ncbi.nlm.nih.gov/pubmed/19877598.

[38] J. R. Hahn, S. H. Jang, K. W. Kim, and S. B. Son, J. Chem. Phys. **139**, 074707 (2013), ISSN 0021-9606, URL http://aip.scitation.org/doi/10.1063/1.4817947.

[39] Y. Takagi, Y. Yoshimoto, K. Nakatsuji, and F. Komori, J. Phys. Soc. Japan **74**, 3143 (2005), ISSN 0031-9015, 0510035, URL http://journals.jps.jp/doi/10.1143/JPSJ.74.3143.

[40] K. R. Rusimova, N. Bannister, P. Harrison, D. Lock, S. Crampin, R. E. Palmer, and P. A. Sloan, Nat. Commun. **7**, 12839 (2016), ISSN 2041-1723, URL http://www.nature.com/doifinder/10.1038/ncomms12839.

[41] P. H. Lu, J. C. Polanyi, and D. Rogers, J. Chem. Phys. **111**, 9905 (1999), ISSN 00219606, URL http://link.aip.org/link/JCPSA6/v111/i22/p9905/s1{&}Agg=doi.

[42] T. L. Pan, P. A. Sloan, and R. E. Palmer, J. Phys. Chem. Lett. **5**, 3551 (2014), ISSN 1948-7185, URL http://pubs.acs.org/doi/10.1021/jz501819n.

[43] D. Lock, K. R. Rusimova, T. L. Pan, R. E. Palmer, and P. A. Sloan, Nat. Commun. **6**, 8365 (2015), ISSN 2041-1723, URL http://www.nature.com/ncomms/2015/150921/ncomms9365/full/ncomms9365.html.

[44] P. A. Sloan and R. E. Palmer, Nano Lett. **5**, 835 (2005), ISSN 1530-6984, URL http://pubs.acs.org/doi/abs/10.1021/nl050142x.

[45] P. A. Sloan and R. E. Palmer, Nature **434**, 367 (2005), URL http://www.nature.com/nature/journal/v434/n7031/abs/nature03385.html.

[46] S. Sakulsermsuk, P. A. Sloan, and R. E. Palmer, ACS Nano **4**, 7344 (2010), ISSN 1936-0851, URL http://pubs.acs.org/doi/abs/10.1021/nn101468e.

[47] P. A. Sloan, M. F. G. Hedouin, R. E. Palmer, and M. Persson, Phys. Rev. Lett. **91**, 118301 (2003), ISSN 0031-9007, URL http://link.aps.org/doi/10.1103/PhysRevLett.91.118301.

[48] P. A. Sloan and R. E. Palmer, J. Phys. Condens. Matter **18**, S1873 (2006), ISSN 0953-8984, URL http://stacks.iop.org/0953-8984/18/i=33/a=S07?key=crossref.4455a7f43ab242c08e3f1fb0ef27dc73.

[49] S. Sakulsermsuk, P. A. Sloan, W. Theis, and R. E. Palmer, J. Phys. Condens. Matter **22**, 084002 (2010), ISSN 0953-8984, URL http://stacks.iop.org/0953-8984/22/i=8/a=084002?key=crossref.2cb28f4bd3741b463b07707f1d35da6d.

[50] R. E. Schlier and H. E. Farnsworth, J. Chem. Phys. **30**, 917 (1959), ISSN 0021-9606, URL http://aip.scitation.org/doi/10.1063/1.1730126.

[51] K. Takayanagi, Y. Tanishiro, S. Takahashi, and M. Takahashi, Surf. Sci. **164**, 367 (1985), ISSN 00396028, URL http://linkinghub.elsevier.com/retrieve/pii/0039602885907538.

[52] G. Binnig and H. Rohrer, Surf. Sci. **126**, 236 (1983), ISSN 00396028, URL http://linkinghub.elsevier.com/retrieve/pii/0039602883907161.

[53] R. J. Hamers, R. M. Tromp, and J. E. Demuth, Phys. Rev. Lett. **56**, 1972 (1986), ISSN 0031-9007, URL http://link.aps.org/doi/10.1103/PhysRevLett.56.1972.

[54] K. D. Brommer, M. Needels, B. Larson, and J. D. Joannopoulos, Phys. Rev. Lett. **68**, 1355 (1992), ISSN 0031-9007, URL http://link.aps.org/doi/10.1103/PhysRevLett.68.1355.

[55] M. A. Lantz, H. J. Hug, P. J. A. van Schendel, R. Hoffmann, S. Martin, A. Baratoff, A. Abdurixit, H.-J. Güntherodt, and C. Gerber, Phys. Rev. Lett. **84**, 2642

(2000), ISSN 0031-9007, URL http://link.aps.org/doi/10.1103/PhysRevLett.84.2642.

[56] T. Eguchi and Y. Hasegawa, Phys. Rev. Lett. **89**, 266105 (2002), ISSN 0031-9007, URL http://link.aps.org/doi/10.1103/PhysRevLett.89.266105.

[57] N. Suehira, Y. Sugawara, and S. Morita, Jpn. J. Appl. Phys. **40**, L292 (2001), ISSN 00214922, URL http://stacks.iop.org/1347-4065/40/L292.

[58] Y. Cao, J. F. Deng, and G. Q. Xu, J. Chem. Phys. **112**, 4759 (2000), ISSN 00219606, URL http://link.aip.org/link/JCPSA6/v112/i10/p4759/s1{&}Agg=doi.

[59] X. Chen, Q. Kong, J. Polanyi, D. Rogers, and S. So, Surf. Sci. **340**, 224 (1995), ISSN 00396028, URL http://linkinghub.elsevier.com/retrieve/pii/0039602895007326.

[60] T. Pan, P. A. Sloan, and R. E. Palmer, Chem. Rec. **14**, 841 (2014), ISSN 15278999, URL http://doi.wiley.com/10.1002/tcr.201402021.

[61] D. Lock, S. Sakulsermsuk, R. E. Palmer, and P. A. Sloan, J. Phys. Condens. Matter **27**, 054003 (2015), ISSN 0953-8984, URL http://stacks.iop.org/0953-8984/27/i=5/a=054003?key=crossref.262f069b55ea971736695a18e3c3b75c.

[62] B. C. Stipe, M. A. Rezaei, W. Ho, S. Gao, M. Persson, and B. I. Lundqvist, Phys. Rev. Lett. **78**, 4410 (1997), ISSN 0031-9007, URL http://link.aps.org/doi/10.1103/PhysRevLett.78.4410.

[63] K.-i. Shudo, S. Takeda, and T. Munakata, Phys. Rev. B **65**, 075302 (2002), ISSN 0163-1829, URL http://link.aps.org/doi/10.1103/PhysRevB.65.075302.

[64] R. Hamers, R. Tromp, and J. Demuth, Surf. Sci. **181**, 346 (1987), ISSN 00396028, URL http://linkinghub.elsevier.com/retrieve/pii/0039602887901762.

[65] M. Mauerer, I. L. Shumay, W. Berthold, and U. Höfer, Phys. Rev. B **73**, 245305 (2006), ISSN 1098-0121, URL http://link.aps.org/doi/10.1103/PhysRevB.73.245305.

[66] T. Ichibayashi, S. Tanaka, J. Kanasaki, K. Tanimura, and T. Fauster, Phys. Rev. B **84**, 235210 (2011), ISSN 1098-0121, URL http://link.aps.org/doi/10.1103/PhysRevB.84.235210.

[67] J. A. McGuire, M. B. Raschke, and Y. R. Shen, Phys. Rev. Lett. **96**, 087401 (2006), ISSN 0031-9007, URL http://link.aps.org/doi/10.1103/PhysRevLett.96.087401.

[68] M. Bernardi, D. Vigil-Fowler, J. Lischner, J. B. Neaton, and S. G. Louie, Phys. Rev. Lett. **112**, 257402 (2014), ISSN 0031-9007, URL http://link.aps.org/doi/10.1103/PhysRevLett.112.257402.

[69] D. E. Brown, Science (80-.). **279**, 542 (1998), ISSN 00368075, URL http://www.sciencemag.org/cgi/doi/10.1126/science.279.5350.542.

[70] J. C. Love, L. A. Estroff, J. K. Kriebel, R. G. Nuzzo, and G. M. Whitesides, Chem. Rev. **105**, 1103 (2005), ISSN 0009-2665, URL http://pubs.acs.org/doi/abs/10.1021/cr0300789.

[71] C. Vericat, M. E. Vela, G. Benitez, P. Carro, and R. C. Salvarezza, Chem. Soc. Rev. **39**, 1805 (2010), ISSN 0306-0012, URL http://xlink.rsc.org/?DOI=b907301a.

[72] C. Nogues and M. Wanunu, Surf. Sci. **573**, L383 (2004), ISSN 00396028, URL http://linkinghub.elsevier.com/retrieve/pii/S0039602804013275.

[73] F. Schreiber, Prog. Surf. Sci. **65**, 151 (2000), ISSN 00796816, 9605103.

[74] R. Shukla, V. Bansal, M. Chaudhary, A. Basu, R. R. Bhonde, and M. Sastry, Langmuir **21**, 10644 (2005), ISSN 0743-7463, URL http://pubs.acs.org/doi/abs/10.1021/la0513712.

[75] K. Rege and I. L. Medintz, *Methods in Bioengineering: Nanoscale Bioengineering and Nanomedicine* (Artech House, 2009), ISBN 978-1-59693-410-8.

[76] O. Azzaroni, M. Cipollone, M. E. Vela, and R. C. Salvarezza, Langmuir **17**, 1483 (2001), ISSN 0743-7463, URL http://pubs.acs.org/doi/abs/10.1021/la000852c.

[77] G. Brunoro, A. Frignani, A. Colledan, and C. Chiavari, Corros. Sci. **45**, 2219 (2003), ISSN 0010938X, URL http://linkinghub.elsevier.com/retrieve/pii/S0010938X03000659.

[78] H. Liu, B. Bhushan, W. Eck, and V. Stadler, J. Vac. Sci. Technol. A Vacuum, Surfaces, Film. **19**, 1234 (2001), ISSN 0734-2101, URL http://avs.scitation.org/doi/10.1116/1.1353538.

[79] A. Lio, D. H. Charych, and M. Salmeron, J. Phys. Chem. B **101**, 3800 (1997), ISSN 1520-6106, URL http://pubs.acs.org/doi/abs/10.1021/jp963918e.

[80] G. M. Whitesides and P. E. Laibinis, Langmuir **6**, 87 (1990), ISSN 0743-7463, URL http://pubs.acs.org/doi/abs/10.1021/la00091a013.

[81] a. GoÌĹlzhaÌĹuser, W. Geyer, V. Stadler, W. Eck, M. Grunze, K. Edinger, T. Weimann, and P. Hinze, J. Vac. Sci. Technol. B Microelectron. Nanom. Struct. **18**, 3414 (2000), ISSN 0734211X, URL http://scitation.aip.org/content/avs/journal/jvstb/18/6/10.1116/1.1319711.

[82] M. Zharnikov and M. Grunze, J. Vac. Sci. Technol. B Microelectron. Nanom. Struct. **20**, 1793 (2002), ISSN 0734211X, URL http://scitation.aip.org/content/avs/journal/jvstb/20/5/10.1116/1.1514665.

[83] C. Roberts, C. S. Chen, M. Mrksich, V. Martichonok, D. E. Ingber, and G. M. Whitesides, J. Am. Chem. Soc. **120**, 6548 (1998), ISSN 0002-7863, URL http://pubs.acs.org/doi/abs/10.1021/ja972467o.

[84] X. Jiang, D. A. Bruzewicz, A. P. Wong, M. Piel, and G. M. Whitesides, Proc. Natl. Acad. Sci. **102**, 975 (2005), ISSN 0027-8424, URL http://www.pnas.org/cgi/doi/10.1073/pnas.0408954102.

[85] S. Takeuchi, W. R. DiLuzio, D. B. Weibel, and G. M. Whitesides, Nano Lett. **5**, 1819 (2005), ISSN 1530-6984, URL http://pubs.acs.org/doi/abs/10.1021/nl0507360.

[86] W.-S. Yeo and M. Mrksich, Angew. Chemie Int. Ed. **42**, 3121 (2003), ISSN 14337851, URL http://doi.wiley.com/10.1002/anie.200250862.

[87] M. Riepl, K. Enander, B. Liedberg, M. Schäferling, M. Kruschina, and F. Ortigao, Langmuir **18**, 7016 (2002), ISSN 0743-7463, URL http://pubs.acs.org/doi/abs/10.1021/la011732n.

[88] R. Shenhar and V. M. Rotello, Acc. Chem. Res. **36**, 549 (2003), ISSN 0001-4842, URL http://pubs.acs.org/doi/abs/10.1021/ar020083j.

[89] M. C. M. Daniel and D. Astruc, Chem. Rev. **104**, 293 (2004), ISSN 00092665, 0403600v1, URL http://pubs.acs.org/doi/abs/10.1021/cr030698{%}2B.

[90] R. Hong, N. O. Fischer, A. Verma, C. M. Goodman, T. Emrick, and V. M. Rotello, J. Am. Chem. Soc. **126**, 739 (2004), ISSN 0002-7863, URL http://pubs.acs.org/doi/abs/10.1021/ja037470o.

[91] Y.-J. Han and J. Aizenberg, Angew. Chemie Int. Ed. **42**, 3668 (2003), ISSN 1433-7851, URL http://doi.wiley.com/10.1002/anie.200351655.

[92] T. J. Huang, B. Brough, C.-M. Ho, Y. Liu, A. H. Flood, P. A. Bonvallet, H.-R. Tseng, J. F. Stoddart, M. Baller, and S. Magonov, Appl. Phys. Lett. **85**, 5391 (2004), ISSN 0003-6951, URL http://aip.scitation.org/doi/10.1063/1.1826222.

[93] L. A. Bumm, J. J. Arnold, M. T. Cygan, T. D. Dunbar, T. P. Burgin, L. Jones, D. L. Allara, J. M. Tour, and P. S. Weiss, Science (80-.). **271**, 1705 (1996), ISSN 0036-8075, URL http://www.sciencemag.org/cgi/doi/10.1126/science.271.5256.1705.

[94] L. Venkataraman, J. E. Klare, I. W. Tam, C. Nuckolls, M. S. Hybertsen, and M. L. Steigerwald, Nano Lett. **6**, 458 (2006), ISSN 15306984, 0603281, URL http://dx.doi.org/10.1021/nl052373+.

[95] J. M. Tour, Acc. Chem. Res. **33**, 791 (2000), ISSN 0001-4842, URL http://pubs.acs.org/doi/abs/10.1021/ar0000612.

[96] T. Sugawara and M. M. Matsushita, J. Mater. Chem. **19**, 1738 (2009), ISSN 0959-9428, URL http://xlink.rsc.org/?DOI=b818851n.

[97] K. Schouteden, P. Lievens, and C. Van Haesendonck, Phys. Rev. B **79**, 195409 (2009), ISSN 1098-0121, URL http://link.aps.org/doi/10.1103/PhysRevB.79.195409.

[98] J. V. Barth, H. Brune, G. Ertl, and R. J. Behm, Phys. Rev. B **42**, 9307 (1990), ISSN 0163-1829, URL http://link.aps.org/doi/10.1103/PhysRevB.42.9307.

[99] D. M. Zehner and J. F. Wendelken, in *Proc. 7th Intern. Vac. Congr. 3rd Intern. Conf. Solid Surfaces (Vienna 1977)* (1977), pp. 1–5, URL https://www.osti.gov/scitech/biblio/5282236.

[100] J. Wendelken and D. Zehner, Surf. Sci. **71**, 178 (1978), ISSN 00396028, URL http://linkinghub.elsevier.com/retrieve/pii/0039602878903254.

[101] M. Van Hove, R. Koestner, P. Stair, J. Bibérian, L. Kesmodel, I. Bartoš, and G. Somorjai, Surf. Sci. **103**, 218 (1981), ISSN 00396028, URL http://linkinghub.elsevier.com/retrieve/pii/0039602881901084.

[102] Y. Tanishiro, H. Kanamori, K. Takayanagi, K. Yagi, and G. Honjo, Surf. Sci. **111**, 395 (1981), ISSN 00396028, URL http://linkinghub.elsevier.com/retrieve/pii/0039602881903976.

[103] K. Takayanagi and K. Yagi, Trans. Japan Inst. Met. **24**, 337 (1983), ISSN 0021-4434, URL https://www.jstage.jst.go.jp/article/matertrans1960/24/6/24{_}6{_}337/{_}article.

[104] U. Harten, A. M. Lahee, J. P. Toennies, and C. Wöll, Phys. Rev. Lett. **54**, 2619 (1985), ISSN 0031-9007, URL http://link.aps.org/doi/10.1103/PhysRevLett.54.2619.

[105] W. Kaiser and R. Jaklevic, Surf. Sci. **182**, L227 (1987), ISSN 00396028, URL http://linkinghub.elsevier.com/retrieve/pii/003960288790001X.

[106] V. M. Hallmark, S. Chiang, J. F. Rabolt, J. D. Swalen, and R. J. Wilson, Phys. Rev. Lett. **59**, 2879 (1987), ISSN 0031-9007, URL http://link.aps.org/doi/10.1103/PhysRevLett.59.2879.

[107] C. Wöll, S. Chiang, R. J. Wilson, and P. H. Lippel, Phys. Rev. B **39**, 7988 (1989), ISSN 0163-1829, URL http://link.aps.org/doi/10.1103/PhysRevB.39.7988.

[108] F. Hanke and J. Björk, Phys. Rev. B **87**, 235422 (2013), ISSN 1098-0121, URL http://link.aps.org/doi/10.1103/PhysRevB.87.235422.

[109] L. Grill, M. Dyer, L. Lafferentz, M. Persson, M. V. Peters, and S. Hecht, Nat. Nanotechnol. **2**, 687 (2007), ISSN 1748-3387, URL http://www.nature.com/doifinder/10.1038/nnano.2007.346.

[110] Y.-C. Xie, L. Tang, and Q. Guo, Phys. Rev. Lett. **111**, 186101 (2013), ISSN 0031-9007, URL http://link.aps.org/doi/10.1103/PhysRevLett.111.186101.

[111] J. Wang, M. McEntee, W. Tang, M. Neurock, A. P. Baddorf, P. Maksymovych, and J. T. Yates, J. Am. Chem. Soc. **138**, 1518 (2016), ISSN 0002-7863, arXiv: 1408.1149, URL http://pubs.acs.org/doi/abs/10.1021/jacs.5b09052.

[112] T. Bürgi, Nanoscale **7**, 15553 (2015), ISSN 2040-3364, URL http://xlink.rsc.org/?DOI=C5NR03497C.

[113] A. Riposan and G.-y. Liu, J. Phys. Chem. B **110**, 23926 (2006), ISSN 1520-6106, URL http://pubs.acs.org/doi/abs/10.1021/jp063774w.

[114] R. Staub, M. Toerker, T. Fritz, T. Schmitz-Hübsch, F. Sellam, and K. Leo, Langmuir **14**, 6693 (1998), ISSN 0743-7463, URL http://pubs.acs.org/doi/abs/10.1021/la980717o.

[115] C. E. D. Chidsey, G.-Y. Liu, P. Rowntree, and G. Scoles, J. Chem. Phys. **91**, 4421 (1989), ISSN 0021-9606, arXiv:1011.1669v3, URL http://aip.scitation.org/doi/10.1063/1.456776.

[116] C. A. Alves, E. L. Smith, and M. D. Porter, J. Am. Chem. Soc. **114**, 1222 (1992), ISSN 0002-7863, URL http://pubs.acs.org/doi/abs/10.1021/ja00030a015.

[117] L. H. Dubois, B. R. Zegarski, and R. G. Nuzzo, J. Chem. Phys. **98**, 678 (1993), ISSN 0021-9606, URL http://aip.scitation.org/doi/10.1063/1.464613.

[118] C. Vericat, M. E. Vela, and R. C. Salvarezza, Phys. Chem. Chem. Phys. **7**, 3258 (2005), ISSN 1463-9076, URL http://xlink.rsc.org/?DOI=b505903h.

[119] K. Beardmore, J. Kress, A. Bishop, and N. Grønbech-Jensen, Synth. Met. **84**, 317 (1997), ISSN 03796779, URL http://linkinghub.elsevier.com/retrieve/pii/S0379677997807643.

[120] P. Fenter, A. Eberhardt, and P. Eisenberger, Science (80-.). **266**, 1216 (1994), ISSN 0036-8075, URL http://www.sciencemag.org/cgi/doi/10.1126/science.266.5188.1216.

[121] F. Terán Arce, M. E. Vela, R. C. Salvarezza, and A. J. Arvia, J. Chem. Phys. **109**, 5703 (1998), ISSN 0021-9606, URL http://aip.scitation.org/doi/10.1063/1.477190.

[122] X. Torrelles, E. Barrena, C. Munuera, J. Rius, S. Ferrer, and C. Ocal, Langmuir **20**, 9396 (2004), ISSN 0743-7463, URL http://pubs.acs.org/doi/abs/10.1021/la048979f.

[123] Q. Sun, A. Selloni, and G. Scoles, J. Phys. Chem. B **110**, 3493 (2006), ISSN 1520-6106, URL http://pubs.acs.org/doi/abs/10.1021/jp053673i.

[124] D. Aswal, S. Lenfant, D. Guerin, J. Yakhmi, and D. Vuillaume, Anal. Chim. Acta **568**, 84 (2006), ISSN 00032670, URL http://linkinghub.elsevier.com/retrieve/pii/S000326700501754X.

[125] L. Sun, Y. A. Diaz-Fernandez, T. A. Gschneidtner, F. Westerlund, S. Lara-Avila, and K. Moth-Poulsen, Chem. Soc. Rev. **43**, 7378 (2014), ISSN 0306-0012, URL http://xlink.rsc.org/?DOI=C4CS00143E.

[126] T. Shimada, H. Kondoh, I. Nakai, M. Nagasaka, R. Yokota, K. Amemiya, and T. Ohta, Chem. Phys. Lett. **406**, 232 (2005), ISSN 00092614, URL http://linkinghub.elsevier.com/retrieve/pii/S0009261405002642.

[127] E. Verveniotis, Y. Okawa, M. V. Makarova, Y. Koide, J. Liu, B. Šmíd, K. Watanabe, T. Taniguchi, K. Komatsu, T. Minari, et al., Phys. Chem. Chem. Phys. **18**, 31600 (2016), ISSN 1463-9076, URL http://xlink.rsc.org/?DOI=C6CP06749B.

[128] J. S. Prauzner-Bechcicki, S. Godlewski, and M. Szymonski, Phys. status solidi **209**, 603 (2012), ISSN 18626300, URL http://doi.wiley.com/10.1002/pssa.201127623.

[129] T. Y. B. Leung, M. C. Gerstenberg, D. J. Lavrich, G. Scoles, F. Schreiber, and

G. E. Poirier, Langmuir **16**, 549 (2000), ISSN 0743-7463, URL http://pubs.acs.org/doi/abs/10.1021/la9906222.

[130] M. A. D. Millone, H. Hamoudi, L. RodriÌĄguez, A. Rubert, G. A. BeniÌĄtez, M. E. Vela, R. C. Salvarezza, J. E. Gayone, E. A. SaÌĄnchez, O. Grizzi, et al., Langmuir **25**, 12945 (2009), ISSN 0743-7463, URL http://pubs.acs.org/doi/abs/10.1021/la901601z.

[131] J. Gao, F. Li, and Q. Guo, J. Phys. Chem. C **117**, 24985 (2013), ISSN 1932-7447, URL http://pubs.acs.org/doi/abs/10.1021/jp410738e.

[132] R. H. Terrill, T. A. Postlethwaite, C.-h. Chen, C.-D. Poon, A. Terzis, A. Chen, J. E. Hutchison, M. R. Clark, and G. Wignall, J. Am. Chem. Soc. **117**, 12537 (1995), ISSN 0002-7863, URL http://pubs.acs.org/doi/abs/10.1021/ja00155a017.

[133] W. D. Luedtke and U. Landman, J. Phys. Chem. B **102**, 6566 (1998), ISSN 1520-6106, URL http://pubs.acs.org/doi/abs/10.1021/jp981745i.

[134] P. Maksymovych, D. C. Sorescu, and J. T. Yates, Phys. Rev. Lett. **97**, 146103 (2006), ISSN 0031-9007, URL http://link.aps.org/doi/10.1103/PhysRevLett.97.146103.

[135] H. Kondoh, M. Iwasaki, T. Shimada, K. Amemiya, T. Yokoyama, T. Ohta, M. Shimomura, and S. Kono, Phys. Rev. Lett. **90**, 066102 (2003), ISSN 0031-9007, URL http://link.aps.org/doi/10.1103/PhysRevLett.90.066102.

[136] M. Roper, M. Skegg, C. Fisher, J. Lee, V. Dhanak, D. Woodruff, and R. G. Jones, Chem. Phys. Lett. **389**, 87 (2004), ISSN 00092614, URL http://linkinghub.elsevier.com/retrieve/pii/S0009261404003082.

[137] M. Esplandiu, M. Carot, F. Cometto, V. Macagno, and E. Patrito, Surf. Sci. **600**, 155 (2006), ISSN 00396028, URL http://linkinghub.elsevier.com/retrieve/pii/S0039602805011490.

[138] J. Zhang, Chi, and J. Ulstrup, Langmuir **22**, 6203 (2006), ISSN 0743-7463, URL http://pubs.acs.org/doi/abs/10.1021/la0605891.

[139] J. A. M. Sondag-Huethorst, C. Schonenberger, and L. G. J. Fokkink, J. Phys. Chem. **98**, 6826 (1994), ISSN 0022-3654, arXiv:0807.1631v1, URL http://pubs.acs.org/doi/abs/10.1021/j100078a027.

[140] J.-P. Bucher, L. Santesson, and K. Kern, Langmuir **10**, 979 (1994), ISSN 0743-7463, URL http://pubs.acs.org/doi/abs/10.1021/la00016a001.

[141] G. E. Poirier and E. D. Pylant, Science (80-.). **272**, 1145 (1996), ISSN 0036-8075, URL http://www.sciencemag.org/cgi/doi/10.1126/science.272.5265.1145.

[142] L. Tang, F. Li, W. Zhou, and Q. Guo, Surf. Sci. **606**, L31 (2012), ISSN 00396028, URL http://linkinghub.elsevier.com/retrieve/pii/S0039602811004742.

[143] F. Li, L. Tang, O. Voznyy, J. Gao, and Q. Guo, J. Chem. Phys. **138**, 194707 (2013), ISSN 0021-9606, URL http://aip.scitation.org/doi/10.1063/1.4806969.

[144] P. Maksymovych and J. T. Yates, J. Am. Chem. Soc. **130**, 7518 (2008), ISSN 0002-7863, URL http://pubs.acs.org/doi/abs/10.1021/ja800577w.

[145] D. Dougherty, P. Maksymovych, and J. Yates, Surf. Sci. **600**, 4484 (2006), ISSN 00396028, URL http://linkinghub.elsevier.com/retrieve/pii/S0039602806007977.

[146] C. Vericat, M. E. Vela, G. Corthey, E. Pensa, E. Cortés, M. H. Fonticelli, F. Ibañez, G. E. Benitez, P. Carro, and R. C. Salvarezza, RSC Adv. **4**, 27730 (2014), ISSN 2046-2069, URL http://xlink.rsc.org/?DOI=c4ra04659e.

[147] L. Tang, F. S. Li, and Q. Guo, J. Phys. Chem. C **117**, 21234 (2013), ISSN 1932-7447, URL http://pubs.acs.org/doi/abs/10.1021/jp4058127.

[148] J. M. Lafferty, *Foundations of Vacuum Science and Technology* (Wiley, 1998), ISBN 0471175935, URL http://physicstoday.scitation.org/doi/10.1063/1.882616.

[149] L. Schulz, CAS - Cern Accel. Sch. Vac. Technol. pp. 37–42 (1999), URL https://cds.cern.ch/record/454179/files/p37.pdf.

[150] G. L. Weissler and R. W. Carlson, *Methods Of Experimental Physics14: Vacuum Physics and Technology* (Academic Press Inc, New York, 1979), ISBN 0-12-475914-9.

[151] M. Schmid and P. Varga, Ultramicroscopy **42-44**, 1610 (1992), ISSN 03043991.

[152] A. Z. Stieg, P. Wilkinson, and J. K. Gimzewski, Rev. Sci. Instrum. **78**, 1 (2007), ISSN 00346748.

[153] B. F. Ju, Y. L. Chen, and Y. Ge, Rev. Sci. Instrum. **82** (2011), ISSN 00346748.

[154] J. P. Ibe, P. P. Bey, S. L. Brandow, R. A. Brizzolara, N. A. Burnham, D. P. DiLella, K. P. Lee, C. R. K. Marrian, and R. J. Colton, J. Vac. Sci. Technol. A Vacuum, Surfaces, Film. **8**, 3570 (1990), ISSN 0734-2101, URL http://avs.scitation.org/doi/10.1116/1.576509.

[155] R. J. Cobley, R. a. Brown, C. J. Barnett, T. G. G. Maffeis, and M. W. Penny, Appl. Phys. Lett. **102**, 023111 (2013), ISSN 00036951, URL http://link.aip.org/link/APPLAB/v102/i2/p023111/s1{&}Agg=doi.

[156] A.-S. A. Lucier, H. Mortensen, Y. Sun, and P. Grütter, Phys. Rev. B **72**, 1 (2005), ISSN 1098-0121, URL http://link.aps.org/doi/10.1103/PhysRevB.72.235420http://prb.aps.org/abstract/PRB/v72/i23/e235420.

[157] G. Binnig, H. Rohrer, F. Salvan, C. Gerber, and A. Baro, Surf. Sci. **157**, 373 (1985), ISSN 00396028.

[158] H. Neddermeyer, Reports Prog. Phys. **59**, 701 (1999), ISSN 0034-4885.

[159] T. Shen, C. Wang, J. Lyding, and J. Tucker, Phys. Rev. B **5** (1994), URL http://prb.aps.org/abstract/PRB/v50/i11/p7453{_}1.

[160] Sigma-Aldrich, *Dimethyl disulfide âĽě99.0% | Sigma-Aldrich*, URL http://www.sigmaaldrich.com/catalog/product/aldrich/471569?lang=en{&}region=GB.

[161] Sigma-Aldrich, *Chlorobenzene, anhydrous, 99.8% | C6H5Cl | Sigma-Aldrich*, URL http://www.sigmaaldrich.com/catalog/product/sial/284513?lang=en{&}region=GB.

[162] D. Vicic and G. Jones, Compr. Organomet. Chem. III **12**, 197 (2007), ISSN 00104485, URL http://linkinghub.elsevier.com/retrieve/pii/0010448580900962{%}5Cnhttp://linkinghub.elsevier.com/retrieve/pii/B008045047400008X.

[163] NIST Mass Spec Data Center director S. E. Stein, in *NIST Chem. WebBook, NIST Stand. Ref. Database Number 69*, edited by P. Linstrom and W. Mallard (National Institute of Standards and Technology, Gaithersburg MD, 20899, 2017), URL http://webbook.nist.gov/cgi/cbook.cgi?ID=C108907{&}Mask=200{#}Mass-Spec.

[164] J. Gao, L. Tang, S. Holmes, F. Li, R. E. Palmer, and Q. Guo, Nanoscale **8**, 19787 (2016), ISSN 2040-3364, URL http://xlink.rsc.org/?DOI=C6NR06864B.

[165] H. Röder, E. Hahn, H. Brune, J.-P. Bucher, and K. Kern, Nature **366**, 141 (1993), ISSN 0028-0836, URL http://www.nature.com/doifinder/10.1038/366141a0.

[166] J. V. Barth, H. Brune, T. Zambelli, and K. Kern, Tech. Rep., Nova Science Pub Incorporated (1998), URL http://www.fkf.mpg.de/52028/kk158.pdf.

[167] D.-e. Jiang and S. Dai, J. Phys. Chem. C **113**, 3763 (2009), ISSN 1932-7447, URL http://pubs.acs.org/doi/abs/10.1021/jp810404n.

[168] A. Franke and E. Pehlke, Phys. Rev. B **79**, 235441 (2009), ISSN 1098-0121, URL https://link.aps.org/doi/10.1103/PhysRevB.79.235441.

[169] S. J. Stranick, A. N. Parikh, D. L. Allara, and P. S. Weiss, J. Phys. Chem. **98**, 11136 (1994), ISSN 0022-3654, URL http://pubs.acs.org/doi/abs/10.1021/j100094a024.

[170] F. Jensen, F. Besenbacher, E. Laegsgaard, and I. Stensgaard, Phys. Rev. B **41**, 10233 (1990), ISSN 0163-1829, URL https://link.aps.org/doi/10.1103/PhysRevB.41.10233.

[171] Y. C. Yang, A. Taranovskyy, and O. M. Magnussen, Langmuir **28**, 14143 (2012), ISSN 07437463.

[172] Y.-C. Yang and O. M. Magnussen, Phys. Chem. Chem. Phys. **15**, 12480 (2013), ISSN 1463-9076, URL http://xlink.rsc.org/?DOI=c3cp51027a.

[173] O. Voznyy, J. J. Dubowski, J. T. Yates, and P. Maksymovych, J. Am. Chem. Soc. **131**, 12989 (2009), ISSN 0002-7863, URL http://pubs.acs.org/doi/abs/10.1021/ja902629y.

[174] D.-e. Jiang and S. Dai, Phys. Chem. Chem. Phys. **11**, 8601 (2009), ISSN 1463-9076, URL http://xlink.rsc.org/?DOI=b902966d.

[175] K.-Y. Kwon, K. L. Wong, G. Pawin, L. Bartels, S. Stolbov, and T. S. Rahman, Phys. Rev. Lett. **95**, 166101 (2005), ISSN 0031-9007, URL https://link.aps.org/doi/10.1103/PhysRevLett.95.166101.

[176] K. L. Wong, G. Pawin, K.-Y. Kwon, X. Lin, T. Jiao, U. Solanki, R. H. J. Fawcett, L. Bartels, S. Stolbov, and T. S. Rahman, Science (80-.). **315**, 1391 (2007), ISSN 0036-8075, URL http://www.sciencemag.org/cgi/doi/10.1126/science.1135302.

[177] M. Schunack, T. R. Linderoth, F. Rosei, E. Lægsgaard, I. Stensgaard, and F. Besenbacher, Phys. Rev. Lett. **88**, 156102 (2002), ISSN 0031-9007, URL https://link.aps.org/doi/10.1103/PhysRevLett.88.156102.

[178] J. S. Raut and K. A. Fichthorn, J. Chem. Phys. **108**, 1626 (1998), ISSN 0021-9606, URL http://aip.scitation.org/doi/10.1063/1.475533.

[179] H. Marbach and H.-P. Steinrück, Chem. Commun. **50**, 9034 (2014), ISSN 1359-7345, URL http://xlink.rsc.org/?DOI=C4CC01744G.

[180] A. Franke and E. Pehlke, Phys. Rev. B **82**, 205423 (2010), ISSN 1098-0121, URL https://link.aps.org/doi/10.1103/PhysRevB.82.205423.

[181] Y. Sugimoto, A. Yurtsever, N. Hirayama, M. Abe, and S. Morita, Nat. Commun. **5**, 1 (2014), ISSN 2041-1723, URL http://www.nature.com/doifinder/10.1038/ncomms5360.

[182] M. Eichberger, M. Marschall, J. Reichert, A. Weber-Bargioni, W. AuwaÌĹrter, R. L. C. Wang, H. J. Kreuzer, Y. Pennec, A. Schiffrin, and J. V. Barth, Nano Lett. **8**, 4608 (2008), ISSN 1530-6984, URL http://pubs.acs.org/doi/abs/10.1021/nl802995u.

[183] B. M. Barngrover and C. M. Aikens, J. Phys. Chem. A **115**, 11818 (2011), ISSN 1089-5639, URL http://pubs.acs.org/doi/abs/10.1021/jp2061893.

[184] Y. Xie, Ph.D. thesis, University of Birmingham (2013), URL http://etheses.bham.ac.uk/4810/1/Xie14PhD.pdf.

[185] a. Cossaro, R. Mazzarello, R. Rousseau, L. Casalis, A. Verdini, A. Kohlmeyer, L. Floreano, S. Scandolo, A. Morgante, M. L. Klein, et al., Science (80-.). **321**, 943 (2008), ISSN 0036-8075, URL http://www.sciencemag.org/cgi/doi/10.1126/science.1158532.

[186] X.-L. Fan, P. Xiao, R.-X. Ran, and W.-M. Lau, Phys. Chem. Chem. Phys. **16**, 2533 (2014), ISSN 1463-9076, URL http://xlink.rsc.org/?DOI=c3cp54315c.

[187] G. D. Barmparis, K. Honkala, and I. N. Remediakis, J. Chem. Phys. **138**, 064702 (2013), ISSN 0021-9606, URL http://aip.scitation.org/doi/10.1063/1.4790368.

[188] J. P. Lewis, in *Vis. Interface '95* (Quebec, 1995), pp. 120–123, URL http://www.cipprs.org/papers/VI/VI1995/pp120-123-Lewis-1995.pdf.

[189] S. van der Walt, J. L. Schönberger, J. Nunez-Iglesias, F. Boulogne, J. D. Warner, N. Yager, E. Gouillart, and T. Yu, PeerJ **2**, e453 (2014), ISSN 2167-8359, 1407.6245, URL https://peerj.com/articles/453.

[190] *MATLAB and Image Processing Toolbox Release 2009b* (The MathWorks, Inc., Natick, Massachusetts, 2009).

[191] R. T. Collins and Y. Liu, Proc. IEEE Conf. Comput. Vis. Pattern Recognition. CVPR 2000 (Cat. No.PR00662) **1**, 537 (2000), URL http://ieeexplore.ieee.org/lpdocs/epic03/wrapper.htm?arnumber=855866.

[192] P. Rahe, R. Bechstein, and A. Kühnle, J. Vac. Sci. Technol. B, Nanotechnol. Microelectron. Mater. Process. Meas. Phenom. **28**, C4E31 (2010), ISSN 2166-2746, URL http://avs.scitation.org/doi/10.1116/1.3360909.

[193] M. Balkanski and R. F. Wallis, *Semiconductor physics and applications* (Oxford University Press, 2000), ISBN 9780198517405.

[194] Y. Cao, X. M. Wei, W. S. Chin, Y. H. Lai, J. F. Deng, S. L. Bernasek, and G. Q. Xu, J. Phys. Chem. B **103**, 5698 (1999), ISSN 1520-6106, URL http://pubs.acs.org/doi/abs/10.1021/jp9904791.

[195] X. Lu, J. C. Polanyi, and J. S. Y. Yang, Nano Lett. **6**, 809 (2006), ISSN 1530-6984, URL http://pubs.acs.org/doi/abs/10.1021/nl0601379.

[196] A. Modelli and M. Venuti, J. Phys. Chem. A **105**, 5836 (2001), ISSN 1089-5639, URL http://pubs.acs.org/doi/abs/10.1021/jp010430r.

[197] I. I. Fabrikant and H. Hotop, J. Chem. Phys. **128**, 124308 (2008), ISSN 0021-9606, URL http://aip.scitation.org/doi/10.1063/1.2841079.

[198] P. Saalfrank, T. Vazhappilly, S. Beyvers, G. Paramonov, and T. Klamroth, Surf. Sci. **602**, 3153 (2008), ISSN 00396028, URL http://linkinghub.elsevier.com/retrieve/pii/S0039602808004500.

[199] D. Kröner, S. Klinkusch, and T. Klamroth, Surf. Sci. **602**, 3148 (2008), ISSN 00396028, URL http://linkinghub.elsevier.com/retrieve/pii/S0039602808004469.

[200] J. Kim, M.-L. Yeh, F. S. Khan, and J. W. Wilkins, Phys. Rev. B **52**, 14709 (1995), ISSN 0163-1829, URL http://link.aps.org/doi/10.1103/PhysRevB.52.14709.

[201] I. Štich, Surf. Sci. **368**, 152 (1996), ISSN 00396028, URL http://linkinghub.elsevier.com/retrieve/pii/S003960289601045X.

[202] G. Lange, J. P. Toennies, P. Ruggerone, and G. Benedek, Europhys. Lett. **41**, 647 (1998), ISSN 0295-5075, URL http://stacks.iop.org/0295-5075/41/i=6/a=647?key=crossref.c11a96033a1f1b21b819ffb7f8206b4b.

[203] W. Daum, H. Ibach, and J. E. Müller, Phys. Rev. Lett. **59**, 1593 (1987), ISSN 0031-9007, URL http://link.aps.org/doi/10.1103/PhysRevLett.59.1593.

[204] K. R. Rusimova and P. A. Sloan, Nanotechnology **28**, 054002 (2017), ISSN 0957-4484, URL http://stacks.iop.org/0957-4484/28/i=5/a=054002?key=crossref.1e5bd47d71337c2f1bbfe50bdbd24330.

[205] *Private communication.*

[206] G. Dujardin, A. J. Mayne, and F. Rose, Phys. Rev. Lett. **89**, 036802 (2002), ISSN 0031-9007, URL http://link.aps.org/doi/10.1103/PhysRevLett.89.036802.

[207] R. M. Feenstra, S. Gaan, G. Meyer, and K. H. Rieder, Phys. Rev. B **71**, 125316 (2005), ISSN 1098-0121, URL http://link.aps.org/doi/10.1103/PhysRevB.71.125316.

[208] J. Mysliveček, A. Stróżecka, J. Steffl, P. Sobotík, I. Ošt'ádal, and B. Voigtländer, Phys. Rev. B **73**, 161302 (2006), ISSN 1098-0121, URL http://link.aps.org/doi/10.1103/PhysRevB.73.161302.

[209] S. Modesti, H. Gutzmann, J. Wiebe, and R. Wiesendanger, Phys. Rev. B **80**, 125326 (2009), ISSN 1098-0121, URL http://link.aps.org/doi/10.1103/PhysRevB.80.125326.

[210] Y. C. Liao, C. K. Yang, T. L. Wu, I. S. Hwang, M. K. Wu, and C. C. Chi, Phys. Rev. B **81**, 195435 (2010), ISSN 1098-0121, URL http://link.aps.org/doi/10.1103/PhysRevB.81.195435.

[211] L. J. Lauhon and W. Ho, J. Phys. Chem. A **104**, 2463 (2000), ISSN 1089-5639, URL http://pubs.acs.org/doi/abs/10.1021/jp991768c.

[212] X.-L. Zhou and J. M. White, J. Chem. Phys. **92**, 5612 (1990), ISSN 0021-9606, URL http://aip.scitation.org/doi/10.1063/1.458493.

[213] S. Sakurai and T. Nakayama, Jpn. J. Appl. Phys. **41**, 2171 (2002), ISSN 0021-4922, URL http://stacks.iop.org/1347-4065/41/2171.

[214] H. Lesnard, N. Lorente, and M.-L. Bocquet, J. Phys. Condens. Matter **20**, 224012 (2008), ISSN 0953-8984, URL http://stacks.iop.org/0953-8984/20/i=22/a=224012?key=crossref.51c06e9c1647f854f4d1882792690e8b.

[215] L. Muzangwa, S. Nyambo, B. Uhler, and S. A. Reid, J. Chem. Phys. **137**, 184307 (2012), ISSN 0021-9606, URL http://aip.scitation.org/doi/10.1063/1.4765102.